Experimental implementation and study of the lightning swept-stroke along an aircraft

Vincent Andraud

Vincent Andraud. Experimental implementation and study of the lightning swept-stroke along an aircraft. Electric power. Université Paris-Saclay, 2022. English. NNT : 2022UPAST030 . tel-03730912

HAL Id: tel-03730912
https://theses.hal.science/tel-03730912

Submitted on 20 Jul 2022

Experimental implementation and study of the lightning swept-stroke along an aircraft

Etude expérimentale du phénomène de balayage de l'arc électrique lors du foudroiement d'un aéronef

Thèse de doctorat de l'université Paris-Saclay

École doctorale n° 575 : electrical, optical, bio : physics and engineering (EOBE)
Spécialité de doctorat : Génie électrique
Graduate School : Sciences de l'ingénierie et des systèmes
Référent : CentraleSupélec

Thèse préparée dans l'unité de recherche **Laboratoire de Génie Electrique et Electronique de Paris (Université Paris Saclay, CentraleSupélec, CNRS)**
sous la direction de **Philippe Testé**, chargé de recherches,
et l'encadrement de **Rafael Sousa Martins,** ingénieur de recherche
et le co-encadrement de **Romaric Landfried,** enseignant-chercheur

Thèse soutenue à Paris-Saclay, le 9 Mars 2022, par

Vincent ANDRAUD

Composition du Jury

Philippe DESSANTE Professeur, CentraleSupelec	Président
Dunpin HONG Professeur, Université d'Orléans	Rapporteur & Examinateur
Laurent PECASTAING Professeur, Université de Pau et des pays de l'Adour	Rapporteur & Examinateur
Philippe DELMOTE Ingénieur de Recherche, Institut franco-allemand de Saint-Louis	Examinateur
Philippe TESTE Chargé de Recherche – HDR, CNRS	Directeur de thèse

THESE DE DOCTORAT

NNT : 2022UPAST030

université
PARIS-SACLAY

DOCTORAL SCHOOL
Electrical, Optical, Bio:
Physics and Engineering
(EOBE)

Titre : Etude expérimentale du phénomène de balayage de l'arc électrique lors du foudroiement d'un aéronef

Mots clés : arcs électriques, foudre, générateur haute puissance, railgun, diagnostics électriques et optiques

Résumé : Lors du foudroiement d'un aéronef, il y a un mouvement relatif entre l'arc électrique de foudre et l'aéronef, qui peut voler jusqu'à 100 m/s en phases de décollage ou d'atterrissage, alors qu'il ne peut éviter l'impact. Ainsi le point d'attachement de la foudre n'est pas statique mais peut se mouvoir sur toute la surface de l'avion – on parle de balayage de l'arc électrique de foudre. Face à ce danger, les avionneurs doivent prévoir de protéger toutes les parties de l'aéronef d'autant plus que les nouveaux modèles d'avions en fibre de carbone supportent moins les dommages thermiques, mécaniques et électriques causés que leurs prédécesseurs recouverts d'aluminium. Actuellement, le manque de retour d'expérience ne permet pas de justifier le caractère prédictif des outils de simulation existants de balayage d'arc électrique. L'objectif de cette thèse est dans un premier temps de reproduire une expérience en laboratoire répétable et représentative d'un foudroiement d'aéronef afin de réaliser dans un second temps une base de données expérimentale sur les grandeurs physiques mesurables du phénomène de balayage dans des situations standardisées. Cette base expérimentale pourra servir de référence pour des protections aéronautiques ou pour valider des outils de simulation.

Pour reproduire une expérience représentative du foudroiement d'un aéronef, un générateur électrique haute puissance de type Buck capable de reproduire un arc électrique respectant la norme de foudre aéronautique est conçu, réalisé et testé. Des arcs de quelques kV représentatifs de l'onde continue de foudre – une consigne de 400 A pendant 50 ms – sont formés et étirés jusqu'à 1.50 m afin de recréer une colonne d'arc libre. La propulsion de plaques test de matériau aéronautiques à des vitesses de plusieurs dizaines de m/s est rendue possible par la conception, le développement et la réalisation d'un lanceur électromagnétique de type Railgun: avec un banc de supercondensateurs, l'injection d'un courant de 25 kA pendant environ 50 ms dans un système de rails de Laplace permet de projeter des plaques de quelques centaines de grammes aux vitesses voulues en 2 m d'accélération. Le couplage du générateur électrique et du lanceur électromagnétique permet alors la reproduction et l'étude du phénomène de balayage: des mesures électriques et des diagnostics optiques par caméras rapides et spectroscopie d'émission permettent de remonter aux grandeurs électriques, hydrodynamiques et thermique de la colonne d'arc en mouvement ainsi que de caractériser le déplacement du point d'impact sur le matériau aéronautique. Ces mesures et analyses sont aussi effectuées avec soufflerie qui provoque le mouvement de l'arc sur la plaque test fixe en remplacement du Railgun. Ceci permet d'établir une comparaison entre les deux modes de reproduction d'un mouvement relatif arc électrique/plaque aéronautique.

Title : Experimental implementation and study of the lightning swept-stroke along an aircraft

Keywords : Electric arcs, lightning, high-power generator, railgun, electrical and optical diagnostics

Abstract : In the domain of aeronautical industry, the risk of lightning strike is taken into account from the conception of the aircraft as the phenomenon statistically occurs every 1000 to 10000 flight hours. As this phenomenon involves a lightning channel that is static in the terrestrial reference frame and an aircraft that can reach a speed of 100 m/s in the take-off or in the landing phase, there is a displacement of the impact area – the arc root - on the aircraft outer skin. This phenomenon is referred to as swept-stroke phenomenon. Thus, all the parts of the aircraft are exposed to the risk of direct electric and thermomechanical damages induced by the lightning strikes. Therefore, it is necessary to understand the physical mechanisms that drive the displacement of the arc root to optimize lightning strike protections. There is a significant bibliography about the modelling of this displacement combining electromagnetism and fluid mechanics equations. Though, the existing simulation codes still have not been validated by the implementation of an experimental aircraft simulation that would be struck down by lightning to create a reference database for the physical parameters of the phenomenon. This PhD thesis aims to reproduce such an experiment and to establish such a reference database.

To reproduce a representative experiment of swept-stroke, a high power electric generator with a Buck configuration and capable to reproduce an electric arc respecting the aeronautical standard lightning waveform is designed, implemented and tested. Electric arcs of a few kV representative of the continuous lightning waveform standard are created and elongated until 1.50 m. The propulsion of test samples to speeds of several tens m/s is realized with the design, development and implementation of an Railgun electromagnetic launcher: a supercapacitor bank enables the injection of a current of 25 kA during 50 ms into a Laplace's rails system and so to propel samples of a few hundred grams to the desired speeds within 2 m of acceleration. The coupling of the electric generator and the Railgun enables the reproduction and the study of the swept-stroke: electrical measures and optic diagnostics through high speed camera and spectroscopy are implemented to characterize the electric, hydrodynamic and thermal behavior of the moving electric arc. The impact point displacement is also characterized and analyzed. These measures and analyses are also conducted with a Wind tunnel that provokes the displacement of the electric arc on the test sample, replacing the Railgun. From this study, the comparison between the two modes of relative motion between the electric arc and the test sample is established.

Chapter I. Overview of lightning strikes to aircraft

Chapter II. Design and implementation of DC-to-DC converter topology for current regulated lightning generator

Chapter III. Development of a low voltage Railgun in the context of lightning swept stroke to aircraft

Chapter IV. Hydrodynamic, electrical and thermodynamic characterization of the lightning arc channel during swept-stroke

Chapter V. Study of the arc roots displacements during the swept stroke

Acknowledgements

Je tiens en premier lieu à remercier profondément Dupin Hong et Laurent Pecastaing d'avoir accepté la tâche de rapporteur et ainsi d'avoir consacré une partie conséquente de leur temps à lire et juger mes travaux de recherche - je tiens à souligner ici la précision des corrections de Dupin Hong qui a réussi à pointer des erreurs jusque sur les années de parution de certaines de mes références, son aide m'aura été précieuse pour corriger ce manuscrit. Je m'estime particulièrement chanceux pour la bienveillance et la qualité des remarques qui transpirent de leurs rapports respectifs. J'ai aussi pu apprécier la qualité de notre échange lors de la soutenance.

Je remercie également le président du jury, Philippe Dessante qui a tenu le rôle d'incarner le jury de thèse à lui seul lors de la soutenance et par la grâce de qui j'ai pu me réveiller en tant que docteur dès le lendemain matin.

Je remercie Philippe Delmote d'avoir accepté d'être mon examinateur pour cette thèse et je le remercie d'un même élan pour son accueil très enthousiaste au laboratoire de l'ISL ainsi que pour ses explications techniques par rapport aux lanceurs.

Je remercie les invités Laurent Chemartin - dont le cumul des travaux antérieurs au sein de l'Onera a été véritablement déterminant pour la réalisation de mes travaux - et Audrey Bigand pour l'intérêt dont ils ont fait preuve pour mes recherches. Intérêt que j'ai pu constater à travers leurs remarques et questions très circonstanciées lors de la soutenance.

Je remercie Carmen Guerra-Garcia avec qui j'ai eu souvent l'occasion de correspondre autour du sujet du balayage durant ces trois années ainsi que Robert C. Youngquist et Stanley Starr qui ont eu la gentillesse de répondre à mes premières questions sur la possibilité de faire un railgun basse tension. Je pense que sans leur aide, je n'aurais pas poursuivi cette piste, et cette étude aurait eu une toute autre allure.

Je remercie bien-sûr Markus Schneider qui a eu l'immense bienveillance de m'approcher lors d'une conférence à Biarritz pour m'inviter à venir constater sur place les performances et les installations écrasantes des lanceurs de l'ISL qui font passer mon railgun pour un lego.

Je profite d'une série plus diffuse de remerciements pour rompre cet effet d'anaphore un peu stupide. Je voudrais ici remercier toute l'équipe FPA de la branche DPHY de l'Onera pour m'avoir soutenu durant ces années de thèses – et tout particulièrement Amélie Jarnac, Paul-Quentin Elias, Victor Desangles et Fabien Tholin qui ont suivi mes travaux de prêt. Je vous remercie sincèrement pour l'intérêt que vous avez porté à ce projet et pour les réponses (et même les questions) que vous avez pu émettre afin de me faire aller toujours plus loin - avec toujours plus d'énergie (cinétique ou capacitive).

Je remercie également Marie-Line Pacou, Martine Ducornet et Hélène Lelièvre pour l'aide et

la disponibilité dont elles ont immanquablement fait preuve dans mes démarches. Je remercie aussi Camille Blosse pour son aide et son soutien même si n'avons malheureusement pas pu aller jusqu'au bout de cet échange pour des raisons très largement indépendantes de nos deux volontés – par exemple une épidémie à échelle planétaire.

C'est maintenant le moment de remercier mes frères d'armes, les doctorants et post-doctorants qui ont pu vivre une situation similaire dans le même espace-temps – en espérant que vos prochains projets vous apportent une certaine forme d'épanouissement… Je pense à Fabrice, mon principal compagnon de fortune avec qui nous avons partagé un bureau et des plans d'évasion pendant plus d'un an et demi, à Jean-Carlos, à Simon, à Vivien, à Eve et à Federico. Je souhaite que nous puissions continuer à garder une amitié intacte pour la suite de nos parcours. Je remercie également les doctorants de l'équipe venus plus tardivement et qui m'ont fait l'honneur de venir voir ma soutenance : Severin, Gabriel et Romain. Enfin j'exprime ma sincère gratitude à Théo, stagiaire au laboratoire qui m'a été d'une aide très précieuse pour mes derniers travaux de développement du railgun et de foudroiement « en vol » et dont j'ai pu apprécier l'enthousiasme et l'intérêt pour mon projet. Je te souhaite une bonne continuation pour tes études en astrophysique. Enfin, merci à Mohamed pour sa disponibilité et son soutien.

Je remercie sincèrement l'ancien chef de l'équipe FPA, Philippe Lalande pour son support tout au long de ma thèse. Tu as pris systématiquement le temps de suivre le projet et de me donner ton avis. Je te remercie de m'avoir fait confiance ces trois années et d'avoir « débloqué » les problèmes d'achats de composants quand il l'a fallu. Il est évident que sans tes interventions, le projet n'aurait pas été une telle réussite. Merci encore pour ta confiance et pour la liberté que tu m'as donnée sur cette thèse ainsi que pour tes conseils et recommandations pour la suite.

A Clément, j'adresse l'expression de toute ma gratitude. Tu m'as permis de rattraper un niveau en électronique de puissance qu'une certaine école pourtant spécialisée n'a pas vraiment été en mesure de m'apporter. Tes remarques, indications et même – le mot est juste – tes enseignements ont été fondamentaux pour ma progression sur les bases de la manipulation haute puissance, ce qui n'est pas rien puisque je suis toujours en vie actuellement pour écrire ces remerciements et c'est très probablement grâce à toi. J'ai aussi apprécié ton implication inconditionnelle dans mon projet et la confiance que tu m'as octroyée, malgré les risques électrotechniques et cinétiques inévitables. Nous avons vécu quelques moments forts que j'aurai beaucoup de mal à oublier (et toi aussi je présume).

A Romaric, j'adresse toute ma reconnaissance. Sans parler de ma thèse, notre relation depuis le stage de 2017 est très certainement un des déclencheurs majeurs de la suite… Ne parlons pas ici encore de vocation mais tu as vu juste dans ton commentaire de fin de stage, j'étais, d'une certaine manière, fait pour faire – au moins un peu plus que pour le temps d'un stage – de la recherche. Merci d'avoir fait tout le nécessaire pour que ta « vision » s'accomplisse – le stage au Geeps, le stage de fin d'étude avec ton contact Marina à Munich, ton accompagnement pendant la thèse. J'espère que suivre ma thèse t'aura amusé comme elle m'a amusée pendant ces trois années.

A Philippe Testé, mon directeur de thèse, j'adresse mes remerciements les plus vifs pour m'avoir lancé dans l'aventure (des arcs électriques). Si j'essaie de me rappeler pourquoi je t'ai suivi depuis 2016, je pense que tu offrais un discours plus censé et plus sincère que le reste des professeurs de cette fameuse école d'électricité. La découverte de Nimier et de Blondin sous tes recommandations un peu plus tard a aussi probablement fait son petit effet à l'époque. Bref, je me suis retrouvé dans ce que tu avais à me proposer sans avoir une idée très claire de comment quoi faire plus tard. Après le reste a été facile… La thèse est une fête… jusqu'à maintenant où je n'ai pas plus d'idées très claires. Mais ces quelques années passées à « rechercher » avec toi auront été un passe-temps formidable. Ce furent de belles années pour moi, vraiment très enrichissantes et aussi passionnantes – un grand merci pour ce que tu m'as appris sur le chemin - et j'espère que les prochaines me réserveront autant de surprises.

A Rafael, …

… Immanquablement, une tentative de remerciements qui serait à la hauteur de ce que je te dois réellement serait vaine et demanderait un mélange trop subtil de personnel et de professionnel, de solennel et de consensuel…

Faisons simple…

…

…

…

Trop difficile…

…Après tout, ce que je n'arrive pas à dire ici, tu le sais déjà très bien… Et ai-je terminé de recenser les nombreuses raisons de te remercier ? Cela me prendra encore quelques temps je pense ! Tu m'as explicitement dit que nous devions désormais nous considérer comme des amis, alors ta première action pour sceller cette amitié sera de te contenter de remerciements aussi évasifs et incomplets… En attendant que je trouve les mots justes - les mots les plus explosifs. Avant cela, nous aurons tout le loisir de nous revoir, et qui sait, un jour prochain, de nous lancer enfin dans une compétition sanguinaire de Churrasqueira… Encore un grand merci, j'espère du fond du cœur que nous aurons encore l'occasion de rechercher – quelque chose, n'importe quoi – ensemble.

Je remercie maintenant mes amis qui m'ont soutenu tout au long de cette épreuve, notamment Benjamin, Baptiste, Mo et Clovis qui ont été particulièrement présents. Ce fut très important pour moi de vous avoir à mes côtés durant chacune des étapes de ma thèse – des étapes de tension ou justement de vacances dans des contrées plus ou moins lointaines. Je remercie aussi François de s'être déplacé jusqu'à Gif-sur-Yvette pour voir ma soutenance. También agradezco a Dani y Jenny que me han realmente recibido como familia con los brazos abiertos este último año.

Je remercie enfin (on arrive au bout) ma famille de m'avoir toujours soutenu et supporté pendant ces trois années… De mémoire pour l'idée du railgun, ça a debuté comme ça, moi, on ne m'avait jamais rien dit là-dessus. Rien. C'est toi, Sylvain, qui m'en a parlé… L'idée à fait son chemin…

Para concluir esta ola de agradecimientos, quiero agradecer a Paula Andrea con quien he vivido un ano maravilloso en Paris durante el toque de queda y un ano de relación en distancia desde Madrid. Gracias por toda tu ayuda y por todos los momentos encantadores. Me alegra de haber hecho tantas cosas contigo cuando estábamos viviendo juntos y espero que eso vuelva después de poco tiempo de distancia. Eres mi vida, de noche a la mañana, cada día, cada hora, cada minuto que yo vivo.

Introduction

Lightning is one of the most unrecognized and misunderstood of all common weather hazards and thus, a critical challenge for flight safety. Damage to aircraft due to lightning strike occurs in the form of arc spots on the skin metal or centimeter-size holes in the fuselage. This risk is taken into account from the conception of the aircraft since the phenomenon statistically occurs every 1000 to 10000 flight hours, roughly one or two occurrences per year. As lightning strikes involve both a static lightning channel in the terrestrial reference frame and a moving aircraft, there is a displacement of the arc spot on the aircraft's outer skin. This phenomenon is referred to as "swept-stroke". The displacement can be either continuous with the sweeping of the arc spot along the aircraft or discontinuous with the occurrence of arc root leaps. Consequently, all the parts of the aircraft are exposed to the risk of direct electric and thermomechanical damage from the passage of the arc root and to the ignition of arcing. For example, in 1976, an Iran Air Boeing 747 crashed because of a fuel tank explosion provoked by arcing induced from direct lightning strike. Therefore, even if for metallic cover, the electric and thermal properties enable a good repartition of the direct damages on the aircraft structure, the swept-stroke has been investigated experimentally with laboratory swept channel tests. Nevertheless, the experimental difficulties to reproduce accurate tests in laboratory, mainly due to the test samples speed requirements - around 100 m/s during take-off or landing phases - and the first conclusions about an appropriate upper bound estimation of the damages produced by the specific swept-stroke phenomenon, caused the suspension of the swept-stroke testing in the middle of the eighties. This suspension has slowed down the understanding of the physical processes occurring during the phenomenon as it was not necessary to ensure aircraft safety.

The need to address this issue has become even more important in recent times as aircraft manufacturer are replacing metallic cover with carbon fiber composite materials instead. This move is to both reduce the weight of the vehicle and facilitate large-scale manufacturing. For example, the weights of the Boeing 787 Dreamliner and of the Airbus A350XWB are composed by around 50 % of carbon fiber and Airbus is considering this material to optimize the wings performances of the A321 neo. However, the carbon fiber composites are more vulnerable to lightning strikes since their relatively poor thermal and electric conductivities do not enable a balanced repartition of the damages over the aircraft structure. These composites are used in parts that are exposed to the formation of arc spots because of swept-stroke. To counteract this, additional metallic meshes have been designed, and experimentally tested for the certification, which has augmented manufacturing costs and delays. In the future, this phase of protection design and testing could be accelerated with a deeper understanding of the physical processes intervening during the swept-stroke. During the last decades, numerous simulation models of swept-stroke have been developed to predict the behavior of lightning arc and so to design more accurate protections. However, no significant experimental measurements of the swept-stroke phenomenon have produced physical characterization of arc behavior and arc spot displacement in order to provide inputs or to serve as comparison to simulation codes for their validation. There is also no reference database demonstrating the likely evolution of swept-stroke quantities of interest in light the relevant experimental conditions. Beyond the establishment of such a database, the aim of this work is to give an insight on the physical processes intervening. Going forward, we consider that the following issues and questions need to be addressed:

- How is the arc channel affected by the swept-stroke?

  In a macroscopic point of view, how its shape and characteristic length varies during the phenomenon for different initial conditions? For electrical concerns, how its voltage, current and electric power varies during the motion? What is the temperature of the arc channel when it is elongated? What are the influences of the test sample speed, the arc current, the test sample length, the arc spot polarity and the initial length of the arc column on these values?

- How is the arc root motion on the test sample affected by the swept-stroke?

  How does the mode of arc spot displacement – continuous, partially discontinuous or jumping modes – vary with the initial conditions? What is the average dwell time of an arc spot on a specific point? During a reattachment between two points of the test sample, what are the spatial and electrical characteristics of the portion of arc channel that extinguishes for the formation of a new conductive portion of arc channel? What is the skip distance between those two points? What are the size and the length of the impacts on the test samples? What are the influences of the test sample speed, the arc current, the test sample length, the arc spot polarity and the initial length of the arc column on these values?

- What are the differences of physical processes considering a swept-stroke produced by a moving test sample and a static electric arc and a swept-stroke produced by a static test sample and a moving electric arc?

  The two modes of relative motion can be produced through a test sample launcher that is developed during this work as an original instrument and through wind tunnel equipment that is able to blow the arc channel. Then, do the effects of the swept-stroke on the arc channel and on the arc motion depend on the mode of relative motion between the test sample and the electric arc?

In order to address these questions, the following technical challenges need to be overcome:

- Implement an experimental setup that would enable the reproduction of the lightning swept-stroke in laboratory: experimental instruments have to be developed and coupled to ensure a representative realization of the phenomenon respecting the orders of magnitudes of the physical quantities intervening. It is required to generate electric arcs that are representative of a lightning channel and to develop a launcher facility that is able to propel aeronautical test materials at the speed of a plane within the laboratory dimensions. In order to conduct an important number of experiments to produce quantitative results, the instruments performances must ensure a good repeatability and present enough robustness. As the developed instruments are not available in the industry and are not the reproduction of instruments already existing in the literature, special attention will be shown to characterize and optimize their performances.

- Develop methods and experimental diagnostics to measure physical properties of the lightning arc channel and of the arc spot displacement during the swept-stroke once the test bench has been validated. The main quantities considered to be important for electric arc characterization and analysis during swept-stroke are the hydrodynamic, electrical and thermal properties of the channel. The macroscopic and electrical properties of the arc root displacement are also investigated.

All these instruments and all the acquired information will enable to build an experimental database that will serve for computational codes comparison and validation. The study of the arc displacement during swept-stroke left apart, this work presents also a research contribution in the domains of power electronics and electric engineering since two years and a half over the three years of PhD were devoted to the development of the two experimental instruments that are coupled to perform the swept-stroke. Such instruments provided performances that were not found in the industry or the literature for the corresponding technology. These instruments consist of:

- A current-regulated lightning generator adapted from a Buck topology capable to reproduce lightning arcs of 1.5 m respecting the continuous lightning current waveform of the aeronautical standard ARP5412A.

- An augmented low voltage Railgun electromagnetic launcher capable of propelling aeronautical test samples of 100-250g to speeds between 60 to 80 m/s within 2 m of acceleration.

The development of these instruments and the specific experimental issues encountered during their implementation are discussed and analyzed in the present work. This dissertation will address the developed questions over the course of the following five chapters:

Chapter I consists in an overview of lightning phenomenon in general and in the specific context of lightning strikes to aircraft with a description of aircraft protection processes. A more specific presentation of the swept-stroke phenomenon is proposed and the earlier experimental and theoretical studies are overviewed. A focus is also made on the other plasma fields that involve a moving arc channel. The main objectives of this work are then presented to conclude the chapter.

Chapter II describes the development, implementation and analysis of the lightning generator. The sweeping lightning electric arc is modeled as an electric component to establish the required electric performances in terms of generator design. Different topologies of switching circuits are compared and experimentally implemented to create a current regulated generator. Overvoltage protections are developed and added to the circuits. Then, electric arcs of 1.5 m respecting the aeronautical lightning standard are produced in laboratory.

Chapter III is devoted the development, implementation and analysis of a mean of propulsion to launch test samples at the speed of an aircraft in the laboratory. After a comparison of different technologies, an augmented Railgun electromagnetic launcher principle is adapted for a low voltage application. The electric generator and the mechanical equipment are presented and experimental issues like the sliding contact are discussed. A model to evaluate the Railgun performances from ballistic and current measurements is developed.

Chapter IV investigates the characterization of the electric arc channel during swept-stroke: the electric arc generator is coupled with the Railgun or with a wind tunnel. High speed cameras and electric measurements are used to evaluate the hydrodynamic and the electric properties of the extending arc channel. Optical emission spectroscopy techniques are implemented to evaluate the arc temperature. The influences of speed, arc intensity, arc root polarity, test sample length, and initial arc length on these properties are measured and discussed.

Chapter V deals with the arc root displacement on the aeronautical test sample during swept-stroke. A fast overview of previous literature's arc motion experiments and of physical processes occurring at the cathode and the anode is presented. Through high-speed cameras and electric measurements, the interaction between the arc and the material, as well as the electric and spatial behavior of the arc root is characterized. The influences of speed, arc intensity, test sample length and initial arc length on these values are discussed. Results are compared for a moving test sample with Railgun and a blown arc with a wind tunnel.

Chapter I. Overview of lightning strikes to aircraft

I.1 Overview of lightning phenomenon

Despite being one of the most impressive and frequent natural phenomena, the understanding of the physic of lightning remains relatively poor. Still, the initiation and the formation of a lightning channel from thunderclouds and the propagation of this channel over several tens of km are an active subject of research, most of the difficulties coming from the transient and unpredictable nature of lightning that is an obstacle to accurate direct measurements inside thunderstorms. Advances in instrumentation and in experiments of in-flight direct measurements are now providing new information about the physics of lightning. Moreover, the recent discoveries of intense bursts of X-rays and gamma-rays associated with thunderstorms and lightning have given new insights and gave impetus to further researches on this field. Here is presented an overview of the understanding of the occurring of lightning phenomenon.

A. Formation and Electrification of Thunderclouds

Lightning can be defined as a very long – greater than 1 km – electrical spark. Most lightning is generated in thunderstorms and their average length is 5–10 km but they can reach a length that exceeds 100 km.

In a thunderstorm, a primary charge transfer process is thought to involve collisions between soft hail (graupel) particles that are heavy enough to fall or remain stationary in the thunderstorm's updrafts and small crystals of ice that are light enough to be carried upward in those updrafts, all happening in the presence of super-cooled water droplets (colder than 0 °C but still being unfrozen). To produce the primary thundercloud charges (Dwyer and Uman 2014), these hail-ice particles interactions must occur at altitudes where the temperature is colder than freezing, generally from−10 °C to −20 °C. The process that results in the apparition of electric charges consists in the collisions and dislocations of the particles in freezing and melting phases. The amount of charges exchanged depends on the temperature and the phase of the particles due to the conversion of energy released through latent heat.

After the charge transfer between the ice and the hail particles that have collided, the positively charged ice crystals that are lighter are carried away due to updrafts and reach the thundercloud top - to an altitude around 10 km - while the negatively charged hail remains at an altitude between 6 to 8 km. Thus, the primary charge structure of a typical thundercloud consists of several tens of Coulombs of positive charge in its top and an equivalent negative charge in its lower levels. A small positive charge is also present below the negative charge levels, at altitudes where the temperature is near the freezing point. Different mechanisms have been suggested to interpret the existence of this lower positive charge: corona discharge from the ground or collisions from different types of particles at temperatures over 0 °C. This results in the formation of a tripole cloud structure.

B. *Lightning initiation*

The observed electric field in thunderclouds with a tripole structure presents local peaks that have been recorded to be in the range of 100-200 kV/m (Marshall et al. 1995). That is an order of magnitude lower than the dielectric strength of air on the ground for standard temperature and pressure conditions – around 3 MV/m according to Paschen’s law. As such a value of electric field in the air is required for several tens of km for the formation of a lightning arc, the commonly accepted physical process is the local intensification of thundercloud electric field and then, the transition of such an intense electric field into a hot lightning channel.

This process of the local intensification of a weak thundercloud electric field is thought to be triggered by a serial combination of two mechanisms (Petersen et al. 2008): the cosmic ray-initiated runaway breakdown and the hydrometeor-initiated positive streamer system. A runaway breakdown event is supposed to first generate a region of locally intensified electric field. This field has to be intense enough to support the generation of positive streamers from nearby hydrometeors and their subsequent development into positive streamer systems.

B.1 Runaway electrons

When an electron moves freely through a gas, it is subject to a frictional force which is the result of elastic and inelastic collisions. Depending on the kinetic energy of the electrons, the frictional force will equilibrate or not the electrostatic force that the ionized gas imposes on the electrons: only electrons that have an initial kinetic energy above few keV are subject to a force eE (e being the elementary charge and E the electric field of the air at standard temperature and pressure (STP)) that is greater that the their frictional force (Peterson et al. (2018)). Those electrons will then continue to gain energy and accelerate until they reach relativistic energy of about 1 Mev. Those very energetic electrons are able to generate either other relativistic electrons (C.T.R Wilson (1924); C.T.R Wilson (1925)) – and so create an avalanche phenomenon called runaway avalanche (Gurevich et al. (1992)) – or large quantities of thermal electrons (low energy electrons (<100 eV)) (Gurevich et al. (2002)).

In the main acceptation of the phenomenon, those very energetic electrons – called runaway electrons – are formed by highly energetic cosmic ray showers. Balloon flights (Eack et al. (1996)) and later ASEC particle detectors (Chilingarian et al. (2017)) measurements revealed that X-rays intensity have an increase of 2 orders of magnitude lasting for approximately 1 min prior to lightning flashes. The processes of gamma rays triggering the formation and the multiplication of energetic electrons in air have been modeled in (Dwyer, J.R. (2003)).

Runaway avalanches require distances in the order of a kilometer for a significant increase of runaway electron population. The large quantity of thermal electrons created by the avalanche (estimated to be in the range of dozens of ions per centimeter by Gurevich et al. (2002)) forms a non-LTE plasma that enhances the ambient electric field of the thundercloud.

B.2 Corona streamer from hydrometeors

Due to the local enhancement of thundercloud electric field described in the previous mechanism, the water contained in either liquid or solid state in hydrometeors tends to polarize and deform it into elongated shapes even more susceptible to start a corona discharge which also enhances the surrounding electric field. Indeed, Richards and Dawson (1971), Griffiths and Latham (1972) and Crabb and Latham (1974) investigated corona on water drops and found evidence that polarized water drops have a threshold electric value for corona lowered from around 900 kV/m to around 500 kV/m. This value is likely to be reached by the previously described mechanism.

A corona discharge is created by avalanche effect of electrons due to local enhancement of electric field: electrons are expelled from polarized hydrometeors and are able to ionize the very surrounding air by collisions but as the electric field decreases rapidly with the distance, it’s not enough to ionize a large channel of air that could turn into an electric arc. But this would be sufficient to start a “streamer” as depicted in Fig. I.1. If electron avalanche occurs nearby a highly curved anode – a freshly polarized hydrometeor in this case- they are collected by it leaving a non-uniform positive charge space around the anode. This very local positive charge space then creates an intensified electric field around it in the opposite direction of the anode, triggering new electron avalanches around it which exposes then more positive charge space and extends its area. If the background field – the thundercloud field locally enhanced – is high enough, this positive charge area can continue to extend. As it extends, the tail of the streamer is subject to attachment and recombination process and thus is neutralized (Phelps and Griffiths (1976)). For STP conditions, the minimum electric field necessary for a stable propagation of streamers in air is around 300 KV/m which is exceeded in our context. The velocity of the streamer is around 10^5 m/s (Allen and Mikropoulos (1999)).

The streamer discharge has two polarities as for electric charges. The process described above involves an anode and so is called positive streamer discharge but there are also cathodic streamer discharges, called negative streamers. They are very similar to positive streamers, with the primary difference being the orientation of the electron avalanches relative to the streamer head. In the case of positive streamers the electron avalanches are directed toward the streamer head, while for negative streamers they are directed outward so positive streamers propagate in the direction of the thundercloud field to a negatively charged region while negative leaders propagate in the opposite direction, towards a positively charged region. The electric field required to sustain negative streamers is about twice the one for positive streamers due to the self-diffusing nature of the discharge in this latter case (Bazelyan and Raizer (1998)) so this is likely that only positive streamers occur in a first part of the process.

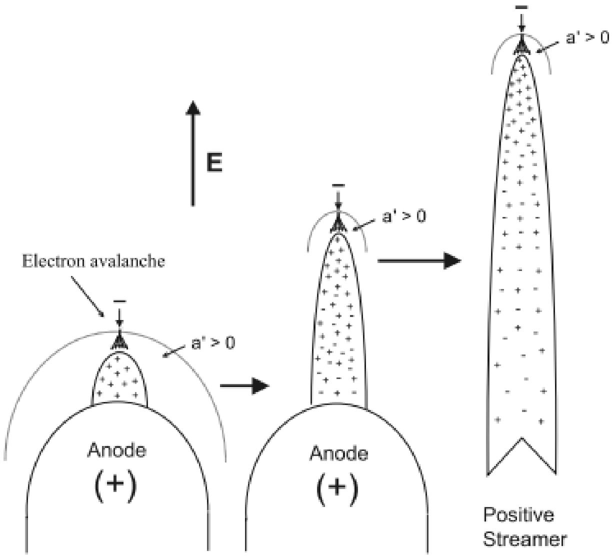

FIG. I.1 Scheme of the formation of a positive streamer in the intensified electric field from an anode – a' being the electron avalanche rate (Petersen et al. (2018)).

B.3 Leader discharges and initiation of lighting

A description of the formation process of a discharge that will initiate the lightning – called leader discharge - is presented in Fig. I.2. Series of positive streamer discharges in a small area is able to boost up the local electric field to level above 1 MV/m over the distance of few meters according to (Griffiths and Phelps (1976)). In those conditions, hydrometeors are subject to both positive and negative corona discharges. While positive streamers develop into branching positive streamer system and thus continue to enhance electric field and are able to enlarge in the process described above (Fig. I.2(a)), bursts of negative streamers are emitted from the hydrometeor, forming a negative streamer system consisting of small, heated and positively charged stems along the negative streamers paths. This negative streamer system is less developed than the positive one but forms space stems (Fig. I.2(b)). The positive space charge in these space stem regions forms a retrograde positive streamer that propagates back to the main negative termination of the channel created along the propagation of negative streamers from the original hydrometeor (Reess et al. (1995)). If the positive streamer emission is energetic enough, a compensatory quantity of negative charge is deposited back into the space stem, resulting in a forward-propagating negative streamer. This discharge sequence is called a ‘‘pilot’’ (Fig. I.2(c)). Those pilots serve as a continuous source of retrograde positive streamers that feed into the main negative channel termination, providing current that heats and extends the channel. There can be numerous pilots in the process of elongating the channel but one of them first reaches the critical temperature for sustaining electrical current via Joule heating and the pilot stem begins to lengthen at both ends – in a process structure called space leader- and finally attaches the termination of the negative channel. This comes with a surge of current and luminosity that is commonly referred to as a ‘‘step’’ (Fig. I.2(d)). This mechanism of propagation of the negative channel is called negative leader. The mechanism of propagation of a positive channel coming from the propagation of positive streamer is called positive leader and is simpler: the tip of the positive leader acts as an anode and generates a strong field in the vicinity of the termination. This field forms positive streamers that propagate and produce a current around the tip that heats it and so enables it to elongate. The association of a positive leader and a negative leader coming from a stem hydrometeor is called a leader.

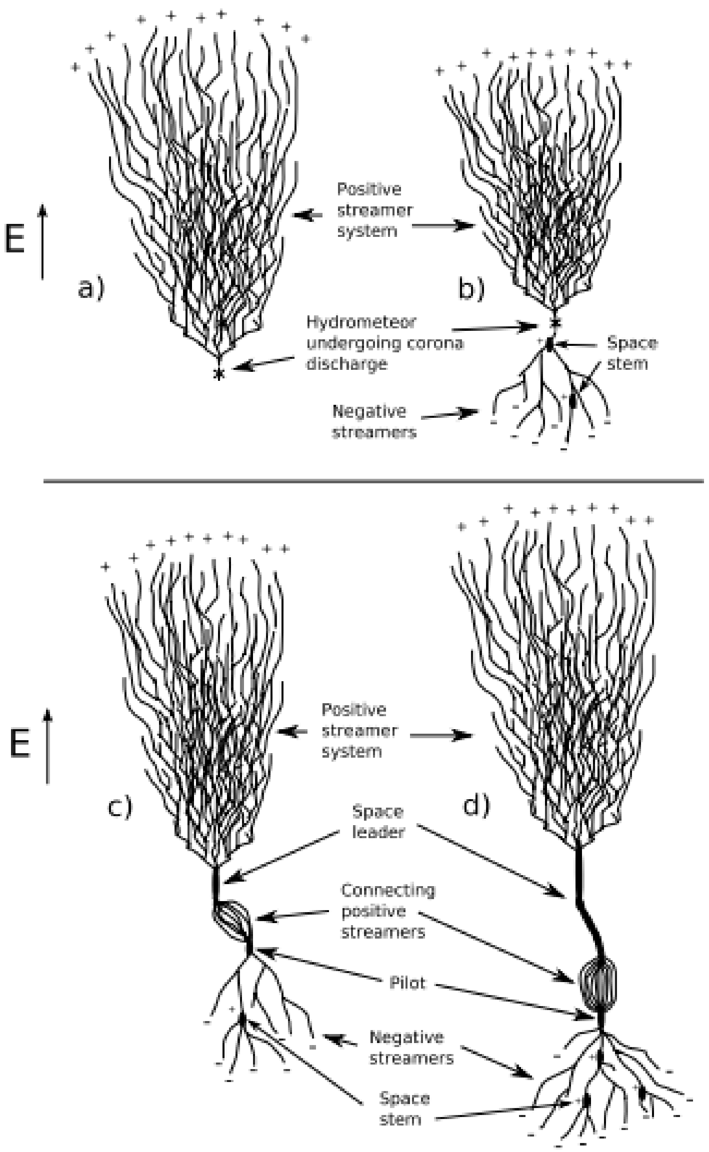

FIG. I.2 Scheme of the hypothetical initial lightning leader formation – formation of positive streamer system (a) – development of negative streamers and space stems (b) – production of other space leader from pilot discharges (c) – elongation of the space leader (d) (Petersen et al. (2018)).

Remote sensing observations of discharges are starting to provide evidence of this bi-directional propagation leader process as the initiator of lightning. Indeed, those bi-directional leaders are sources of strong VHF (very high frequencies) (Le Vine (1980)) that have been collected and analyzed in (Stock et al. (2017)) through high-speed VHF interferometer and electric field change measurements.

B.4 Lightning channel and classification of lightning flashes

When a bi-directional leader reaches the ground after the process of elongation described above and establishes a connection with the thundercloud, a very high pulsed current (thousands of amperes and few microseconds) strikes back from the ground to the cloud using the air channel heated by the leader. This high current is then followed by lower continuous current (hundreds of amperes during a few hundreds of milliseconds) superposed with other highly intense and short peaks of currents.

A typical small thunderstorm system produces a lightning flash to ground every 20–30 s for 40–60 min and covers an area of around 100–300 km^2. Large storm systems are able to produce one flash or more to ground each second over areas a hundred times larger or even more (Dwyer and Uman (2014)). All lightning discharges can be divided into two categories: (1) those that bridge the gap between the cloud charge and the Earth and (2) those that do not. The latter group is referred to as ‘‘cloud discharges’’ and represents the majority of all lightning discharges. Cloud discharges within a single cloud (or ‘‘cell’’) are called intracloud lightning (it is thought to be the most common cloud lightning and the most common of all the forms of lightning); the discharges between clouds are called interclouds lightning (they are less common than intracloud lightning); and the discharges between one of the cloud charge regions and the surrounding air are called cloud-to-air lightning (Dwyer and Uman (2014)).

There are four types of lightning flashes that occur between the cloud and ground. The four types, illustrated separately in Fig. I.3, are distinguished from each other by the sign of the electrical charge carried in the initial ‘‘leader’’ and by the direction of propagation of that leader. Fig. I.3(a) and I.3(c) present flashes referred to as downward lightning; Fig. I.3(b) and I.3(d) depicts upward lightning. About 90% of cloud-to-ground lightning flashes are initiated by a negatively-charged, downward-propagating leader, as shown in Fig. I.3(a), and results in the lowering of negative charge from the negative charge region in the middle of the cloud to the ground. About 10% of cloud-to-ground lightning flashes are triggered by a positively-charged, downward propagating leader, as shown in Fig. I.3(c), and results in the lowering of positive charge from the cloud to the ground, either from the upper or lower positive charge regions. The two remaining types of cloud-to-ground lightning discharges (Fig. I.3(b), I.3(d)) are less common and are initiated from mountaintops, tall man-made towers, or other tall objects, towards the cloud charge regions.

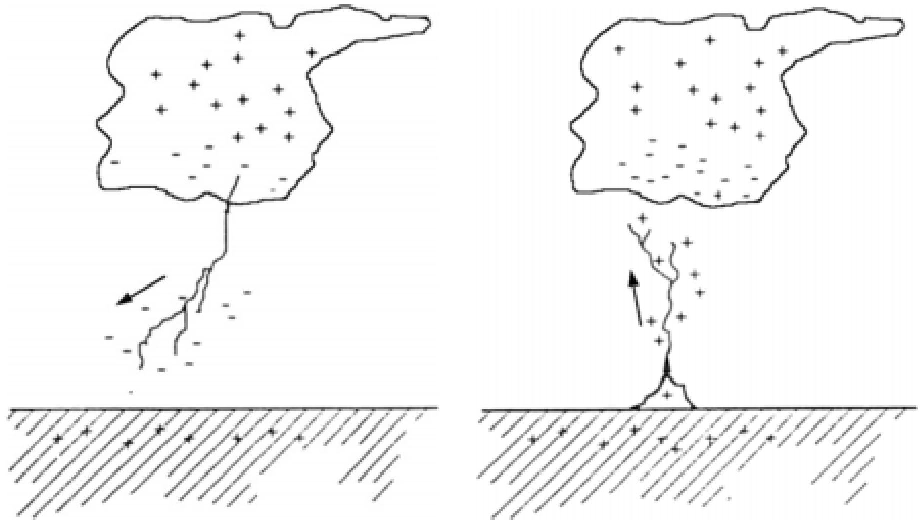

(a) Downward lightning negatively-charged leader. (b) Upward lightning positively-charged leader.

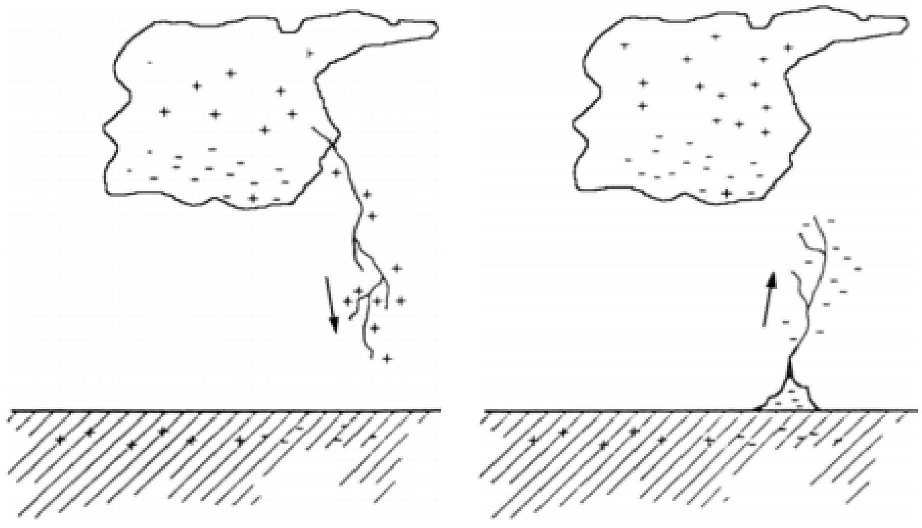

(c) Downward lightning positively-charged leader. (d) Upward lightning negatively-charged leader.

FIG. I.3 The four types of cloud-to-ground lightning flashes (Dwyer and Uman (2014)).

I.2 Lightning to Aircraft

A. *Statistics and concerns*

Lightning strike to aircraft is an event that must be considered in the design of aircraft: statistical in-flights measurements show that commercial airliners are subject to a lightning flight for every 1000 to 10000 hours of flight – this being roughly equivalent to one or two lightning strikes for each airplane per year (Fisher et al. (1988); Jones et al. (2001)). This frequency is high enough to be dealt with for flight safety issues: indeed, a lightning strike provokes direct damages on the structure of the plane due to the application of high mechanical and thermal constraints and indirect damages due to induction and electromagnetic interferences on the electrical equipment. An understanding of the physical processes in lightning strikes to aircraft is therefore essential to design and certify them especially since aircraft safety is more and more relying on the development of new materials to alleviate the aircraft.

The lightning hazards to aircraft are usually minimized by avoiding thunderclouds areas during the cruise phase but it is not possible to totally eliminate them since take-offs and landings are precisely scheduled in time and space. Indeed, those take-offs and landing lightning strikes account for around 95% of the cases (Roussel et al. (2015)). Therefore, the protection of aircraft to lightning strikes is a main issue and multiple studies are devoted to understand the physics process to correctly evaluate the threat.

B. Aircraft lightning initiation

The process of lightning strike to aircraft differs from the cloud to ground lightning charge. The aircraft is made of metal which is a very conductive material easily subject to corona discharges and the shape of an aircraft presents tips that locally enhance the electric field (the amplification coefficient can be over 5 to 10 to extremities such as the front, the tail or the wings tips of the plane). Thus, the ambient electric field makes static charges to accumulate in the vicinity of the tip shapes of the airplane and creates an inhomogeneous distribution of electric potential along the aircraft (even under zero charge net conditions). The aircraft is polarized with a positively charged end subject to positive streamers and a negatively charged end subject to negative streamers. These cumulated effects can trigger a bi-directional leader originated from the aircraft with the same pattern as described in previous section (Castellani et al. (1998a); Castellani et al. (1998b)) and initiate a lightning channel. The origin area of positive leader in the airplane – the anode- then becomes the exit point of the current whereas the origin of negative leader becomes the entrance point of current.

The in-flight measurements have shown that there are two different case scenarios for lightning to strike an aircraft. The first is the interception by the aircraft of a branch of a natural lightning leader developing in the vicinity of the aircraft. The second case is that the aircraft itself triggers the lightning discharge when it flies into a region of intense electric field or a highly charged region. The process of aircraft itself triggering a lightning discharge is experimentally shown in (Mazur et al. (1984)) using UHF band radar echoes of aircraft during thunderstorm penetrations. All lightning strikes to aircraft at high altitudes (>7 km) are of the second kind whereas it decreases to 90% at lower altitudes (<7km).

C. Lightning current and lightning swept stroke

The measurements of the current going through the aircraft during lightning strikes are mainly based on campaigns involving instrumented aircraft flying into thunderclouds regions with the aim of being struck by lightning (Fisher et al. (1988)), (Reazer et al. (1987)), (Moreau et al

(1992)). Once the lightning channel has been established through the process described above, the lightning arc develops between the cloud or the ground which are stationary electrodes and the aircraft which is moving. The measured current consists of a superposition of a continuous component of several hundred amperes that lasts between a few hundred of milliseconds and a second and many return strokes of pulses of several tens of kA lasting few hundreds of microseconds as depicted in Fig. I.4 (Lalande et al. (1999)).

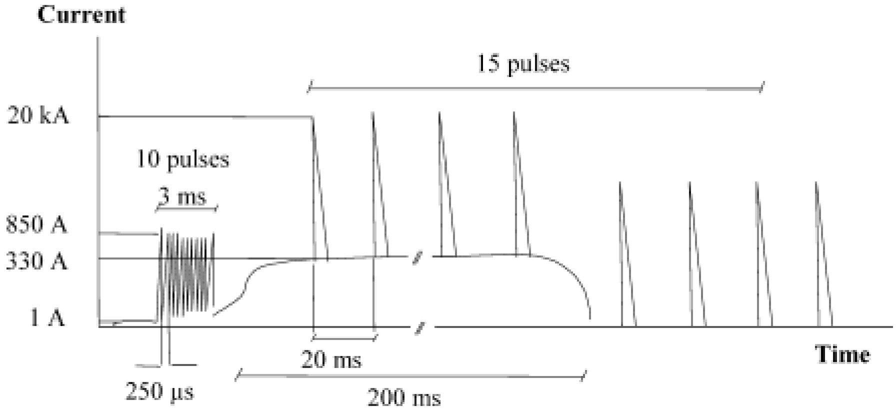

FIG. I.4 Typical current waveform from a lightning strike to an aircraft (Lalande et al. (1999)).

As there is a relative movement between the airplane and the lightning cloud or the ground, it is likely to happen that during the discharge, the attachment point on the plane moves along the aircraft. Indeed, as the average velocity for an airplane during a take-off or landing phase is 100 m/s, as the airplane length can vary from a few meter to more than 50 m and as that the discharge lasts up to 1 s, the lightning channel can be displaced along the whole aircraft length. The motion of the lightning attachment point on the aircraft is known as the swept stroke phenomenon and is the main focus of this present thesis. More specific concerns about the physic process of this specific phenomenon are to be discussed in the next section. The swept stroke phenomenon is an issue of main interest for the certification of aircraft since it requires not only to protect the parts of the airplane with a local increased electric field due to tip shapes but every part of the airplane is subject to be swept by the arc channel. Therefore, all the parts must to endure the electrical, thermo-mechanical constraints. Moreover, indirect damages such as electronic interferences or sparkles can be induced by this phenomenon at every part of the aircraft. We can mention the catastrophic accident in the USA on a Pan Am Boeing 707 in 1963 that is reported by the civil aviation investigation board to be due to induced electromagnetic effects in the fuel tank, which has ignited fuel vapors (Boeing (1963)).

D. *Lightning damages on aircraft*

The interaction between the arc column and the aircraft and the propagation of a high current through the fuselage causes stresses and damages to the aircraft that can be divided in direct and indirect damages.

Direct effects of lightning strike on aircraft structures consist in a coupling mechanism of thermal, electrical and mechanical constraints (Chemartin et al. (2012)). These constraints are represented in Fig. I.5. Those effects are of primary concern because of the massive use of carbon-composite material in the aircraft structure. The thermal constraints are more likely to happen during the continuous component of the current since its duration time is long enough for heat exchanges. The heat sources are the direct plasma heat flux (conduction and electronic or ionic recombination) and Joule effect within the material. There is also a heat exchange due to radiative flux that can be emitted by high temperature plasma channel.

The mechanical constraints consist in two main effects: a shock wave propagates in the radial direction of the arc due to the formation of the lightning channel. Indeed, this formation involves a fast increase in the temperature of the plasma channel (up to 30000K) thus creating an overpressure. The other effect is due to magnetic force coming from the high current circulation in the arc: the current creates a Laplace force that applies on itself constricting the column and adding internal pressure. The current circulating on the fuselage also adds overpressure constraint on it.

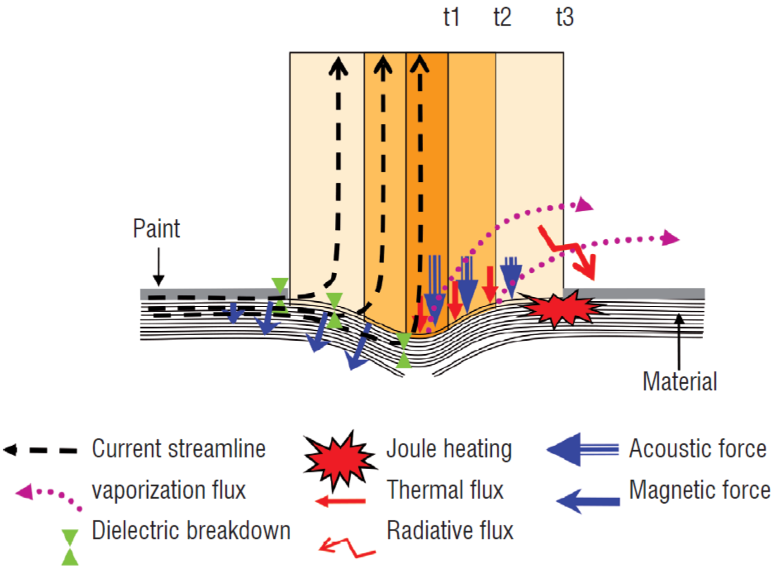

FIG. I.5 Representation of the various constraints of the arc attachment point on an aircraft cover surface (Chemartin et al. (2012)).

Other direct effects that have to be considered are the dielectric breaking at the attachment point or sparking at junctions and fasteners.

Indirect effects are resulting from the interference phenomenon caused by lightning's high electromagnetic field on the electronic equipment of the aircraft (well known as EM coupling phenomenon). Indeed the fast variations of current during the high pulse phases of lightning may induce parasite currents in wires and the electronic net system. This problematic have particularly raised the interest of aircraft's manufacturer since the main trend is to design all electric planes with higher electronic power for embedded systems. The indirect effects are not on main focus of the present work.

E. Introduction of composite material in aircraft and damage patterns

The previous twenty years have seen the interest for carbon fiber composites material increasing for the manufacturing of aircraft. Its compromise between strength and lightness makes it being highly used for various parts of the new generation of aircraft including the fuselage and wing boxes. The main advantages over the metallic material used for the old generation are its lightness (the density of carbon composite is around 1500 kg/m^3 whereas the Aluminum Al2024-T3 has a density of 2700 kg/m^3) that mainly reduces the fuel consumption and its malleability that makes it easy to manufacture. There is also no corrosion issue and the maintenance process is significantly relieved. Indeed, The Boeing 787 Dreamliner and the Airbus A350XWB programs employ carbon composite for around 50% of the aircraft weight. Airbus is considering this material to optimize the wings performances of the A321 neo.

The most employed carbon composite structure in aircraft is the quasi-isotropic laminated composite, which is made of unidirectional multi-layup of carbon plies oriented in different directions in an epoxy matrix. The ply is formed from carbon fiber tows. Typically, each tow is about 3 mm wide strand of continuous fibers. A strand, in its turn, may consist of 12000 individual filaments impregnated with an epoxy resin (Chawla (2012)). Figure I.6(a) shows a micrograph of the carbon fibers present in a tow and Fig. I.6(b) the structure of the multi-layup in a laminated composite with structure [0°, 90°, -45°, +45°].

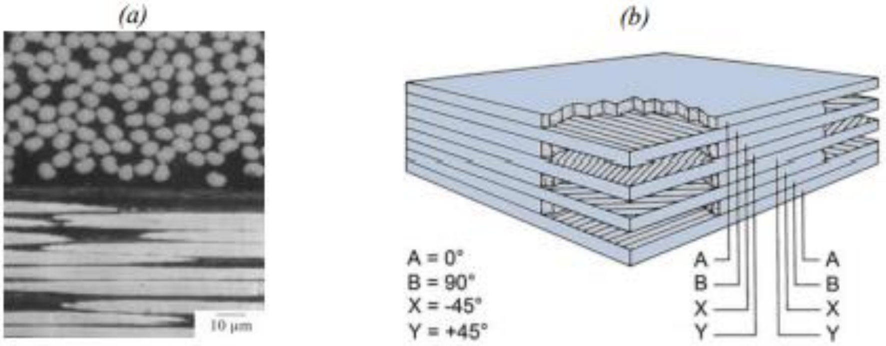

FIG. I.6 Micrograph of the carbon fibers present in a tow (a) and structure of the multi-layup in a laminated composite (b) (Chawla (2012)).

Even if this structure represents a considerable improvement for the strength and lightness of the aircraft, it does not have a good resistance for lightning. Actually, the carbon composites are subject to deep structural damages when it comes to sustain high electrical currents: the electrical conductivity of a carbon tow is around 60 kS/m whereas the one of aluminum is three orders of magnitude higher (37000 kS/m). Moreover the laminated structure makes it worse since the conductivity becomes anisotropic: as this is a fiber structure, transverse conductivity (transverse to fibers in the same plies) drops to 1 kS/m while perpendicular conductivity (transverse to fibers in different plies) falls to 0.1 kS/m. This low conductivity results in a poor evacuation of the thermal energy that is released by Joule heating: the high energy is difficult to be dispersed rapidly and provokes damages on the structure. Three kinds of damage morphology are presented in (Hirano et al. (2010)): fiber fracture, resin deterioration and delamination. Each damage mode shows strong correlation with a particular lightning parameter. Thus, the fiber damaged area and damage thickness is governed by the peak current phase of the lightning, while the resin deterioration area and the delamination projection area are determined by the electrical charge and the action integral of the current waveform, respectively. The most severe damages usually occur at the attachment point of lightning current.

Protection solutions have been developed to overcome those damages on carbon composite. The main ones are listed in (AGATE NASA (2002)) and include covering with expanded metal foil, arc or flame sprayed metals, woven wire fabrics, solid metal foils, aluminized fiberglass, conductive paint, metalized carbon and interwoven wire. A discussion is established in the paper about the pros and the cons of each of the protection systems. The main drawback effect being that the additional weight due to the protection causes counterbalance of the weight saving from the use of composite and also increases the manufacturing and maintenance costs of the aircraft.

F. Aircraft test process: lightning current test

As the phenomenon of lightning strike is very likely to aircraft and is able to cause severe damages to their structure, certification has been established to guarantee the resistance of aircraft to lightning strike. Civil certification authorities such as EASA (European Aviation Safety Agency) and FAA (Federal Aviation Administration) require from airplane manufacturer to conform to recommendations about lightning protection. Those recommendations are met through normative documentation established by standard committees such as EUROCAE (European Organization for Civil Aviation Equipment) and SAE (Society of Automotive Engineers).

The recommendations present a standard current waveform – which consists in the upper limit of the different components of measured currents occurring during lightning strikes – defined in the document SAE Aerospace Recommended Practice ARP5412A (2005). This standard current is composed of four current waveforms named A, B, C and D. The A component refers to the first high current return stroke; The B component refers to the transition of the current peak to the continuous current; The C component reproduces the continuous phase and the D component relates to the subsequent strokes. These components are defined in Fig. I.7. In addition to the current level, the A and D components are characterized by their action integral (2×10^6 A^2s and 0.25×10^6 A^2s, respectively), and the B- and C-components are defined by their transferred charge (10 C and 200 C, respectively).

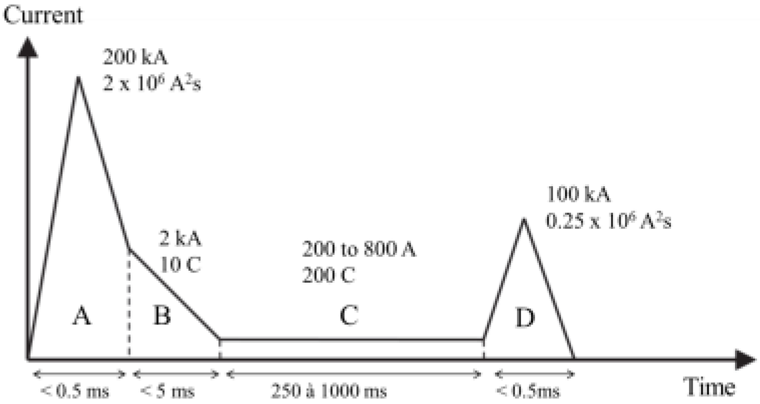

FIG. I.7 Standard lightning current waveforms for lightning direct effect tests [ARP5412A].

To simulate a lightning strike, the material test has to be subject to an electrical discharge in laboratory that reproduces the norm characteristics imposed by the aeronautics standards as described above. Beside the current waveforms, the test procedure has a specific configuration: in the standard certification test procedure, the lightning arc is created between two electrodes. One is formed by the aeronautical object under test. The other, called jet diverter electrode is formed by a tungsten rod on which a dielectric sphere or a fireclay is fixed at its tip. An initiating wire (usually made of copper) that helps to heat the air and so to trigger the discharge between the tungsten electrode and the test object may be used. Figure I.8 shows the recommended arc diverter electrode from ED105 (Leichauer (2019)).

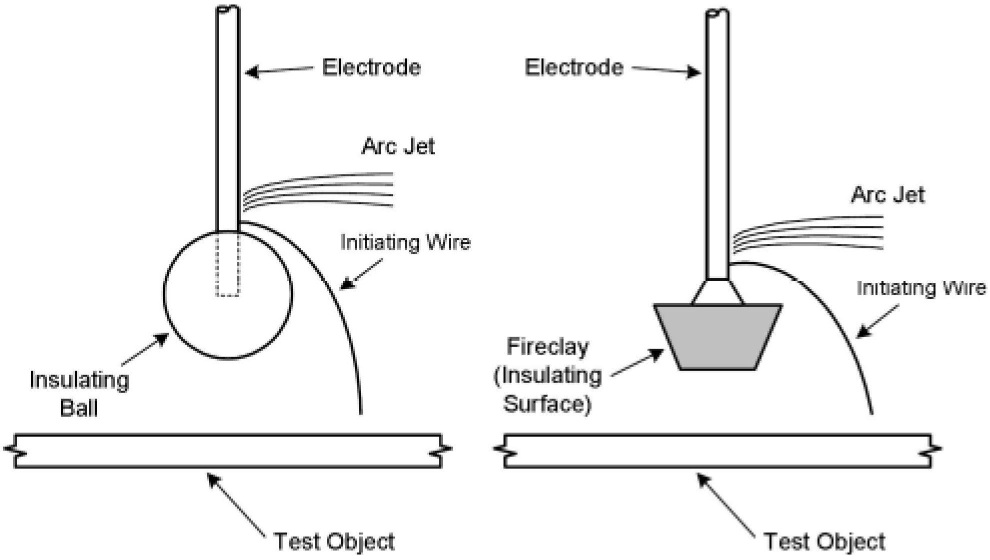

FIG. I.8 Test diverter electrode examples (Leichauer (2019)).

G. *The zoning*

During a lightning strike on an aircraft not all of the current components (pulsed current and continuous current) enter and exit an aircraft at the same spot. The lightning channel can remain stuck to certain zones, like the wingtips, while the attachment point remains only for a limited time on other parts of the aircraft. So the SAE ARP5414A certification establishes that the different standard components of lightning current have to be tested for the relevant areas. Indeed, the dwell times at each attachment point vary according to the nature of the surface, the local geometry, the air flow and the current waveform which could cause reattachment. The purpose of establishing lightning strike zones (Zoning computation) is to locate and classify surfaces on an aircraft which are exposed to a part of these four composite current components. Thus, the aircraft is divided into different lightning strike zones which are labeled with a number and a letter. The number describes the kind of physical interaction with the arc: 1 is attachment, 2 is sweeping whereas 3 is neither of them. The letter associated then describes the behavior of the arc: A is for sweeping and B is for dwelling at the same location. According to ARP5414A, ARP5416 and (Sweers et al. (2012)), the corresponding zones are represented in Fig. I.9 and defined by:

· Zone 1A – “First Return Stroke Zone: All areas of the airplane surfaces where a first return is likely during lightning channel attachment with a low expectation of flash hang on”. The current sequence associated to these zones is ABC*-components (C*-component is a shorter C-component associated to the dwell time and the surface coating).

· Zone 1B – “First Return Stroke Zone with Long Hang-On: All areas of the airplane surfaces where a first return is likely during lightning channel attachment with a high expectation of flash hang on”. Those zones are subjected to the total standardized current sequence (ABCD-components).

· Zone 1C – “Transition Zone for First Return Stroke: All areas of the airplane surfaces where a first return stroke of reduced amplitude is likely during lightning channel attachment with a low expectation of flash hang on”. The current sequence associated to this zone is AhBC*-components (Ah-component is a reduced A-component associated to swept leaders at flight altitudes between 1500 and 3000 m).

· Zone 2A – “Swept Stroke Zone: All areas of the airplane surfaces where a first return of reduced amplitude is likely during lightning channel attachment with a low expectation of flash hang on”. The current sequence associated to these zones is DBC*-component.

· Zone 2B – “Swept Stroke Zone with Long Hang-On: All areas of the airplane surfaces into which a lightning channel carry subsequent return stroke is likely to be swept with a high expectation of flash hang on”. The current sequence associated to these zones is DBC-component.

· Zone 3 – “Current Conduction Zone (Strike locations other than Zone 1 and Zone 2): Those surfaces not in Zone 1A, 1B, 1C, 2A, or 2B, where any attachment of the lightning channel is unlikely, and those portions of the airplane that lie beneath or between the other zones and/or conduct a substantial amount of electrical current between direct or swept stroke attachment points”.

(a)

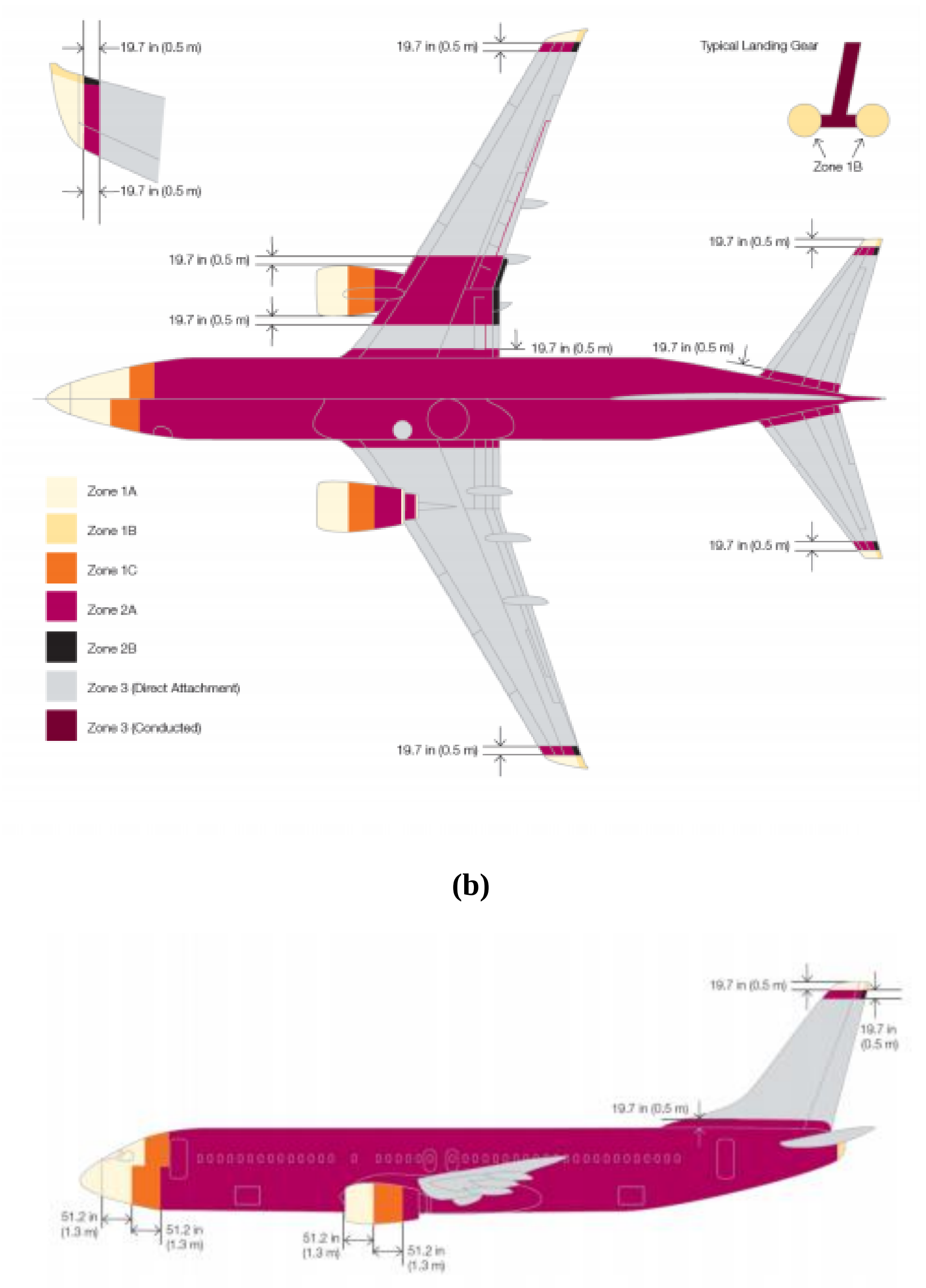

(b)

FIG. I.9 Lightning zone applied to a Boeing airliner – overview (a) and sideview (b) (Sweers et al. (2012)).

Therefore, to respect the certification and to ensure that the aircraft is resistant to lightning, the manufacturer has to apply in the laboratory condition the different current waveforms on the proper part of the aircraft according to the zoning.

I.3 Overview of the swept stroke phenomenon

Even if the process of protection of aircraft from lightning is well defined, the trend of replacing the maximum percentage of aluminum parts with carbon fiber material leads to a dead end if there is no understanding of the physics driving the phenomenon involved in the process of lightning strike. Currently, one of the main concern in this problematic is the lack of experimental data for the swept stroke phenomenon which does not allow to feed and validate numerical simulations. A good understanding of the phenomenon would enable to predict the path for the sweeping arc and to protect efficiently the relevant parts of the airplane that are indeed at risk. Thus, the raw and heavy upper-bounded protective layer could be exchanged for a refined and efficient protection layer. This section discusses about the main physic processes involving the swept stroke before presenting the main experimental and numerical approaches that has been conducted around this problem.

A. *Physical description of the sweeping arc*

An electric arc is an electric discharge in a gas creating a plasma whose electric current heats and ionizes it enough to keep it self-sustained. Lightning arc belongs to Newtonian magnetic fluid category and MHD (magneto hydrodynamic) theory has been established to study the discharge evolution mechanism. MHD equations consist of Navier-Stokes and Maxwell equations, which can be used to calculate the electromagnetic, flow, temperature and pressure field distributions in the arc channel also considering Lorenz Force and Joule heating. Due to high temperature and pressure, lightning arc is commonly considered hot plasma and is expected to be highly collisional so that the local thermodynamic equilibrium state is assumed.

The problem of lightning strike to aircraft has a main difference compared to lightning strike to based structure: once the lightning arc has been established, the arc develops between a stationary electrode (the cloud or the ground) and a moving electrode (the aircraft). Thus the majority of the arc is stationary with respect to the air but the part very close to the surface of the aircraft has a relative velocity as a consequence of the aircraft's motion and is elongated or swept. Depending on the surface properties this can lead to a gliding movement or a reattachment of the arc to a new reattachment point.

Even if the electric arc current is a superposition of very intensive pulses (up to a few hundreds of amperes during a few microseconds) and a continuous phase (a few hundreds of amperes for durations up to one second), it is commonly supposed that only the continuous part has to be considered for explaining the physics beyond this swept stroke phenomenon. Indeed, the relative movement between the airplane and the lightning channel has a speed of around 100 m/s, during the landing or the take-off phases. Then, considering the duration of basic pulse current, the application of very high currents occurs for around several hundreds of µm which is under the average characteristic size of the attachment point radius - from 1 to 20 mm (Peyron (2012)). As the focus of this work is the swept stroke phenomenon no further discussion will be sustained around the topic of high transient pulse current component and its effects. Indeed the mechanical, electrical and thermal properties of the arc channel are very different between high pulse and continuous current phases. High pulse current phase involves higher temperatures - up to 30000K – higher pressures – up to 50 bars – transient phenomena, shock waves, inductive effects and significant radiative transfers. These characteristics lead to a very different special interaction with aircraft's structures and damages. Interested readers are referred to (Sousa Martins (2016a)).

Laboratory experiments that will be presented later in this section show that the discharge channel either sweeps continuously along a bare metal surface or that it dwells shortly at each attachment point as can be observed on Fig. I.10.

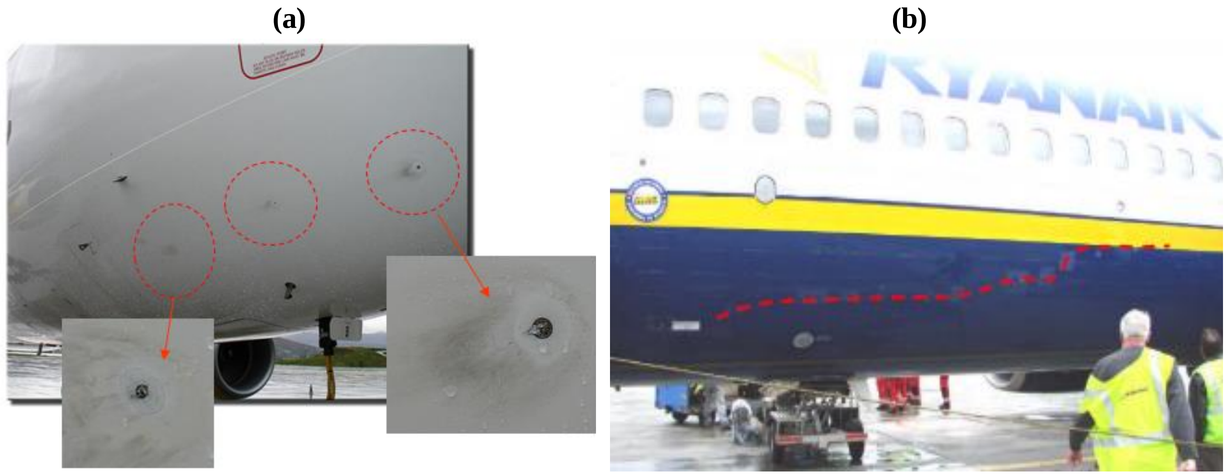
(a) **(b)**

FIG. I.10 Picture of a discontinuous swept stroke (fuselage of A320) (a), picture of a partial continuous swept stroke along fuselage of B737 airplane (b) (Plumer (2012)).

The kind of sweeping rather depends on the surface structure: bare metal surfaces, edges and rivets, painted metal surfaces or carbon composite. A simplified physical mechanism of the swept-stroke is presented in Fig. I.11.

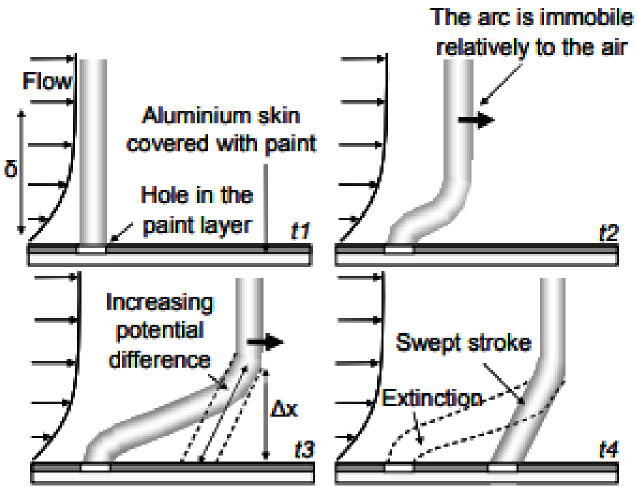

FIG. I.11 Schematic of the physical processes occurring during swept-stroke to aircraft (Tholin et al. (2013)).

A Blasius profile of air flow blowing on the aircraft's surface due to the relative movement of the aircraft and the static electrode is considered – that is to say that the speed of air is zero at the immediate vicinity of the surface and reaches 99% of the speed of the relative motion after a continuous and increasing speed profile on a distance called boundary layer thickness. At t1, the lightning strike channel has broken through the insulating layer covering the aircraft skin and an electric contact is settled between the arc and the conductive aluminum or carbon composite skin, delivering a continuous current. As the relative motion takes place and the arc attachment point dwells, the arc bends and elongates to maintain the electrical contact as shown at t2. As the electric field distribution in the arc channel is constant, the elongation of the channel makes its electric potential grow as well. Beside, Blasius profile induces a high stretching at the attachment point as the flow constraint is low in the boundary layer and high out of it so that the arc rather elongates parallel to the aircraft skin. This configuration creates thermal constraints and electric field in the aircraft insulating layer in the region close to the attachment point. Reattachment occurs when the potential drop along the channel is higher that the dielectric breakdown of the air and of the dielectric layer under thermal and electrical constraints (t4). The channel has a new attachment point with electric contact and the previous electric contact is short-circuited thus the old arc channel gets cold and so extinguishes. The distance between two consecutive attachment points is called a skip distance. This reattachment phenomenon may start again several times during the continuous current phase with a characteristic time for reattachment referred as dwell time. This explanation of the phenomenon suffers from three main simplifications : first, the Blasius profile may not be relevant at a flow or aircraft speed up to 100 m/s - a turbulent boundary layer with instantaneous velocity fluctuations and laminar to turbulent flow transitions have to be taken into account (Guerra-Garcia et al. (2016)). Second, in addition to the continuous current phase, superposed high current pulses (return strokes) may occur and increase instantaneously but temporally the voltage gradient along the channel and so help the reattachment to happen (A. Larson (2002)).

The last simplification concerns the self-induced electromagnetic forces: as the reattachment process is driven by the maximum difference potential point between the arc and the surface, if we suppose that the arc extends straightforward, the prediction for reattachment location using insulating layer voltage breakdown criteria seems easy. However, finding the maximum difference potential point is non intuitive since the arc is not straight and is likely to present high tortuosity due to the complex instabilities in the boundary layer (Tholin et al. (2013)). The high current in the arc that is bending produces a high and non-uniform magnetic field surrounding the arc that induces a self Lorentz force on the column. This magnetic pressure force is likely to form loops of current in the arc channel, introducing high tortuosity as shown in Fig. I.12.

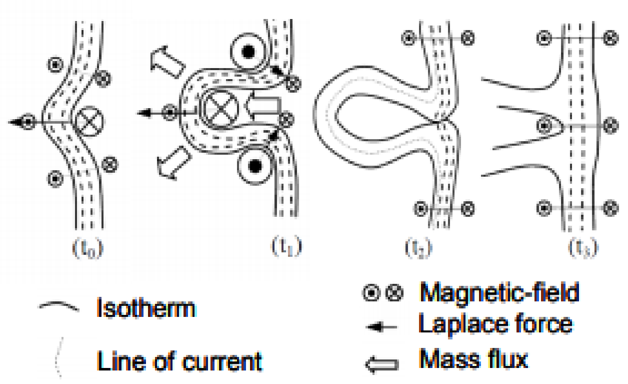

FIG. I.12 Process of the formation of loops of current in an arc channel (Tholin et al. (2013))

B. Experimental studies for swept-stroke reproduction

B.1 In aeronautical field

In this section, only the references for experiments involving the swept stroke phenomenon will be reviewed but for being exhaustive, let's mention that the first laboratory lightning test methods were developed in the early part of the 20th century to simulate the effects of lightning currents entering on elevated electric power lines and opened the field of vast series of experiments to determine the physical properties of lightning discharges.

During the period 1965-1985, different approaches were conducted to reproduce experimentally the swept stroke phenomenon. As the phenomenon involves a relative motion between the arc channel and the materiel sample under test, test approaches can be divided in two main categories: settings that put the materiel sample in motion through a static arc channel and settings that put the arc channel in motion along the static materiel sample.

Moving the arc can be made using transverse airflow from a wind tunnel or using rail electrodes (so that the other electrode of the arc can move freely) and external or self-induced magnetic field. As the mass of a heat plasma of air is negligible compared to the one of an aeronautic material sample, those approaches may seem easier to implement even if techniques for controlling the flow of air profile or the magnetic field require much precaution.

Experiments using a wind tunnel are described in Clifford and Crouch (1974), Clifford and Mc Crary (1982) and Oh and Schneider (1975). The wind tunnel experiments may seem unrealistic for the comprehension of the phenomenon and the relevance of measured data for three main reasons. First, the arc sweeps across both electrodes so that the other extremity of the arc is also moving and is subject to the very same phenomenon of sweeping which could change the whole dynamic of the arc channel displacement; in reality, the lightning channel is stationary in air and only the part in the very vicinity of the aircraft surface is affected by the relative velocity. Second, the air blow is likely to cool the arc channel and so add thermal constraints that may change the physic characteristics of the arc. Third, as the displacement of the arc channel consists in the heat and the state change of surrounding gas air to plasma involving electronic recombination processes, the energy toll is different in the configuration where the all channel is blown and moves than in the configuration that only a segment of the arc plasma in the vicinity of aircraft surface extends. Magnetically driven arcs present similar problems to wind tunnel tests and external magnetic field may also induce supplementary magnetic pressure constraint effects that would skew the dynamic of the arc column. Experiments using magnetic self-induced forces to move arc channel are described in T. N. Meyer (1977) and external magnetic forces in Novak and Fuchs (1974). Dobbing and Hanson (1978) presents results of a magnetically swept stroke experiment without giving details about its setup and reports a potential gradient of the arc two times higher than for the one measured in moving surface setup for the same speed.

A moving surface test setup leads to a more realistic simulation but its main inconvenient is the relative high speed to reach - up to 100 m/s - to reproduce the lightning to aircraft phenomenon accurately. Moreover, supposing such a speed is achieved the acceleration distance it would require propelling a test sample from 0 to 100 m/s is likely to overcome the usual distances of an experimental laboratory whereas the low inertia of air makes it simpler to accelerate over small distances. This addresses many problems since the experiment may requires several dozens of meter of acceleration and thus may not take place in a usual laboratory environment. This would prevent from using accurate diagnostics that would require heavy and specific setups.

The literature furnishes a bunch of various approaches to simulate a moving surface. Figure I.13 presents the approaches encountered in the literature. Plumer (1974) placed an aircraft wing fuel tank on the top of truck and reached a speed of 15 m/s beneath an electrode at 1500 kV rms 60 Hz (Fig. I.13(a)). A study involving a releasing of a stretched elastic to propel a sample at 20 m/s along a single rail track was performed by Lightning Technologies laboratory (Plumer (2012)) (Fig. I.13(b)). The experiments that reached the highest speeds was the one involving a rocked sled on a track using chemical propellant in (Dobbing and Hanson (1978)) (fig. I.13(c)). It was able to reach 72 m/s, and to be impacted by an arc that could reach 5 m long, providing a current of 600 A during 3s. The paper presents current and voltage measurement, video recordings from which distances and dwell times are directly obtained. Tests with bare metal, carbon fiber, painted protection and scratches are reported and give experimental data that are widely used for numerical simulations as validity criteria (A. Larsson (2002); Lalannde et al. (1999); Chemartin et al. (2012), Tholin et al. (2013)). But the main problem of this last experiment is the lack of accurate electric and optic measures that prevents from reaching further physical characteristics of the arc column and its interaction with the sample surface.

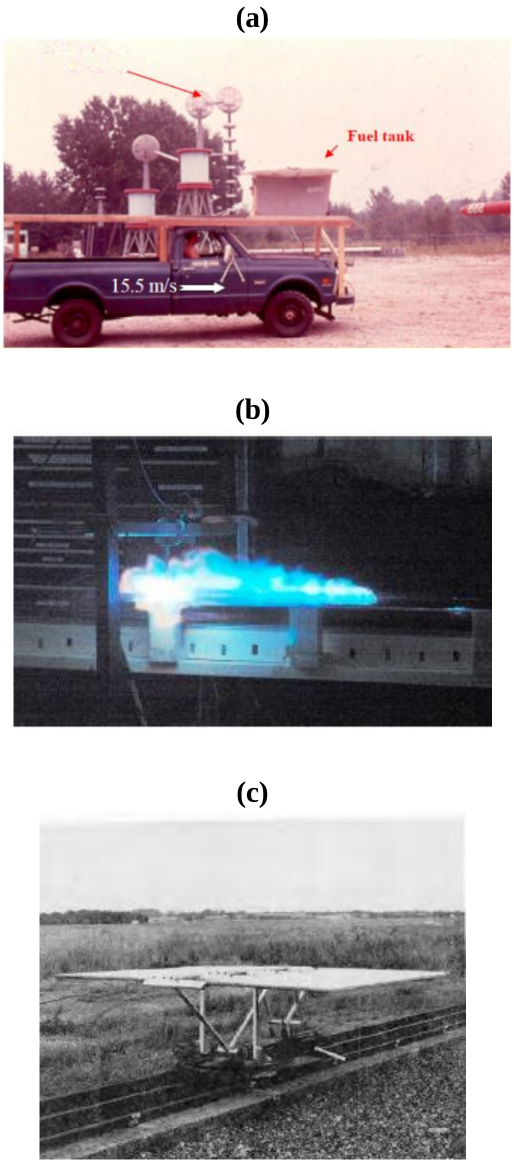

FIG. I.13 Different approaches to reproduce a swept-stroke with a moving electrode: the electrode is either propelled by a truck (a) (Plumer (2012)), a stretched elastic (b) (Plumer (2012)) or gas release (c) (Dobbing and Hanson (1978)).

A third category of testing method has to be reported here because this one is necessary to confirm the representativeness of the experimental simulations: direct in-flight measurements that basically consist in driving a measurement aircraft through a thunderclouds area. Frequent flight research programs have been conducted. Rustan and Moreau (1985), Pitts and Thomas (1981), Bailey and Anderson (1987) and Boulay (1994) contributed to feed databases for statistical analyses (Uhlig et al. (1999)). Even if those kind of experiments present the advantage to pass the criteria for representativeness of the phenomenon, there are still main problems for building a database. First, there is very low possibility to control the experiment features: there is no control of the lightning channel parameters and it is quite impossible to get accurate electric and optic measurements to characterize swept stroke phenomenon and plasma interactions to aircraft surface. Second, the cost of those experiments is not negligible and so prevents from any good repeatability.

Swept channel testing was suspended after those flight research programs confirmed the results of laboratory tests. The need for testing of moving surfaces has subsided and standards for such tests no longer exist in the aircraft certification processes. That may also be due to the complexity and the heaviness of the setup that has to be used to reproduce the swept stroke testing. Swept channel tests still exist in the certification to reproduce the damages of C-waveform (the one involving swept-stroke) on an aircraft but in the standard test, the electric arc and the sample under test are stationary (SAE ARP 5416), (EUROCAE ED-10). Estimations of the sweep distance and the dwell are otherwise obtained from the breakdown voltage of the dielectric materiel on the surface of aircraft.

B.2 In other plasma fields

Even if the rise of interest for experimental simulation of the swept stroke phenomenon has decreased after the middle of the eighties, several studies of electric arcs presenting characteristics similar to the arcs encountered in lightning strikes have been carried on these last decades. Thus, considering the continuous current phase of few hundreds amperes, fields of high current electric arcs such as welding arc and circuit breakers performed fine optic measurements using high-speed imaging and optical emission spectroscopy (OES) measurements. Measurements of temperature and electron density from 330 A DC current plasma of metal inert gas welding arc are reported in Valensi et al. (2010). High-speed imaging and OES measurements are used to estimate an electron density of 10^{17} cm^3 using Stark Broadening method and a temperature up to 12500K using Boltzmann plot method.

Besides, the field of plasma torches seems to be quite relevant to our studies since in most of these studies, only the arc root in the very vicinity of the anode electrode is immersed in the cross flow and interaction of arc with the anode and the boundary layer is investigated. A typical set-up for a Plasma torch is represented in Fig I.14. The main difference with lightning strike is the dimension of experiment. Indeed, in most of the studies about plasma torches, the distance between the anode and the cathode is in the order of magnitude of a few millimeters – ultimately few centimeters - thus addressing an issue for representativeness of our phenomenon even if the physical parameters such as the temperature and the electric field of the channel are in agreement with it. Kelkar and Heberlein (2000) report arc temperature up to 11 000 K and electric field up to 10 kV/m for a 200 A arc with electrode distance of 2 mm and a cross flow of 100 m/s. Moreover, there are obvious advantages from this configuration. First, the concentrated cross section of the arc enables to better control the airflow profile and to reach way higher velocities (up to 300 m/s in Wutzke et al. (1967)). Second, the small dimension of arc channel makes it easier to produce with an electric generators thus enabling to reach high values of current in the order of 100 A (which is at the low end of C-waveform current intensities) and maintain it for longer times. Third, the small dimensions of the setup enable to use very precise electric and optic diagnostics to produce fine experimental database.

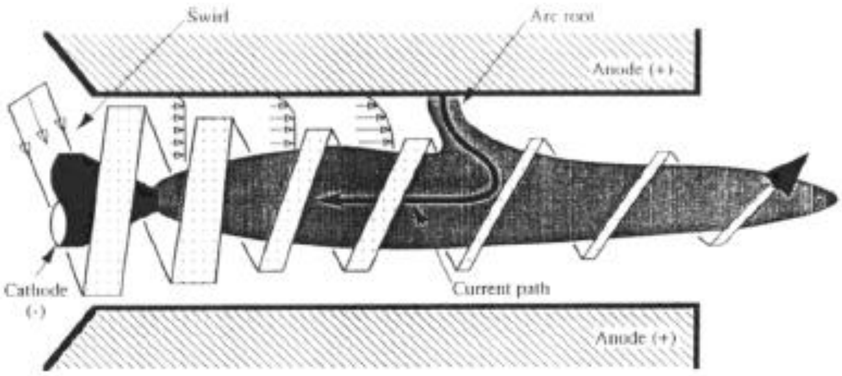

FIG. I.14 Plasma torch configuration (Heberlein et al. (2010)).

As the lightning swept stroke phenomenon, restrike phenomenon is observed in this configuration : a distinction between a steady mode – the arc channel behaves like a steady arc column with fixed attachment - and a restrike mode – the arc column is elongated in the direction of the cross-flow until a reattachment occur - is made. The main focus of the studies in this field that is relevant to swept-stroke is the transition between the two modes. Wutzke et al. (1968) present experimental results of the dependence of this transition to the pressure, flow speed, arc current and Reynolds number, parameters in argon, nitrogen and other gases and shows that the critical velocity for transition into the restrike mode is around 20 m/s for 100 A.

Further studies have been led in Yang et al. (2006), Yang and Heberlein (2007) investigating modes transitions of argon plasma electric arc in atmospheric conditions by sweeping the airflow velocity parameter or the current intensity. The studies present very interesting diagnostics: high speed camera is used for measuring restrike frequency and skip distance, segmented anode for anode heat and current transfer, Langmuir probe for electron temperature and electron and current densities, laser Thomson scattering system for three-dimensional electron temperature and electron density distributions, and Schlieren system for flow field distribution. Experimental observations show that during the transition to the restrike mode, the flow becomes turbulent and the electron temperature at the attachment increases significantly, indicating the non-LTE (local thermodynamic equilibrium) nature of the sheath and boundary layer. The restrike mode was proposed to be initiated by electron overheating instabilities triggered by flow instabilities.

C. *Modeling and Simulations of the swept-stroke*

The theoretical studies and models developed for lightning arcs can be separated according to the arc current phase. Only the part concerning the continuous phase is described in this work even if the physical equations that build the models are the same for the two components. But the numerical investigations for the swept-stroke phenomenon involve a different kind of physics which made its development only increase lately.

First models describing the physical equations responsible for the displacement of an arc and the energy balance of an arc channel subject to cross-flow or magnetic effects are described in Maecker (1971) and Bublievskii (1978). Maecker (1971) describes the arc discharge channel as a region of hot air with strong temperature gradient so that the movement of the channel is seen as a heat wave. Thus the motion is divided between the mass flow motion of the arc and the maximum temperature motion. This main distinction enables to consider curvatures effect on the channel which are added in Bublievskii (1978) in the free burning arc model, the transverse aerodynamic flow also being a factor of thermal losses to the arc. The first attempt to use algorithms and computational calculations to produce first simulation results is described in Lalande et al. (1999). These calculations are based on the physical arc energy, mass and momentum balances developed in Vérité et al. (1995), assumption of a cylindrical plasma channel and of LTE and perturbations from cross-flow settled in Maecker (1978) and Bublievski (1978). Even if the order of magnitudes of temperatures and electrical conductivity matches the experimental values of Dobbing and Hanson (1978), the model fails to predict an acceptable value for the electric field of the arc column due to the severe simplifications concerning air flow effects.

The first introduction of MHD (magneto-hydrodynamic) approach to study the interaction between a DC high current arc and electrodes is detailed in Hsu and Pfender (1983). This study simulates the physics of an axisymmetric arc and stationary such as the ones found in gas tungsten arc welding, plasma welding and plasma cutting. The model is then gradually introduced to simulate lightning channel and Lago et al. (2005) are the first to use MHD approach to simulate the interaction of lightning arc with a surface. Chemartin et al. (2011) adopt MHD method to understand the discharge physic involving the electrodes and characterize the distortion of arc column. These computational results are though verified in Tanaka et al. (2000) which gives details about lightning discharge experiments. Chemartin et al. (2012) then present computational simulation results of the swept stroke phenomenon considering MHD equations and a Blasius profile airflow. Some of their simulation results are presented in Fig. I.15. The electric characteristics simulation results are in agreement with the experimental results of the experiment in Dobbing and Hanson (1978). Tholin et al. (2013) conduct further investigations and predicts reattachment points for more interactions between arc and aircraft surface including dielectric layer and also studies the influence of the thickness of the boundary layer on the reattachment process.

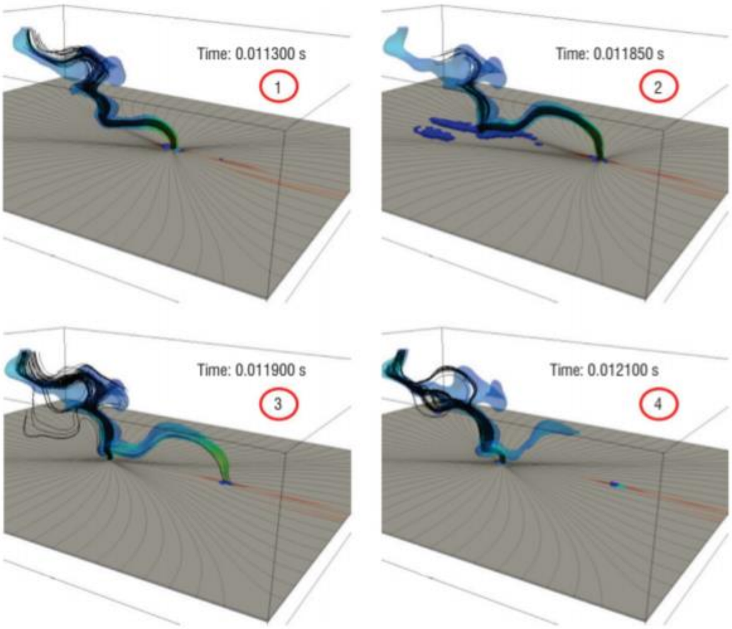

FIG. I.15 Simulations of reattachment during swept-stroke along a panel (Chemartin et al. (2012)).

In parallel, computational investigation to predict the damage induced by lightning on aeronautical protection layers - considering a model of stationary arc in a first approach – are developed. Ogasawara et al. (2010), Chemartin et al. (2012), Abdelal and Murphy (2014) and Wang (2017) used Finite Element Methods (FEM) to consider the effects of a multi-physics damage coupling – electric-thermal-mechanical-chemical to carbon/glass reinforced composite. These simulation advances are coupled with the MHD model to investigate the damage of the spcific swept-stroke phenomenon in Ma et al. (2020) and thus predict the enlarged thermal damages due to aerodynamic flow.

A more relevant airflow profile is proposed in Guerra-Garcia et al. (2016) to take into account the turbulent instabilities that are neglected in the mainly used Blasius laminar profile. The arc is represented as a fluid line, attached to the surface of the aircraft. This fluid line is simplified and do not present radial dimension or plasma properties. The elongation of the arc under a velocity field is evaluated by integrating the trajectories of the fluid particles belonging to that line and a linear electric field along the line is assumed – the reattachment occurring when a point of the line has enough potential to defeat the voltage breakdown threshold of air and insulating layer. It results in the prediction of very severe conditions for reattachment to occur that are in contradiction with the experimental measurements.

I.4 Research objectives

The previous description of aircraft protection process against lightning shows that the lightning damage are taken into account from the aircraft design phase and leads to drastic simulation and experimental test certifications. However, the current understanding of the physical processes driving the swept-stroke phenomenon and therefore the existing tools for the prediction of the location and the amplitude of damage induced by the moving arc spot do not enable to design accurate and optimized protections that would minimize the aircraft weight while ensuring its endurance and resistance to lightning strike. The previous experimental studies conducted to reproduce and understand the swept-stroke phenomenon did not provide sufficiently accurate and quantitative data to evaluate the physical quantities intervening, mainly for the arc channel description during the phenomenon. This lack of experimental information is mainly due to the difficulties to implement an in-lab experiment with complex and sophisticated diagnostics. Therefore, this lack of information provokes an issue with the validation of the developed models for computational simulation tools. Indeed, these models are currently compared to data issued from in-flight measurements – where the initial conditions are not controlled and standardized – and from static arcs measurements – where no swept-stroke occurs.

To establish a relevant experimental database fulfilling the scientific needs, the present study first consists of implementing an experiment representative of the swept-stroke with good repeatability and good control of the initial conditions. For this, we need to design, develop, experimentally implement and couple two complex instruments that are not available in the industry or in the literature:

- A lightning generator capable of reproducing electric arcs respecting the lightning arc waveform as defined in the aeronautical standards

- A launcher instrument capable of propelling aeronautical test sample at speed levels characteristic of aircraft take-off and landing

These two instruments have to ensure high operational safety since they involve high power electric storage and release: The lightning arc generator needs to deal with current levels up to 1.5 kA and a voltage of 2 kV, leading to stored energy of around 250 kJ. To reach a speed of around 100 m/s with samples of a few hundreds of grams, the launcher will need to work with a current level of 25 kA and an storage energy of almost 1 MJ, resulting in a kinectic energy of approximatively 500 J. For the sake of comparison, this energy is equivalent to a typical 9x19 mm Parabellum cartridge of 8g with a muzzle speed of 350 m/s.

After the development and the coupling of the two instruments reproducing the swept-stroke, the second step of the present study is to develop and implement electric and optical diagnostics in order to evaluate the physical quantities evolution of the arc channel during the swept-stroke and the interaction of the arc roots and the aeronautical test sample. As exhibited in the introduction, the objective of this second part of the study is to provide first answers the following questions:

- How the arc channel is affected by the swept-stroke?

In a macroscopic point of view, how its shape and lengths vary during the phenomenon for different initial conditions? For electrical concerns, how its voltage, current and electric power vary during the motion? What is the temperature of the arc channel when it is elongated? What are the influences of the test sample speed, the arc current, the test sample length, the arc spot polarity and the initial length of the arc column on these values?

- How the arc root motion on the test sample is affected by the swept-stroke?

How the mode of arc spot displacement – continuous, partially discontinuous or jumping modes – varies with the initial conditions. What is the average dwell time of an arc spot on a specific point? During a reattachment between two points of the test sample, what are the spatial and electrical characteristics of the portion of arc channel that extinguishes for the formation of a new conductive portion of arc channel? What is the skip distance between those two points? What are the size and the length of the impacts on the test samples? What are the influences of the test sample speed, the arc current, the test sample length, the arc spot polarity and the initial length of the arc column on these values?

- What are the differences of physical processes considering a swept-stroke produced by a moving test sample and a static electric arc and a swept-stroke produced by a static test sample and a moving electric arc?

The two modes of relative motion can be produced through a test sample launcher that is developed during this work as an original instrument and through wind tunnel equipment that is able to blow the arc channel. Then, do the effects of the swept-stroke on the arc channel and on the arc motion depend on the mode of relative motion between the test sample and the electric arc?

Chapter II. Design and implementation of DC-to-DC converter topology for current regulated lightning generator

To reproduce the swept-stroke phenomenon, the first step is to design and implement a lightning generator that would be able to create electric arcs with the characteristic of the lightning arc phase intervening in the phenomenon. This generator has to be robust and accurate enough to enable the formation of an electric arc with a good repeatability in its electrical properties for an important number of experiments. As the arc column is elongated during the phenomenon, the generator has to ensure the respect of the electric properties of a standardized lightning arc channel despite the time growing arc geometrical instabilities.

For those purposes, a model of the elongating electric arc with the characteristics of a lightning arc is established through the analysis of previous works in the literature in order to determine the electric performances required in terms of generator. Then, two topologies of DC/DC generators - the Buck and the Buck-Boost - are adapted and compared through simulations with the minimum energy criteria since they are theoretically able to generate the required electric performances. These topologies are then experimentally implemented with a resistor modelling the electric arc and resorting to a feedback loop to ensure the respect of the lightning arc electrical properties. As these topologies are based on several kHz switching components and on kV voltage levels, transient overvoltage cannot be avoided and might provoke breaking of the components. This issue is solved with the design and the implementation of snubber filters that enable to increase the power of the generator without risk. Then the two topologies are experimentally compared with an initial voltage of over 1 kV for a resistance modelling the arc and, after validation, for electric arcs. Thus electric arcs respecting the lightning arc characteristics are produced with a length reaching 1.5 m and their robustness with elongation are tested and validated.

II.1 Electrical characterization of the electric arc in C-waveform phase

A. Characteristics of C-waveform current

As developed in the Chapter I (Sec I.2), the current profile of a lightning arc is a superposition of highly intensive current pulses – up to hundreds of kA for hundreds of µs in a bi-exponential shape – and a continuous current phase – hundreds of amperes during up to 1 second. Only the continuous phase has to be taken into account during the swept stroke phenomenon as the pulse phase duration is negligible compared to the reattachment process duration even if a high intensive pulse is likely to give a punctual boost of energy to the arc column and foster reattachment.

However, as during the continuous phase the arc has a relative motion to the aircraft due to the airflow, the arc root does not dwell on the same point of the aircraft for the total duration of the C-waveform. Thus, the standards also introduce a truncated C waveform called C* that is simply a shorter version of the C-waveform: its intensity is 400 A in average, maintained for 5 to 50 ms thus delivering 2 to 20 C (Eurocae ED-84 (2013)). The standard also states a charge transfer of ±20% around the set point. To ensure the respect of these boundaries, the objective in this work is to limit variations of ±10% around the 400 A set point current level. This more severe limitation will enable accurate physical parameter estimations in further experimental studies.

This relative motion between the arc and the aircraft also triggers considerations about the length of the arc column for the representability of the phenomenon. Indeed, during the lightning strike, the steady arc column is elongated in the crossflow direction until it reattaches to another point of the aircraft fuselage. As discussed in Chapter I (Sec I.3), Wutzke et al. (1968) measured a minimum relative velocity of 20 m/s above which the electric arc channel diverts from a steady column and is subject to reattachment. So, in order to reproduce experimentally a lightning restrike with a relative velocity of 20 m/s and respecting the 50 ms arc duration recommended by the standards, the minimum length of the electric arc has to be 1 m considering the worst-case scenario where no arc reattachment occur. Therefore, the objective of our lightning generator is to reproduce an electric arc of 1 m respecting the standard C*-waveform – a 400 A average intensity with a maximum variation of ±10% during 50 ms. Moreover, when the arc length is extended due to a relative motion between the arc and the aircraft, its electrical potential increases (Tholin et al. (2013)). When restrike occurs, as the length of arc suddenly decreases, its electric potential does as well and the lightning generator has to be robust enough to provide a regulated current of 400 A respecting the standard C*-waveform. For further design the lightning generator, the electrical behaviour of the electric arc has to be set.

B. *Electrical model of the sweeping continuous arc*

Neglecting the phenomenon of plasma sheath that is located at few hundreds of micrometers in the vicinity of the electrodes, the common electric model of the electric arc consists in time-varying resistor. This model is all the more relevant as the arc column is longer (Weizel (1947); Vlastov (1969); Vlastov (1972)). In particular, Sunabe and Inaba (1990) measured the equivalent arc resistance for a range of current values of few hundreds of amperes. A domain of inter-electrode distance from 0.6 to 3 m for current from 50 A to 10 kA is investigated and the mean electric field and linear resistance (assuming the arc channel is axisymmetric) are given for integration times over 100 ms. The mean electrical field and linear resistance obtained from experimental results are given by:

$$E = p\, I^{-q} \tag{II.1}$$

$$r = pI^{-(q+1)} \tag{II.2}$$

Where E is the arc channel electric field in V/cm, r is the linear resistance in Ω/cm, I is the arc current in A, p and q are constant factors with respective values 13.8 V/cm and 0.06. The electric field is then almost constant depending on the current so that the linear resistor- which is obtained in dividing the electric field by the current – is conversely proportional to the current. These experiments present a linear arc resistance of 5 Ω/m for a current of 200 A and 2.4 Ω/m for a current of 400 A. In his simulations of the electrical mean resistance values of a DC arc, Chemartin (2008) indicates a mean value of 4 Ω/m for 500 A electric arcs considering the first 50 ms of arc lifetime as depicted in Fig. II.1. So, in order to take into account the upper estimation of resistance for an electric arc at 400 A, a 4 Ω equivalent resistor is considered to model a 1 m long arc at 1 atm and for the duration of 50 ms.

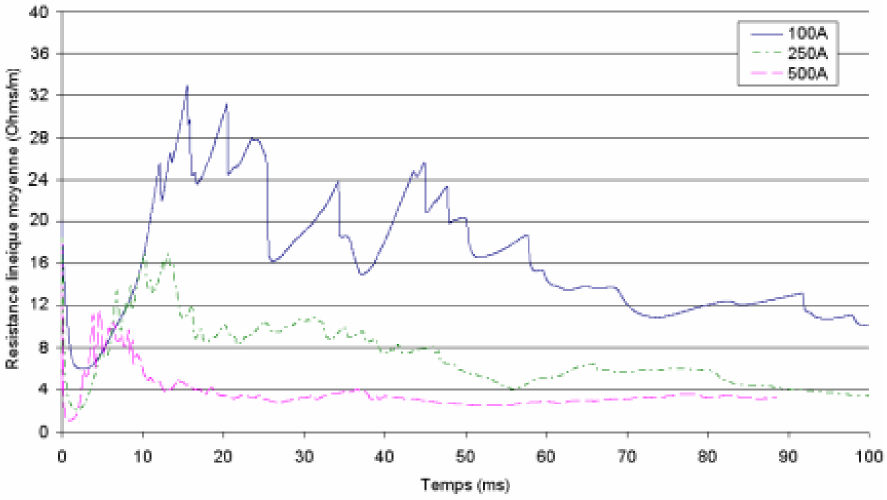

FIG. II.1 Evolution of mean linear resistor for three current values (Chemartin (2008)).

It is worth noticing that the linear resistor is likely to reach high values in the initiation process before reaching the time-integrated values presented in Sunabe and Inaba (1990). This is due to transient effects happening in the establishment of the arc column which is more resistive for the first instants because the channel is not heated enough to stabilize. Thus the initiation phase is shorter for higher currents. But the initiation high resistance problem is often experimentally resolved by adding an ignition wire that offers a small resistance and heats up very fast to foster the establishment of the channel.

C. Impacts of the magnetic and hydrodynamic phenomena on the electrical model

The previous model only considers the arc as a straight static conductor line with no perturbations, but the electric model has to take into account the effects of self-induced magnetic field (through tortuosity shape) and the air-cross flow.

Due to self-induced Lorentz force, loops of current grow from the arc channel under the effect of its magnetic pressure and are likely to divert the arc column from a straight axisymmetric shape thus elongating its total length. The ratio of the arc column length to the gap length is referred to as normalized length (NL) in the literature and expresses this tortuosity shape in the equations. A representation of the evolution of this phenomenon pointing out the loop reconnection process is shown in Fig. II.2.

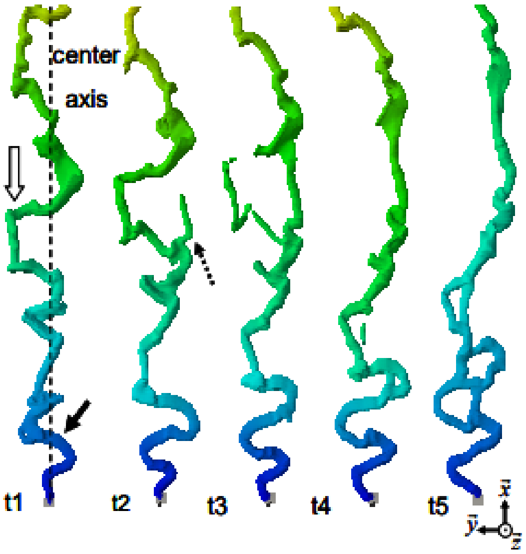

FIG. II.2 Loop reconnection process in the arc column (Tholin et al. (2013)).

Tanaka et al. (2000) experimentally reported that the normalized length only depends on the current values – ranging from 1.6 for DC arcs at 100 A to 2.1 for 2000 A. For a 400 A arc, this factor is between 1.6 and 1.8. This is a really important parameter because, for an inter-electrodes distance of 1 meter, the high-power generator has to supply energy to a 1.8 m arc which increases the arc resistance: as the linear resistance for a 400 A arc is 4 Ohms/m, a total resistance of almost 8 Ohms has to be considered.

In addition to the self-induced magnetic field, the arc channel is subject to a transverse aerodynamic flow. Considering the experimental configuration where the test sample is in motion and the lightning channel is static, numerical simulations Tholin et al. (2013) have shown that the arc channel rather elongates along the aircraft surface – the arc column is stuck to the surface and only the part of the channel in the vicinity of the boundary layer is subject to motion as shown in Fig. II.3. Thus, only the arc root has to be considered to be – artificially – blown by the transverse aerodynamic flow. When it comes to considering the experimental configuration where the lightning channel is in motion due to a transverse airflow or to an external or self-induced magnetic field, all the arc column is subject to air-cross flow or magnetic effects.

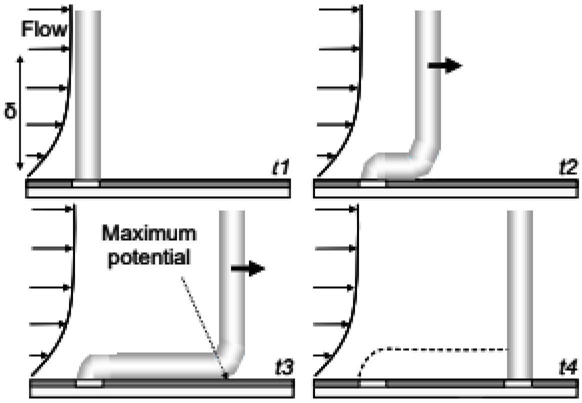

FIG. II.3 Schematic representation of a swept-stroke on a flat surface (Tholin et al. (2013)).

The first effect that has to be considered in all the configurations is the additional energy that has to be delivered to enable the elongation of the channel along with the aircraft between two reattachments. In the worst-case scenario – no reattachment occurs – the channel elongates up to 1 meter. In this elongation process, the arc channel has to heat a new available volume of plasma so that this volume gets physical thermodynamic characteristics homogeneous to the rest of the column. (Larsson et al. (2000)) propose a model of artificial energy loss term to model the channel elongation and gives a conclusion about the development over time of the linear resistance for the different magnitude of the elongation velocity for a 100 A current as represented in Fig II.4.

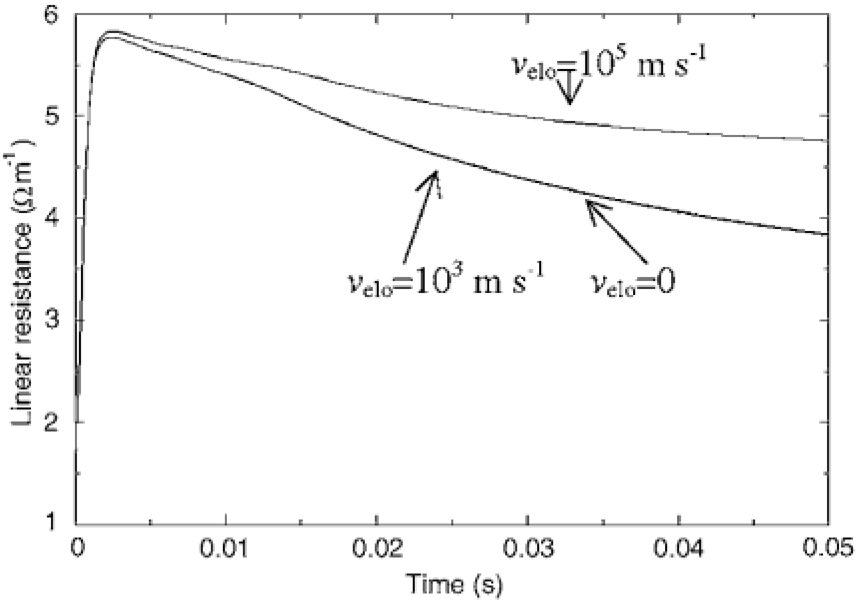

FIG. II.4 Linear resistance time evolution for different elongation velocities for a 100 A arc current (Larsson et al. (2000)).

It is worth noting that up to 1km/s of arc channel elongation velocity, its linear resistance evolution with time is similar to the case without arc elongation. As the 400 A current that is investigated in this work is in the same order of magnitude, it is expected that the arc channel elongation velocity neither has a noticeable impact on its arc resistance especially if we only consider a speed of 100 m/s.

Models with considerations for thermal losses due to the interactions between the airflow and arc plasma or for the effects of an external magnetic field present a more dramatic influence on the electrical parameters of the arc column. Two theoretical treatments give the internal electric field strength as a function of both the current *I* and the airflow velocity *v*. Bublievskii (1978) studied the thermal losses of an arc channel that was balanced by aerodynamic and magnetic fields. Pellerin et al; (2000) studied the behavior of a magnetically driven arc referred to as gliding arc. They reached the following expressions for the internal electric field:

$$E_{Bubl} = 1.83\ 10^3 \left(\frac{v^2}{I}\right)^{\frac{1}{3}} \tag{II.3}$$

$$E_{Pel} = 5.3\ 10^3 \frac{v^{0.48}}{I^{0.52}} \tag{II.4}$$

These formulas are subject to significant simplifications since they do not take into account MHD equations and suppose a simplified airflow profile. The approximations chosen to evaluate the constants in the expression have to be discussed – since the expressions are not valid with experimental results for airflow velocity close to zero and currents close to zero. Choosing 100 m/s for airflow velocity and 400 A for the intensity and dividing the electric field by the intensity, the linear resistances are 13 Ohms/m for Bublievskii's formula and 5.4 Ohms/m for Pellerin's. Choosing 50 m/s for the same current and those results drop respectively to 8.4 and 3.8 Ohms/m. Lalande et al. (1999) uses the expression presented in Bublievskii (1978) to build a swept-stroke model and compare his results to the Dobbing and Hanson (1978) experiment. The results are not in good agreement with the moving rocket sled (the electric field obtained with computational simulations is two times higher than the experimental one) but are in good agreement with the magnetically swept stroke experiment results also mentioned in Dobbing and Hanson (1978). This might be explained by the fact that in the moving sled rocket experiment, only a part of the channel close to the vicinity of the sled surface is subject to arc cross flow perturbations so that the electric field calculated in Bublievskii's expression is valid in a very negligible part of the arc column.

Thus, depending on the configuration, the arc electric model is not the same: if we consider that the test sample is in motion, then the thermal losses due to channel elongation and to aerodynamic flow or external magnetic effects can be neglected because they only affect a short part of the electric column and so – considering the tortuosity effect that introduced a normalized length factor of maximum 2 for airflow of 100 m/s, the electric arc is supposed to behave as a resistance of 8 ohms for a 1 meter. It is worth noticing that the resistance calculated here is an upper bound since the arc is supposed to elongate up to 1 meter only if there is no reattachment and its mean value is thus inferior to 1 meter. Therefore, the objective of the high power generator is to supply a current of 400 A with a 10% margin through an 8 Ohm resistor for at least 50 ms.

If we consider that the arc is set into motion due to aerodynamic flow or external magnetic field then the Bublievskii formula is supposedly valid for the entire column and so the arc equivalent resistance reaches 13 Ohm for 1 meter at 100 m/s and 8.4 Ohm at 50 m/s.

A last important characteristic of the electrical arc model is that the high-power generator has to deliver a constant current even if a restrike happens – meaning that the voltage potential would drop suddenly as the arc column gets shorter and so the resistor would drop as well. Table II.1 presents the electrical characteristics of the C*-waveform that is expected to be reproduced in this work.

TABLE II.1 Electrical characteristics of the C*waveform studied in this work.

Current (A)	Equivalent resistor (Ω)	Time duration (ms)	Charge (C)	Current margin (%)	Maximum/Minimum Current (A)
400	4-8	50	20	10	440/360

Next subsection will discuss about the most relevant source of energy to reproduce such a waveform in a laboratory in terms of practical and cost issues.

II.2 Overview of high energy storage technologies for lightning generators

A few references of other lightning generators are available in the literature. Whereas the high-current transient A, B and D waveforms issued from the lightning standard can be reproduced using passive electric circuits – Sousa Martins (2016b) and Leichauer (2019) present a RLC circuit triggered by a spark-gap and Kovalchuk (2016) present an adapted Marx generator, the C and C* require most complex structures of electric circuits – a passive circuit being insufficient to produce a square wave. In this section, the energy storage options to produce such a waveform are investigated and some circuits are presented:

A. Grid Power

Using directly three-phase grid power would be the cheapest and the simplest option to run the experiment with no limit in time and so in charge transfer, even if it would require a transformer rectifier with additional passive components to deliver a proper C or C* waveform. However, considering high power requirements, the current in the arc is roughly 400 A and as its resistor is 8 Ω, its voltage drop is equal to 3.2 kV. Considering there is no loss of power in the supply, the grid power would have to deliver up to 1.3 MW. The supply of the laboratory building is not sufficient to provide such a high power.

B. *Batteries*

Banks of batteries have long been used as a DC source and so the technology is well established. Many different battery types are available but the best option that presents the highest energy density and the cheapest cost is lead-acid batteries. Supply and disposal/recycling chains are therefore well established. This solution has already been used in in Dobbing and Hanson (1978) as a lightning generator and is easy to implement since the batteries are easily connectable in series strings to level up the voltage. Batteries are also shortly resistive in Dobbing and Hanson (1978) present a discharge of 4 batteries, with initial voltage up to to 150 V, through a highly inductive coil (0.56 H for a mass of 3 tonnes) and charges it up to 700 A after 3 s – this storage through a coil is called inductive storage. Then the current in the coil is released through the electric arc. The electric circuit is presented in Fig. II.5.

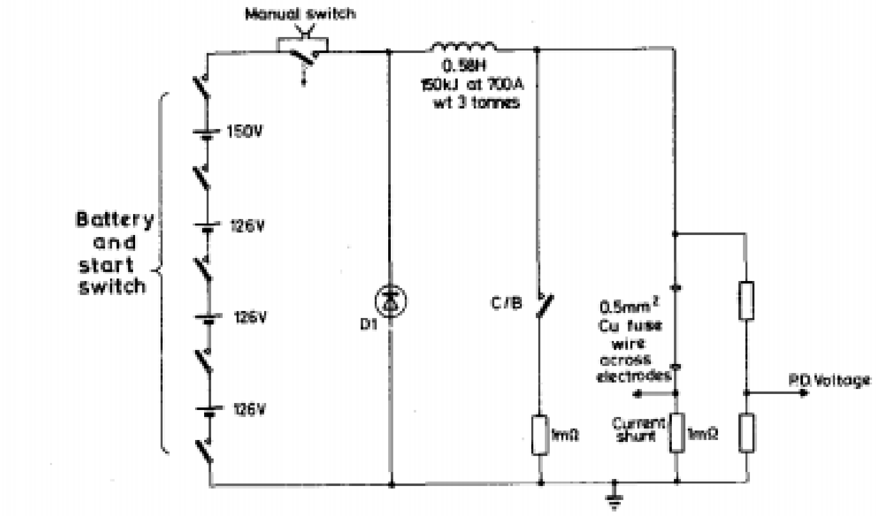

FIG. II.5 Lightning generator using batteries and inductive storage from Dobbing and Hanson (1978).

Moreover, this option is the cheapest one but it has many drawbacks: it usually necessities high maintenance with a cooling system and a replacement of the resistive cells and has a limited life (7 to 10 years depending on the quality of cells). It is dangerous because the electrodes remain at high DC potential if the battery is not empty and lead-acid technology presents security issues. The battery bank would also require a ventilation system to ventilate the escaping hydrogen gas (Dobbing and Hanson’s experiment takes place outdoors) out of a confined room. There are also concerns for shorting issues that could start a fire (several battery banks have been reported to have caught fire because shorting delivered a high amount of power for a long duration). This option was rejected mainly due to the cost of the installation of a proper ventilation system and the experiment has to be conducted indoors to use accurate optical and electrical measurements.

C. *Flywheel*

A flywheel consists of rotational storage of energy: energy is stored converting DC energy to a spin-up of a massive rotor and so rotational energy through a motor. The energy is released in converting the deceleration of the rotor into DC energy using the motor as a generator. The principle is presented in Fig. II.6.

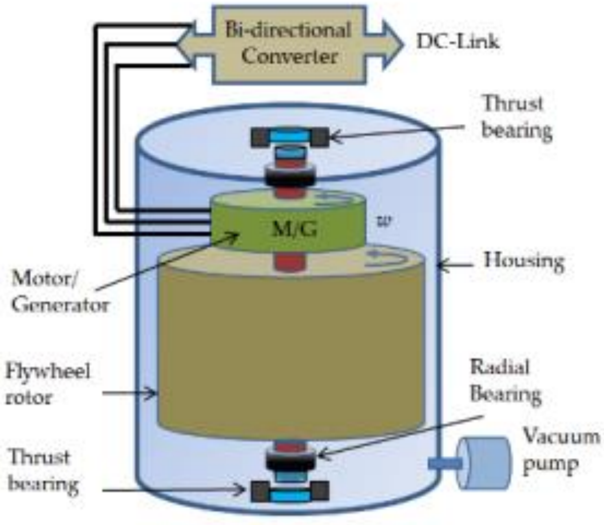

FIG. II.6 Structure and components of a Flywheel (Amiryar (2017)).

This solution is currently used for C-waveform reproduction in the Sandia Lightning Simulator (Caldwell (2005)). The most powerful application of this technology is implemented by UKAEA (UK Atomic Energy Authority) and the European Atomic Energy Community (EURATOM) to run the JET (Joint European Torus). The JET power supply consists of two large flywheels of 776 tonnes capable of supplying up to 400 MW for 30 s to supply current in the electromagnets and coils to generate a magnetic field up to 3.45 T that confine the plasma fusion in the tokamak (Keen and Kupschus (1987); EUROfusion (2016)). This solution is the one that enables the storage of the highest quantity of energy. However, it is a complex system that requires its own design room due to the dangers of having a rapidly rotating assembly of several tonnes. The yield of the power available considering the rotational energy is around 60% at best and requires an electric rectifier structure before delivering DC-energy to the arc. In addition, depending on the technology of the motor/generator converter - asynchronous, variable reluctance, or permanent magnet synchronous – the price per kW is between 20 and 40 euros (Amiryar (2017)) and the cost of the flywheel is at least of 400 euros per kW for a low scale of power application (<10 kW) (Buchroithner (2016)). Thus, considering the need for 1.5 MW to sustain the arc and the low rate of power conversion without energy loss is above 600 000 euros only for the machine and without the complicated infrastructure and the control systems.

D. *Inductive Energy Storage*

The inductive energy storage method is well established and is referred to as a clamped circuit. A capacitor or battery is used to ring energy into an inductor coil. Once the voltage on the capacitor has reduced to zero and the peak current in the inductor is reached, the capacitor is shorted out. This allows the inductor to discharge its current through the load. There is usually some added resistance to enable the tail of the current to be controlled. It is worth noticing that the energy is stored as a current and thus once the inductor coil is charged, a disconnection to the load without any secondary discharge circuit available would provoke a really high overvoltage in the coil subcircuit which means that – unlike other energy storage principles – there cannot be any delay between the charge and the discharge of the inductive energy storage. The lightning generator presented in Dobbing and Hanson (1978) also consists in inductive energy storage since the batteries load current in a 0.56 H coil during 3s until a set point value of 700 A is reached and then a manual switch triggers the discharge in the arc. As the discharge is similar to a LR discharge since the arc can be modeled as a resistor (Sunabe and Inaba (1990)). A typical arc waveform during discharge is presented in Fig. II.7.

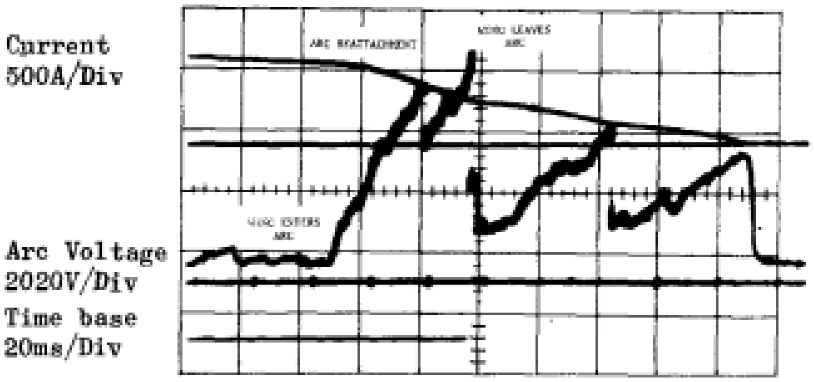

FIG. II.7 Current and Voltage waveforms of electric arc during swept-stroke (Dobbing and Hanson (1978)).

Thus, the courant wave has the shape of an exponential discharge and the current lose around half of its intensity during the electric time constant. According to fig. 8 the current drops from 700 A to 350 A in the first 50 ms and thus is not entirely representative of a C*-waveform with fluctuations inferior to 20% of the set point current value.

In our case, as a maximum current variation of 10% of the set point current is permitted for 50 ms, the characteristic electric time $\tau = L/R$, with L being the inductance value and R the load resistance, of the energy discharge has to be around 10 times the arc duration time 50 ms. As the equivalent resistor of the circuit is 8 Ω, this would result in an inductance value of around 4 H to have a τ of 500 ms. A fast calculation shows that for an air coil component, considering the coil wire has to have a sufficient section size so that its resulting resistance is less than 1 Ω, this equipment could weigh up to several tones. Indeed, for a raw estimation, the inductance L of an infinite solenoid is given by:

$$L = \frac{\mu_0 N^2 A}{l} \tag{II.5}$$

with μ_0 the vacuum permeability, N the number of turns, A the cross-section area of the flux density and l the length of the coil. The number of turns is limited by the length of the wire that is coiled around the coil's axis l_{tot} and by the radius r of the cross-section area by:

$$N_{max} = \frac{l_{tot}}{2\pi r} \tag{II.6}$$

Thus, using equations (5) and (6), in the most compact geometry achievable, the inductance is given by:

$$L = \frac{\mu_0 l_{tot}^2}{4\pi l} \tag{II.7}$$

Introducing the total resistance R of the coil that is given by:

$$R = \frac{l_{tot}}{\sigma S} \tag{II.8}$$

with σ being the conductivity of the material and S the wire section. Thus, considering that a resistance over 1 Ω would consume too much energy in regard of the lightning equivalent resistance, the total mass m of the coil is given by:

$$m = \frac{4\rho L}{\sigma R \mu_0} l = \alpha\, l \tag{II.9}$$

with ρ being the volumic mass of copper and α being the coefficient representing the proportion of the mass of the air coil per unit of coil's length. For our configuration, this coefficient is equal to 2 tonnes per meter. As the soleinoid is supposed to be infinite, it can be assumed that the coil's length has to be over few tens of cm, which results in a mass over 1 tonne. However this result is an underestimation since the weight of the coil reported in Dobbing and Hanson (1978) is 3 tonnes for a resulting inductance of 0.58 H. Thus it can be expected that the order of magnitude to reach 4 H is largely over 1 tonne, that would make this solution difficult to be implemented and manipulated in a laboratory.

It is worth notice that for this level of magnetic field from a current of 400 A and a coil with an inductance of 4 H, this is irrelevant to consider magnetic core material as a possible solution. Indeed, the required flux is in the range of 1600 Weber and as the saturation field of a magnetic material is no more than a few Tesla, the maximum magnetic flux storage would be about few Weber for a core with a 1 m diameter.

E. *Capacitive energy storage*

The most interesting solution for our problem resorts to capacitive energy storage as for their safety advantages - they can be drained out of energy and can be utilized indoors – that for their use of ease. Also, they do not require much maintenance, are compact and are relatively fast to load. Their main drawback for the detailed application is that they do not provide a DC current when connected to a resistor. This can be solved using DC/DC converter topologies that will be discussed in the next section. Their only counterpart is that their main fast-switching components, the high-power IGBT and diode, have a limited operative voltage. For the available high-power components in the laboratory, the model of IGBT chosen has a limit operative voltage of 4.5 kV. Considering an energy transfer from the capacitor energy storage to the electric arc resistor without any losses, the minimum capacitance value that is required to limit the voltage level is given by:

$$C = \frac{2\,RI^2\Delta t}{V^2} \tag{II.10}$$

where *R*, *I*, *Δt* and *V* are respectively the equivalent arc resistor (8 Ω), the average current (400 A), the required duration time (50 ms) and the maximum voltage of the capacitors (2.5 kV). This results in a minimal capacitance of 60 mF. In this work, a bank of 5 capacitors of 22.5 mF each and with maximum voltage of 2.5 kV for a resulting capacitance of 112.5 F is used to grant some leeway and is presented in the following sections.

II.3 Theoretical comparison and design of high-power Generators

A. *Context and Adaptation*

DC/DC converters are electronic circuits that convert a source of direct current from one voltage operative level to another. There are different kinds of topologies, but they all use the same conversion pattern with few variations: a switch enables to shift the circuit from an Off-state to an On-state so that the source of energy – a capacitor bank in our case – provides energy with a regulation on the current level to the load – an arc equivalent resistor. Standard schemes involve a coil that helps to slow down the current variations and to provide an intermediate storage of energy and also a diode that regulates the current flow.

Two converter topologies, Buck and Buck-boost, are compared in this thesis. Fig. II.8 presents the schemes of both configurations. In the Buck configuration, when the switch is activated in Fig. II.8(a), the energy from the capacitor is discharged in the load resistor through the coil. When the switch is deactivated in Fig II.8(c), the current is maintained in the load resistor passing through the coil and a free-wheeling diode. In the Buck-boost configuration, when the switch is activated in Fig II.8(b), the capacitor discharges its energy in the intermediary coil whereas the current is maintained in the load resistance thanks to a filter capacitor. When the switch is deactivated in Fig. II.8(d), the energy stored in the coil is discharged through the resistor and the filter capacitor.

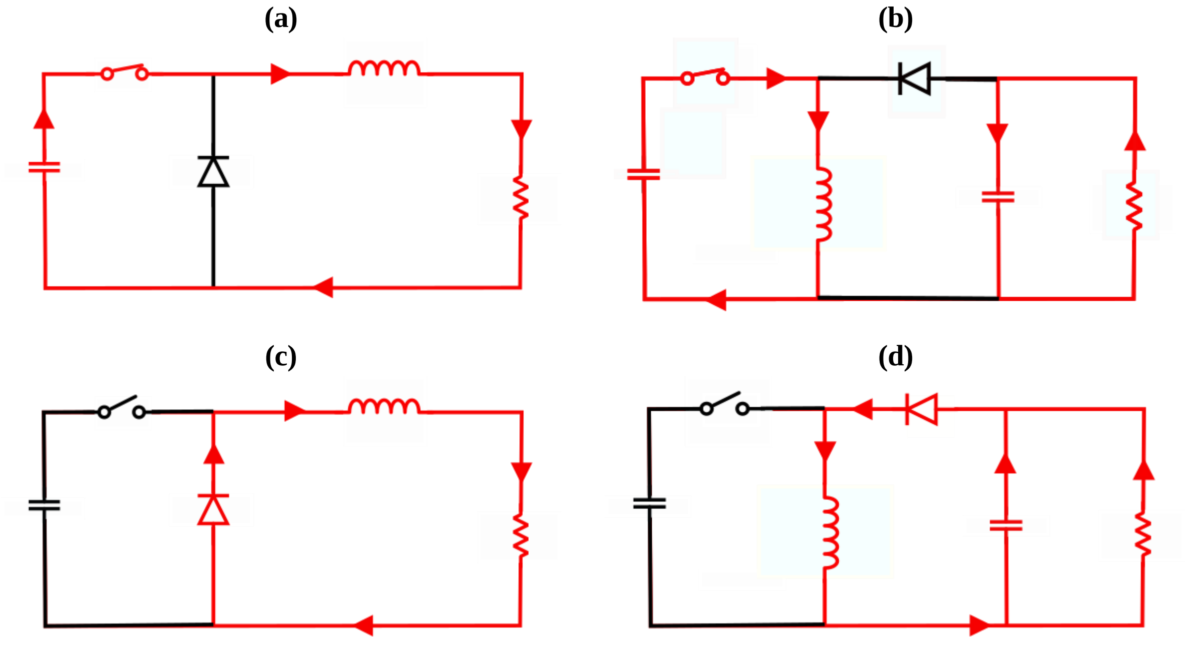

FIG. II.8 Presentation of Buck on-state (a), Buck off-state (c), Buck-boost on-state (b) and Buck-boost off-state (d).

Buck converter is referred to as a step-down converter because it steps down the voltage of the supply to the load. Thus, the operative voltage of the load resistors – the electric arc in this application - is limited by the maximum voltage of the supply capacitors. Buck-Boost converter is able to function as a step-down or a step-up converter so that the operative voltage of the load resistor is able to outreach the maximum voltage of the supply capacitors.

The main utilization of DC/DC converters consists in controlling the output voltage by implementing a fixed duty cycle using a PWM mode (Fuad et al. (2001)). For example, Leichauer (2019) presents a Buck converter using a PWM mode with a frequency of operation of 5 kHz that produces a square shaped current waveform of 200 A with a margin of ±25% and lasting 1 s through a 2 Ω resistor. As in this application the objective is the reproduction of the C* current waveform, the focus is the regulation of the load current. Then a closed loop command structure has been selected: the current in the load is measured and depending on its value, the switches enable the circuit to provide energy to it or not, increasing or decreasing its current level, thus creating the regulation.

B. Theoretical comparison of the Buck and Buck-boost performances

In order to compare the different topologies, our criteria are, from the available capacitor bank of around 110 mF, the minimum voltage – and thus the minimum energy – that is required for maintaining a current of 400 A through resistors of 4 Ω and 8 Ω – that are, respectively, upper bound values of electric arcs of 50 cm and 1 m, as mentioned in previous section, during at least 50 ms. The current variation must not exceed 10% of the set point current. As all the topologies resort to a load inductance that help to smooth the current waveform, the analysis also has to consider the minimum value of inductance L that is required for every configuration.

In the simulation, the topology of RLC-circuit, Buck circuit and Buck-Boost circuit are compared – the RLC circuit not being a proper DC/DC converter but serving here as a reference case. For all the topologies, the algorithm that is implemented for simulations consists in calculating the electric parameters of currents and voltages in every node and branch at the different instants of commutation of the switches, and the different durations of On-state phases (the time duration the circuit requires to increase its load current from 360 A to 440 A) and Off-state phases (the time duration the circuit requires to decrease its load current from 440 A to 360 A). The varying parameters are the initial voltage in the source capacitor bank and the inductance value.

The algorithm equations are represented with the associated schematic diagrams in Fig. II.9. During On-phase, the average load current I_R is 400 A and the load current variation ΔI_R is 80 A for the Buck and -80 A for the Buck-Boost whereas during the Off-phase, the load current variation is -80 A for the Buck and 80 A for the Buck-Boost. For every iteration, the algorithm calculates the new values of the node voltage of the bank capacitor U_C and of the coil branch current I_L and the phase duration Δt. The iteration number is referred as n in the equations presented.

(a)

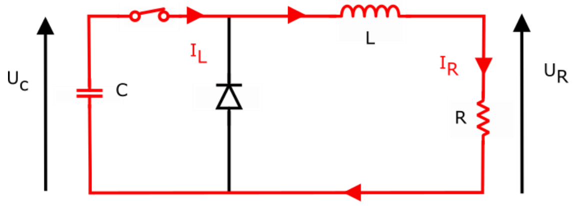

$$U_R = R\, I_R$$

$$\Delta U_R = R\Delta I_R$$

$$I_L = I_R$$

$$\frac{U_C^{n+1} + U_C^n}{2} - U_R = L\frac{I_L^{n+1} - I_L^n}{\Delta t^n}$$

$$I_R = C\frac{U_C^{n+1} - U_C^n}{\Delta t^n}$$

(b)

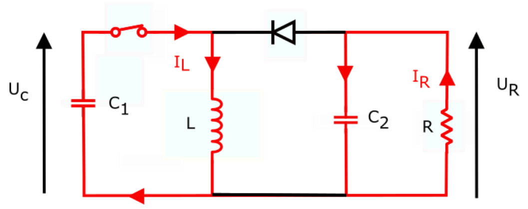

$$U_R = R\, I_R$$

$$\Delta U_R = R\Delta I_R$$

$$I_R = C_2\frac{\Delta U_R}{\Delta t^n}$$

$$\frac{U_C^{n+1} + U_C^n}{2} = L\frac{I_L^{n+1} - I_L^n}{\Delta t^n}$$

$$\frac{I_L^{n+1} + I_L^n}{2} = C_1\frac{U_C^{n+1} - U_C^n}{\Delta t^n}$$

(c)

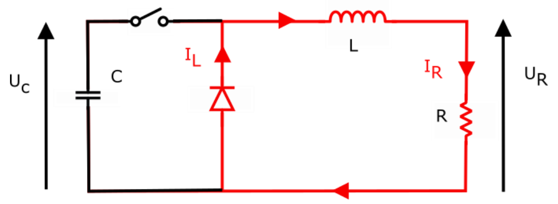

$$U_R = R\, I_R$$

$$\Delta U_R = R\Delta I_R$$

$$I_L = I_R$$

$$-U_R = L\frac{I_L^{n+1} - I_L^n}{\Delta t^n}$$

$$U_C^{n+1} = U_C^n$$

(d)

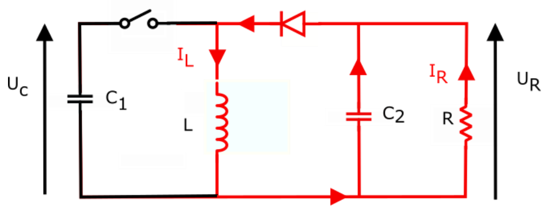

$$U_R = R\, I_R$$

$$\Delta U_R = R\Delta I_R$$

$$U_R = L\frac{I_L^{n+1} - I_L^n}{\Delta t^n}$$

$$\frac{I_L^{n+1} + I_L^n}{2} - I_R = C_2\frac{\Delta U_R}{\Delta t^n}$$

$$U_C^{n+1} = U_C^n$$

FIG. II.9 Electrical equations of the Buck on-phase (a), Buck-Boost on-phase (b), Buck off-phase (c), Buck-Boost off-phase(d).

The graphics presented in Fig. II.10 show the duration time for that the load current is maintained around its set point as a function of the initial capacitor voltage and for the minimum value of the intermediary inductance in the circuits considering resistors of 4 and 8 Ω as loads.

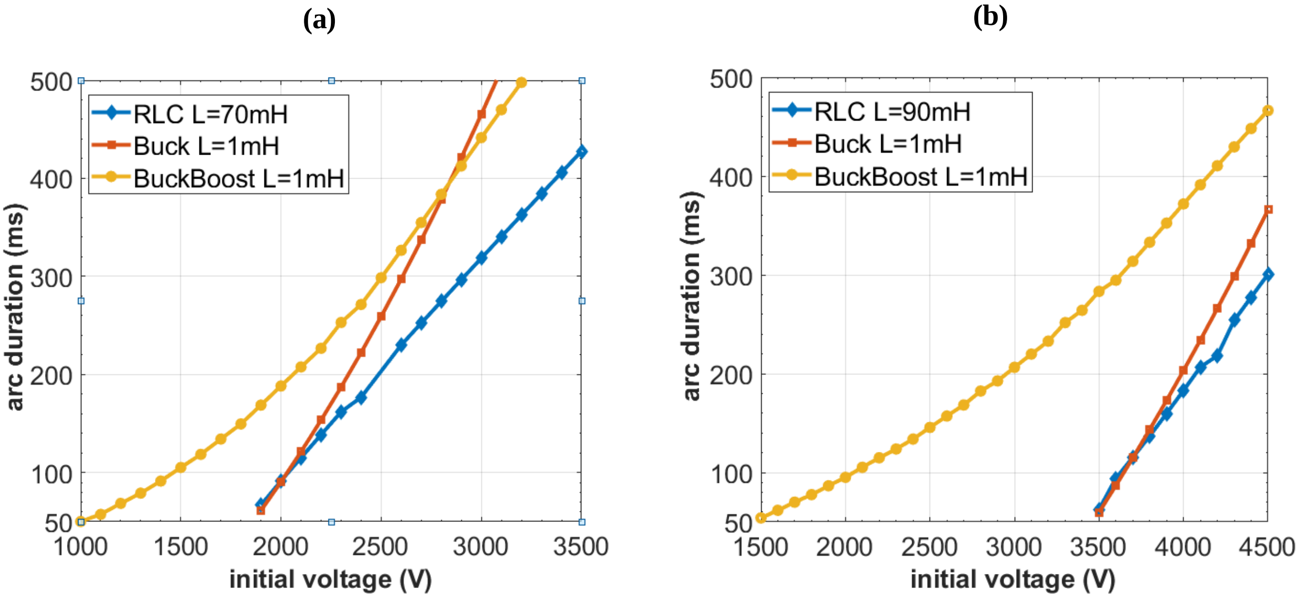

FIG. II.10 Comparison of the performances of RLC, Buck and Buck-boost circuits considering a load resistance of 4 Ω (a) and 8 Ω (b).

Table II.2 summarizes the minimum initial bank capacitor voltage and the minimal inductance coil values for which the different topologies under test can generate a regulated current of 400 A with a ±10% margin through respective load resistor values of 4 and 8 Ω for at least 50 ms.

TABLE II.2 Results of the electric performances of the different topologies.

Topology	**Equivalent resistor (Ω)**	**Time duration (ms)**	**Capacitor Voltage (V)**	**Coil Inductance (mH)**
RLC	4 (8)	50	1900 (3500)	70/90
Buck	4 (8)	50	1900 (3500)	1
Buck-Boost	4 (8)	50	1000 (1500)	1

It can be concluded from this table that the circuit that reaches the best performances for our problem in terms of energy efficiency is the Buck-boost topology. It can match the criterion charging the capacitor bank to only 1 kV for a 4 Ω load and 1.5 kV for an 8 Ω load thanks to the use of the intermediate coil that is able to transform the capacitive energy into inductive energy with better energy density. The use of inductive energy decouples the voltage level of the capacitors from the voltage level of the equivalent arc load resistance. Indeed, in the Buck configuration, the initial voltage in the capacitors needs to be superior to the arc voltage of 3.2 kV resulting from a 400 A current flowing through an 8 Ω resistor.

In the other hand, the inductance value given by the RLC configuration value is in the order of magnitude of 0.1 H, which would result in a coil mass of more than one tonne to keep a resistance inferior to 1 Ω. So, despite RLC circuit has the advantage over DC/DC converters of not requiring any power switch IGBT or power diode, it is excluded in the rest of this work.

Looking closer to the Buck-boost configuration, the conversion of the capacitive energy to inductive energy is only effective if a high level of current is stocked in the intermediary coil – reaching up to a few kA in our configuration. This represents a non-negligible problem because the available power switches IGBTs have a 1.2 kA current limit. A solution for this issue is to add several of these components in parallel. Two IGBTs were added in parallel for the Buck-Boost configuration to reach an operative current of 1.5 kA but this solution increases driver issues and costs. The solution implemented in this work is to add another feedback-loop regulation on the current that flows into the coil that has a priority over the one regulating the load current, so that the switch components are protected from a level of current they cannot endure. Meanwhile, if the priority is given to the intermediary coil current, the load current square form is inevitably deteriorated as the only way to prevent a surge of current in the coil is to discharge it in the load resistance. However, this might be acceptable and stay in the limit of the 10% margin over the set point current value. This issue will be treated in the following sections.

Another problem with the Buck-Boost configuration is that the voltage at the terminals of the IGBTs devices is higher than the initial voltage of the bank capacitor because of the inversion of polarity of the load resistance whose high voltage point is referred to the circuit mass. Consequently, when IGBTs devices switch off, one of their terminals is raised to the voltage level of the capacitor bank V_{CAP} whereas the other terminal is referred to the negative voltage point of load resistance $V_{ARC} = - R\ I_{ARC}$ with R being the equivalent arc load resistor. Thus, the voltage between the terminals of the IGBT´s devices is given by:

$$V_{IGBT} = V_{CAP} + R\ I_{ARC} \tag{II.11}$$

Considering the values of Table II for respective equivalent load resistors of 4 Ω and 8 Ω, this voltage reaches 2600 V and 4700 V. The value of 4700 V is inacceptable as operative voltage because it is over the IGBTs voltage limit. The resume of operative voltages and currents of Buck and Buck-Boost configurations main components to reproduce a C*-waveform of 400 A is given in Table II.3.

TABLE II.3 Comparison of Buck and Buck-Boost components operative voltages and current.

Topology	**Equivalent resistor (Ω)**	**Capacitor initial voltage (V)**	**IGBTs operative voltage (V)**	**IGBTs operative current (A)**	**Feedback loop regulations**
Buck	4(8)	1900(3500)	1900(3500)	400	1
Buck-Boost	4(8)	1000(1500)	2600(4700)	1500	2

II.4 Experimental set-up and design of a snubber

A. Description of materiel under-test

The same equipment has been used for the both Buck and Buck Boost topologies: This consists of a capacitor bank composed of five capacitors of maximum voltage 2.5 kV and with 22.5 mF each, another capacitor bank composed of two capacitors of 10 mF each and with a maximum voltage 5 kV, an air-coil of a variable inductance from 2 to 10 mH for an internal resistance of only 30 mΩ with a total weigh of 300kg, single switch IGBT modules from Dynex Semiconductor (DIM1200ASM45-TS000) that possess a collector-emitter maximum voltage value of 4.5 kV and a maximum continuous collector current of 1.2 kA, fast recovery diode modules from Dynex Semiconductor (DFM750AXM65-TS000) with a maximum repetitive peak voltage of 6.5 kV and a total forward current of 2.25 kA (750 A per arm).

The current measurements are realized using a PEM CWT AC CWT60LF probe. The voltage measurements are made using voltage probes of reference North Star PVM-1 - and of reference Lecroy PPE5KV.

Figure II.11 presents photography of the high-power lightning generator assembled; the red cylindrical coil has been moved 3 m away using long wire so that its magnetic field does not disturb the signals of the electronic microcontroller closed-loop part of the generator.

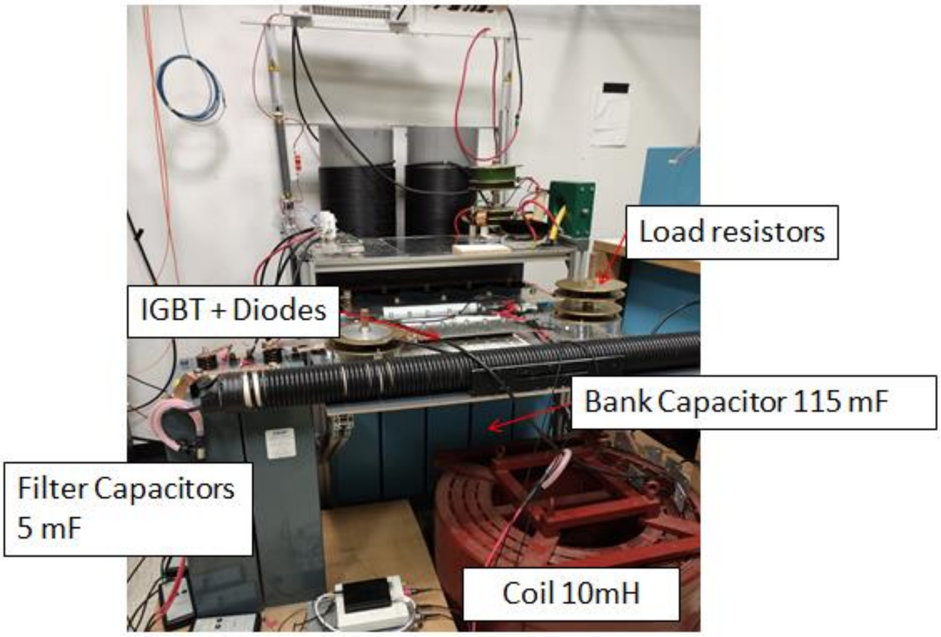

FIG. II.11 Assembly of the high-power lightning generator.

B. Experimental discussion about the feedback loop

An important source of discussion in this experiment is the way to create a feedback-loop regulation for the load current in the Buck topology and for both the load current and the intermediary coil current in the Buck boost topology. It involves one or two measurements of current, a treatment and a comparison to a set point value from a microcontroller and a communication to the IGBT switch to activate or deactivate it.

The simplest ways to introduce a non-intrusive measurement of current in the electric circuits and to send them to a micro-controller are the use of a shunt of current resorting to relatively high values of resistance, and the use of a current coil probe considering our timescale. As the available current probes – rather designed for AC current – have a droop measuring DC current, it might introduce an error of measurement for signals that last over few milliseconds. For the two available relevant models of probe of this technology, CWT6LF and CWT60LF, the sensitivity of the first one would result in a level of voltage of 2 V for 400 A and the second one to 200 mV for the same current level. Thus, the first model has two advantages for the values involved. First, it has a better sensibility and so a more precise regulation. Secondly it sends a signal in the magnitude of the volt to the microcontroller – an Arduino ATmega328P - that is more accurate for this scale of voltage - without any need for re-scaling active filter. On the other hand, the droop level of the CWT6LF reference introduces an error of 0.25 %/ms that is to say 12.5% minimum considering a waveform of 50 ms. Meanwhile, the droop level of the CWT60LF model introduces an total error of 1.25% for the same duration, which respects the upper bound error limit of 10%. The other option is to use a shunt of current, choosing two resistors with a resistance value of a few orders of magnitude over the equivalent arc load resistor and with a ratio chosen to convert a 400 A current into a voltage value between 0 and 5 V for the micro-electronic controller. This solution has the advantage to be simple and efficient and was first implemented for the Buck configuration with a relative success using two resistors of 10 and 100 kΩ in parallel of the load resistor. This solution is more complicated to implement for the Buck boost configuration, mainly because it requires two different measurements. Indeed, the two measurements of the two shunts must be treated by the same micro-controller that controls the IGBT switch causing a mass potential reference issue as presented in Fig. II.12. As the positive polarity of current in the load flows from the mass to the intermediary coil, the low potential nodes of the shunt in the coil branch and in the load branch are not referred to the same potential. This could produce a path of current through the micro-controller from the negative voltage point of the low potential node of the load shunt and the mass.

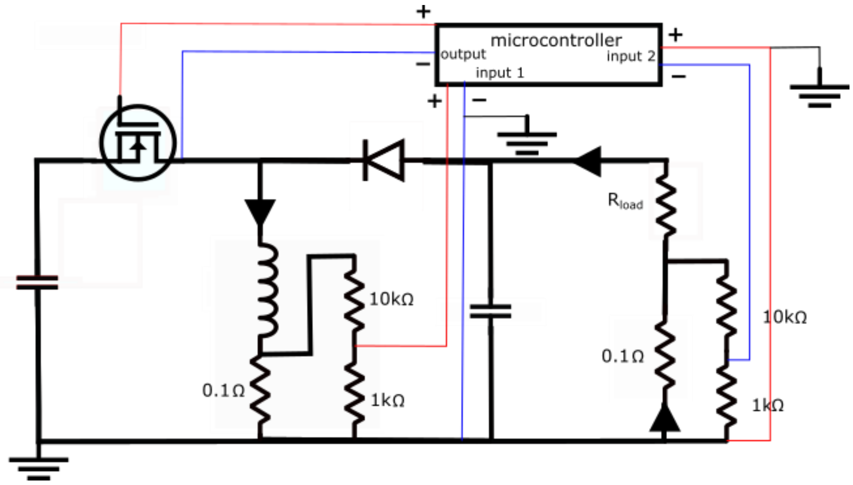

FIG. II.12 Illustration of the mass issues introducing two shunts in the Buck-boost topology.

The solution for this issue consists in inverting the polarity of the voltage measurement of the load shunt using an operating amplifier and an inverting circuit before the signal is sent to the micro-controller. Unfortunately, this solution was greatly subject to the noise of the commutation of the IGBT in the main circuit and the signal reaching the controlled turned out to be unstable. In the end, only the current probe of reference CWT60LF was used for the rest of the experimental study.

Considering the treatment and the comparison to a set point value from a micro-controller, the model technology has to be chosen - in terms of speed and precision performances - in order to be faster than the variations of the electrical parameters of the circuits. Examining the closed-loop channel, putting the microcontroller aside, the limiting component in terms of speed processing is the IGBT switch. Indeed, it requires a turn-off delay time of 3.1 µs, which limits its frequency of utilization to 300 kHz. Thus, there is no need to resort to a 1 GHz-clock FPGA microcontroller, a 16 MHz clock Arduino microcontroller is fast enough for this application. However, if the Arduino microcontroller is used to do an analog-to-digital conversion (A/D) of the analogical signals coming from the current probes, and then a comparison to an internal referred numerical value before sending a 0 V or 5 V signal to the gate command channel of the IGBT, the limit frequency would be around 5 kHz. As the frequency of commutation is a main parameter in this experience in terms of current regulation, a larger choice in its range of value would be greatly appreciated. An effort is made to avoid a time-consuming A/D: before of their treatment by the microcontroller, the voltage signals from the probes are compared with a constant potential value – made of a 5V source and a variable value resistor – that is selected to match the set point current through a comparator. Depending on whether the voltage of the signal is superior or not to the set point reference voltage, the comparator sends a signal of zero or 5 V in the analogic terminals of the microcontroller so that this last does not have to make the internal comparison. The ready-made command functions of the Arduino are also replaced in the coding by bitwise operations to improve the algorithm time performance. These two implementations result in a frequency limitation of 260 kHz that is very close to the limit of commutation of the IGBT. Thus, it makes it possible to control the maximum commutation frequency by introducing controlled delay in the algorithm of regulation.

Once the microcontroller has treated the signal coming from the probes and has sent an instruction, it reaches an opto-isolator that dissociates the mass reference of the Arduino from the emitter voltage node reference of the IGBT branch and activates a transistor that feed the gate branch of the IGBT using a 24 V battery. The feedback loop is schematized in Fig. II.13.

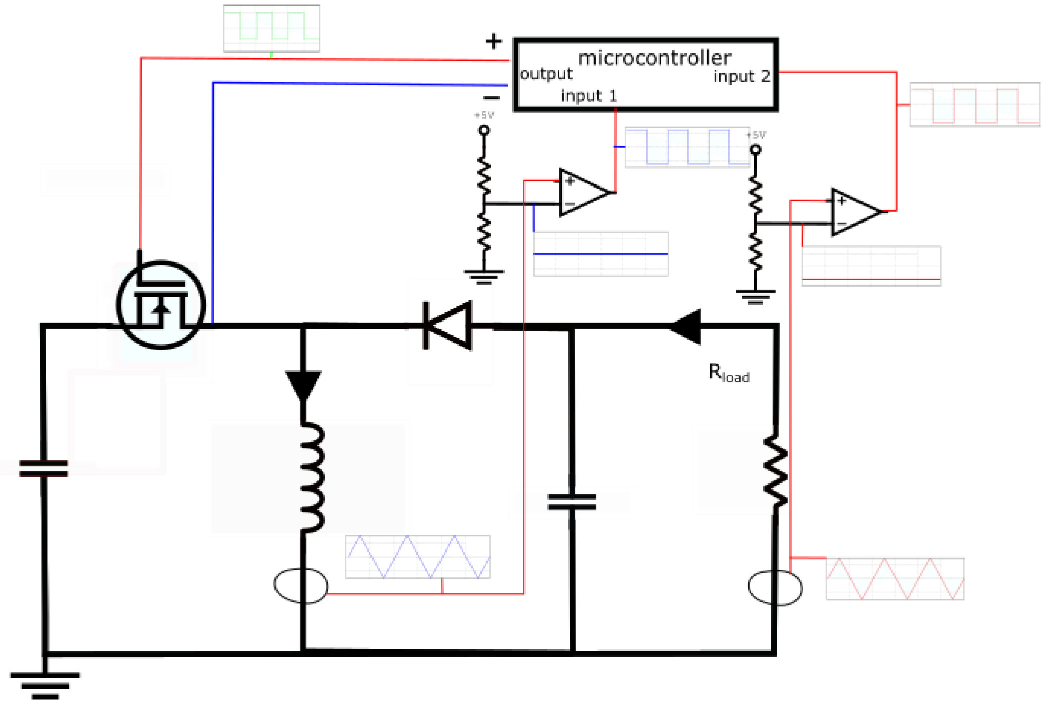

FIG. II.13 Schema of feedback loop of Buck-boost circuit. The current signals are measured in the branch of the coil and of the resistor, compared to a consign value with an amplifier and processed with a microcontroller.

C. Transient Overvoltage problems and snubber design

First, lightning generator regulation loop principle is tested and characterized experimentally at low power (a few hundreds of volts maximum in the energy source capacitor bank for set point currents of a few hundreds of amperes) for both Buck and Buck-boost configurations. Peaks of voltage of hundreds of volts that are not predicted by the simulation models are appearing at the IGBT terminals, especially during the switch-off phases. Indeed, a configuration of a capacitor bank of 10 mF initially charged at 400 V and using an air-coil of 2 mH (internal resistance of 0.5 Ω) and aiming to discharge a regulated 200 A current in a 0.1 Ω load was carried out. Figure II.14 represents the experimental graphs obtained for this configuration with the Buck circuit.

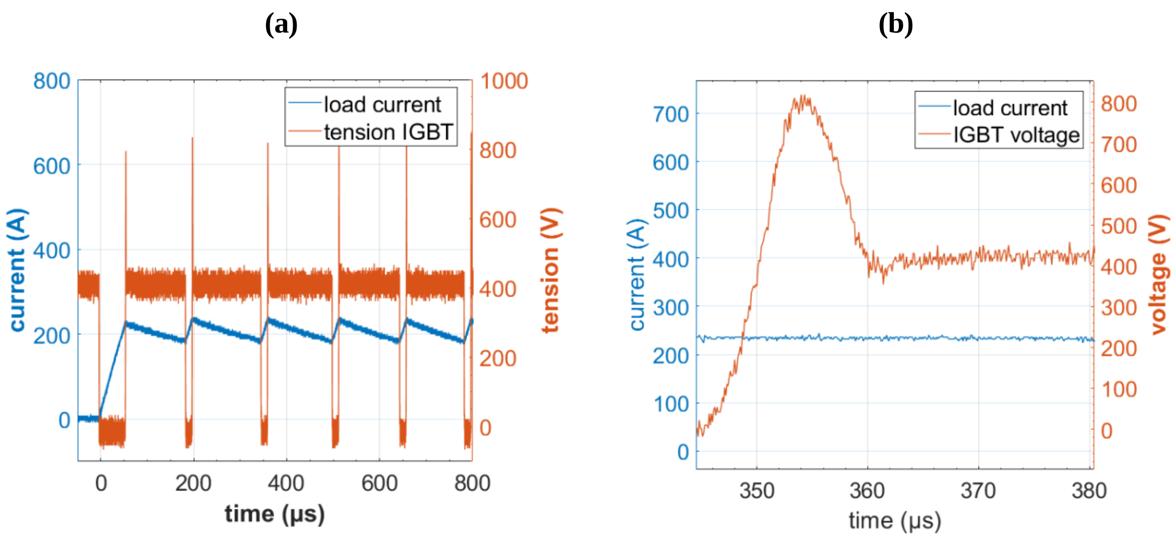

FIG. II.14 Presentation of experimental curves with Buck configuration for low power applications (a) shows the overvoltage peaks of IGBT for 5 commutations and (b) is a zoom of one overvoltage peak.

As it can be seen in the curves, the overvoltage can reach almost 2 times the initial voltage level in the capacitors – reaching a value higher than 700 V in the Buck topology for an initial voltage of 400 V. So, expecting to charge the capacitors to an initial voltage of 2 kV as required for an electric arc of 1 meter minimum, an overvoltage peak of 4 kV might be expected in case of a proportional overvoltage peak.

This overvoltage peak issue is a wide subject of studies in the area of power converter circuits and is mainly caused by peripheral parasitic inductances (Yamashita et al (2017); Li et al. (2018)). Indeed, in both Buck and Buck-boost configurations, when the IGBT converter switches off, the current that goes through the loop involving the source energy bank capacitor and the IGBT suddenly drops from a value up to 400 A for Buck configuration

(1500 A for the Buck-boost case) to zero. And when the IGBT converter switches on, the current that goes through the loop involving the diode suddenly drops as well.

Considering the inductance formed by this branch composed by the parasite inductances of the IGBT device and of the capacitor bank, and by the wire's equivalent inductance, this steep variation of current provokes the apparition of an overvoltage peak expressed by the following equation (Yamashita et al (2017)):

$$V = L_p \frac{\Delta I}{\Delta t} \tag{II.12}$$

With V being the transient overvoltage, L_p being the total peripheral parasitic inductance and ΔI being the current variation during the switch-off phase and Δt being the turn-off delay time (3.1 µs for the described model of IGBT module).

Power switch technologies are usually protected from this overvoltage peak resorting to damping circuits called snubber circuits. Amongst other advantages, it also reduces the electromagnetic interferences (EMI) that could affect the circuit and the commutation losses of the switches (Algaddafi and Elnaddab (2016)). The two main kinds of snubber filters are the Resistor-Capacitor (RC) and Resistor-Capacitor-Diode (RCD) damping circuits and consist in converting the magnetic energy of the parasite inductance circuit in electric energy through a capacitor placed in parallel to the switch (Severns and Reduce (2009)). The resistor and the diode enable to control the flow of current going from the switching circuit to the snubber circuit.

The snubber capacitor must have a capacitance (C_{snub}) as low as possible to be able to evacuate quickly the overvoltage peak in a RC circuit but also high enough to damp the magnetic energy from the parasite inductance. Thus, the C_{snub} parameter of the RC circuit is given by equation (Severns and Reduce (2009)):

$$C_{snub} = \frac{L_p \Delta I^2}{\Delta V^2} \tag{II.13}$$

with ΔI being the absolute current variation during the switch-off and ΔV the maximum overvoltage peak acceptable at the terminals of the IGBT switch. Thus, a capacitance snubber value can be designed only with access to the total peripheral parasitic inductance.

The total peripheral parasitic inductance can be roughly evaluated by a geometrical model of the circuit to determine the wire inductance as done by Yamashita et al (2017). It can also be evaluated experimentally measuring a ringing cycle between the inductance circuit and a known value capacitor placed at the terminal of the IGBT switch during a switching-off phase (Severns and Reduce (2009)). This last method is implemented in this work: different values of capacitance C have been added in parallel to the switch. Measuring the frequency of the ringing cycle from the capacitor to the parasitic inductance, a mean value of L_p is determined with:

$$L_p = \frac{1}{4\pi\, f^2 C_{test}} \tag{II.14}$$

Where f is the ringing frequency experimentally measured and C_{test} is the value of the test capacitance. Figure II.15 presents the curves obtained with Buck configuration for different values of C as a test capacitor and shows the ringing phenomenon. The dataset and the measured values of the ringing frequency and the estimation of L_p are summarized in Table II.4. The additional stray inductance brought by the paralleling of the different test capacitors is neglected is this calculation because the capacitors terminals have been welded directly on the IGBT switch terminals.

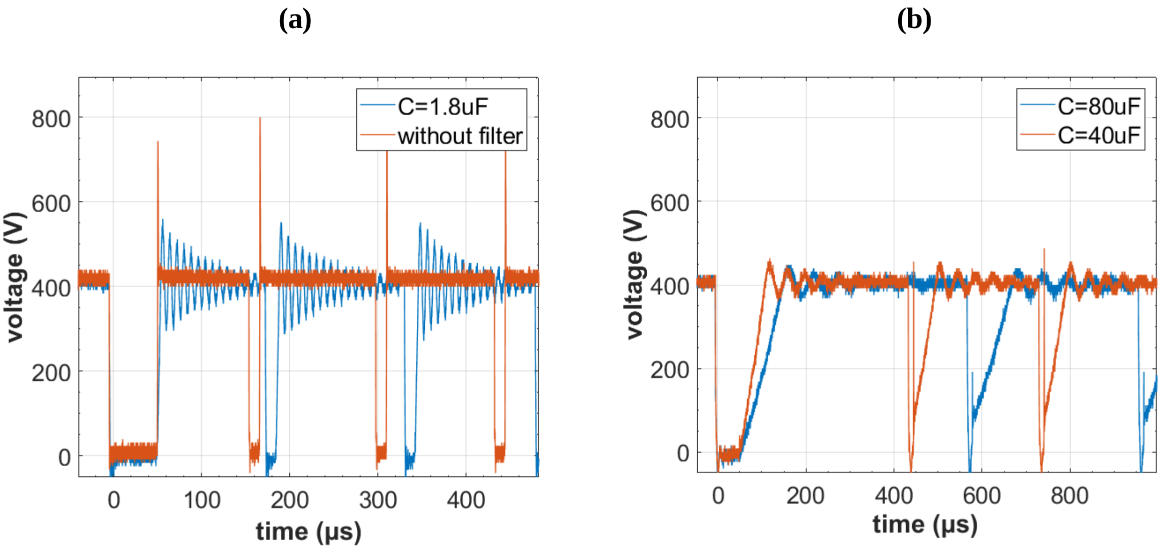

FIG. II.15 Presentation of the ringing phenomenon using different values of C: (a) without filter and with C = 1.8 µF and (b) with C = 40 µF and C = 80 µF.

TABLE II.4 Experimental determination of L.

Capacitor value (µF)	Frequency of ringing (kHz)	Parasitic Inductance (µH)
1.8	125	0.9
40	25	1.01
80	18	1.03

The experimental results give a parasitic inductance in the order of magnitude of 1 µH. It appears also from those results that the addition of a capacitor in parallel to the switch is already sufficient to damp the switching-off overvoltage. However, this simple option is dangerous and stresses the IGBT switch as during the switch-on phase the energy accumulated by the parallel capacitor is discharged back in the IGBT without any current limitation. This discharge is a potential source of breakdown for the device. For this reason, most snubber circuits possess a resistor that limits this current. Considering that the variation of current is up to 400 A in the Buck circuit and 1500 A in the Buck boost circuit when the IGBT switches-off, the maximum overvoltage peak acceptable being set at 100 V and with the parasitic inductance mean value of 1 µH, snubber capacitors of respective capacitance values 16 µF and 190 µF can be chosen using Eq. (14).

From these values of capacitances, a RCD-snubber circuit is added in parallel to the switches. Its operation is represented in Fig. II.16. During the switch-off phase, the current going through the parasitic inductive circuit do not abruptly vanishes but is able to charge the snubber parallel capacitor passing through the diode module as shown in Fig. II.17(a). The diode is advantageous here: it enables to by-pass the resistor so that the peak of voltage is rapidly absorbed by the capacitor and no energy is lost in the resistor. During the switch-on phase, the snubber capacitor gives back its energy, discharging its current through the IGBT as shown in Fig. II.17 (b) – the resistor value being chosen so that the current intensity remains in acceptable levels.

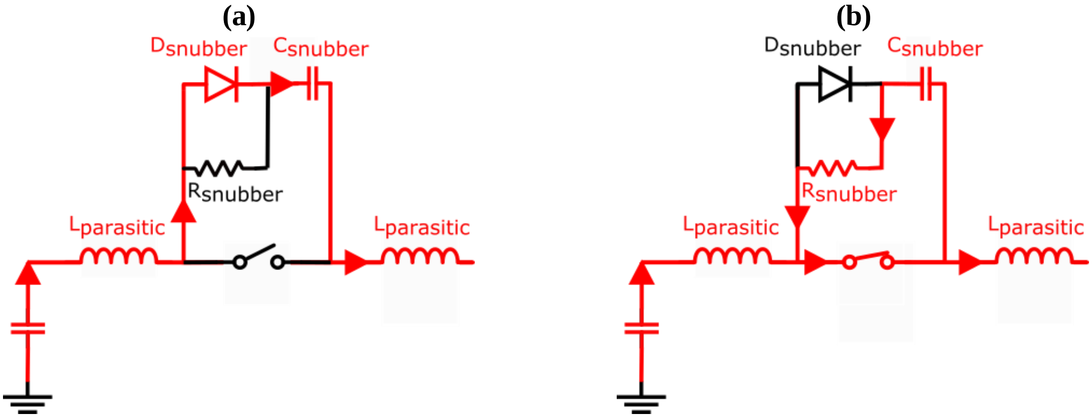

FIG II.16 Representation of an RCD-circuit operative damping of overvoltage peaks during (a) switch-off phase and (b) switch-on phase.

To ensure an efficient damping, the cycle composed by the charging and the discharging phases of the snubber capacitor must be faster than the cycle of switch-on and switch-off phases of the IGBT. Indeed, if the capacitor does not evacuate all its energy during the switch-on phase, it would be partly charged during the next switch-off phase and might not be able to damp the magnetic energy – and so the overvoltage peak - of the next cycle. This problem is illustrated in Fig. II.17 with the Buck-boost configuration. In Fig. II.17 (a), a snubber RCD of values C = 100 µF and R = 1 Ω is implemented whereas in Fig. II.17 (b), a snubber RCD of values C = 100 µF and R = 10 Ω is implemented. During the switch-off phase, the current that is stocked in the snubber capacitor is measured positively and the overvoltage in the terminals of the IGBT is reduced. During the switch-on phase, the capacitor discharges its energy with a RC time constant of 100 µs in Fig. II.17(a), reaching a peak current value of 300 A and a RC constant of 1 ms for a peak current of 30 A in Fig. II.17(b), those current peak levels are linked with the operating voltage V (300 V in this example) and the snubber resistance R by $I_{peak} = V/R$. It can be observed that in the Fig. II.17(a), the current going out of the snubber capacitor drops to zero before the next switch-off phase and no overvoltage peak occurs in this next phase whereas in Fig. II.17(b), the current does not drop to zero at the switch-off phase and an overvoltage transient peak is observed. However, the peak of current that occurs during the discharge of the snubber capacitors is traversing the IGBT in addition to the operating current and stresses the device. Thus, an overvoltage peak level has to be accepted to limit this peak current as a compromise.

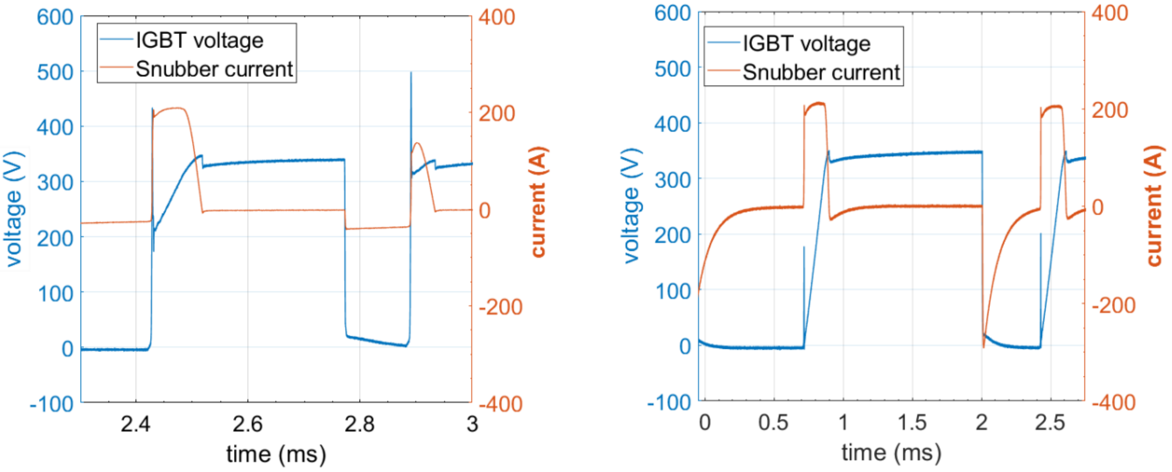
(a) **(b)**

FIG II.17 Comparison of two snubber designs with $C = 100$ µF and $R = 10\ \Omega$ (a) or $R = 1\ \Omega$ (b).

Another solution is to reduce artificially the frequency of the regulation adding a delay in the microcontroller code so that the switch-on phase lasts longer than the RC snubber discharge. This idea is illustrated Fig. II.18. For the Buck-boost configuration, a frequency limitation is established to switch the IGBT – 50 kHz in Fig. II.18(a) and 250 Hz in Fig. II.18(b). In Fig. II.18(b), a RCD snubber is implemented, with R and C values of $10\ \Omega$ and 100 µF respectively. In both configurations, the set point load current is 200 A and the limitation current in the intermediary coil is set to 800 A. In Fig. II.18(a), it can be observed that the set point current is respected, with a maximum variation of 10 A (5%), but the overvoltage peaks reach over 1 kV in Fig. II.18(c) whereas in Fig. II.18(b), the maximum variation is 100 A (50%) of the setup current but the overvoltage peak does not exceed 100 V in Fig. II.18(d). Thus, a compromise must be found between the acceptable overvoltage peak level and the regulation of the current waveform.

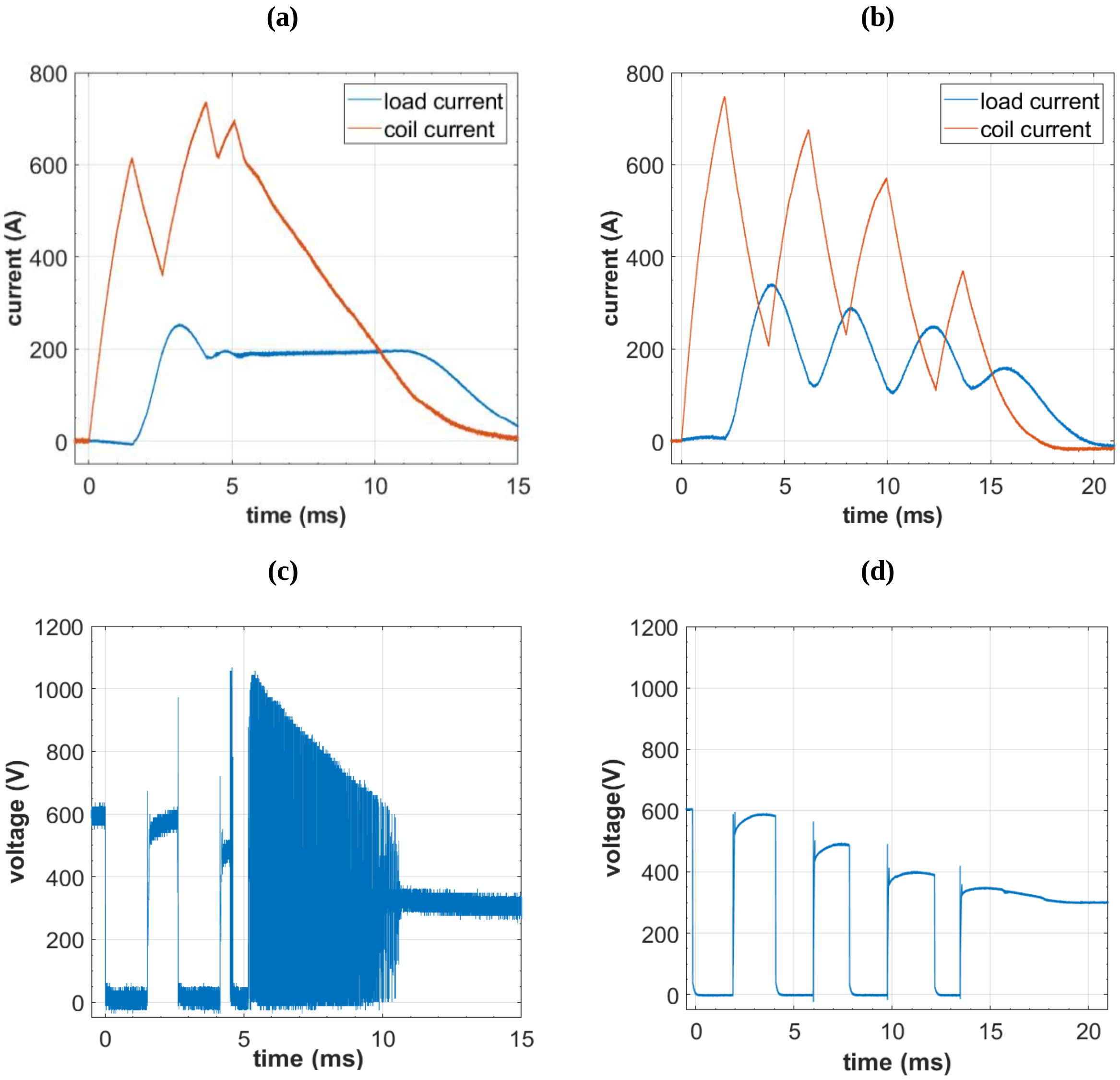

FIG. II.18 Comparison of current waveforms and overvoltage peaks for switching frequencies of 50 kHz (a), (c) and 250 Hz (b), (d).

In addition, to minimize this overvoltage peak in the high-power level experiments, an effort is made to reduce the peripheral parasitic inductance changing the geometry of the circuit. Indeed, whereas the previous circuits were mainly made of bus bars to connect the components, a second circuit version for high-power tests is built with large and thin plates of aluminum or copper.

II.5 High-power experiments and results

A. *Experiments with resistor as an arc and comparison of Buck and Buck-boost performances*

Before comparing the performances of Buck and Buck-boost topologies in the case of a real lightning arc, a first comparison is made replacing the arc by a 4 Ω resistance. This resistance is supposed to represent, for a current of 400 A, an arc of 1 m according to Sunabe and Inaba (1990) and of 0.5 m for Chemartin (2008). For both topology, the initial voltage of the capacitor bank is incremented until finding a setup that could create a C*-waveform (400 A for 50 ms) through the load resistance to respect the energy criterion. A close attention is taken for the tension in the terminals of the IGBT switch and the diode modules to avoid destruction of these components due to commutation overvoltage as discussed in Sec. II.4. The maximum allowed frequency of commutation is finally set to 5 kHz. Indeed, it turns out experimentally that it is enough to respect the 10 % margin of current set point and because this is one order of magnitude less than the maximum switching frequency of the IGBT, then this component is not stressed. A special effort was placed in the compactness of the resulting electric circuit with an arrangement of the components optimized to reduce the total stray inductance. This effort proved to be strongly efficient to reduce the overvoltage peaks caused by the transient switching phase of the IGBT discussed in the previous section. As it will be depicted in this section, this overvoltage was reduced to maximum 200 V above the operating voltage level. This resulting overvoltage level does not endanger the functioning of the IGBT. Thus, no Snubber circuit structure was necessary for the following experiments. In both configurations, once the current set point is reached, the microcontroller stops the regulation algorithm after 100 ms. In the case of the Buck-boost configuration, the efficiency of the regulation also depends on the level of current that is allowed in the intermediate coil. This current is limited to 1500 A as this is the limit level for the coil and for the IGBTs (two IGBT with a limit of 1200 A each are placed in parallel in this configuration). Moreover, whereas in the Buck configuration, the current at the load resistance is directly regulated, in the Buck-boost configuration, the intermediary coil is first charged until it reaches its limit current value (1500 A) then, the current in the coil is discharged in the load resistance until the load current reaches the set point value (400 A). However, the load resistance might consume all the energy gathered in the coil before it reaches the set point value. To avoid this, the IGBT is switched on every 2 ms to reconnect the coil to the capacitor bank and so to reload its current until it reaches again its limit value as long as the load current does not reach the set point value. The load current during the switch-on phase is maintained thanks to a 5 mF filter capacitor placed at the terminals of the load. When the load current reaches 400 A, the proper regulation phase starts: the current in the load is regulated except in case the coil current exceeds its imposed limit current. In this last case, the IGBTs switch off and so the coil evacuates its current in the load for 200 µs before the load regulation restarts. Results of Buck-boost and Buck configurations for a 4 Ω resistance are represented in Figs. II.19 and II.20. In the Buck-boost configuration, the initial voltage is 1600 V and curves of the load and intermediary coil current waveforms are represented in Fig. II.19(a), whereas the voltage at the terminals of IGBT and diode are shown in Fig. II.19(b) for one commutation. In the Buck configuration, the initial voltage is 2000 V, and the load current waveform is represented in Fig. II.20(a), whereas the voltage at the terminals of IGBT and diode are shown in Fig. II.20(b) for one commutation.

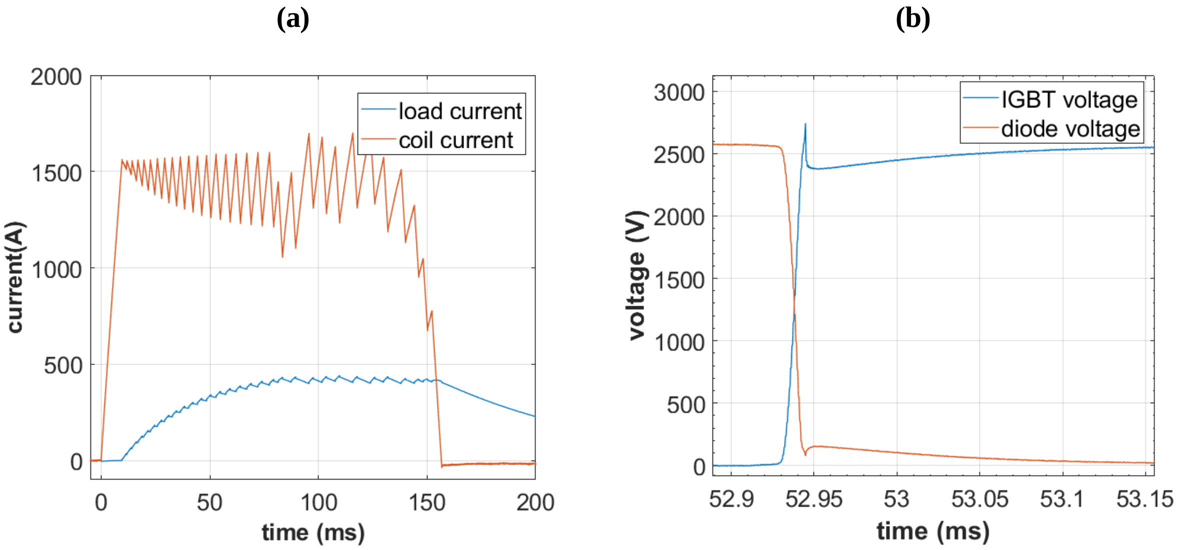

FIG II.19 Currents (a) and voltages (b) waveforms of Buck-boost configuration for a 4 Ω load resistance.

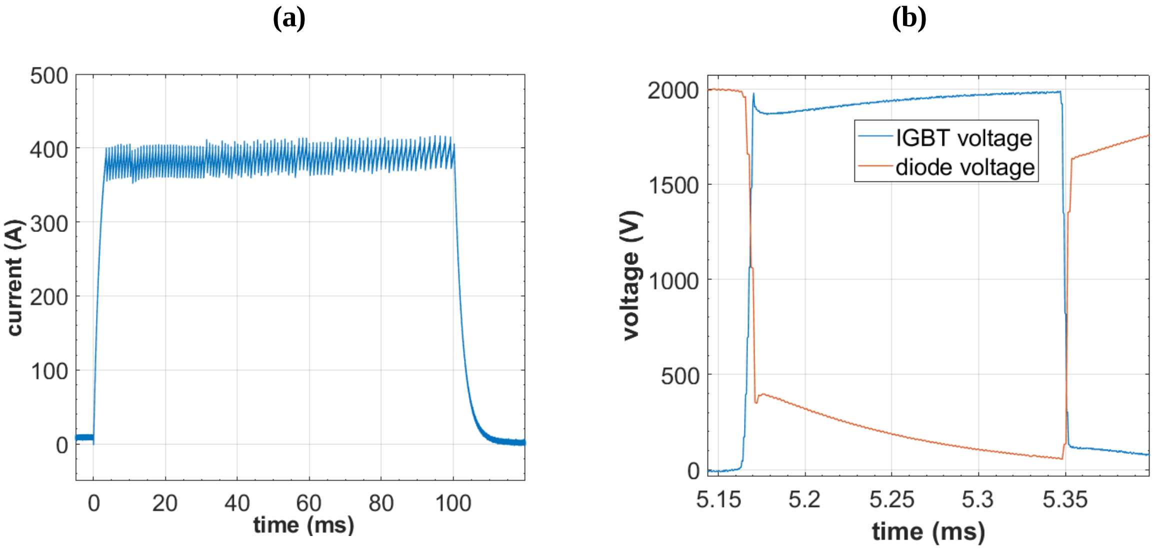

FIG II.20 Current (a) and voltages (b) waveforms of Buck configuration for a 4 Ω load resistance.

In Fig. II.19(a), initially, the IGBT switches on and the capacitor bank charges the coil for 10 ms until this reaches its limit current value of 1500 A. Then, a first regulation phase of the current in the coil starts: the current is sent from the coil to the load resistance during 200 µs and then the coil is reconnected to the capacitor bank until it reaches its maximum value. This regulation lasts until the load current reaches 400 A at 74 ms. Then, the proper regulation of the load current starts and is maintained from 74 ms to 157 ms. In this configuration, the regulation of the load current and the limitation of the coil current are both respected. In Fig. II.19(b), voltage waveforms of the same setup are represented at the terminals of the IGBT and diode modules for one commutation. The voltage level at the terminals of both modules – maximum 2800 V – is higher than the initial voltage of the bank capacitor because of the inversion of polarity of the load resistance whose high voltage point is referred to the circuit mass. As discussed in Sec. II.4 the transient overvoltage peaks is measured from Fig. II.19(b) and reaches a level of 2800 V whereas the operative voltage of the IGBT reaches 2700 V in the non-transient phase. A 100 V difference voltage is considered acceptable in terms of destruction risks for the switching devices.

In Fig. II.20(a), load current waveform of the Buck topology is represented for an initial voltage of 2000 V. The regulation of the load current at a set point level is direct and lasts 100 ms until the microcontroller algorithm stops it. In Fig. II.20(b), voltage waveforms of the same setup are represented at the terminals of the IGBT and the diode modules for one commutation. Conversely to the Buck-boost configuration, the low voltage point of the dipole resistor is directly connected to the reference mass in this case, and the highest operative voltage point of the circuit is the positive terminal of the capacitors. It can also be observed from Fig. II.20(b) that the transient overvoltage peak reaches a level of 2000 V whereas the operative voltage of the IGBT also reaches 2000 V at the end the cycle in the non-transient phase. In this configuration, the effect of the overvoltage peak is shown to be negligible.

Both Buck-boost and Buck topologies enable to perform a regulated C*-waveform of 400 A through a load resistance of 4 Ω. As predicted in the theoretical simulations of Sec. II.3, an initial voltage level of 2000V is enough to achieve this performance for the Buck configuration whereas the initial voltage level required is highest than expected for the Buck-boost configuration. This is probably due to the current coil limitation that deteriorates the energy conversion from the capacitor voltage to the coil current – the advantage of getting a higher energy density from an inductance source than from a capacitive source is minimized if the level of current is limited. Still, for the same performances, the Buck-boost configuration requires 20% less voltage for the initial load of the bank capacitors, which represents 36% less energy. In the other hand, the Buck-boost circuit introduces a higher level of operative voltage at the terminals of the switching elements, which remains acceptable for a 4 Ω resistor load.

B. Experiments with electric arcs and comparison of Buck and Buck-boost performances

Figures II.21(a) and II.21(b) present the performance results of, respectively, Buck-boost and Buck configurations current waveforms with electric arcs instead of a load resistance. The ignition of the electric arc is made using a conductive thin wire that is likely to explode when the current rises in it by Joule effect. This rapidly heats the surrounding air and contributes to generate lightning-like plasma (Kadivar et al. (2020)). The wire is placed between a positive electrode, being a tungsten rod of 10 mm diameter, and a negative electrode consisting of a square aluminum plate of 400 × 400 × 2 mm^3. A high speed camera (HSC) is used to evaluate the arc's shape and behavior. The HSC is a Phantom V711 from Vision Research (CMOS sensor of 1280 × 800 pixels of 20 µm^2) and is set to work with a sampling rate around 20 kfps.

In Fig. II.21(a), arc current waveforms of the Buck-boost topology are represented for an initial voltage of 1100 V, an electric arc of 150 mm as an inter-electrode distance, a set point value of 400 A for the arc current and a limit of 800 A for the intermediate coil current. Initially, the IGBT switches on and the capacitor bank charges the coil for 7 ms until it reaches its limit current value. Then, the first regulation phase starts: the current is sent from the coil to the arc resistance. It can be observed that the current in the wire does not increase fast in this phase during the first 31 ms, and then a sudden surge occurs that matches the wire explosion – as it is confirmed by the HSC. This surge reaches the set point current value at 32 ms and provokes the saturation of the current probe that is operative for current levels under 1.2 kA. Then, the regulation of the arc current starts and is maintained until 132 ms. Nevertheless, despite the set point value, the arc current is not only unstable – it varies from 250 to 1000 A after the first peak of current – but also has a mean value of around 600 A. This can be explained by the fact that the electric arc does not consume enough energy to evacuate the coil current correctly. Indeed, the coil current regulation has the priority over the arc current regulation to avoid a surge of current in the coil that could damage the switching devices.

In Fig. II.21(b), the arc current waveform of the Buck topology is represented for an initial voltage of 2 kV, an electric arc of 1 m as inter-electrode distance and a set point value of 400 A of the arc. Figure II.22(a) presents the arc voltage waveform for this case and Fig. II.22(b) presents the time varying resistor of the arc that is obtained by dividing the voltage at the terminals of the arc by the arc current. It can be observed that the current reaches the set point value in less than 2 ms whereas the voltage of the arc rises to 2.8 kV. During this time, it has been confirmed by HSC that the ignition wire has not exploded yet. The surge of voltage might be explained by the increase of resistivity of the copper wire at high temperature and when this wire starts phase change due to Joule heating. Indeed, the maximum resistivity of solid copper is reached at temperature 1085 °C just before the fusion point. For a copper wire of 1 m and of 280 µm diameter, it results in a resistance of 1.7 Ω considering the resistivity as a function of temperature. This value, that is inferior to the 8.5 Ω measured in Fig. II.22(b), indicates that this surge of voltage can be a result of a phase change effect. At 3.5 ms, the current suddenly drops to 320 A and the voltage to 1.7 kV. The HSC confirms that the wire has already exploded and plasma is forming. Then the current takes 5 ms to reach again the set point. From this point, the current is regularized until 100 ms when the microcontroller stops the algorithm, while the voltage variates from 1.7 kV to 1 kV and the arc resistance varies between 2 and 3 Ω. At the end, the current regulation around the value of 400 A lasts more than 90 ms. After the end of the regulation, the arc vanishes and the resistor value measured between the two electrodes increases. No overvoltage peaks are observed at the terminals of the switching devices during the transient switching off phases of the regulation.

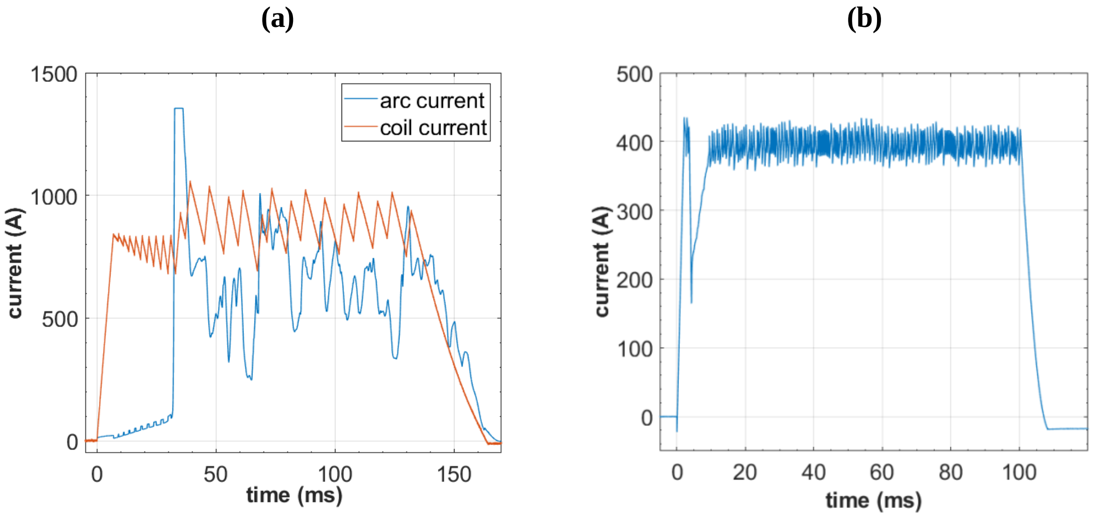

FIG. II.21 Current waveforms of Buck-boost configuration for a 150 mm arc (a) and of Buck configuration for a 1000 mm arc (b).

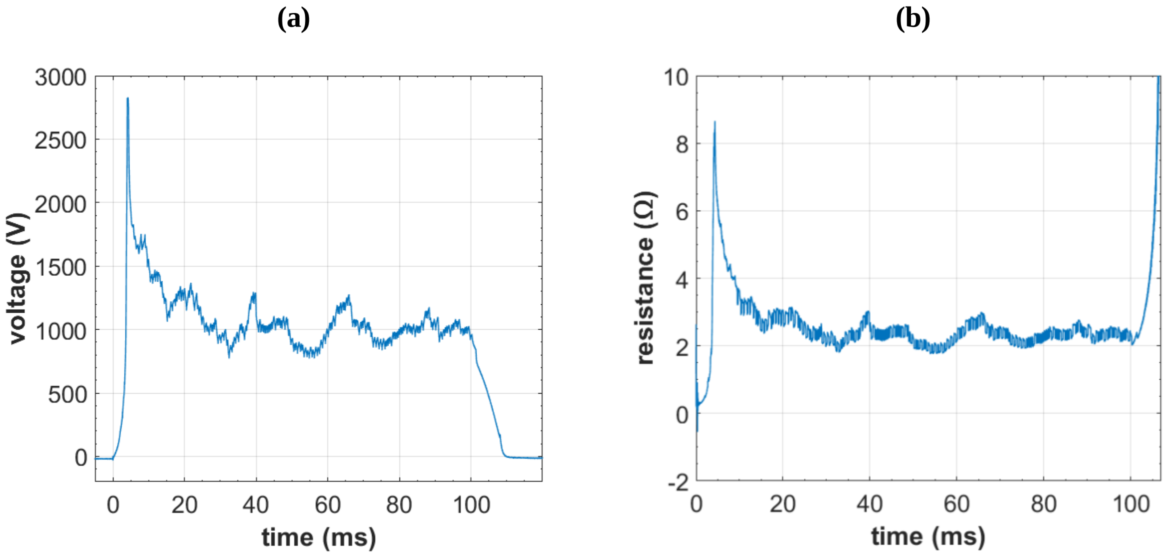

FIG. II.22 Voltage waveform (a) and time varying resistance (b) of Buck configuration for a 1000 mm arc.

C. Discussion and Analysis of different topologies performances

These results showed that for a load resistor of 4 Ω, both Buck and Buck-boost configurations can perform the C*-waveform of the lightning standard – with an advantage for the Buck-boost configuration that requires less energy. For the case with electric arcs, only the Buck generator is robust enough to perform this C*-waveform. Indeed, the fact that it has a direct feedback loop on its current level makes it more flexible to the fast variations of the plasma resistance – especially during its ignition phase when the conductive medium changes from a wire of copper at room temperature conditions to high-density plasma. The Buck-boost is less flexible due to his intermediate conversion of energy using a coil. The main problem being that the low-resistance and highly-inductive coil must be limited in terms of energy storage to avoid an operative current higher than a few kA. A simple solution would be to use an external resistive circuit to damp the energy of the coil in case the current in the arc is too high. But adding this extra circuit would have two drawbacks: this would consume energy by damping the coil current and thus deteriorate the efficiency of the circuit. Also, this would require at least two other IGBT switches in addition to the two ones that are already implemented in the Buck-boost configuration to regulate the flow of current going out of the intermediary coil. As previously mentioned, the IGBT module is the weakest component, using as less units as possible is a preferable strategy. In the end, only the Buck was able to perform a C*-waveform for arcs up to 1.5 m. Table II.5 summarizes the final parameters and components of the Buck generator used for these arcs.

TABLE II.5 Summary of parameters and components for the selected configuration.

Topology	**Initial voltage (V)**	**Capacitance (mF)**	**Stored Energy (kJ)**	**Coil Inductance (mH)**	**IGBT peak transient voltage (V)**	**Current set point (A)**	**Maximum Current ripple (A)**	**Current duration (ms)**
Buck	2300	112.5	298	10	2400	400	±50	100

Based on the work of Sunabe and Inaba (1990) and Chemartin (2008), the linear arc resistance value was firstly supposed to be between 2.4 and 4 Ω/m without considering the tortuosity factor, and between 4 and 8 Ω/m considering it. Therefore, for the Buck configuration, different arc lengths were experimentally reproduced by increasing the inter electrode distance, with a 100 mm increment, and increasing the initial voltage level. The highest length performed with the experimental setup described was 1.5 m with an initial voltage of 2.3 kV, and reminding that 2.5 kV being the absolute maximum operating voltage of the available capacitor bank. An image of this arc taken by HSC is presented in Fig. II.23 As it can be observed, the arc column is not straight, presents tortuosity and does not seem likely to be planar as discussed by Tholin et al. (2013). Considering inter electrode distances from 100 mm to 1.5 m and without referring to the real length of the tortuous electric arc, the mean linear arc resistance can be measured by dividing the mean arc voltage by the regulated current level. The mean value obtained is around 2.5 Ω/m and is in accordance with the experiments results of Sunabe and Inaba (1990).

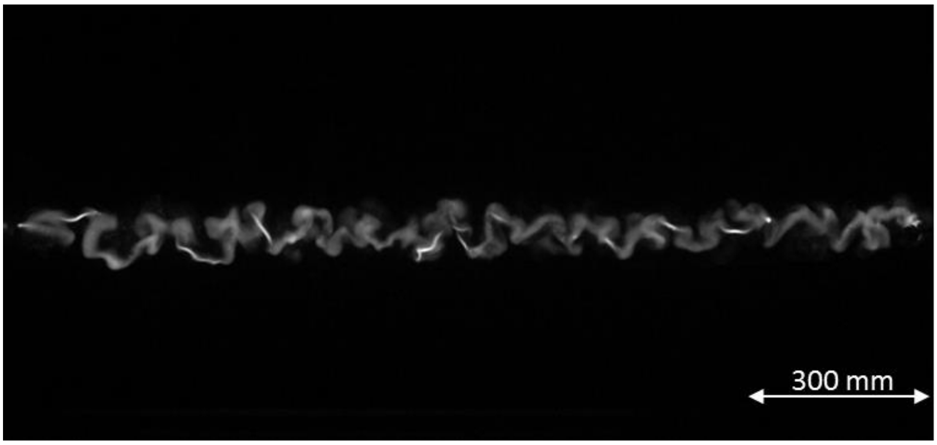

FIG. II.23 Image of a C*-waveform electric arc of 1.5 meters.

Moreover, to check the robustness of the lightning generator when a restrike phenomenon occurs, tests were conducted using an air blower placed at 50 mm of the arc column. The muzzle velocity of the air was about 60 m/s and its velocity dropped to 25 m/s at 300 mm. the positive electrode - a tungsten rod of 10 mm diameter and 0.5 meter long – is placed horizontally at 10 cm over the negative electrode - a square aluminum plate of 400 × 400 × 2 mm^3 recovered by a layer of 500 µm dielectric paint. The initial voltage in the capacitor is 2 kV and the current set point is 400 A. A picture of the setup is presented in Fig. II.24. The current and voltage waveforms are depicted in Fig. II.25.

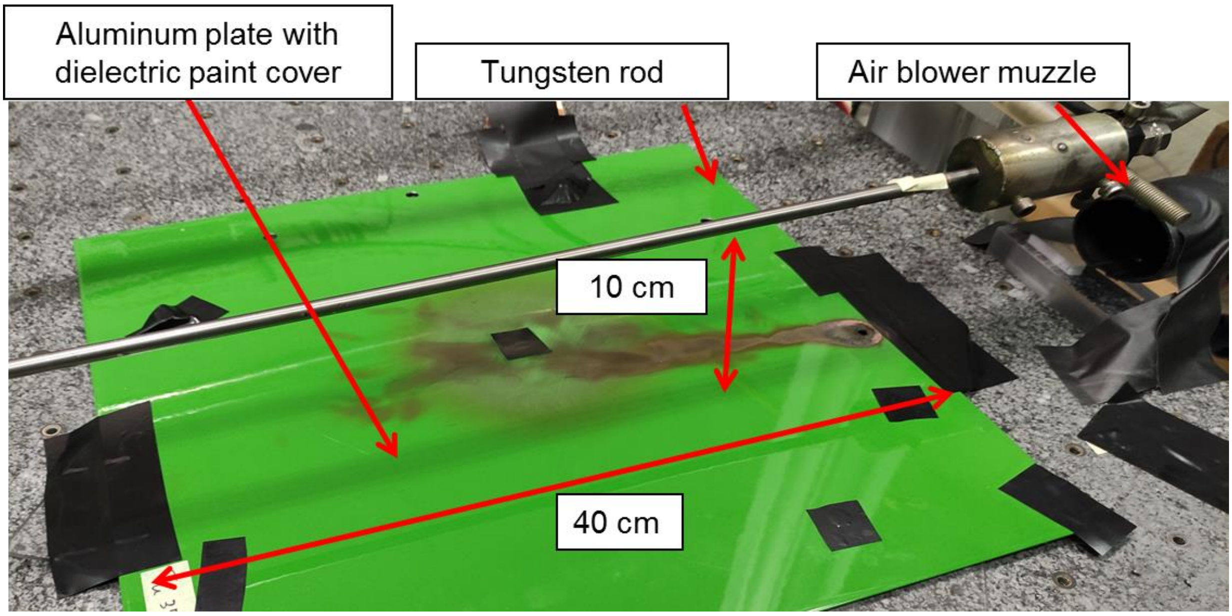

FIG. II.24 Picture of the blown arc experiment setup.

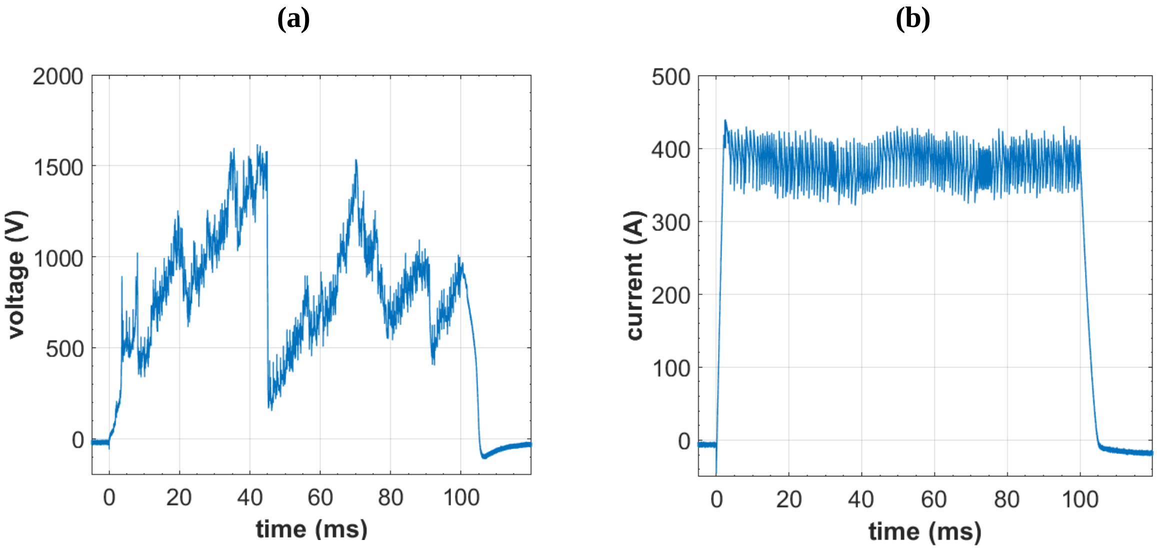
(a) (b)

FIG. II.25 Voltage (a) and current (b) waveforms of a blown arc of 400 A and initial inter-electrode distance of 10 cm.

It can be observed in the Fig. II.25 that despite the significant drops of arc voltage, especially the one occurring at 45 ms, the current waveform remains stable between its set point values. The arc voltage drop occurring at 45 ms is a result of a restrike, and decreases from 1.6 kV to 200 V in less than 300 µs. A sequence of images of this restrike is presented in Fig. II.26.

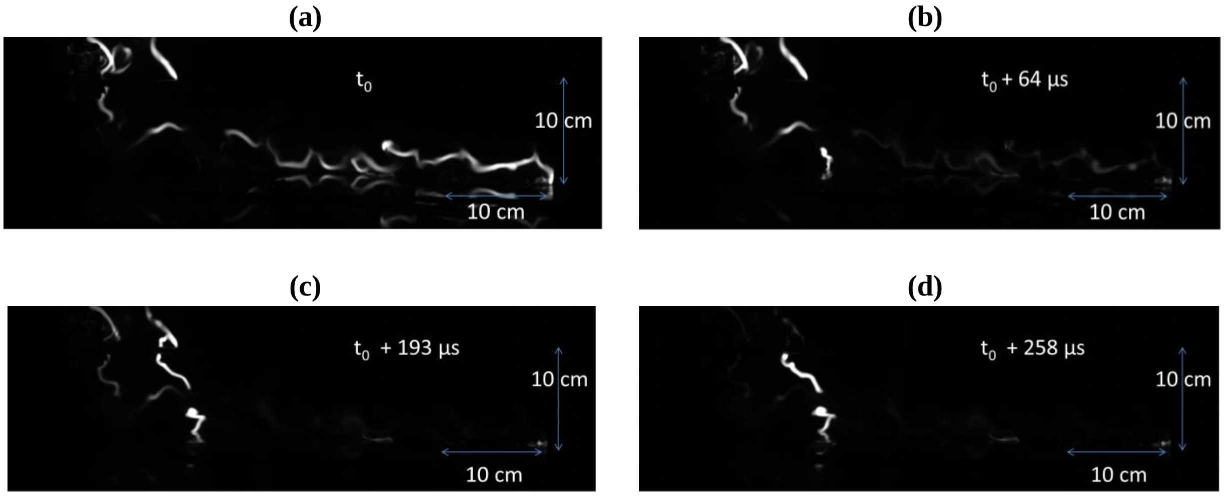
(a) (b) (c) (d)

FIG. II.26 Sequence of pictures issued from a restrike phenomenon from instant t_0 = 44.904 ms (a) t_0 (b) t_0 + 64 µs (c) t_0 + 193 µs (d) t_0 + 258 µs.

It can be observed from the Fig. II.26 that the observed phenomenon consists in two consecutive restrikes: one for the square aluminum plate electrode in the bottom electrode from images (a) to (b) from Fig. II.26 followed by on for the tungsten rod above electrode from images (c) to (d). For the first restrike, as the layer of dielectric paint recovers the square aluminum plate, no restrike can occur at its surface. Thus the observed restrike occurs because the electric arc crosses the total 400 mm length of the plate and is able to restrike at its other edge which is not protected by the layer. A distance of 400 mm is measured between the two successive arc roots but it is not possible to estimate the real distance of the arc channel that is vanishing during this restrike since just one camera was used. For the second restrike, the arc channel that is vanishing is even partially out of the pictures. Considering that the arc resistance is around 2.5 Ω/m, as measured in the previous part, and that there is a drop of 1.4 kV for a 400 A arc current, 1.4 m of arc column are estimated to have vanished during the two restrikes. Thus, the lightning generator developed in this work has proved to be able to provide a robust current regulation that enables to overcome the fast length variations of the arc column occurring during restrikes.

II.6 Conclusion

A theoretical and experimental study comparing the performances of Buck and Buck-boost topologies as high current generators for lightning arc up to 1 m long and respecting the C* waveform was carried out.

As previous electric simulations of arcs showed that such C*-waveform arcs can be modeled as linear resistors from 2.4 to 8 Ω/m, a comparison of DC/DC converters Buck and Buck-boost topologies and RLC circuit, using a capacitive load as energy source, was conducted considering the lowest level of energy criterion to furnish a C*-waveform through an 8 Ω resistor. Buck topology turned out to require an initial voltage level of 3.5 kV in the capacitor whereas the Buck-boost topology only needed 1.5 kV from a capacitor bank of 100 mF.

The experimental implementations of Buck and Buck-boost topologies have been conducted focusing on the optimization of the feedback loop for the current regulation. The need to find a compromise between the accuracy of the regulation and the respect of the operative electrical parameters of every device of loop has been addressed. Amongst other problems, the transient overvoltage peak occurring at the switching-off of IGBT switch devices – that is likely to break components – is solved by designing a Snubber filter and by reducing the commutation frequency, as well as the reduction of peripheral parasitic inductance coming from the geometry.

With these last optimizations, the Buck and Buck-boost configurations have been experimentally tested and compared with the given performance criteria for a 4 Ω load resistor and for electric arcs from 0.1 to 1.5 m. Whereas the Buck configuration performed a C*-waveform through both the load resistor and electric arcs starting from 100 mm and up to a value of 1.5 m, the Buck-boost configuration turned out to be inefficient to reproduce this waveform for electric arcs. In the other hand, Buck-boost had a best performance for a static resistor of 4 Ω, requiring 1.6 kV against 2 kV for the Buck configuration. This diversion of the Buck-boost experimental performances from the simulations is likely to be caused by the limitation current in the intermediate coil that was implemented to avoid damaging the switching devices. Eventually, the 1.5 m C*-waveform electric arc has been achieved with an initial voltage of 2.3 kV and an equivalent linear resistance of 2.5 Ω/m was experimentally found for 400 A arcs. It proved also to provide an accurate regulation even in case of a restrike phenomenon. For the rest of the present work, the lightning current generator presented in this chapter will be used to study and characterize the physical parameters present in the interaction of long lightning arcs with aeronautical materials especially to study the restrike phenomenon. Thus, the aim of next chapter is to develop an efficient launcher instrument capable to propel aeronautical test samples at the speed of an aircraft to study the interaction of the samples and the electric arc produced with the developed lightning arc generator.

Chapter III. Development of a low voltage Railgun in the context of lightning swept stroke to aircraft

To reproduce the swept-stroke phenomenon, after the creation of a lightning generator in the previous chapter, the second step is to design and implement launcher equipment that would be able to propel aeronautical test sample at a speed characteristic of an aircraft before striking it down with an electric arc. This launcher has to be robust and accurate enough to ensure the propulsion of test samples with a good repeatability and a good control in its ballistic performances for an important number of experiments. Moreover, as this equipment is aimed at being coupled with a high power electric generator in an indoor experiment, great caution must be taken for safety issues.

For those purposes, this chapter first presents and compare several technics of propulsion based on different physical processes in terms of ballistic performances and safety for an adaptation with our specific problem. Ultimately, the selected solution is an electromagnetic launcher – an augmented Railgun. As it requires the injection of a high current level to be efficient and low voltage operative point for safety issues, specific and original electric generator and rails structure are designed and experimentally implemented. A particular attention is brought on the experimental problems encountered and mainly on the sliding contact since almost no literature is available for Railgun equipment at this level of performances. Then, based on different experimental implementations, a dynamic and ballistic model of the projectile is developed to evaluate and characterize the friction forces aiming at predicting the launcher performances for different inputs. This will serve to control the speed of the material test sample during the swept-stroke.

III.1 Overview of the different techniques of propulsion

In order to lead a representative lightning strike to aircraft experiment, a mean to propel an aeronautical test material to a speed of an aircraft during take-off or landing – that is to say several 10 m/s and up to 100 m/s - has to be found. As this experience has to be conducted indoors to enable the use of fine optical diagnostics, there is a limit of available space. If a limit of 5 m is set, the technology of propulsion has to produce a mean acceleration of hundreds of g's to propel the test equipment to the given speeds. Aluminum plates with a thickness between 0.4 and 1 mm, length and width dimensions of few tens of cm are considered for equipment test resulting in samples weight varying between 100 and 500 g. Thus, the mean force applied on the test equipment has to reach 500 N all along the motion.

A. Mechanical release of energy

This section aims to present different methods of linear acceleration considering the fast release of potential energy from a mechanical system and how they could be implemented for our problem. Severe simplifications are made to access a raw order of magnitudes of the acceleration, speed and length parameters to highlight the feasibility or the non-feasibility of the method. Some calculations are detailed in the ANNEX.

A.1 Free falling

One of the simplest ways to get a fast acceleration would be considering the free falling since it would only require to bring the sample in high altitude in some way – maybe a crane should be considered – and to release it in free falling so that all the potential energy would be transformed in kinetic energy. Then a guidance system could be designed so that the free-falling sample is trapped between rail tracks. Then the rail could be hit by the lightning before hitting the ground.

Not considering how to deal with the shock issue, a raw calculation will give an order of magnitude for the feasibility of the experiment. First, let's consider there is not any friction from the air nor from the guidance system. Only the mass of the object make it fall so that only the potential energy of gravity is considered. The minimum altitude to place the sample before letting it fall is given by:

$$z = \frac{v^2}{2g} \tag{III.1}$$

With v being the final velocity and g the acceleration constant. For a final velocity of 100 m/s, a distance of 500 m is necessary. Finding such a crane would be very problematic.

A.2 Stretched elastic release

Such a method is implemented in Plumer (2012) by Lightning technic laboratories to observe lightning stroke phenomenon: the samples are propelled up to 20 m/s with the release of a stretched elastic band. In the field of elastic materials, elastomers offer a possibility of elongation of up to 10 times their normal length. An elastomer is a polymer with viscoelasticity (that is to say both viscosity and elasticity) and has very weak intermolecular forces, generally low Young's modulus and high failure strain compared with other materials. A sudden release of an elastomer is thus a source of potential energy that could be used to furnish kinetic energy when the elastic recovers its normal length.

However, considering the waves propagation in continuum materials with a spring model of interaction between the atoms, it is shown that the waves of compression have a maximum speed of for the longitudinal disturbances given by:

$$c = \sqrt{\frac{E}{\rho}} \tag{III.2}$$

Where E is the elasticity modulus or Young modulus of the material and ρ its density. As the Young modulus and the density of rubber are E = 1.5 MPa and ρ = 990 kg/m^3, the speed of sound in rubber is 39 m/s.

However, the spring model simplifies the interaction between atoms – considering they are subject to the linear Hooke's law. This is in agreement with measures conducted in Vermorel et al. (2007) but only for small initial stretching – thus the elastic rubber band can be considered in its elastic domain. But the speed of front wave can reach slightly higher values, about 50 m/s. This is likely due to the effect of the strain rate on the elongation modulus known in rubber (Kolsky (1949)).

To conclude, the stretched elastic release seems to be a rather simple and easily implementable idea to obtain high speeds but it is impossible to outcome the speed of sound in the material that is below our expected values.

A.3 Metal Spring release

Considering spring material, as the Young modulus can reach a few tens of GPa and the density is about 10 000 Kg/m^3, the maximum speed of waves in the material is in the order of magnitude of few 1000 m/s which is more than desired for our application. But for the metals, the maximum relative longitudinal elongation is at maximum 0.1 % to be able to consider a Hooke's law. Then it would be more relevant to look for the energy that can be stored in a metal spring.

In order to design a spring for an application, two points have to be respected: first, the spring has to resist to the maximal loads that are applied on it – an admissible constraint resistance is usually set up. Second, the spring's stiffness has to meet the need for compression force. The speed of propagation of the compression and elongation waves in the spring coming from the equation of d'Alembert is defined by:

$$c = \sqrt{\frac{kL}{\mu}} \tag{III.3}$$

Where k is the spring stiffness, L is the spring length and μ is its linear mass. A model of a spring is established in ANNEX B: for our specific application and considering a spring, the required release force is $F = kL = 1 - 5$ kN and the linear mass is obtained with geometrical and shear constraints considerations and results in the following equation:

$$\mu = \frac{\pi^2}{0.12} \rho_{steel} d^2 \tag{III.4}$$

With ρ_{steel} being the density of steel and being equal to 7500 kg/m^3 and d being the diameter of the spring wire. Considering the minimal acceptable spring wire diameter so that no breakdown occurs – 6 mm from the model and the calculations developed in ANNEX B – the linear mass of a steel wire is 22 kg/m and results in a wave speed of 15 m/s. This result is insufficient for our application.

A.4 Flywheel

A flywheel consists in a rotational storage of energy: energy is stored converting DC energy to a spin up of a massive rotor that has a big inertial momentum. The energy is released in converting deceleration of the rotor into DC energy using the motor as a generator.

The idea would be to store enough energy in the rotational motion of the flywheel so that it gets sufficient power to pull the test sample to a speed of 100 m/s using an inextensible wire over a distance of 5 meters. If a high level of power is required, the flywheel has to be designed to get a high inertia momentum and a high rotational velocity. For our application, a peripheral point of the flywheel has to be able to reach 100 m/s in order to drag the test sample at such a speed. However, the speed of peripheral points of the flywheel is limited by the mechanical resistance to traction constraints of the material. The expression of the limit velocity is given in [Ahmed 2007] for a rotor with a full cylindrical shape:

$$V_{pmax} = \frac{3+\nu}{8}\sqrt{\frac{R_e}{\rho}} \tag{III.5}$$

Where ν is the Poisson coefficient, R_e the mechanical constraint resistance to traction in the elastic domain and ρ the density of the material. The material that has the best performances in the field of flywheels is carbon fiber .Its poison coefficient is between 0.3 and 0.5, its Re is around 1500 MPa and its density is around 1500 kg/m^3(Ahmed et al. (2007)). Thus, its maximal peripheral velocity is about 500 m/s – not taking into account the margin that is advised to respect for the Re factor in order to prevent flywheel breakdown fatigue. This would fit our application. In addition, this speed can be increased using a shallow cylinder shape for the rotor.

In this case, considering that the inertia of the flywheel is high enough so that during the dragging of the hundreds grams sample test, the rotational speed of the rotor barely decreases, the assumption of a constant force overtime applied on the sample is made and so the acceleration is considered constant. To reach a speed value of 100 m/s within 5 meters, a constant force of 500 N has to be developed and so a power up to 100 kW must be available. With the price references given in Chapter II (Sec. II.1) for this technology, the costs are 40 000 euros only for the machine and without the infrastructure and the control systems.

B. Liquid, Gas and Chemical propulsion

If the mechanical release of energy methods are not enough to obtain the required performances, it seems to be relevant to look at propulsion techniques. Acceleration can be gained by expelling a body – liquid or gas – very fast according to the conservation of impulsion principle.

B.1 Liquid propulsion: hot water rocket

The propulsion of a rocket using pressurized water is a very widespread and impressive experiment for early science classes. The pressurized water has the potential to offer a good propulsion body due to its density and its order of magnitude of pressure achievable and basic experiment using only half a liter of water and a pumping system to reach 6 bar of pressure in a PET bottle enables to reach up to 100 meters of altitude. These performances can be upgraded using hot water: for example, using electrical resistance heating elements and adding external pressure in respect to the phase diagram line of water separating liquid and gaseous states. AQUARIUS group performs hot water rockets where the water is heated in a hermetically sealed pressure tank until it reaches a vapor pressure up to 130 bar with a corresponding temperature of 330°C (Pilz et al. (2004)). When the nozzle is released, the tank pressure drops abruptly below the boiling point, and water under partial vaporization is expelled producing propulsion. Figure III.1 presents the experiment developed by AQUARIUS group and Fig. III.2 explains the physical principal.

FIG. III.1 Single stage hot water rocket with its test facility (AQUARIUS group - http://www.aquarius-aerospace.de/).

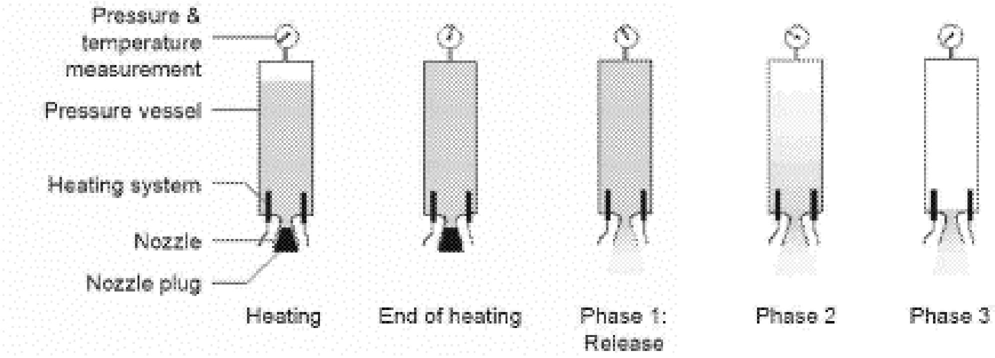

FIG. III.2 Principle of hot water propulsion (Pilz (2004)).

A simple model is developed in ANNEX C and show that the expected performances can be reached with a pressure of 10 bars and at least 10 L of water. Such an experiment would require big infrastructure to expel the water. As the experience has to take place indoors in order to use electric and optics diagnostics for the electric arc interaction, it represents significant safety issue to be implemented.

B.2 Gas and Chemical propulsion: light gas gun

Rocket propulsion experiments consist in releasing a high pressurized gas at a speed of a few km/s to provide a thrust to a projectile. This method is used in the work of Dobbing and Hanson (1978) in order to propel a test sample to a speed 72 m/s before it gets hit by an electric arc to experimentally reproduce the swept arc phenomenon. But to reproduce the experiment in an indoor laboratory, the release of the corresponding amount of gas is not an available option so that we cannot reproduce the propulsion of a test sample with an expelling of gas as it is made in the rocket sled experiment of Dobbing and Hanson, especially if it involves chemical reactions. But still, it is possible to propel the test sample using gas propulsion by increasing the pressure in a gas chamber – compressing a gas to high pressure or releasing it by a chemical reaction. At a specific pressure, a seal separating the gas chamber and the barrel containing the test sample is broken: the gas is released in the barrel, pushing the sample test that is accelerated until it reaches the muzzle. The equipment is referred as gas gun and the physical principle is depicted in Fig. III.3.

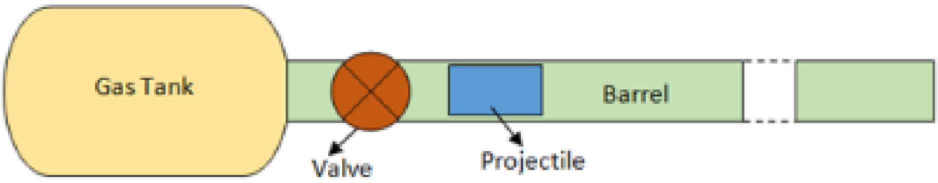

FIG. III.3 Schematic of a single stage gas gun (Koka (2016)).

Gas gun are mostly used as a launcher technology for impact testing in laboratories: as an example, the laboratory STAR of Sandia (NISA) has a two stages light gas gun that can propel a projectile of few dozens of grams up to 7.5 km/s resorting to a pressure of 650 GPa [Sandia.gov]. This technology is used for civil aircraft certification for resistance to bird impacts - which represents around 90% of all in-flights impact incidents (Mao et al. (2008)) or for spacecraft protection to impacts from micrometeoroids and orbital debris (Christiansen and Miller (2016)).Figure III.4 represents the single stage gas gun developed by THIOT ingenierie group.

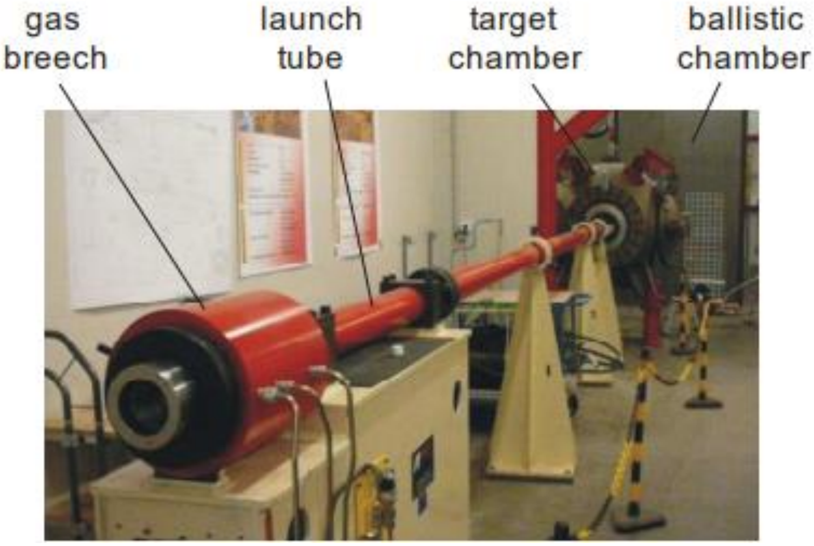

FIG. III.4 Single stage gas gun TITAN (THIOT Ingenierie group - www.thiot-ingenierie.com)

The two relevant parameters that drive the performance of the launcher are the level of pressured achieved in the gas chamber and the limitation due to the speed of sound in the gas. This speed is given in the following formula:

$$a = \sqrt{\frac{\gamma P}{\rho}} \tag{III.6}$$

Where a is the speed of sound in the gas, γ the heat capacities ratio in the gas, P and ρ are respectively the pressure and the density of the gas. The term light gas gun is used to refer to those gas guns because light gas such as helium or hydrogen are mostly used for the main reasons that their low molecular weight make them easier to compress to high pressures level and that their speed of sound is higher due to their low density.

There are two ways to obtain a high pressurized gas in the gas chamber that define two kinds of launchers: in a single-stage light gas gun, a light gas (hydrogen or helium) is compressed to high pressures by the mean of a compressor. In a chemical launcher, powder or liquid ergols are subject to a redox reaction in a combustion chamber. This very exothermic reaction produces a mixture of $C0_2$, N_2, H_20 and H_2 with a mean molecular mass of 28 at a temperature up to 3000K and a high-pressure level that can be controlled by the flux of ergols injection (Jamet and Wegner (1989)).

The advantage of light gas gun facility is to improve the achievable speed using a light gun with a low density but the advantage of the chemical gas gun is to produce hot gases that also increase the achievable speed. The two-stages light gas gun technology takes advantage of the two methods and is mostly used to reach very high speeds of propulsion: it is composed of a first stage where a detonation produced from gunpowder releases energy to compress and warm up a light gas in the second stage.

As hydrogen or helium reach a limit speed of sound of around 1000 m/s with the facility of a single stage light gas gun (Rahner et al. (2014)), this factor is not a limit in the application as the sample test only has to achieve a speed of 100 m/s. The performances of the light air gun only depend on the pressure in the gas chamber. A simple model is developed in ANNEX D and gives the following results: for a volume of 5 L for the gas tank, the minimum required pressure for the desired performance is 100 bar (140 bar for 1 L of gas tank volume). The price for for a double-stage light gas gun that does not require ergol injection system of a chemical gas gun is estimated to be about 150000 euros by THIOT for our desired performances.

C. Electromagnetic propulsion: electric motors

Means of propulsion using electromagnetic forces in a system of high transient currents or magnets or coils is a common way to reach high velocities and high accelerations. Figure III.5 from Cassat et al. (2003) shows the different performances of such system in the industry. Depending on the accuracy, the payload and the speed performances, those different technologies - both using electromagnetic phenomenon – are more or less relevant for our application: indeed, rollercoasters, conveyors, machine tools, robotics, precision manufacturing and small strokes machines are not aimed to reach at the same time accelerations levels more than few g and speed levels for than a dozen m/s but are rather useful in precision applications which is not a main concern for our problem. It can be inferred from Fig. III.5 that the only technology of linear motors that are able to provide acceleration of more than 100 g’s and velocity superior to several tens m/s for projectiles from 0.1 to 1 kg are the electromagnetic launchers.

(a)

Category	EM launcher		Catapults		Maglev		Rollercoaster		Conveyors		Machine tools		Robotics		High precision manufacturing		Small stroke	
																		
Applications	Electromagnetic guns		Aircraft launcher and aircaft recovery		Magnetically levitated and wheel trains		Rollercoaster, urban transport, ropeless elevators		Atmospheric and clean room conveyors, long stroke handling		Metal machining, laser cutting, wood processing, plastic injection machines,…		Assembly automation, Pick'n'place machines, Electronics manufacturing, inspection, CMM,…		Semiconductor manufacturing, fiber optics, biomedical, flat panel displays,…		Oscillators and vibrators, indexers, focusing device, wire bonders, shakers, automotive industry, consumer electronics,…	
	From	To	From	To	From	To	From	To	From	To	From	To	From	To	From	To	From	To
P [kW] (peak)	100000	4000000	40000	60000	1560	12000	13	180	0.1	5	1	100	0.5	5	0.05	5	0.001	400
Payload [kg]	0.05	5	5000	45000	50000	400000	400	10000	0.5	50	0.5	1500	0.05	25	0.05	5	0.01	1500
Stroke [m]	1	5	95	105	1000	300000	5	1000	5	100	0.3	6	0.3	2	0.01	0.5	0.001	0.075
Accuracy [mm] (1)	-	-	-	-	10	30	5	20	0.5	5	0.002	0.1	0.005	0.5	0.0001	0.01	0.0001	0.1
Speed [m/s]	1000	3000	28	105	30	200	2	50	1	15	0.0005	3	0.0003	5	0.0001	2	0.0001	3
Acceleration [g]	1000	250000	2	6	0.15	0.33	0.2	2	0.2	0.5	0.1	3	0.05	20	0.02	40	0.02	150
Motor type	2		1, 2		1, 2, 3, 4, 5		1, 2, 3, 4, 8		2, 8, 9, 10		7, 8, 10		3, 6, 7, 8, 9, 10		7, 8, 9, 10		12, 13	

Note: Data to cover 90% of the applications in each category.

(1) Single axis

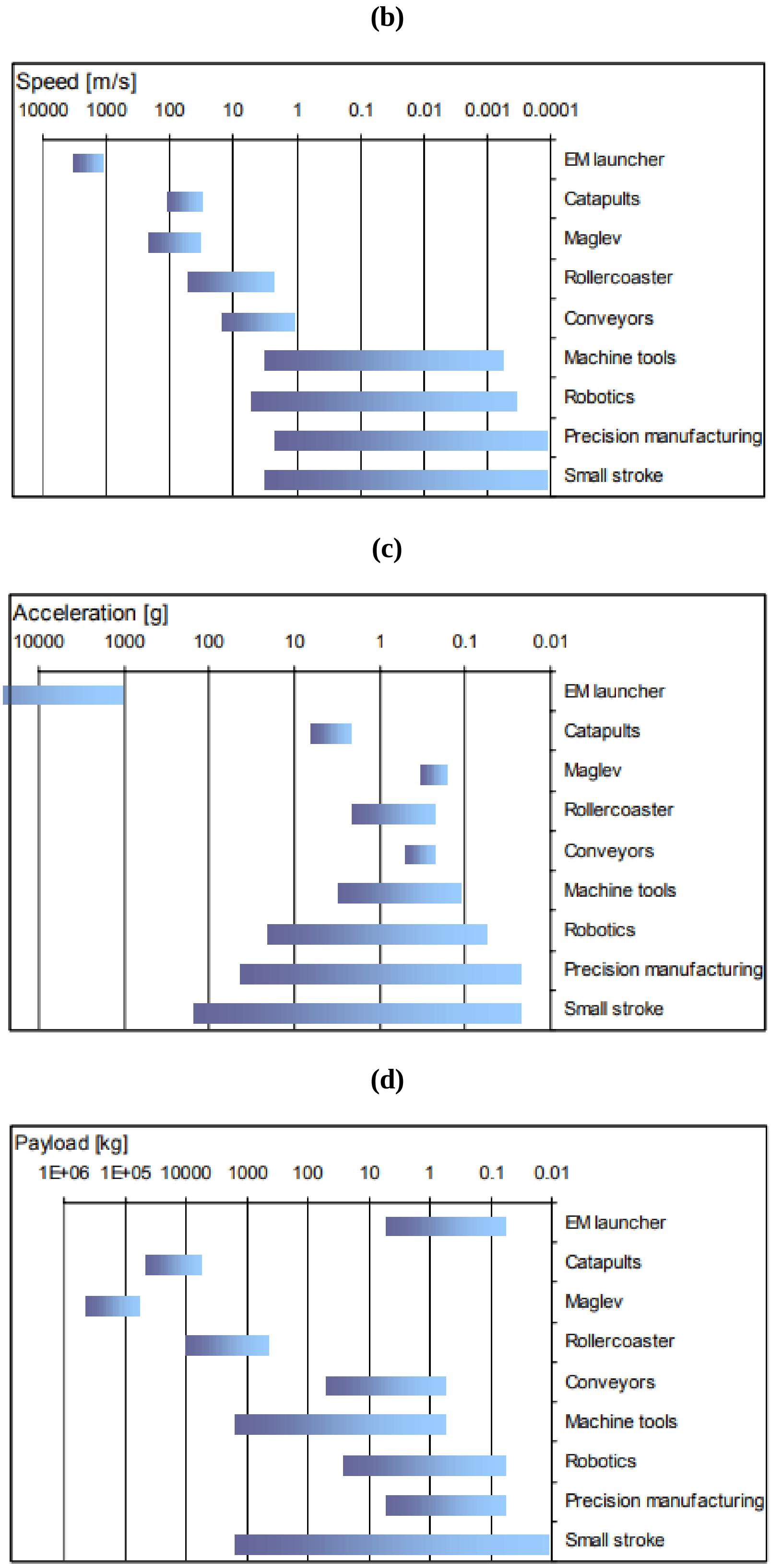

FIG. III.5 Performances of the different technologies of the linear motors (Cassat et al. (2003)).

This section focuses on the description and performances of technologies such as spinning electric motor, linear electric motor and EM launchers (Coilgun and Railgun) with a specific concern on their practical implementation to our situation.

C.1 Spinning electric motor

The spinning electric motor can be a DC motor, a synchronous or asynchronous motor driven by coil currents or permanent magnets. A spinning electric motor involves a rotating core constructed from coils of magnetic wire – the rotor – inside a magnetic casing – the stator. The torque is produced by current-carrying conductors subject to a Lorentz force coming from the magnetic field of the stator. In this configuration, the motor produces a torque that enables to drag the test sample that is set on rails by the mean of an inextensible wire, the wire being wrapped around a rotating axis during the movement. Figure III.6 represents the pulling of a test sample by the spinning motor.

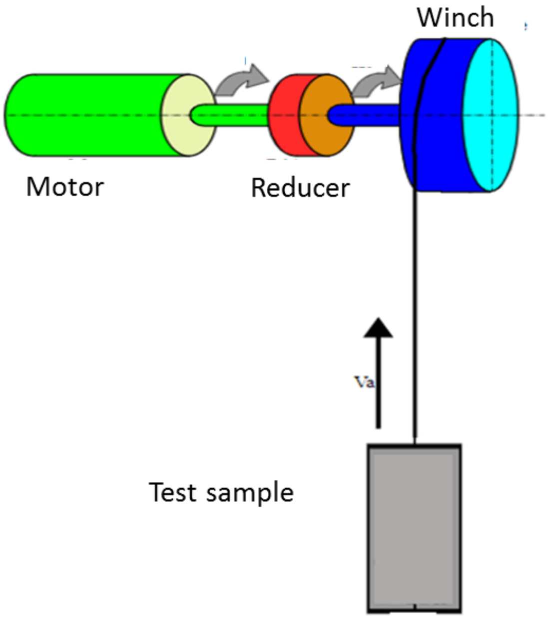

FIG. III.6 Acceleration by pulling from a spinning motor.

As the motor nominal speed of rotation and torque not necessarily corresponds to the torque need and the speed of rotation of the winch to drag the sample test to the required speeds, it is common to use a reducer that multiplies the rotational speed and lower the torque. Considering the reducer transmits all the power coming from the motor, it is not necessary to take it into account for the calculations of the required power (thus, the additional inertia coming from the reducer is also neglected). In the design of an electric motor, the reducer is usually chosen after the determination of the characteristics of the motor.

Simple models and calculations to evaluate the performances of such a technology are presented in ANNEX E. This results in a minimum required power of 150 kW whose price is around 15000 euros. This technology is thus affordable. However, the main difficulty of this application is to assure that the dragging of the test sample does not represent a safety issue: an inextensible wire of minimum 5 meters is being wrapped around an axis at a speed of several thousand rounds per minute. Supposing the wire is detached or cut during the motion, its movement will become unpredictable and dangerous.

C.2 Linear electric motor

The linear electric motor resorts to the same Lorentz force than for the rotational motors. Indeed, it consists in the rolling-out of the rotational motor as depicted in Fig. III.7. The rotor becomes a flat platform called the mover and the stator becomes a track of magnet or charged coils. Few differences exist between the two technologies such as the fact that the magnetic circuits are open and there are border extremities effects.

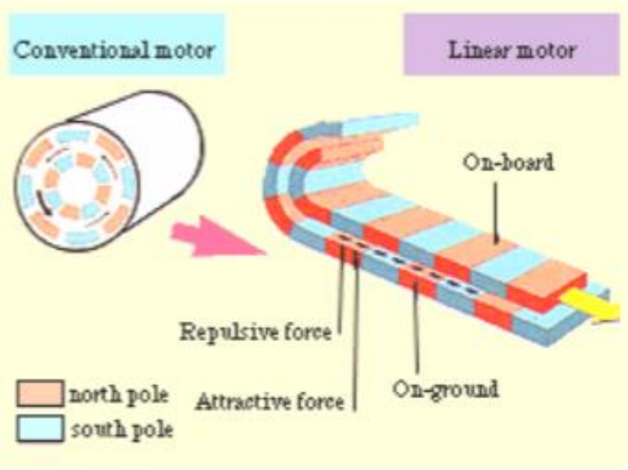

FIG. III.7 Equivalence between Conventional spinning motor and Linear motor (Ahmed et al. (2005)).

The main types of magnetic propulsion are the LIM (linear induction motor) and the LSM (linear synchronous motor) (Mustapha and Bababe (2016)).

The LIM consists in a primary winding of the stator and a secondary winding of the mover. When the primary winding is supplied by a three-phased current, the resulting magnetic field induces currents in the secondary winding and so a reactive magnetic field. The interaction of those two magnetic fields produces the controlled motion of mover. H2W technologies proposes an industrial solution of LIM technology that is able to reach 45 m/s (H2W)

The LSM has also a primary winding of the stator but the mover is fixed on two permanent magnets or reluctance structure. The main difficulty for this system is to synchronize the phase of the currents in the primary winding along the track to get a travelling magnetic field that drives the magnets of the mover on time. Thus, the position of the mover has to be controlled with an external system. However as the mover does not require winding, it is lighter.

With further discussions with ETEL group, this technology cannot reach velocities above 20 m/s for industrial applications: indeed, the velocity is primarily limited by the industrial tracks ball bearings that are used to guide the mover. However, Maglev train technology solve this guidance issue using levitation from superconductive coils of niobium-titanium alloy that are cooled to temperature near absolute zero – 273,25 °. The velocities reached with Maglev are over 600 km/h. Such an infrastructure might be too complex as well as too expensive to implement and the industrial ready-made solutions are not developed enough to meet the desired performances. But the same physic principle of induction phenomenon to reach high velocities might be experimentally implemented designing an electromagnetic launcher such as a Coil-gun - also referred to as Gauss-gun – or a Railgun.

C.3 Coilgun

A coilgun consists of a motionless coil and a mobile coaxial coil or a magnet that are electrically isolated. When a pulse of current is injected in the motionless coil, it forms a magnetic field that induces an electric current in the mobile coil. This current produces a magnetic field in the opposite direction. The mobile coil is then rejected by the magnetic force given by the expression:

$$F = I_A I_B \frac{\partial M}{\partial x} \tag{III.7}$$

Where I_A is the inductive current, I_B the induced current and $M$the mutual inductance. Then, the idea is to mount a tube with several coaxial motionless coils and to synchronize the arrival of the mobile coil with the current injection on each motionless coil to produce a constant force all along the movement (Fair (1999)). Figure III.8 presents a schematic of the coilgun principle.

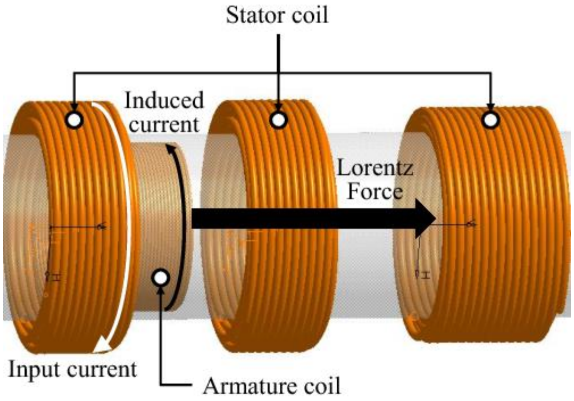

FIG. III.8 Representation of the Coilgun electromagnetic launcher physical principle (Go et al. (2017)).

The main advantage of this kind of electromagnetic launchers is the absence of frictions but radial forces applied on the mobile coil create ballistic control issues (Schmitt (1998)).

C.4 Railgun

Railguns have been studied and developed as very high-speed launchers for various applications from military developments, launch of commercial and military aircraft, to launch of micro-satellites into space and impact-fusion implemented by acceleration of fusible materiel (Fair (1997); Mc Nab (2003); Tamura et al. (1992); Parker (1989)). It consists in injecting a high current in a sliding armature inserted between two rails. This high current generates a large magnetic field that interacts with the current that forms it to provide a Lorentz force that applies on the sliding armature and thus provokes its propulsion as shown in Fig. III.9. Speeds reaching up to 10 km/s are reported (Parker (1989)). For projectiles of few grams whereas the ISL institute has reached a speed of 2.3 km/s for a load of 0.6 kg resorting to a current of 2 MA in the Railgun circuit (Lehmann et al. (2001)). Figure III.10 presents the Railgun PEGASUS developed in the ISL institute.

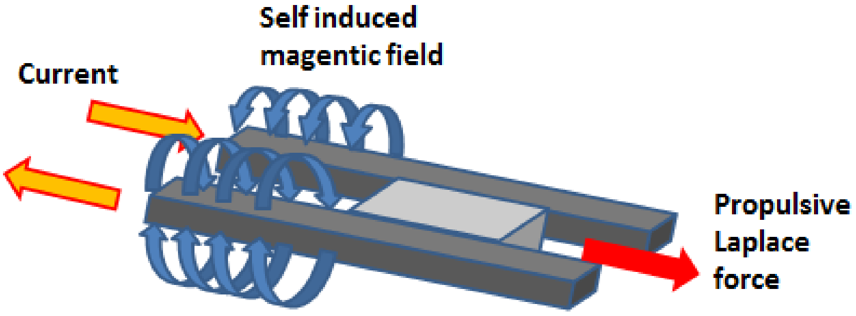

FIG. III.9 Schema of principle of Railgun.

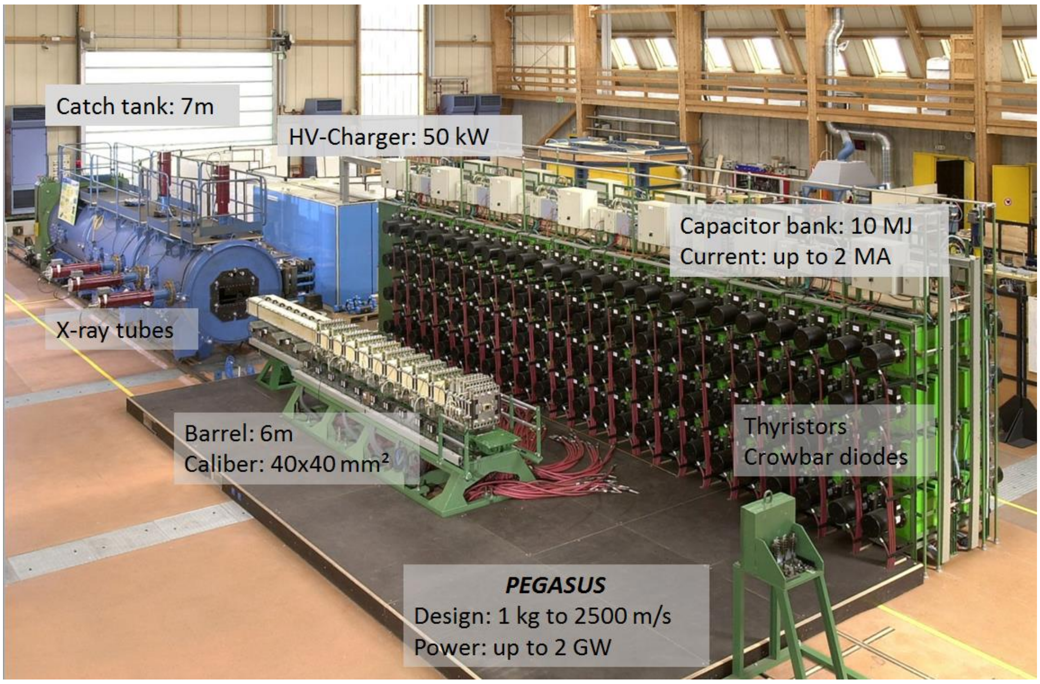

FIG. III.10 Railgun PEGASUS (Hundertmark et al. (2017)).

To calculate the current level that is required for our application, assuming the desired force is 500 N, the standard result in the literature is used (Rashleigh and Marshall (1978)):

$$F = \frac{1}{2} L' I^2 \tag{III.8}$$

Where F is the force provided to the sliding armature, L' is the inductance gradient of the Railgun and I is the current. L' depends only on the rail geometry and is assumed to be constant with time for a geometry consisting in two parallel rails. Its value in the literature varies between a few tenths to one µH/m. Thus, it makes the level of current in the range of 30 kA if the parameter L' is set to 1 µH/m. However, as the current must be provided for a few meters and the desired speed is of a few 10 m/s, a good electrical sliding contact must be ensured for several tenths of ms, which is unusual for conventional Railguns where the maximum sliding contact duration is about a few ms. Nevertheless, this solution appeared to be more simple to implement from zero than a coilgun because the entire power needs to be triggered just at once and there are no synchronization issues for a first version.

III.2 Design of the low voltage electric circuit, geometry and experimental set-up

A. *Paradigm of low voltage Railgun*

Most of the Railgun electric systems require a bank of capacitor capable of storing a few MJ and to deliver a power up to a few GW and a current up to 2 MA (Lehmann et al. (2001)). Thus, the standard capacitors used for this application have an operating voltage of few tens of kV to few hundreds of kV but with a capacitance equal or inferior to few mF (Dai et al. (2015)). Thus, the peak level of current cannot be maintained more than few hundreds of µs even with several distributions of currents all along the rail using several capacitor banks (Parker (1982)). In our application, the speed of 100 m/s for few hundreds of grams could be reached in hundreds of µs with a current over few hundreds of kA. However, this would require a very high-power bank of capacitors. Moreover, as the Railgun has to be coupled with an electric arc provided by an electric generator charged up to 2 kV, it is interesting to work with the minimum voltage level possible for safety and practical reasons.

The objective is to achieve a mean current injection that does not exceed 30 kA in order to design a current generator with the minimum of energy possible that could provide the required propulsion. Considering a mean force of 500 N is required all along the entire rail's length – a few meters - to get a constant acceleration of 1000 m/s^2, the time of current injection has to be around 100 ms. As in an RC discharge injection circuit, the electrical time constant τ has to be over 10 times the application time to guarantee a decrease in current level inferior to 10%, the electrical time RC is set to 1s. The typical value of R in Railguns is between 1 mΩ and 10 mΩ, the capacitance of the capacitor bank has to be above 1000 F.

As a new technology of capacitors – referred as ultra-capacitors – with high capacitances and low voltage has been available for a few years (Sharma and Bhatti (2010)), this range of values can be achieved in a compact volume. The models employed in this experiment are the Maxwell Technology 3000 F capacitors, part number BCAP3000P and the Eaton technology 3000 F capacitors, part number XL60-2R7308W-R and have been already used for a low voltage railgun application in the work of Starr and Youngquist (2013). Indeed, they used 24 of these capacitors to provide 4 kA to a 300g armature that reached an acceleration of 120 m/s^2 and a speed of 13 m/s after 1 m of rails. The main drawback of this technology is the low maximum operative voltage of the component – 2.7 V. To deliver the required 30 kA a bank of capacitor of 12 × 12 capacitors of the mentioned models has been used. The maximum operative voltage is thus 32 V. The maximum allowable peak current per capacitor is 1900 A for the Maxwell model and 2400 A for the Eaton model, therefore a maximum current of 24 000 A was operated to avoid degradation.

B. Electrical design

A maximum voltage of 30 V enables to provide a current of 24 kA only if the total resistance of the circuit is close to 1 mΩ. Therefore, the electrical components, the geometry and the materials of the rails have to be selected with accuracy. A schematic of the electrical circuit is given in Fig. III.11. The resistive elements of the circuits are the capacitor bank, the switch component – that is necessary to trigger the current injection, the connecting wires, the rail itself and the electrical contact between the armature and the rail as well as the contact losses in general.

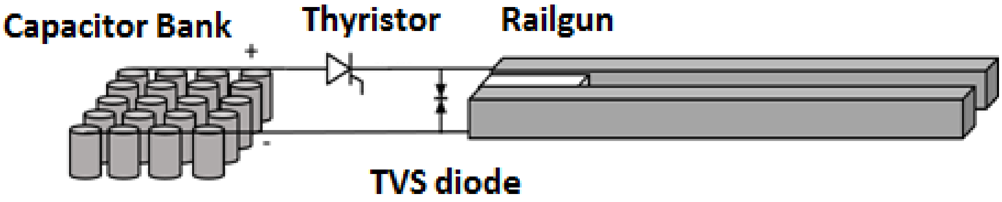

FIG. III.11 Electrical schema of the Railgun circuit.

The model of capacitor presents an equivalent series resistance of 0.23 mΩ and as a bank of 12 series layers of 12 parallels capacitors is used, the equivalent resistance is 0.23 mΩ. For the switch component, a model of thyristor DCR7610H28 is selected because it is able to endure a continuous courant of 30 kA with an equivalent resistance of 52 µΩ but provokes a voltage drop of 1 V. Three of these components are assembled in parallel to lower the equivalent resistance to 17 µΩ and decrease the stress on each component while keeping a similar voltage drop of 1 V. The conductive wires are bars of copper adding a 0.45 mΩ resistance mainly due to the supplementary losses of threaded contacts. The rails consist of two bars of copper with section 12×22 mm^2 and 2 meters length. Thus, the resistance of the rails varies from zero to 0.26 mΩ when the armature reaches the end of the track. As it will be discussed in Sec. III.3, the resistance loss due to the contact between the armature and the circuit can be neglected. Thus, the total resistance of the circuit is about 1 mΩ at the beginning of the movement and reaches 1.25 mΩ at its end. Considering a constant voltage in the capacitor bank, this resistance surge during the armature movement will induce a loss of 25 % on the injected current at the end of the rail affecting the acceleration accordingly.

C. Mechanical design

As the passage of the armature between the rails can provoke damage due to sparkling and bad electric contact, replaceable aluminum angles are screwed on the copper bars and ensure the electric contact with the armature. These angles are 2 mm thick and can be easily changed when they turn out to be too damaged after several shots of the Railgun. Two PTFE bands, 1 mm thick, are screwed below and above the rail to encapsulate the projectile and reduce the friction with the armature body. Aluminum bands of 2 mm thick are screwed above the PTFE bands to provide it more rigidity. All of those elements are screwed together in a bulk plane of TIVAR. The distance between the two rails is 50 mm. An image of the assembly of the rails is presented Fig. III.12 and a front view is presented in Fig. III.13.

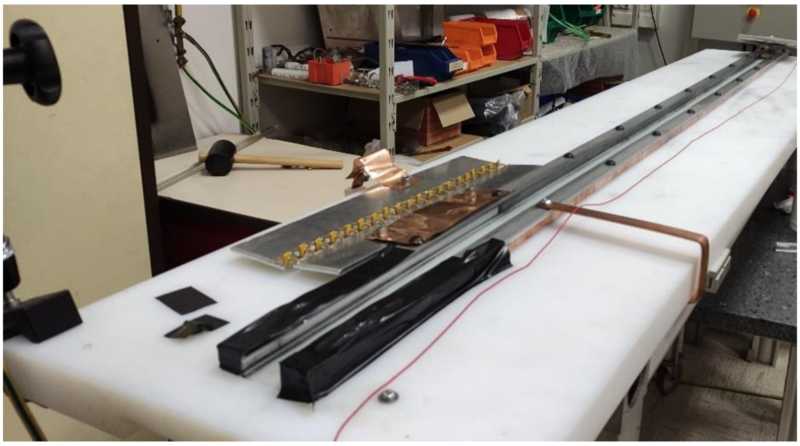

FIG. III.12 Assembly of the rails.

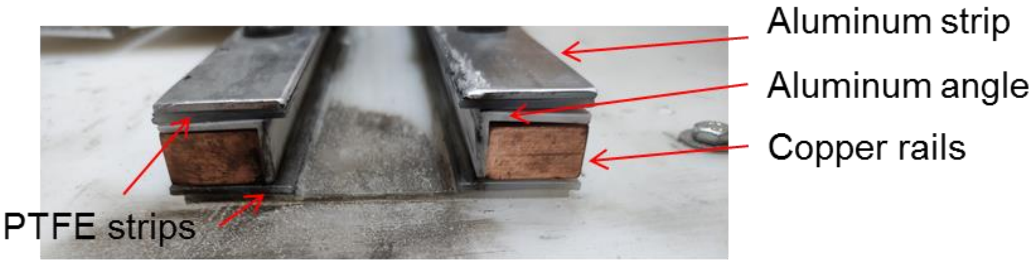

FIG. III.13 Front view of the rails highlighting the different parts of the mechanical setup.

From these geometrical parameters, estimation of the inductance gradient is given in the formula for parallel rectangular conductors (Giacoletto (1977)).

$$\boldsymbol{L' = \frac{\mu_0}{\pi}\left(ln\left(\frac{l+w}{w+h}\right) + \frac{3}{2} + \Delta_k - \Delta_e\right)} \tag{III.9}$$

Where L' is the inductance gradient, μ_0 is the vacuum permeability, l is the distance between the rails, w is the width of the rails and h is the height of the rails as illustrated in Fig. III. 14. Δ_k and Δ_e are defined in tables and depend on the l, w and h geometrical parameters (Giacoletto (1977)). For our geometry, these two last terms are negligible. Thus, the calculation with l, w and h being respectively equals to 50, 22 and 12 mm gives a L' of 0.9 µH/m which is close to the 1 µH/m desired. A picture of the final setup is presented in Fig. III.15.

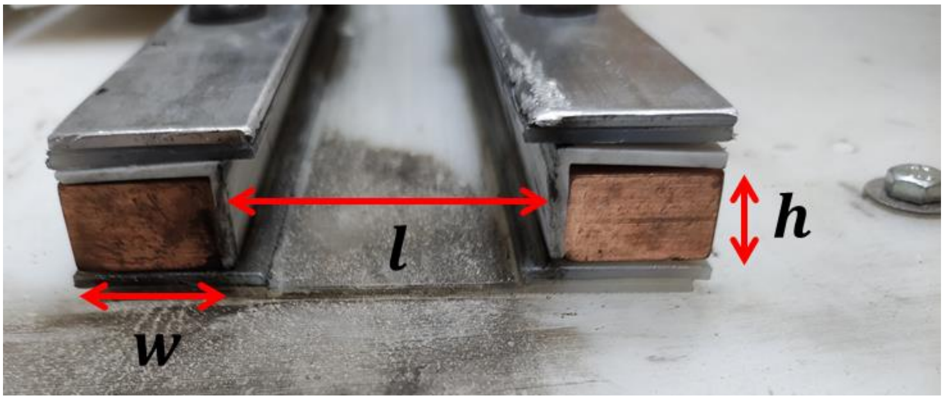

FIG. III.14. Illustration of the Railgun geometrical parameters.

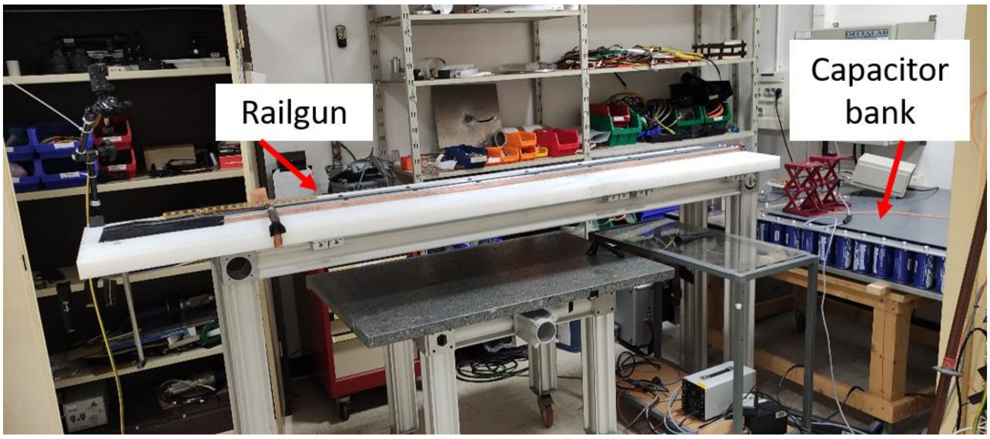

FIG. III.15. Picture of the complete electrical and mechanical set-up of the Railgun.

Magnets of NdFeB are added in the structure to give an extra magnetic field that interacts with the current injected in the Railgun and increase the Lorentz force. This addition of permanent magnets in a Railgun facility is often referred as Augmented Railgun (Katsuki et al. 1995). Eleven blocs of length 150 mm, width 30 mm and height 30 mm are inserted in the bloc of TIVAR all along the Railgun tracks and recovered by a PTFE band of 2 mm thick. They are thus separated by 3 mm from the armature with the additional 1 mm bands of PTFE under the copper bars that encapsulate the armature. Figure III.16 presents a truncated side-view of the rails showing the insertion of the permanent magnets in the bloc of TIVAR under the rails.

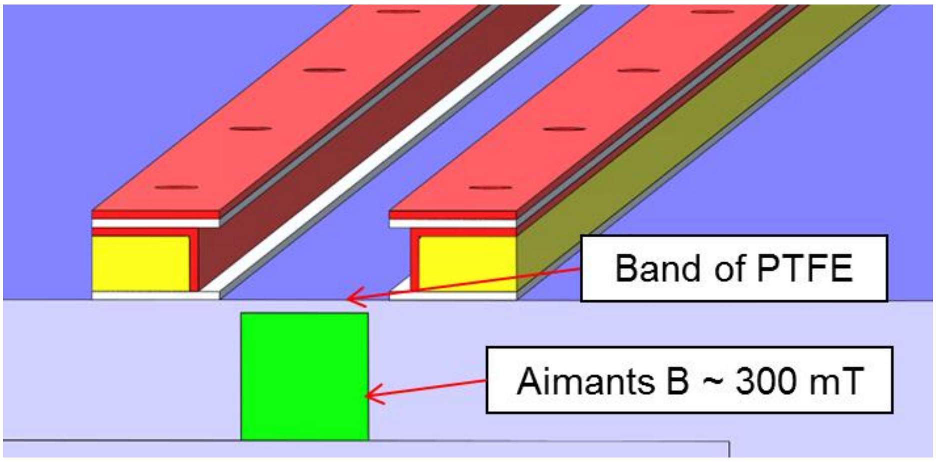

FIG. III.16 truncated front-view of the Augmented Railgun.

The flux density imposed by the magnets at this distance is measured using a gaussmeter and have a value of around 300 mT at 2 mm from the rails at the center of the magnet. Thus, the extra-force brought by the magnets is given by the formula:

$$F = BwI \tag{III.10}$$

Where F is the Laplace force, B is the density flux at the position of the armature, w is the magnets width and I is the current in the Rail. If the current is equal to 24 kA, the extra force has a value of 220 N.

D. Set-up measurements

The current measurements are realized using a PEM CWT AC CWT60LF probe. The voltage measurements are made using voltage probes of reference Lecroy PPE5KV. A high-speed camera (HSC) is used to evaluate the projectile position and speed. The HSC is a Phantom V711 from Vision Research (CMOS sensor of 1280 × 800 pixels of 20 μm^2) presented in Chapter II (Sec II.5).

III.3 Main experimental issues

A. Contact Transition

The main practical difficulty of the implementation of a Railgun is to maintain the current injection during the movement of the projectile. A good electrical contact has to be ensured when the projectile is subject to a high acceleration to avoid the formation of a gap between the conductors and the rails. Any gap would form an electric arc to maintain the electrical contact thus causing pitting and erosion to the rail. In addition, arcing would provoke an increase in resistance for the complete system and so would reduce the Laplace force. Accumulated pitting and erosion reduce the possibility of a good contact and provoke arcing and wear that shorten the rails life. The two main conditions of a good contact are the guarantee of a sufficient normal force from the contacts to the rails and a limitation of the overheating of the contacts due to Joule effect (Schneider et al. (2003a)).

The threshold for a sufficient normal force to ensure good contact is referred as Marshall's law: 10 N/kA are required (Barber et al. (2003)). For our application, as the current is around 24 kA maximum, the corresponding contact force is around 240 N. In order to match this level of force, several projectile geometries have been tested at low current to select the more efficient one. They are represented in Fig. III.17. The first one consists in wires of copper inserted in an armature of Delrin thermoplastic that is chosen for its rigidity, low-friction and low-deformability to chocks and heat properties. It results in a weight of 40 g and is represented in Fig. III.17(a). The second one is a 170g X-shaped aluminum projectile with four feet having its extremities attached by a band of elastic to ensure a restoring force as can be seen in Fig. III.17(b). The third one consists in a raw plate of aluminum that is stuck up between the two rails of 70 g and is represented in Fig. III.17(c). Figure III.18 presents the current waveforms measured during shots of Railgun for these three different geometries.

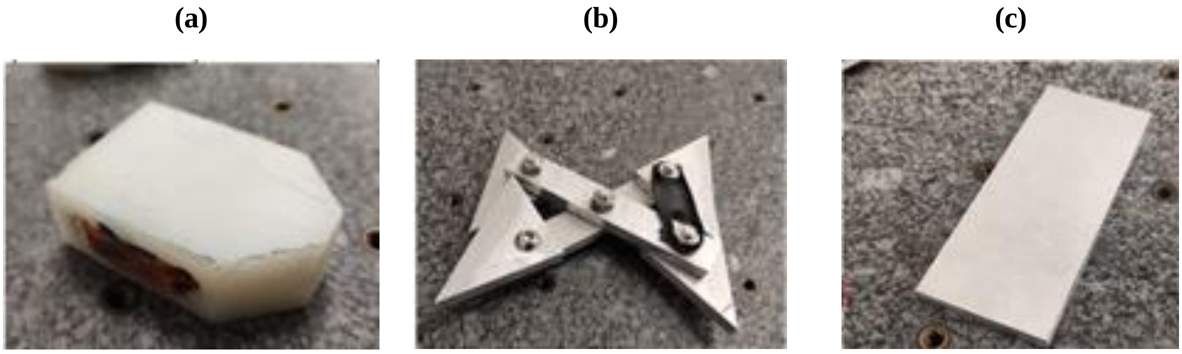

FIG. III.17 Photos of projectile 1 (a), 2 (b) and 3 (c).

It can be observed that for the raw plate of aluminum and the X-shaped projectile, the current is initially established but is not maintained when the movement starts whereas for the last projectile, the current reaches a higher level and is maintained continuously until the electrical contact is lost at 37 ms. Even if peaks of current reappear after that moment, a good contact is never set again and the projectile does not gain consistent acceleration anymore. The last projectile is thought to be able to keep a good contact during the movement because its copper wire conductors that are stuck up between the Delrin armature and the rails present enough spring tension to apply a sufficient normal force even if the wire are partially melted due to Joule effect and frictions.

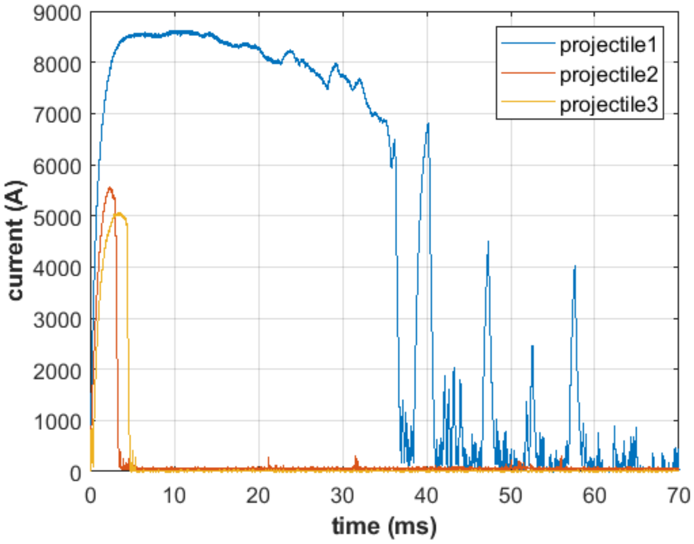

FIG. III.18. Current waveforms of railgun shots for different projectiles with an initial voltage of 12 V.

To avoid the melting of the contacts, the dimensions of the copper wires have to be designed to endure heat load neglecting the frictions. Indeed, considering that the wires are only heated by Joule effect, an energy balance gives the required section of wire that is required to avoid melting:

$$S = \sqrt{\frac{\int I^2 dt}{\rho c \sigma \Delta T}} \tag{III.11}$$

Where S is the section of the wires, I is the current, t is the time, ρ is the density, c is the heat capacity, σ is the electrical conductivity and ΔT is the acceptable temperature variation. Considering that the generator delivers a current of 24 kA during the predicted 100 ms and that the fusion point of copper is 1085°C, the resulting minimum surface is 14 mm^2.

This section has to be compared to the dimension of the skin effect, whose expression for AC current is:

$$\delta = \sqrt{\frac{2}{\mu_0 \sigma \pi f}} \tag{III.12}$$

Where δ is the dimension of the skin effect, μ_0 is the magnetic permeability of vacuum, σ is the conductivity and f is the frequency. For square current waveforms between 50 ms and 100 ms, this dimension varies between 2 and 3 cm. As the dimensions of the rails section are 22 mm width and 12 mm height, the current is distributed into the whole section. Conventional Railgun with timescales of less than 10 ms have a skin effect dimension of a few mm so that the current flows in a small section of the conductors and of the wire inserted in the armature that ensure the contact and so provokes its melting. However, the addition of several wires in parallel in the armature does not solve this problem by offering more conduction path. Indeed, for the insertion of several wires in parallel and a skin effect of less than a mm, most of the current flows through the back wire. This problem is referred to as velocity skin effect (Gallant and Lehmann (2005)). In our case, the dimension of the skin effect is high enough due to a long duration of current injection so that the current is well distributed in case of the insertion of several wires in the armature. This prevents the wires from melting due to Joule effect. For our application, wires composed of several hundred of conductors with sections from 10 mm^2 to 15 mm^2 were inserted like a serpentine in the five holes of the Delrin armature to ensure three effective paths of current so that the thermal load for every wire is reduced by a factor of three.

The final Delrin thermoplastic armature consists in a rectangular bloc of between 80 and 110 mm depending on the selected configuration of length, 47 mm of width and 12 mm of height with five through holes in its side to insert the conductor wires. The conductor wires have a total section of 10 mm^2. The aeronautical test material – consisting of plates of aluminum of dimensions from 200 to 400 mm for the length, 100 to 200 mm for the width and 0.4 to 1.6 mm for the thickness – are mounted to the armature using plastic threaded rods. A presentation and a specific discussion about the test sample geometry will be conducted in Chapter IV. An image of a typical armature without the test sample is presented in Fig. III.19(a) and a schematic showing the insertion of the copper wire within the armature as a serpentine is proposed in Fig. III.19(b).

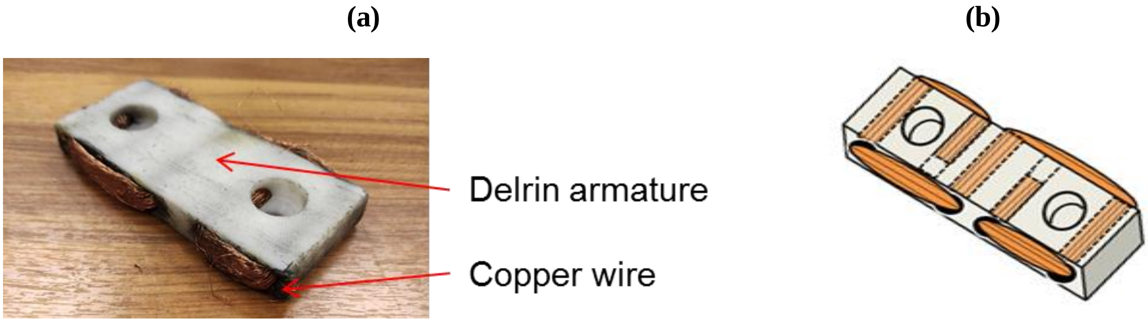

FIG. III.19 Typical projectile composed of a Delrin armature and wrapped copper wires (a) and schematic of the insered copper wires (b) .

B. Evaluation of contact and rails resistance

As stated before, the resistance of the Railgun is a key parameter since 24 kA of current are expected with a 20 to 30 V setpoint from the capacitor bank. The measurement of the circuit and the rails resistance during a shot is made by recording the voltage of the capacitor bank and of the rails and the current in the circuit as shown in Fig III.20.

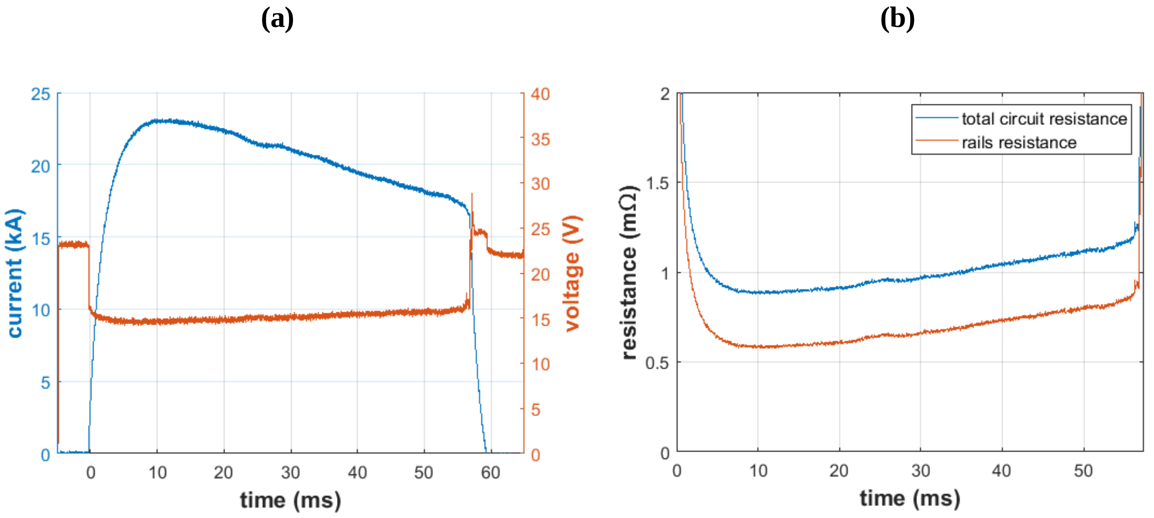

FIG. III.20. Current and voltage waveforms at the terminals of the capacitor bank during a shot (a) and resistance of the circuit and of the rails (b).

During this shot, the capacitor bank is initially charged to 24 V, at the instant initial, the thyristor is activated, and the current starts to increase in the circuit. The voltage measured at the terminals of the capacitor bank drops suddenly from 24 V to 17V. This is due to the equivalent series resistance of the capacitor bank that is around 0.29 mΩ: as the current reaches values up to 24 kA, it triggers a voltage drop of around 7 V so that the voltage of the circuit is considered to remain at 24 V during the shot as only a loss of 1 V is measured after the shot. As can be observed in Fig III.20(a), the current requires 10 ms to reach its maximum peak value of 24 kA due to the inductance of the circuit. This corresponds to the time when the total resistance of the circuit reaches its minimum. After reaching its peak, the current drops from 24 kA to 17 kA in 46 ms almost linearly, the resistance of the circuit rises from 0.9 mΩ to 1.2 mΩ and the resistance in the rails rises from 0.6 mΩ to 0.9 mΩ as can be measured in Fig III.20(b). This current drop is therefore explained by the additional rails portion leading to a final additional resistance of around 0.26 mΩ that fits the measurements. After 56 ms, the projectile goes out of the rails: the current suddenly drops to zero and the capacitor bank voltage returns to its initial value. It is interesting to notice that for this magnitude of current, despite a longer current injection time compared to the ones of conventional railguns, the complex physical phenomenon occurring in the contact point between the rails of aluminum, the wires of copper and the lubricant - Joule heating, the formation of a thin aluminum melt film, the ablation and wear of the rails (Schneider et al. (2003b)) - do not have a noticeable impact on the current waveform at this initial contact force.

C. *Use of Lubricant*

To lower frictions during movement, the use of hydrodynamic lubrication technique has been discussed these last years (Singer et al. (2010)). Even if during the movement, the formed melting layer of copper and aluminum has a lubricant effect, the resulting erosion is able to provoke a separation of contact surfaces and degrade the current. The main investigations for a lubricant compatible with Railgun technology have been carried for liquid lubricant, solid lubricant, and low-melting alloy lubricant (Chen and Lv (2018)), (Singer et al. (2011)). Whereas liquid lubrication addresses experimental issues for the injection system and low-melting alloy lubrication requires an initial surface coating all along the rails, the solid lubrication ensure ease of implementation that enable to take less precautions. Despite Singer et al. (2011) has reported that the use of PTFE reduces the wear of armature contact surface in a configuration of copper rails with aluminum armature, thus reducing friction and ensuring a longer lifetime for the rails, this solution was found to be dangerous because the PTFE lubricant is highly flammable and is susceptible to start a fire with the melting contacts of the aluminum rails or the wires of copper in the projectile. Thus, the application of a grease of graphene was preferred and demonstrated a noticeable improvement in the electric contact during the movement of the projectile as can be seen in Fig. III.21.

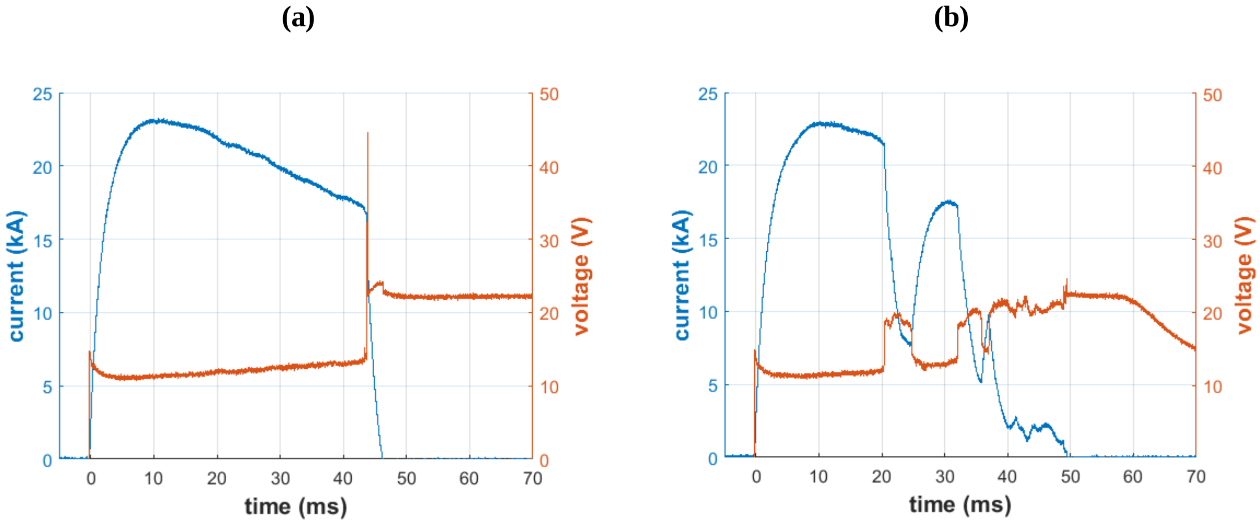
(a) **(b)**

FIG. III.21 Comparison of current and voltage waveforms at the rail terminals with (a) and without (b) the use of graphene solid lubricant.

In both Figs. III.21(a) and III.21(b) the peak current during the shot reaches a value of 23 kA, but whereas in Fig. III.21(a) the current linearly drops to 18 kA at the exit of the projectile due to reasons evoked in Sec. III C, in Fig. III.21(b) a sudden drop of current from 22 kA to 7 kA in few ms appears at 20 ms and sparks are observed at the same moment in the contact between the projectile and the rails with the HSC. At this moment, the erosion of the rails after a few shots provokes the concentration of the electric contact in a shorter surface, focusing the Joule effect on these areas. Thus, the contacts points from the copper wire in the projectile and from the rails start to melt, producing electric sparks. Evidence of this melting is observable in Fig. III.22 that shows a deposition of copper and erosion areas in the aluminum angles of the rails. After this drop, the current rise again as the electric contact is reestablished further on the rails but another drop of current occurs at 30 ms. This erosion is not only a problem because it provokes the obsolescence of the rails but as it reduces the current level, it reduces the electromagnetic force applied on the projectile thus lowering its final speed. The use of a graphene lubricant helps to maintain the electric contact during the crossing of the rails and so no drop of current occurs, this is at the same time a very efficient solution for the repetitiveness of the shots as the current waveforms from different shots then become very similar and for the enhanced longevity of the aluminum angles covering the copper rails.

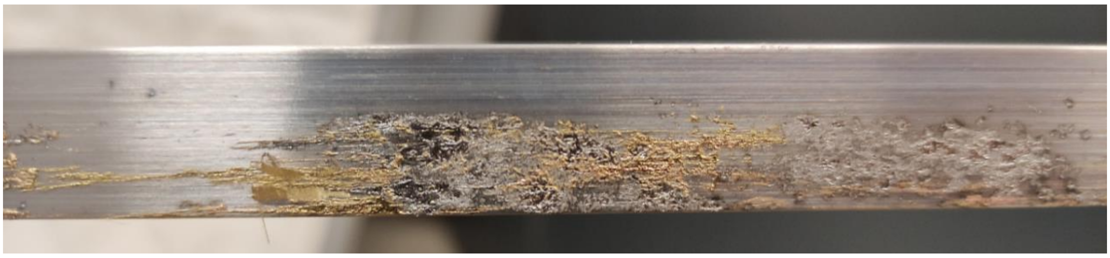

Fig. III.22 Front view of an aluminum angle after several shots.

D. Overvoltage protections

A well-known problem with Railguns is the formation of an electric arc when the projectile leaves the rails, triggered by the opening of the electrical circuit as shown in Fig III.23. In Fig III.23(c), the electric sparks issued from this arc can be observed. If the electric arc only provokes pitting and erosion damages to a relatively small area situated at the very end of the rails, the current disruption represents a danger for the electrical components as represented in Fig III.24. Indeed, a fast drop of current – around 20 kA in few ms - at the end of the rail imposes an overvoltage of up to 100 V that is propagating to the Ultra capacitors bank as can be seen in Fig. III.24(a) and (c). This bank cannot endure more than 34 V and protection is thus mandatory. 20 TVS diodes of model AK10-030C-Y are used in this purpose. As can be seen in Fig. III.24(b) and (d), when the current suddenly drops after the projectile exit, they switch in less than a µs into a conducting state and damp the overvoltage at the terminals of the bank of capacitors.

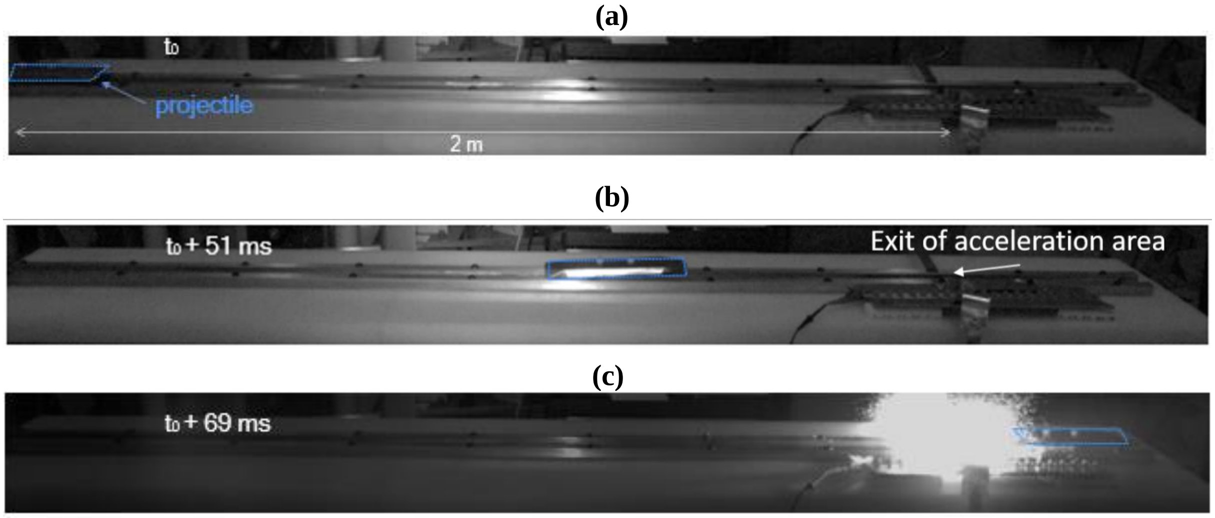

FIG. III.23 Succession of images during a typical shot and apparition of an arc.

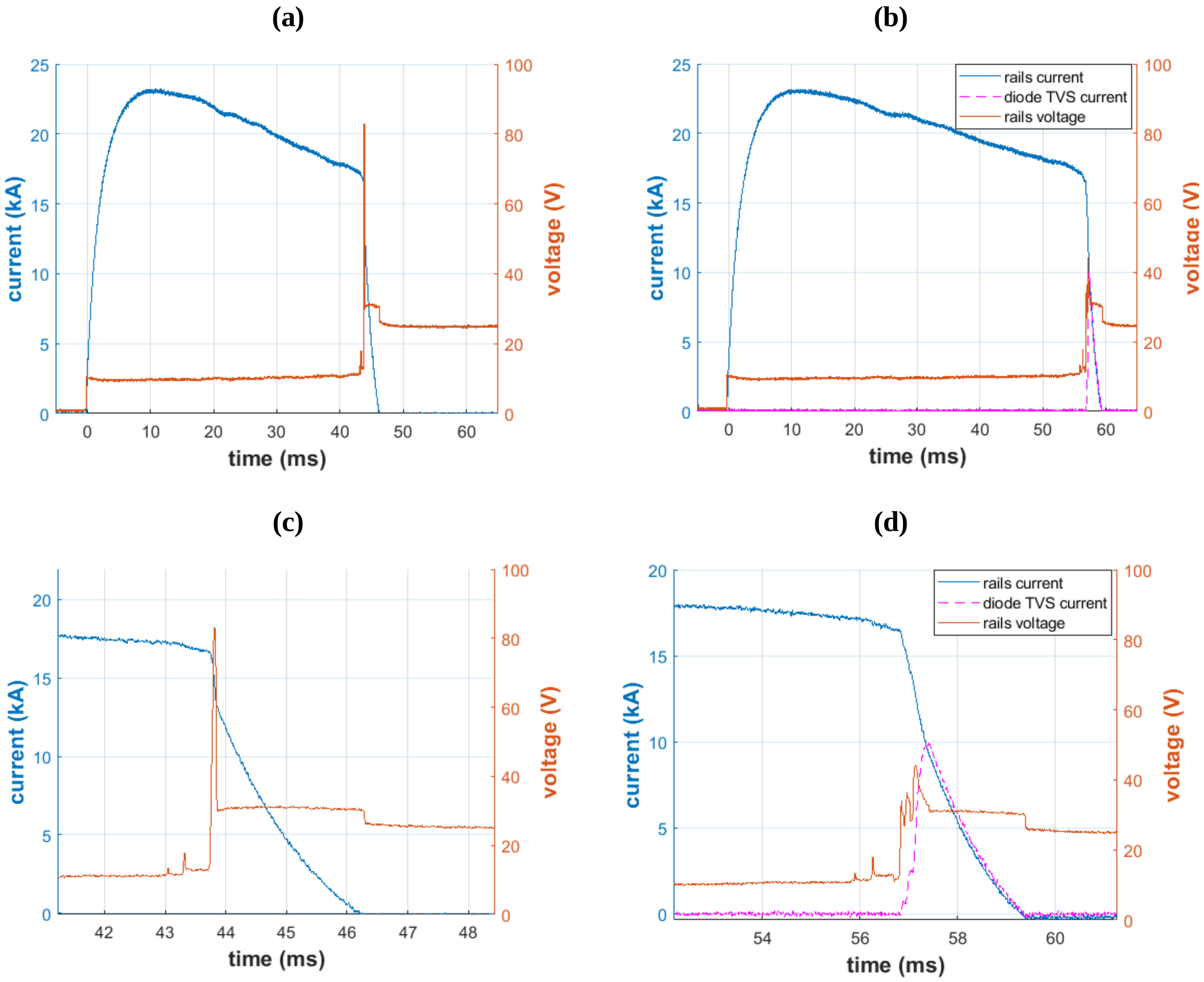

FIG. III.24 Overvoltage measurement at the exit of the projectile (a) and (c) and action of the TVS diodes (b) and (d).

E. Eddy currents and Demagnetization

The interactions of the magnetic fields from the Railgun and from the permanent magnets provoke two side effects: the degradation of the propulsion efficiency by the creation of eddy currents and the demagnetization of the magnets with the Railgun magnetic field.

The eddy currents are formed by the speed of the conductive projectile subject to the permanent magnet field. They are in opposition with the current circulating in the Railgun so that they have to be removed to evaluate the real propulsion with the equivalent current. They can be evaluated using the formula:

$$I = \frac{Blv}{R} \tag{III.13}$$

With I being the eddy currents, B the magnetic density flux from the permanent magnets in the conductive wire, l the length of the conductive wire, v the velocity of the projectile and R the total resistance of the circuit. These currents are overestimated by introducing a velocity of 100 m/s, the magnetic density flux is around 0.3 H, the length of conductive wire in the projectile is 5 cm and the resistance of the circuit is around 1 mΩ. The resulting current is at maximum 1500 A, which represents 6% of the maximum current and is consequently neglected in this study.

The demagnetization of permanent magnets is more complicated to evaluate since the magnetic field induced by the Railgun is orthoradial in the projectile referential. Thus, when the projectile passes over the magnets, its backward magnetic field is oriented in the opposite direction of the magnetic field induced by the permanent magnets and so participates to their demagnetization whereas its rear field is oriented in the same direction and so magnetizes them as is represented in Fig. III.25.

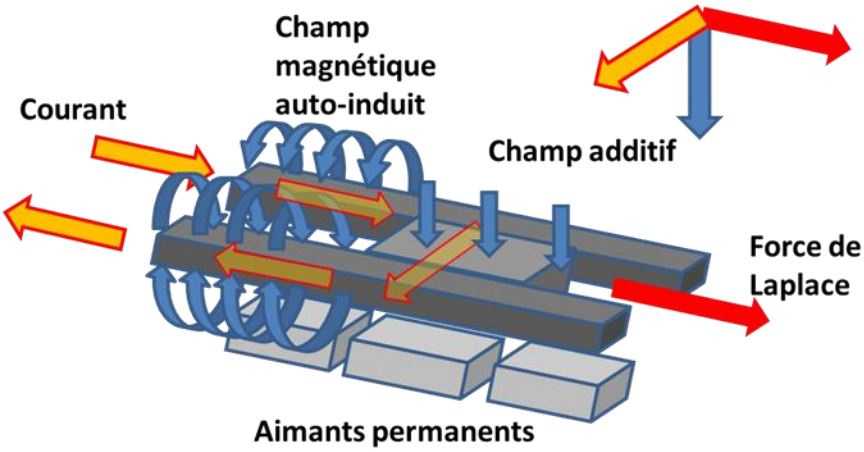

FIG. III.25 Scheme of magnetic fields produced by the Railgun and by the augmented magnets.

Considering the expression of a magnetic field formed by the passage of current in an infinite wire in a plan perpendicular to the wire's direction, the projection of the magnetic field in the direction of the permanent magnets magnetic field, using Cartesian coordinates, is given by:

$$B = -sgn(x)\frac{\mu_0 I}{2\pi}\frac{x}{x^2+y^2} \tag{III.14}$$

Where the origin of the coordinates is the wire, the x-axis is the axis of the projectile displacement; the y-axis is the axis perpendicular to the projectile displacement and parallel to the direction of magnetic field from permanent magnets. *Sgn* is the function sign, μ_0 is the magnetic permeability in vacuum and I is the current that flows in the wire. This last expression is maximized when x equals y so that the maximum magnetic field for a given y-coordinate is:

$$B = -sgn(x)\frac{\mu_0 I}{4\pi y} \tag{III.15}$$

As the surface of the magnets is situated at minimum 3 to 4 mm from the wire in our configuration, the evaluated field is at maximum 800 mT and decreases to 260 mT in the centerline of y-coordinate in the magnet. Those fields are inferior to the specific flux of 1160 mT of these magnets so that they are not demagnetized by the magnetic field produced by the Railgun. Moreover, this field is opposed to the direction of the magnet's field in the back of the projectile (x negative) and collinear to it in the rear of the projectile (x positive). Experimentally, no noticeable variation of the magnets flux density was measured with a Gauss meter during the whole time of the experiments.

III.4 Experimental results and comparison to theory

A. Ballistic analysis and evaluation of electromagnetic and friction forces

The performances of the developed Railgun are analyzed by establishing the time varying displacement, speed and acceleration of the projectiles during the different shots with different input parameters such as the mass of the projectile, the current waveform and the initial friction force. These ballistic curves are obtained using the videos of the HSC and a software of tracking. Graphs of displacement and speed over time of a typical shot are presented in Fig. III.26. The mass of the projectile is 186 g in this example.

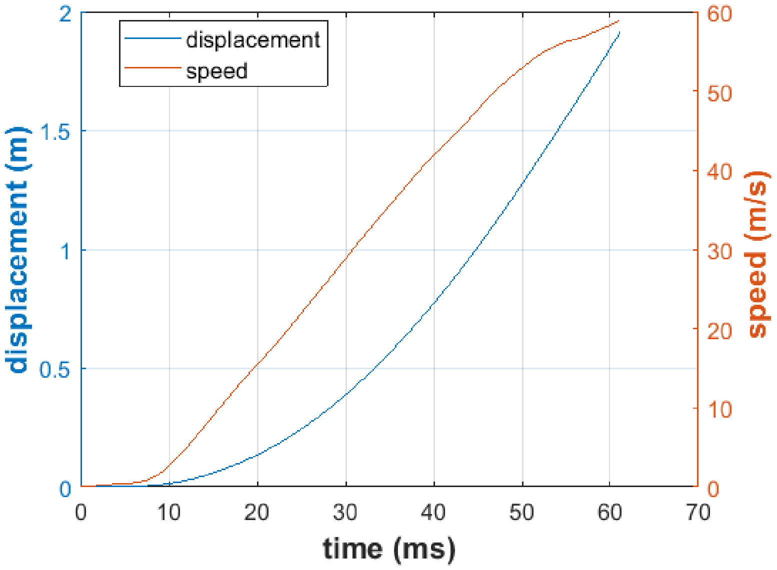

FIG. III.26 Displacement and speed of a typical shot of Railgun.

From these graphs, the acceleration of the projectile can be evaluated and the friction forces over time can be estimated using the fundamental principle of dynamics and Eqs. (III.8) and (III.10):

$$ma = \frac{1}{2}L'I^2 + BwI - F_f \tag{III.16}$$

Where m is the mass and a the acceleration of the projectile. The two terms representing the electromagnetic force on the right side, are evaluated by measuring the current waveform applied in the rails. F_f represents the friction force. Figure III.27 shows the repartition of the different terms of Eq. (III.16) the friction forces being evaluated with the difference of the other terms.

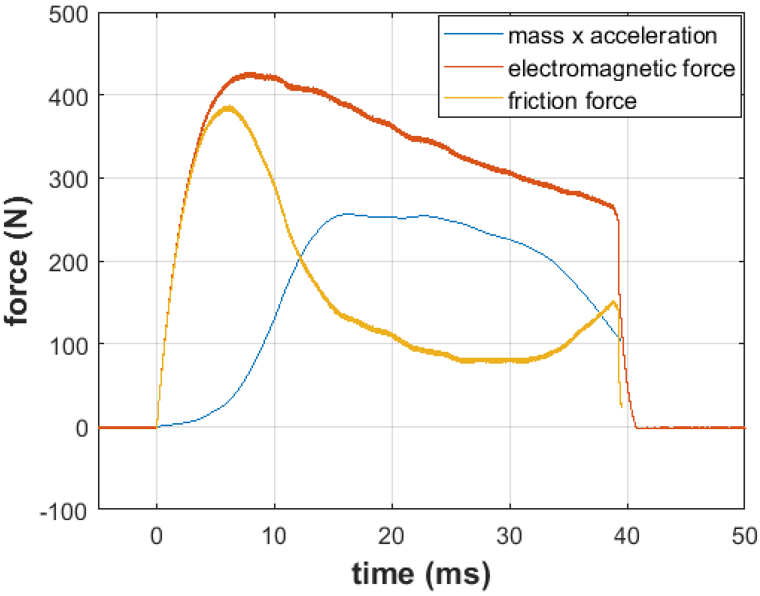

FIG. III.27 Evolution of the terms of Eq. 12 during a shot.

It can be seen from Fig. III.27, that most of the electromagnetic force is lost in the static friction at the first ms of the shot. Then the friction forces reach a peak before dropping in few ms whereas the projectile acceleration increases and reaches a stable value of 250 N. This stable phase lasts around 25 ms before it starts to drop when the friction forces are becoming dominant again. Looking at the length of the rails, even if this ultimate boost of friction forces occurs in the last ms of the shot, it corresponds to a position in the middle of the rails. This suggests that this friction becomes important when the projectile already reached a certain speed.

B. Evaluation of contact frictions

As good performances are possible only if a good electrical contact is ensured, the friction forces cannot be neglected in a Railgun application and represents the main loss of efficiency. The friction force is proportional to the normal force between the projectile and the rails. This normal force has a mechanical component due to the spring tension of the wires of copper inserted between the rail and the armature and an electromagnetic component due to the bending of copper wires at the contact surface with the rails that slightly diverts the electromagnetic propulsion force from the direction of the projectile displacement (Gallant and Lehmann (2005); Zhu and Li (2020)). This electromagnetic component is proportional to the propulsion force and is expressed with an electromagnetic coefficient factor that varies between 10 to 50 % in the literature (Gallant and Lehmann (2005); Zhu and Li (2020); Schneider et al. (2003a)). Thus the expression of the friction force F_f is given by:

$$F_f = \mu\left(F_m + \gamma\frac{1}{2}L'I^2 + \gamma BwI\right) \tag{III.17}$$

Where μ is the friction coefficient, F_m is the normal mechanical force and γ is the electromagnetic coefficient. Even if a model of dynamic friction coefficient as a function of the velocity is presented in Gallant and Lehmann (2005), the dynamic friction coefficient is chosen constant since the range of reached velocities does not provoke a dramatic drop of this coefficient. For a contact between copper and aluminum, the static coefficient is equal to 0.28 whereas the kinetic one is equal to 0.23 (Blau (1992)). However, the use of a lubricant, as detailed in a further subsection, lowers this friction coefficient.

An estimation of F_m is possible using a simple model and a measurement of the initial resistance of the inserted projectile. Indeed, as a high value of normal contact force is necessary to ensure good contact, this compression can be evaluated with a simple Holm model for a-spots. When the current flows through a contact surface, using a model of perfectly flat, circular, and isolated a-spots of radius a that concentrate current lines, Holm proposes a formula of the contact resistance (Holm (1967)):

$$R_c = \frac{1}{2a\sigma} \tag{III.18}$$

Where R_c is the contact resistance, a is the radius of a-spot σ is the conductivity of the material. As in the contact with aluminum rail and copper wire, the material with the smaller elastic modulus is aluminum; it will be the material provoking the formation of the a-spots.

As the resistance of the copper wire of length 5 cm and of surface 30 mm^2 is around 30 µΩ, the values from 200 to 600 µΩ measured as initial resistance before each shot are only due to the multiple points of contact. This extent of initial resistance is obtained by slightly varying the section of the copper wires inserted in the Delrin armature between 10 and 15 mm^2. With this range of initial resistances, the dimension of a a-spots varies between 22 to 66 µm. Under the assumption of elastic deformation, the relation between the compression force F_m and the surface of a-spots S is given by Hooke´s law:

$$Fm = ES \tag{III.19}$$

Where E is the elastic modulus of aluminum. The resulting mechanical force is between 100 and 1000 N and is estimated to keep constant during the sliding contact for most models even if the mechanical bending of the wires is presumably changing with their partial fusion (Gallant and Lehmann (2005)).

In order to predict the performances of the Railgun for different configurations, it is important to further analyze the dependence of the friction forces on the input parameters. The two components of friction forces are the friction coming from the contacts and the friction coming from the air resistance (Zhu and Li (2020)). Using the expression of the contact friction given in Eq. (III.17), Eq. (III.16) can be developed:

$$ma = (1 - \mu\gamma)\left(\frac{1}{2}L'I^2 + BwI\right) - \frac{1}{2}C_D\rho_{air}Av^2 - \mu F_m \qquad \text{(III.20)}$$

Where C_D, ρ_{air}, and A are, respectively, the coefficient of windward resistance, the air density, and the windward area. In the case of a square shaped windward area, the coefficient C_D is around 1. The factor γ represents the fraction of the electromagnetic force that is oriented in the transverse direction of the projectile's displacement and is due to the bending of the copper wires at the contact area with the rails. It is assumed in Gallant and Lehmann (2005) and in Schneider et al. (2003) that this fraction is mainly due to geometric configuration and is the image of the proportion of copper wires that is bended due to the contact with rails to the total length of the wires in the projectile. As Gallant and Lehmann (2015) report a value of γ of 0.154 for copper wires and an inter-rails distance of 15 mm, it is expected that the factor γ is even lower for our copper wires and inter-rails distance of 50 mm. Moreover, as the coefficient of dynamic friction μ between copper and aluminum is estimated to be inferior to 0.3, the factor μ times γ in Eq. (III.20) is less than 0.05 and is thus neglected in the rest of the analysis.

In addition, as seen in Sec. III.3, after the current applied to the rails has reached his maximum peak – this delay being due to the parasitic inductive behavior of the circuit – the evolution of the current can be correlated to the longer part of rails crossed by the current during the shot. Thus, an expression of the current depending on the displacement of the projectile can be found. Indeed, as the rails voltage is constant during the shot, the expression of the current over displacement can be written as:

$$I(l) = I_{peak}\frac{R_0}{R_0 + rl} \qquad \text{(III.21)}$$

Where R_0 is the initial resistance of the circuit, r is the linear resistance of the rails and l is the displacement of the projectile. Fig. III.28 shows a comparison between a typical current waveform during a shot and the plot of expression 14 with R_0 being 0.9 mΩ and r being 0.26 mΩ/m and using the ballistic curves of the shot. It can be seen that beside the initial part where the current increases due to the circuit inductance, the current drops at the same rate of the theoretical expression.

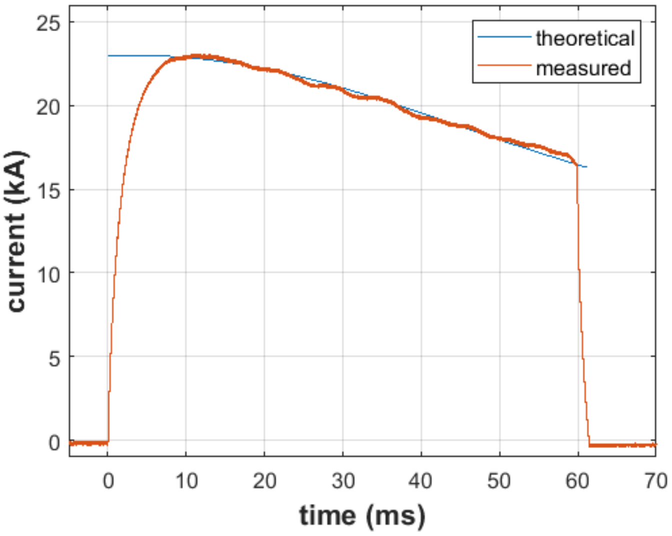

FIG. III.28 Comparison of theoretical and measured currents in the Railgun during a typical shot.

Thus, if we replace Eq. (III.21) in Eq. (III.20), this last becomes a non-linear differential equation:

$$m\frac{d^2l}{dt^2} = \frac{1}{2}L' I_{peak}^2\left(\frac{1}{1+\left(\frac{r}{R_0}\right)l}\right)^2 + BwI_{peak}\frac{1}{1+\left(\frac{r}{R_0}\right)l} - \frac{1}{2}C_D\rho_{air}A\left(\frac{dl}{dt}\right)^2 - \mu F_m \quad \text{(III.22)}$$

With the limitation that it can be applied only after the projectile starts to move due the hypothesis on Eq. (21) and with the factor μ being set as the dynamic friction. In all the shots, it was observed that the projectile started to move before the current reached its peak so that the second condition is the limiting one. From this equation, it is interesting to deduce the dynamic friction coefficient to complete the model and then predict the performances of the circuit for different configurations.

To obtain an estimation of μ, three shots with the varying parameters mass, input current and initial transverse mechanical force F_m, were successfully analyzed. Their displacement, speed, acceleration and current waveform were recorded and the factor μ is determined by fitting the measured displacement and the calculated displacement resulting from the solving of the differential Eq. (22) using a least-square procedure. An example of adjusting is represented in Fig III.29. Table III.1 summarizes the results of the analyzed shots.

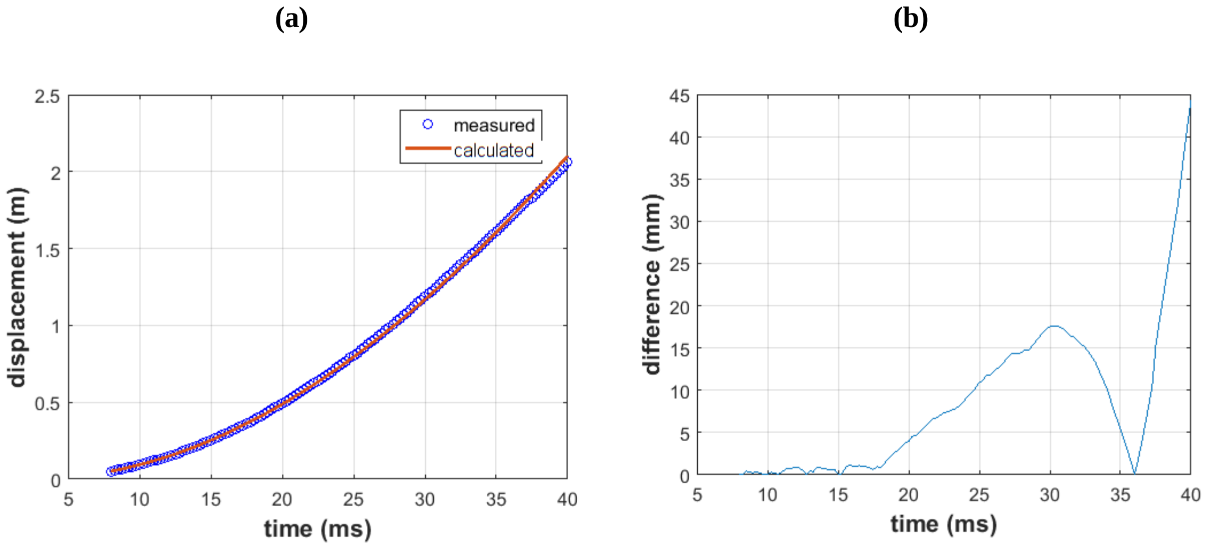

FIG. III.29 Fitting of a measured curve by using a least-square procedure to calculate the friction forces for a projectile of 80 g (a) and absolute difference between the measured and calculated values over time (b).

TABLE III.1 Analysis of the different shots.

Shot n°	**Mass (g)**	**Current peak (kA)**	**Initial contact resistance (μΩ)**	**Initial mechanical force F_m (N)**	**Muzzle velocity (m/s)**	**Start of motion after trigger (ms)**	**μ**	**μ F_m (N)**
1	79.6	22.5	280	486	90	5	0.307	149
2	101.7	22.9	540	136	77	2	1.165	158
3	186.2	23	230	748	60	10	0.1895	142

In table III.1, the initial mechanical force is calculated using Eq. (18) and Eq. (19). The coefficient μ is the fit parameter when comparing calculated and measured displacement. Despite the coefficient of dynamic friction was expected to be constant for the three shots, it turned out it was able to vary from less than 0.2 to more than 1 which is physically impossible. A possible interpretation is that the mechanical force is uncorrelated to the friction force after the motion has started. Indeed, the resulting average friction force μF_m, appears to be a constant quantity in the three shots even if the initial mechanical forces present a difference of a factor up to 5 between shots 3 and 2. Thus, a model of a constant friction force not dependent on the initial mechanical force seems more relevant for our Railgun facility.

However, the initial mechanical force does have an influence on the instant of motion after the insertion of the current: a high initial mechanical force delays the instant of motion. Indeed, the current in the rails has to exceed a threshold value so that the electromagnetic force becomes high enough to defeat a given level of static friction forces and thus the moment of initial motion depends on the current rise time to reach this threshold. If the initial mechanical force exceeds a certain threshold, the electromagnetic force will not be enough to defeat the static friction forces at the peak of the current and the motion will never occur. Moreover, if the initial mechanical force is too low, a good electrical contact cannot be ensured and the current in the rails is likely to drop dramatically during the shot (see Sec. III.3). Indeed, for initial resistances over 600 μΩ, and initial mechanical forces below 100 N, the recorded shots never presented a stable current waveform. It can be noted that the Marshall's law, evoked in Sec. III.3, that predicts that 240 N as mechanical force are required to ensure a good electrical contact for 24 kA of current injection, is not always respected in our case since shots with an initial mechanical force between 130 and 240 N were successfully carried out. To explain this behavior, we can mention that the Holm formula is an approximation as well as the Marshall's law and that a good electric contact for shots between 100 and 300 N of initial mechanical force was not always ensured during the shot.

After this initial motion phase, the initial mechanical force does not influence the displacement of the projectile and a model of constant friction force due to the rails is able to describe the experimental results.

C. *Performances achieved by the low voltage Railgun*

The experimental performances of the developed Railgun in terms of speed, acceleration, and kinetic energy for various parameters of voltage, peak current and mass are listed in Table III.2.

TABLE III.2 Experimental performances of the Railgun.

Shot n°	Mass(g)	Voltage (V)	Current peak (kA)	Muzzle Velocity (m/s)	Mean acceleration (m/s^2)	Kinetic energy (J)
1	45	25	22	125	7810	351
2	100	25	24	100	5000	500
3	150	25	24	80	3200	480
4	175	25	24	77	2960	518
5	210	25	24	66	2180	457

The results of this table show that projectiles from 100 to 200 g can be propelled to a speed between 66 and 100 m/s – the limiting factor being the maximum peak current acceptable for the capacitor bank. This range of speed is in the order of magnitude of the speed of an aircraft when the risk of lightning strike is more likely – at the take-off or landing phases. Therefore, the use of this railgun facility is relevant to the problematic of the sweeping of lightning arcs even if the values are in the lower range of the phenomenon.

III.5 Conclusion

An experimental implementation of an unconventional Railgun capable of launching projectiles of a few hundreds of grams at speeds up to 100 m/s with an initial voltage of around 20 V was carried out to study the interaction between an electric arc representative of the lightning C* waveform and an aeronautical aluminum test sample.

As a first overview of the means of linear propulsion showed that electromagnetic launchers are a relevant solution in terms of acceleration performances and of safety issues, a design of a railgun electric circuit was realized: this circuit differs from the conventional Railgun electric circuits since it involves high capacitive and low voltage capacitors, also referred to as Ultra capacitors in the literature. It has the direct advantage to perform a launch with an operating voltage of only 20 V which makes it safe to use since it is meant to be coupled with a high-power lightning facility.

With this electrical configuration, the experimental implementation of a Railgun has been conducted. The low operating voltage and the requirement of a good sliding contact time duration of several tens of ms raise experimental issues that have not been discussed before in the literature. The different problematic aspects are the maintenance of a good electric contact through the study of the mechanical frictions and of the electric resistance of the circuit. The addition of permanent magnets providing a supplementary magnetic field of 300 mT and the problems of overvoltage are also discussed.

Once these technical problems have been addressed, Railgun shots were operated for different initial conditions such as the payload of the projectile, the initial friction force and the peak current in order to perform ballistic studies. A model of friction forces during the shot is then developed analyzing the motion of the projectile and establishing a force balance. The model shows that a constant friction force can be assessed to fit the data after the projectile has started to move and is interesting to predict the performances of shots varying the initial conditions. Then, projectiles from 100 to 200 g have been propelled to speeds between 66 and 100 m/s. As this range of speed is in the order of magnitude of the speed of an aircraft when the risk of lightning strike is more probable – at the takeoff or the landing phases, the developed Railgun proved relevant to the study of the swept stroke phenomenon.

For the rest of the present work, the Railgun facility will be coupled with the lightning generator to experimentally simulate the swept-stroke phenomenon. This will enable to conduct a wide campaign to study the swept-stroke in details for many different configurations and establish a relevant database of the physical parameters of the phenomenon.

Chapter IV. Hydrodynamic, electrical and thermodynamic characterization of the lightning arc channel during swept-stroke

As the experimental instruments for the reproduction of the swept-stroke in laboratory have been developed in the previous chapters, the characteristics of the phenomenon can be measured for a wide range of parameters. To facilitate this study, the characterization of the electric arc channel during the swept-stroke and the interaction of the moving arc spot with the aeronautical test sample will be discussed and detailed over two separated chapters. The present chapter focuses on the arc channel characterization aiming at establishing the evolution of its physical quantities during swept-stroke for various experimental conditions.

At first, the experimental coupling of the lightning generator with the Railgun and with a wind tunnel is presented with discussions about the representability of the experiment, mainly about the influence of the projectile geometry. Then, high-speed cameras and voltage and current probes are used to measure the electrical and geometric behavior of the electric arc channel during swept-stroke: the shape, the length, the voltage and the power evolution of the arc channel are evaluated for different input parameters such as the speed of the projectile for the Railgun or the airflow for the wind tunnel, the polarity of the arc spot on the test sample, the arc current level, the test sample length and the initial distance of the arc column at first attachment. Besides, the influence of these parameters on the temperature of the arc channel is studied, resorting to optical emission spectroscopy technique. The results are presented and discussed with the objective to give physical insight into the arc elongation phenomenology during swept-stroke.

IV.1 Experimental coupling of the Railgun / Wind tunnel facility and the lightning generator

A. Coupling of Railgun facility and lightning arc generator

To reproduce the sweeping of a lightning arc, both electrodes of the electrical generator are positioned just after the extremity of the rails so that the aircraft test plate is hit by the electric arc when the current of the Railgun does no longer flow in the copper wires of the projectile. This precaution is taken to prevent the high voltage of the arc generator from discharging through the Railgun electrical circuit. The electric separation is assured by the additional 50 cm long angles of PTFE screwed at the copper bars of the rail and placed after the screwed angles of aluminum that assure the electric contact during the shot. Then the electrodes of the lightning generator are placed at the end of the PTFE angles and of the copper bars. An electric tape is wrapped around the last 10 cm of copper bars to avoid any discharge. A receptacle consisting in a sand filled wooden box to stop the projectile is placed 1 m after the electrodes. Three types of electrodes have been tested: a bare rod of tungsten, a rod of tungsten protected by a diverter at its extremity to avoid the influence of the plasma jet, and a plate of aluminum. Figure 1 presents the configuration of the electrodes where the electrode above is a rod of tungsten of 10 mm diameter with a dielectric diverter ball at the tip, and the electrode below is an aluminum plate.

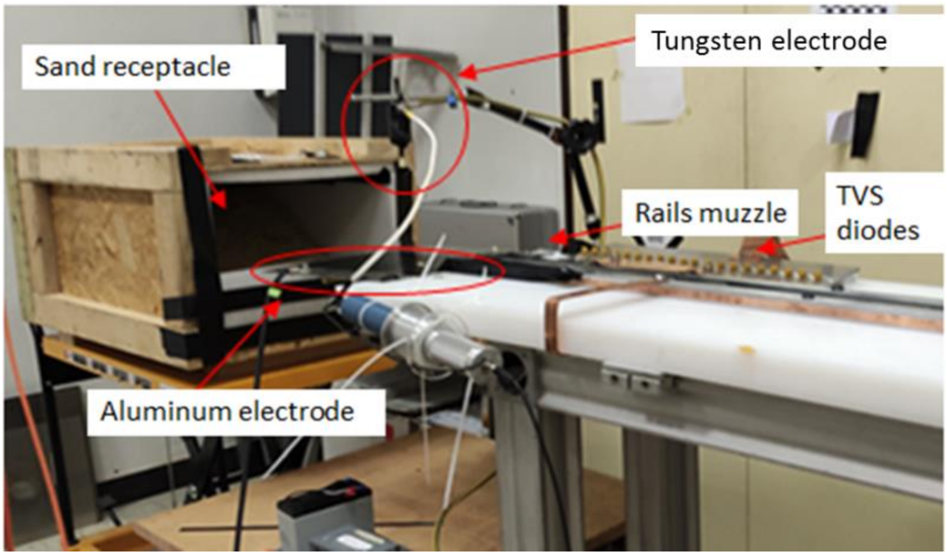

FIG. IV.1 Photo of the electrode’s configuration at the exit of the Railgun facility.

To synchronize the lightning strike with the projectile, the lightning arc is initiated 20 ms before the estimated time of arrival based on the velocity value of the projectile. The ignition of the electric arc is made using a conductive thin copper wire that vaporizes by Joule effect when the current rises. This rapidly heats the surrounding air and contributes to generate the high-density plasma. The 20 ms margin gives enough time to the electric arc to achieve a stable column shape.

In order to analyze the influence of the air flow profile on the sweeping phenomenon and to be more relevant with the aeronautical context, the shape of the aircraft material for the coupling with lightning have been changed from a plate to a NACA 0012 airfoil. The material test, a foil of aeronautical aluminum alloy (reference AL-2024-T3) with 0.4 mm thickness is modelled in respect to the NACA airfoil and hangs out on the projectile armature using two rods of plastic. Figure IV.2 presents a succession of images recorded by HSC of a lightning strike on this NACA shape.

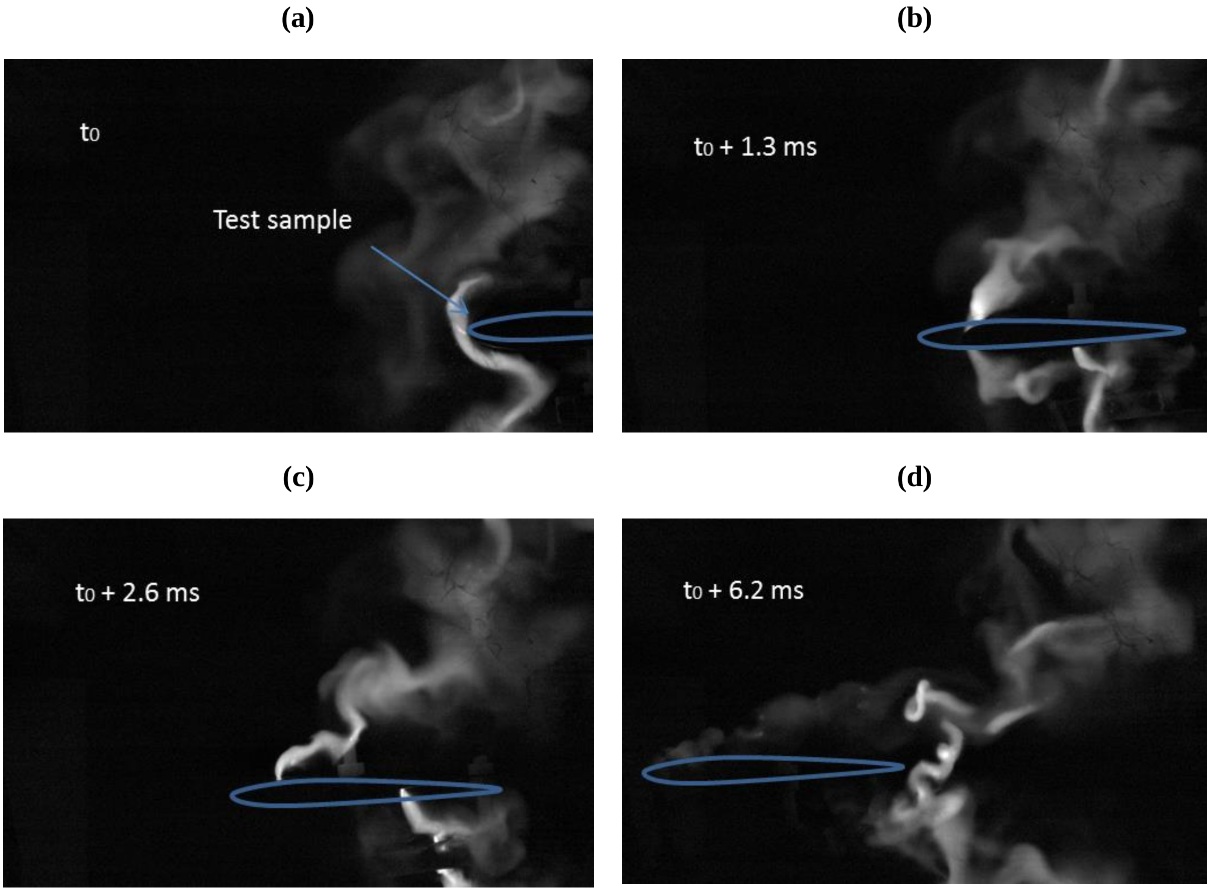

FIG. IV.2 Succession of images of a projectile crossing an electric arc with cathodic arc root above and anodic arc root below.

In Fig. IV.2(a), the arc channel is already formed between two electrodes consisting of two rods of tungsten with a diverter ball and the material test sample is pushing the electric arc. In Fig. IV.2(b) the sample has divided the arc column in two smaller arc columns, thus forming two arc roots on its surface so that the lightning current flows from the cathodic root (above) to the anodic root (below) through the aluminum sample. During the movement of the sample, the two formed columns are elongated, and the arc roots are either sticking, having a continuous sweeping movement, or leaping on the material test surface. After the passage of the sample, the lightning channel can either reform from the two columns channel or extinguish. However, it is preferable to study only one arc root to avoid any coupling in the displacement of the two arc roots along the material test. This situation is more relevant for the study of the lightning strike to aircraft since in this case the two arc roots (the entry and exit current points) are not displacing on surfaces belonging to the same pieces, or even in the same vicinity. To bypass this difficulty, a wire of copper with a section of 0.15 mm^2 and a length of 3 m has been screwed on the lower surface of the materiel test sample. This wire is extended before the shot and the other extremity is screwed on the lower electrode of the lightning generator, near the exit of the Railgun facility. Figure 3 shows a succession of images of a shot with the displacement of the copper wire.

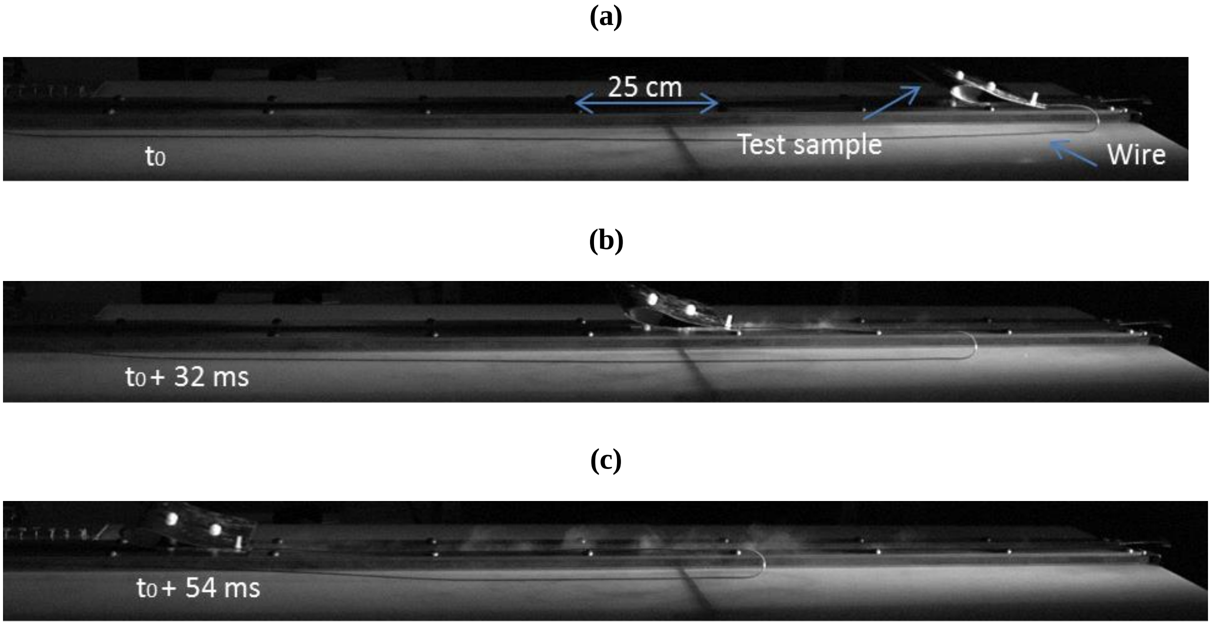

FIG. IV.3 Succession of images of a shot of a test sample connected to a wire.

It can be noticed that the acceleration of the projectile is so important that it moves faster than the propagation of the elongation wave in the wire. Figure IV.4 presents a succession of different images of the interaction of a projectile crossing an electric arc, the projectile being connected to the electrode beneath with a copper wire

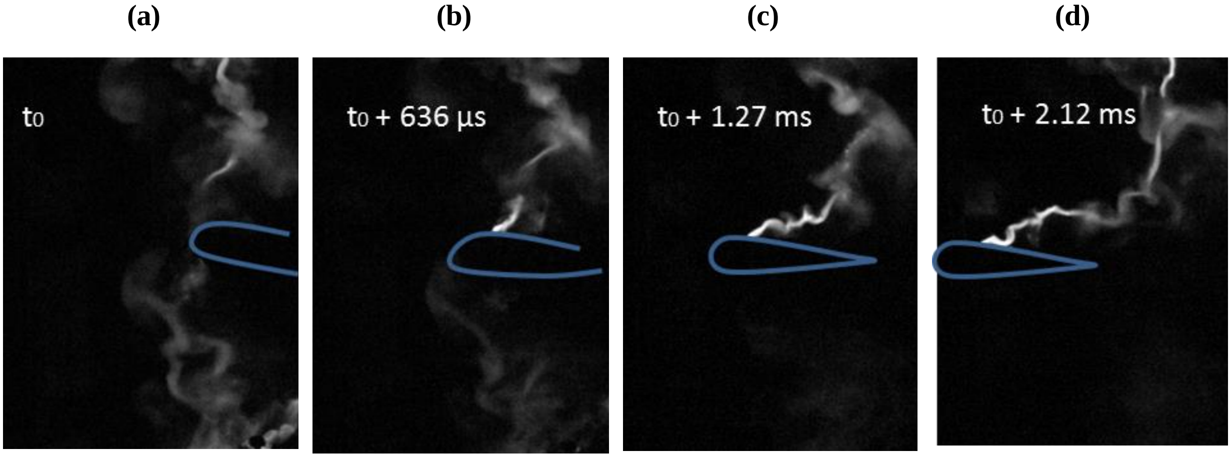

FIG. IV.4 Succession of images of a projectile crossing an electric arc with cathodic arc root above and a copper wire beneath.

In Fig. IV.4(a), the arc channel is already formed between two electrodes consisting of two rods of tungsten with a diverter ball and the material test sample is pushing the electric arcs. In Fig. IV.4(b) the sample has crossed the arc column: only the part of the electrical channel above the sample has remained, forming an arc root on its surface whereas the part beneath starts to fade away because all the current flows now through the copper wire to reach the ground. Indeed, the copper wire is less resistive than the electric arc – 90 mΩ for the copper wire against around 0.5 to 1 Ω for 25 cm of a 400 A electric arc according to the experimental results of Chapter II. In Figs. IV.4(c) and IV.4(d) the electric arc is elongating, and the arc root is sticking on the test sample. As the electric arc channel cannot reconnect to the other electrode by bypassing the current branch in the copper wire, it is extended until it reaches a length above 1 m provoking its extinction because the lightning generator cannot provide enough voltage. Therefore, this configuration of projectile propelled with a copper wire connected to an electrode of the lightning generator has proved relevant to study the motion of a unique arc root during the lightning strike. However, the addition of a wire that is pulled during the experiment reduces the speed reached by the test sample. Indeed, whereas a projectile of 150g is able to reach 70 m/s, it dropped to 57 m/s using the wire.

The distance between the upper electrode and the projectile axis is set to 20 cm: it is supposed to be long enough for that the plasma jets at the vicinities of the electrodes do not affect the interaction of the electric arc and the test plate during the lightning strike. This behavior was observed and verified by HSC (High Speed Camera). This aims to reproduce the conditions of a real lightning arc channel that can measure up to tens of km. It was chosen not to exceed 20 cm in order to compare the results obtained by the Railgun facility with the results from the Wind tunnel facility. Indeed, the dimension of the wind tunnel muzzle equipment is 250 mm and for this configuration, as the arc channel is set into motion, all the channel must be blown uniformly. In the other hand, a low initial inter-electrode distance consumes less energy from the lightning arc generator and so enables to extend the arc channel for more time during the swept-stroke. Anyway, the effect of the initial inter-electrode distance on the representativeness of the swept-stroke is discussed in the next sections.

B. *Description of the Wind Tunnel facility*

The Wind Tunnel (WT) used in this work is powered by a 15 kW motor from DELTALAB. A photo of the facility is represented in Fig. IV.5. An adapter of square section is added at the exit of the WT to homogenize the outgoing flow. Its dimensions are 250 mm long and 175 mm large.

The WT flow can be monitored for velocities up to 70 m/s. As the projectiles launched with the Railgun equipment are studied for speeds from 40 to 60 m/s. The wind tunnel facility is used for two flow velocities – 40 m/s and 60 m/s – that represents respectively 52 % and 90 % of the maximum power of the equipment – in order to compare the results of swept-stroke phenomenon for the two means. The test samples are NACA0012 profile as for the Railgun experiments: aluminium alloy foils of 200 mm and 400 mm long are wrapped and stiffened around a resin pattern of a NACA0012 profile. As for the Railgun facility, to avoid the coexistence of two arc roots, the sample is directly connected to the mass or to the positive potential and directly plays the role of a cathode or an anode as can be seen in Fig. IV.6. The other electrode is a horizontal rod of tungsten placed at 200 mm above the sample to respect the inter-electrode distance that was chosen for the Railgun facility.

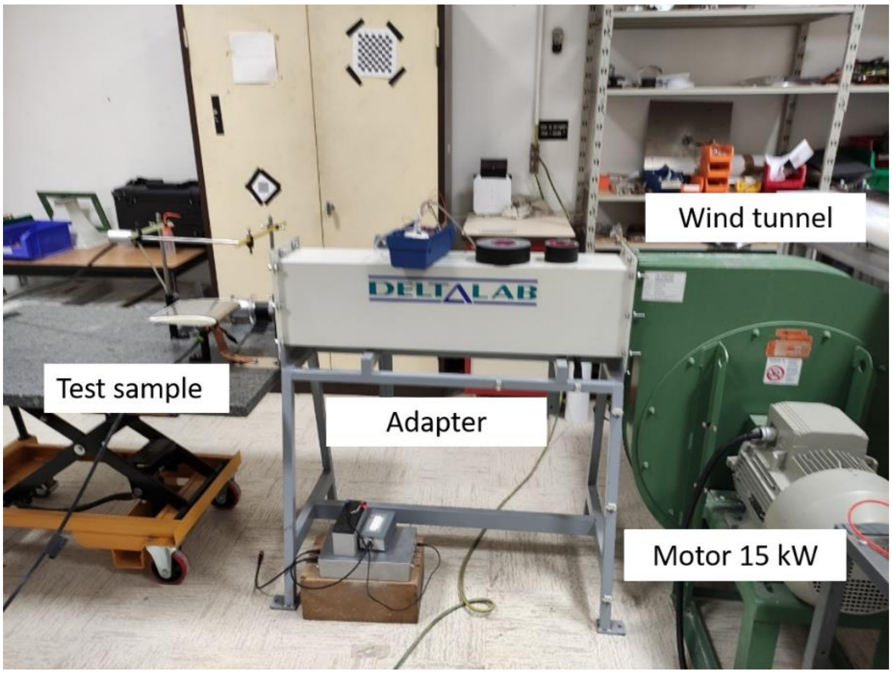

FIG. IV.5 Wind tunnel facility with motor and flow adapter.

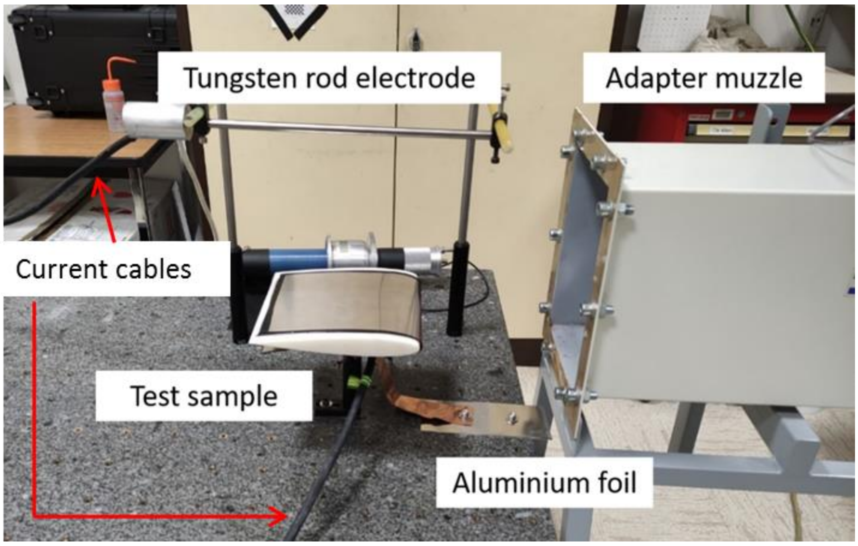

FIG. IV.6 Sample and electrodes positions at the exit of the adapter.

It was chosen to place a horizontal rod as the second electrode rather than a vertical one in order to allow the arc root to displace freely. Indeed, a vertical electrode would prevent the arc root from moving as it was the case in the experiment with the Railgun. But in the case of the Railgun, the projectile, playing the role of an electrode, is moving whereas in the wind tunnel facility, the test sample is static. Thus, letting the arc root moving freely on the upper electrode better represents the relative movement occurring in the Railgun experiment as the arc column keeps a similar shape as depicted in Fig. IV.7.

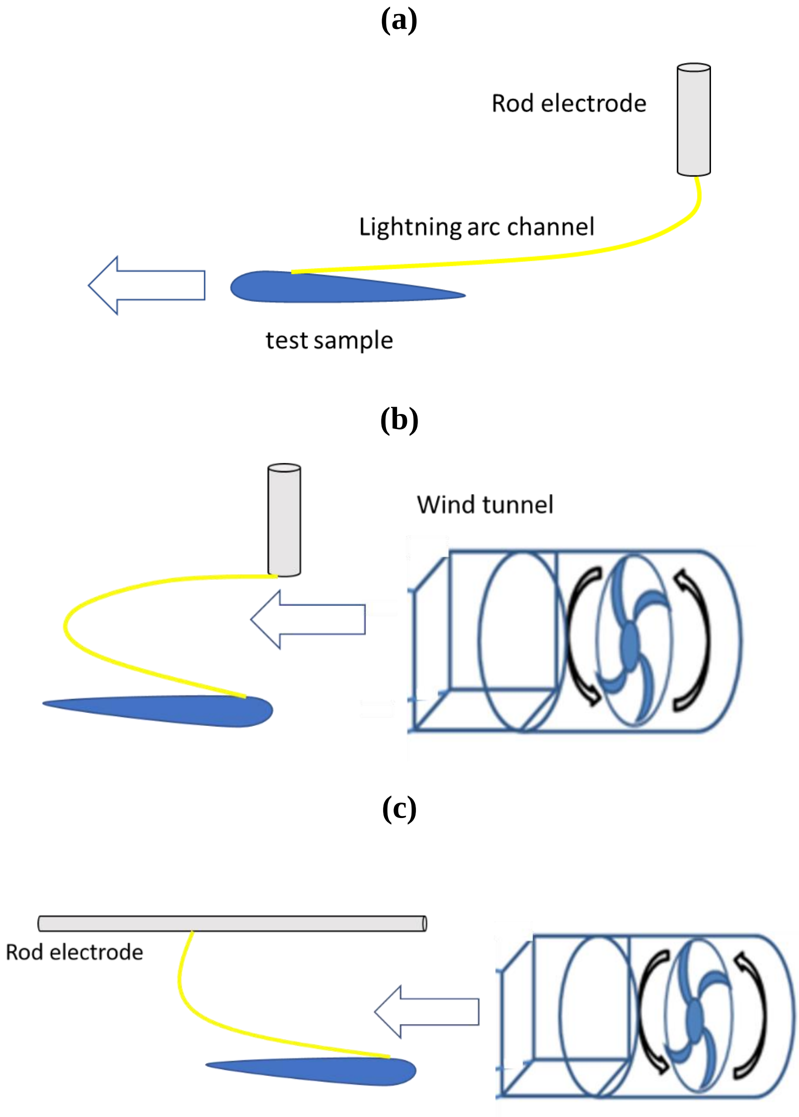

FIG. IV.7 Illustration of the arc column shape for the experimentation using the Railgun equipment (a) and by using the wind tunnel facility for vertical upper electrode (b) and horizontal upper electrode (c).

The electric arc is initiated between the upper electrode and a sheet of aluminium connected to the sample. The ignition is made with a thin wire of copper placed at 5 cm upstream the test sample. After the formation of the arc channel when the current rises in the copper wire and provokes its explosion, the lightning is convected by the airflow toward the sample and reattaches on it.

However, despite the addition of an adapter, the flow on the test sample is not totally homogeneous. Measurements of the flow velocity at different points on the test sample surface and at different heights above the sample are conducted using a Pitot probe. Figure IV.8 presents the setup and the results.

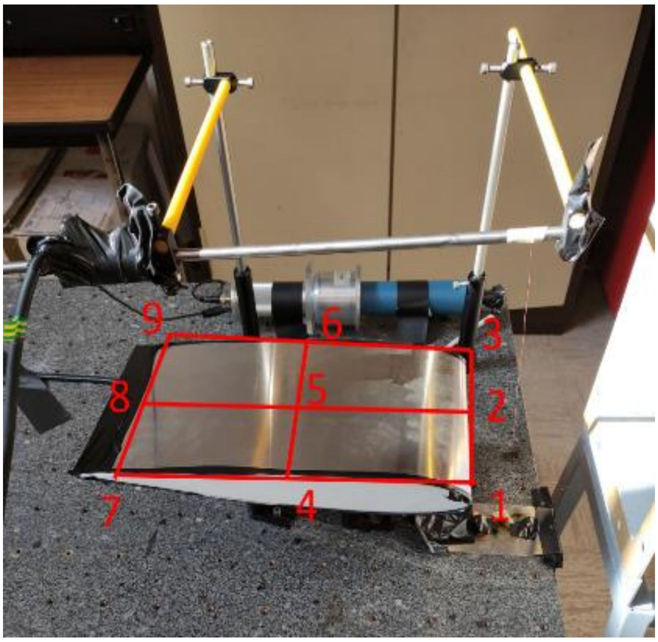

Point	Velocity at 90 % (m/s)
1	58
2	58
3	58
4	60
5	60
6	60
7	57
8	57
9	52

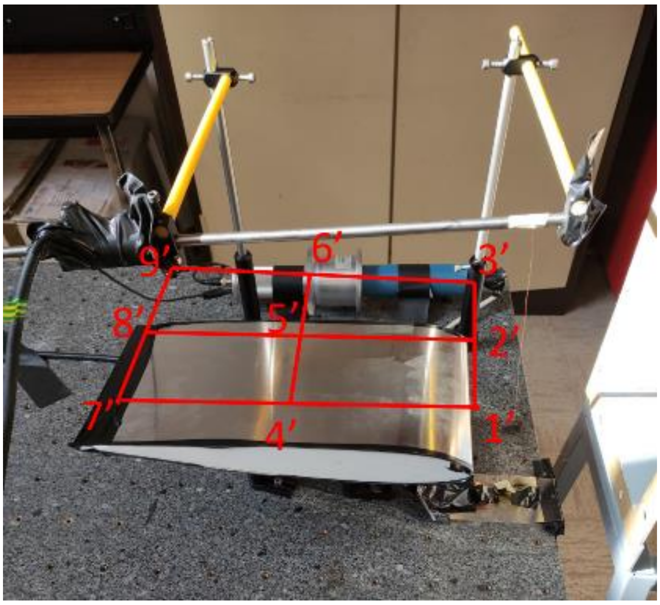

Point	Velocity at 90 % (m/s)
1’	57
2’	57
3’	62
4’	60
5’	62
6’	61
7’	60
8’	60
9’	61

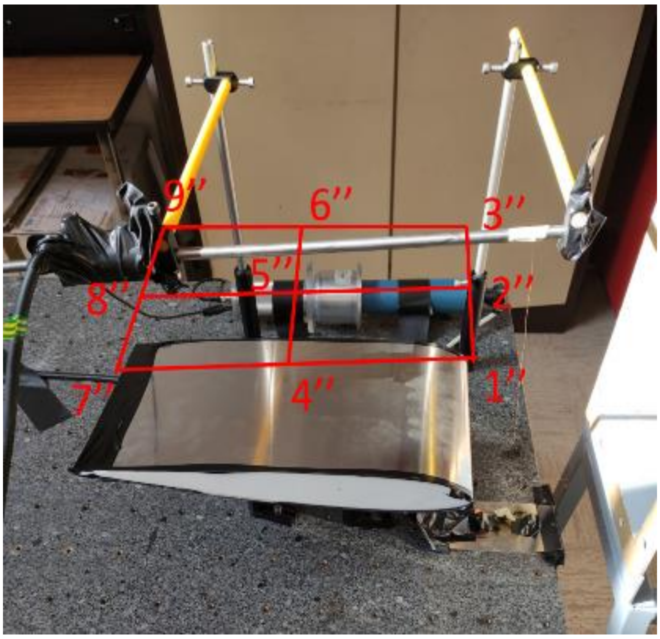

Point	Velocity at 90 % (m/s)
1’’	55
2’’	55
3’’	54
4’’	45
5’’	45
6’’	45
7’’	42
8’’	41
9’’	41

FIG. IV.8 Measures of the airflow for different points of the swept-stroke space. The measurements at points X’ are performed at 10 cm above the sample and the point X’’ are realized at 20 cm.

C. Discussion about the projectile geometry

The first choice for a projectile geometry to analyse the swept stroke experiment was to send a flat plate of aluminium. In this case, beside for the edge effects, there would be no geometry effect to consider and the fluid mechanics phenomenon as boundary layer would also be best known for a plane surface. However, taking a plane surface was impossible because of the acceleration of the projectile for the Railgun experiment. Indeed, Fig. IV.9 shows the time changing shape of a plane surface of an aluminium alloy foil of 0.4 mm thickness and 400 mm long under the effects of acceleration for the Railgun experiment. It is visible that due to the acceleration, the sample is deformed and that its straightness at the moment of arc impact is impossible to ensure and dramatic effects of electric field variation would interfere with the understanding of the swept-stroke phenomenon. A solution for this problem could be to use a thicker foil of aluminium to ensure more stiffness and resistance to acceleration but the weight would have been prohibitive to ensure an interesting speed for the sample.

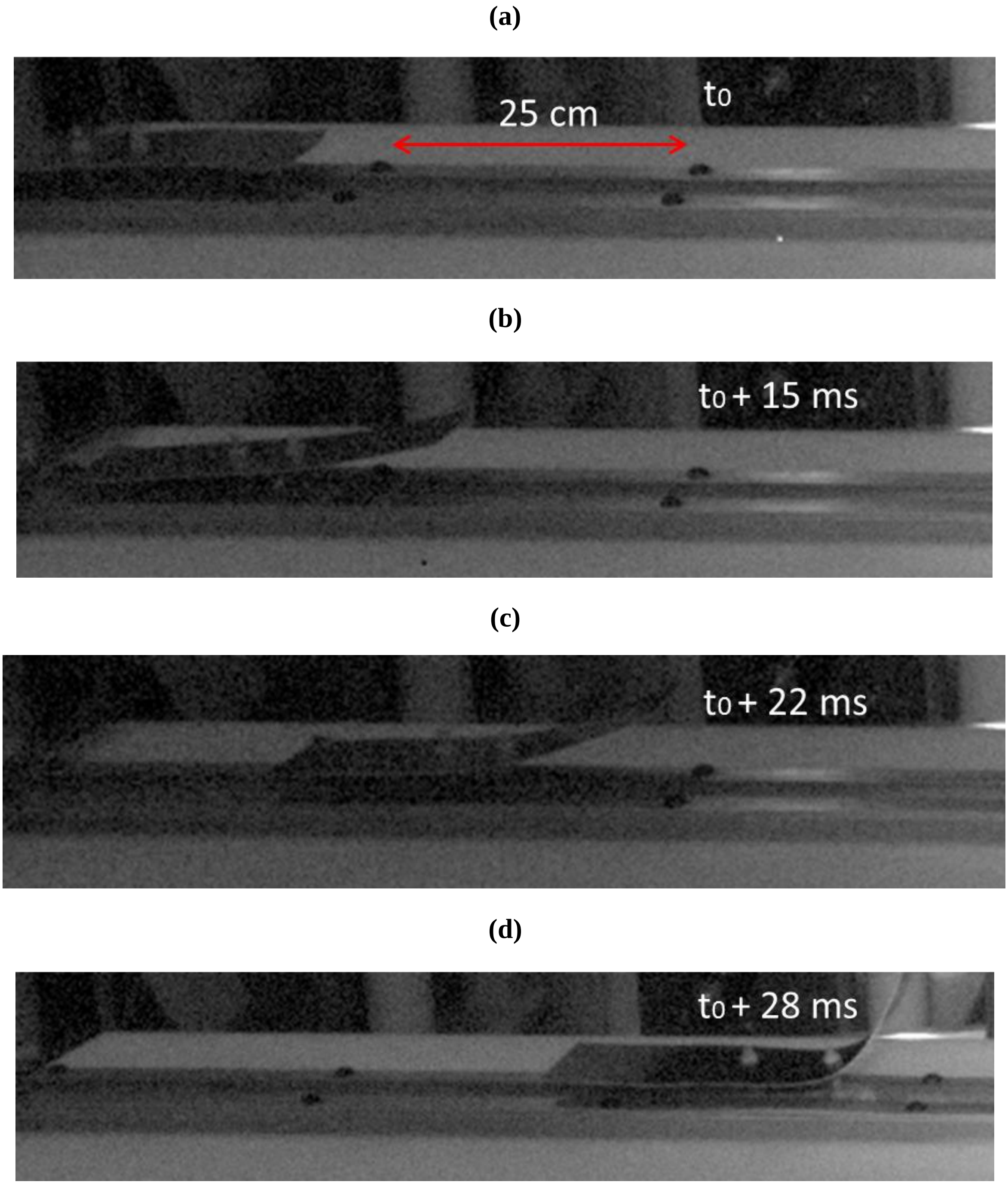

FIG. IV.9 Deformation of a 30 cm x 7 cm flat plate of aluminium alloy of 0.4 mm thickness under the effect of acceleration.

The considered solution is to use a NACA 0012 profile: NACA airfoils are airfoil shapes for aircraft wings designed by the National Advisory Committee for Aeronautics (NACA). The series of digits after the word "NACA" completely determines the geometrical parameters of the cross-section of the airfoil. For the NACA0012, "00" indicates that there is no camber and that the profile is symmetrical. "12" indicates that the maximum thickness of the profile is 12% of the chord. In this case, it is situated at 30% of the chord. To create our samples, two resin pattern pieces were built with a 3D printer. One has a chord of 200 mm and the other has a chord of 400 mm. These two lengths have been chosen to eventually study the impact of the length of the sample in the swept-stroke phenomenon. The resin model with a 400 mm chord length is shown in Fig. IV.10 with a test sample reproducing this shape. In the Railgun and in the wind tunnel experiments, plate of aluminium with a thickness of 0.4 mm are wrapped and stiffed around the patterns. In the case of the Railgun, the pattern is withdrawn from the sample before the launch because the impact with the sand to stop the projectile would destroy it. However, if in the case of the 200 mm length sample, the plastic tods are enough to stiffen the NACA 0012 profile, they are not enough for the 400 mm length sample. For that reason, expensive foam was added within the sample, even if it increased the weight of the projectile. Figure IV.11 presents a picture and a schematic of the sample mounted on the projectile by using two plastic rods. In the case of the wind tunnel facility, the plate of aluminium is fixed on the pattern and the pattern is screwed on a bulk table. This has also the advantage to guarantee the 0° incidence of the sample to the flow of the wind turbine whereas in the case of the Railgun facility, this is a parameter that is difficult to control as a torque is applied to the plastic rods during the projectile acceleration.

FIG. IV.10 Pattern of resin profile NACA0012 with a chord of 400 mm and the corresponding test sample.

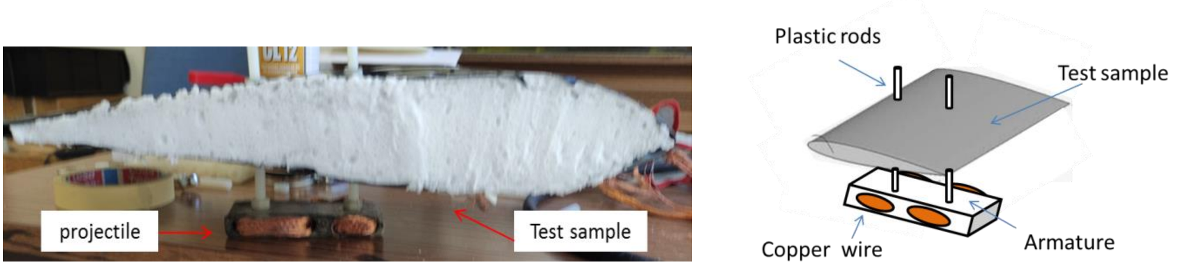

FIG. IV.11 Picture (a) and schematic (b) of the Railgun projectile with a NACA 0012 profile presenting a chord of 400 mm.

The NACA 0012 profile is chosen because it has been used in many model references as the B-17 Flying Fortress, the Cessna 152 and the helicopter Sikorsky S-61 SH-3 Sea King (Eleni et al. (2012)) and because it is a well-known profile: indeed, there is a lot of literature about this particular airfoil (Eleni et al. (2012); Sheldahl and Klimas (1981); Ahmed et al. (2013); Swanson and Langer (2016)) for computational as well as experimental descriptions. For these profiles, the simulation of the airflow and the experimental results are totally determined by the Reynolds number, the Mach number and the angle of attack (Polhamus (1996)); Abbott and Von Doenhoff (1959)). The Reynolds number, that predicts the laminar or turbulent behaviour of the flow, is given by the expression:

$$Re = \frac{\rho u L}{\nu} \tag{IV.1}$$

Where *Re* is the Reynolds number of the flow, ρ is the air density, *u* is the speed of the flow, *L* is the chord of the NACA 0012 profile and ν is the air dynamic viscosity. In our case, u varies between 40 and 60 m/s and L varies between 200 and 400 mm. Thus, *Re* varies between $5x10^5$ and $1,6x10^6$. As the Reynolds number depends on the chord of the wing, great caution must be kept for transferring our results from small scale to full-scale experiments. Indeed, as our Reynolds number values are lower than the full-scale ones, the viscous forces within the fluid play a more important role compared with inertial forces. Large-scale conventional aircraft rather operate with Reynolds number over one million. Figure IV.12 from (Winslow et al. (2018)) shows the variation of lift-to-drag ratio with the Reynolds number.

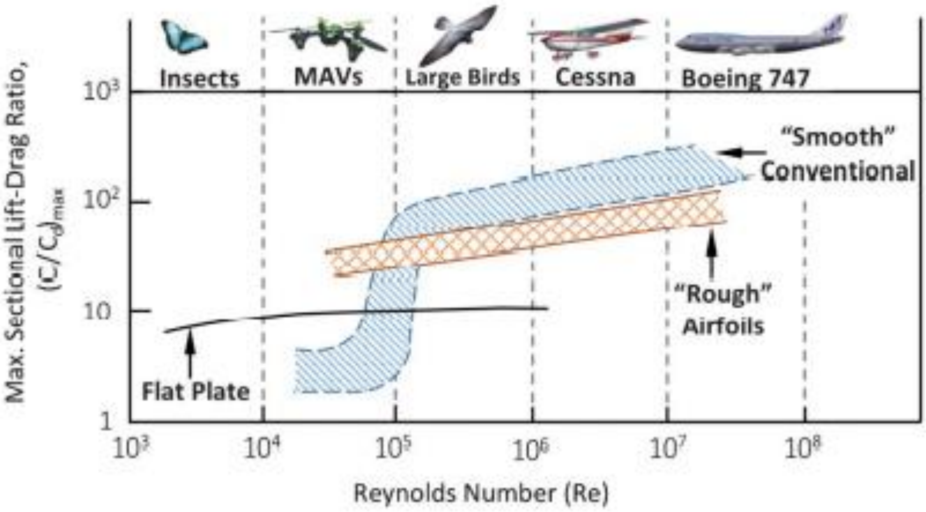

FIG. IV.12 Effect of Reynolds number on lift-to-drag ratio for conventional wing profiles (Winslow et al. (2018)).

The lift coefficient *Cl* and the drag coefficient *Cd* represent the effects of the boundary layer on lift and on drag and are widely used in the literature to characterize a profile. They are calculated from the Reynolds number and depend on the angle of attack – the angle between the chord of the profile and the flow. A high lift over drag ratio shows that the lift effects are preponderant over the drag effects and is a condition for the high efficiency of the wing. It can be inferred from Fig. IV.12 that, as *Re* in our experiment is between 5x10^5 and 1,6x10^6, the maximal lift-drag ratio might be a few times inferior the one of a real aircraft, whose *Re* can exceed 10^7.

The Mach number is defined by the ratio of the flow speed to the speed of sound. In our case, it varies between 0.1 and 0.2. It is shown in Ahmed et al. (2013) that the effect of the flow on the coefficients Cd and Cl is only important for Mach numbers close to the unity. Thus, no effects of overpressure waves have to be considered.

For Reynolds number between 5x10^5 and 1.6x10^6, the boundary layer might present combined effects of laminar and turbulent flow (Winslow et al. (2018); Guerra-Garcia et al. (2016)). The boundary layer is the fluid in the close vicinity of the wing surface where viscous forces play an important role so that the fluid does not have the same speed that the freestream. This is due to the no-slip condition that imposes the flow velocity at the surface of the wing to be zero. The viscosity effects of the fluid create a thickness of flow close to the surface where the speed is between zero and the freestream velocity. The higher the Reynolds number of the airfoil, the thinner the boundary layer. For relatively low Reynolds number, the flow in the boundary layer is laminar: it can be described as layer of fluids displacing past the adjacent layers with no mixing. There are no eddies nor fluid swirls nor vortex effects. An estimation of the thickness of the laminar boundary layer δ is given according to the Blasius solution for a plate surface without roughness considerations (Schlichting (1979)):

$$\delta(x) \cong 5\frac{x}{\sqrt{Re}} \tag{IV.2}$$

Where x is the position of the surface in the axis of the flow direction. For our values, this thickness varies between 0.7 and 3 mm. (Thus, it is not able to affect considerably the arc column that has a length of few tens of cm but might affect the displacement of the arc roots, especially on the sheath electrode region where the net charge equilibrium is not respected. Indeed, Yang and Heberlein (2007) shows that the sheath thickness might reach a several hundreds of µm for an electric arc blown by airflow in a plasma torch configuration). For previous theoretical work of the swept-stroke phenomenon, most of the papers consider a laminar flow defined by the Blasius boundary layer profile (Larsson et al. (2000); Lago et al. (2005); Chemartin et al. (2012)).

However, for our range of Reynolds number and for our geometry, there is a coexistence of laminar flow and turbulent flow: the boundary layer is characterized by unsteady swirling flows inside the layer. An estimation of the thickness of the turbulent boundary layer is given for a plate surface without roughness considerations (Schlichting (1979)):

$$\delta(x) \cong 0.37 \frac{x}{Re^{\frac{1}{5}}} \quad \text{(IV.3)}$$

For our values, this thickness varies between 4 and 10 mm at the trailing edge. The repartition of the laminar boundary and the turbulent boundary layer over the surface of the profile depends on the angle of attack. The transition from laminar to turbulent flow is likely to take place with the formation of a laminar separation bubble: as laminar flow over the leading edge of the wing is subjected to a strong adverse pressure gradient, the flow separates as a shear layer between the free-stream with high kinetic energy and the laminar flow with low kinetic energy. This shear layer is sensible to disturbances and gains momentum from the free-stream layer. For high Reynolds numbers and low angles of attacks, it reattaches on the surface as a turbulent boundary layer thus creating a laminar separation bubble (Abbott and Von Doenhoff (1959); Al Mutairi et al. (2017)). A schema of this process is represented in Fig. IV.13. The turbulent boundary layer is not affected by such a separation process because it gets enough energy from the free stream (Winslow et al. (2018)).

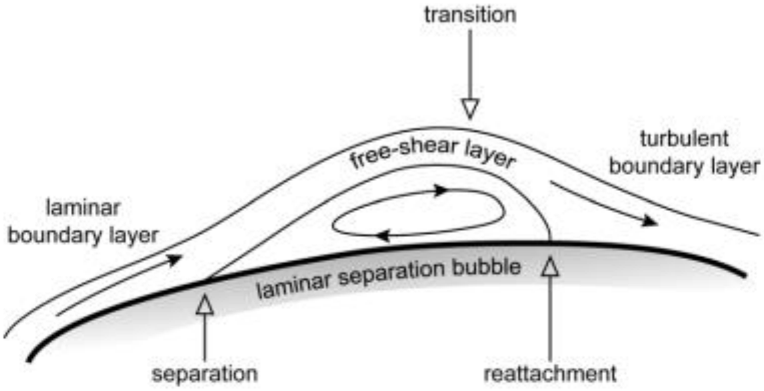

FIG. IV.13 Flow structure in a laminar separation bubble (Uranga (2011)).

For higher angles of attack, the separation point goes along the surface of the wing: the bubble decreases in size until it bursts and separates, provoking the rising of the drag and the dropping of the lift and thus the airfoil stall. This effect of stall has been widely studied (McCullough et al. (1951); Jones (1933); Gault (1949); Gaster (1969) Wong and Rinoie (2009)) but the size of the bubble is still difficult to predict (Al Mutairi (2017)). In the simulations of Guerra-Garcia et al. (2016), whereas a lightning restrike was not predicted for the considerations of a laminar boundary layer nor a turbulent boundary layer, the presence of a reattachment location was made possible by the introduction of a laminar recirculation bubble.

For our experiment, an attempt to visualize the flow along the projectile in the Railgun experiment has been conducted resorting to smoke flow visualization techniques. A sequence of photos of the smoke flow perturbation due to the passage of the projectile is represented in Fig. IV.14. The smoke comes from burning incense sticks. The speed of the projectile is 60 m/s and the chord of the projectile is 200 mm.

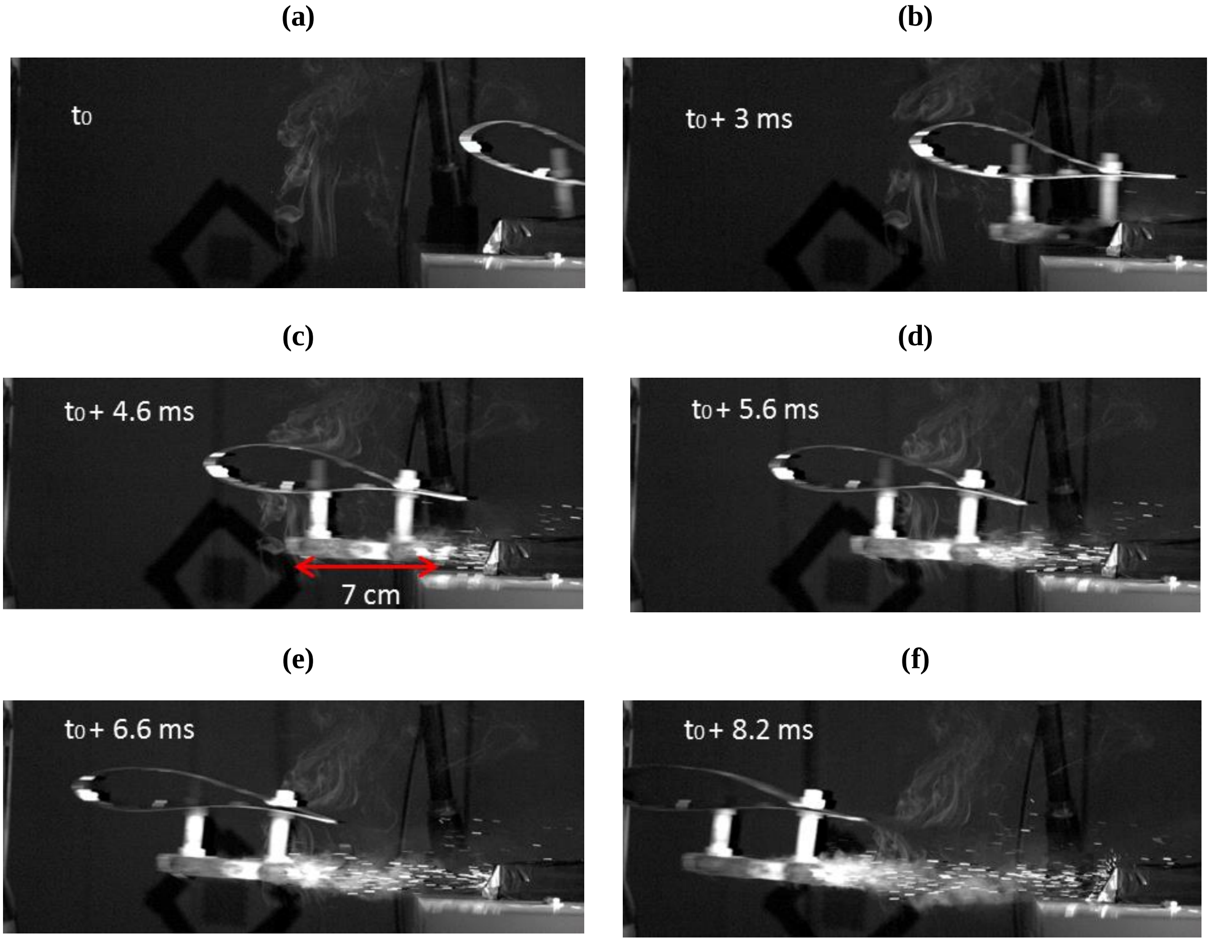

FIG. IV.14 Successive images of smoke flow for the Railgun experiment.

It can be seen that the smoke seems to fit the shape of the test sample and no evidence of perturbations are visible. However the visualization technique might appear a bit rustic and more sophisticated techniques could be considered for future works.

This short analysis of the airflow profile for our experience shows that the flow streamlines around the test sample are theoretically subject to turbulences even if the current experimental setup does not enable to characterize it. These turbulences address two problems: as the thickness of the laminar and turbulent layers are higher than the arc root sheath dimension, these airflow perturbations might affect the physical processes occurring in the sheath and therefore might have an impact on the displacement of the arc roots. The other problem is the representativeness of the experiment: as these perturbations magnitude highly depends on the test sample geometry, their impact might be exacerbated or underestimated in our experiments comparing to the in-flight swept-stroke conditions. In addition, in our experiments, the angle of attack cannot be controlled despite it has a dramatic effect on the magnitude of the flow perturbations.

D. Experimental set-up

The swept-stroke phenomenon is visualized by two high speed cameras (HSC). The HSC are the same than the model presented in Chapter II (II.V.B) Phantom V711 from Vision Research (CMOS sensor of 1280 × 800 pixels of 20 μm^2). One camera is positioned perpendicular to the axis of the projectile movement in the case of Railgun experiment and perpendicular to the flow direction in the wind tunnel experiment and is adjusted at the height of the sample. This enables to access to a 2-D visualization of the arc displacement in the axis of the relative movement. This camera is used for the measurements that are presented in this chapter and in the Chapter V. However, the relative movement of the arc root is not entirely straight forward as it was proved by the left tracks that were not always entirely parallel to the axis of relative motion. Thus, a second camera is positioned forming an angle of 45° with the direction of projectile motion or the airflow. This camera is elevated above the height of the plan where the test sample is struck down by the electric arc in order to give additional information about the 3D elongation of the arc. The set-up is represented in Fig. IV.15.

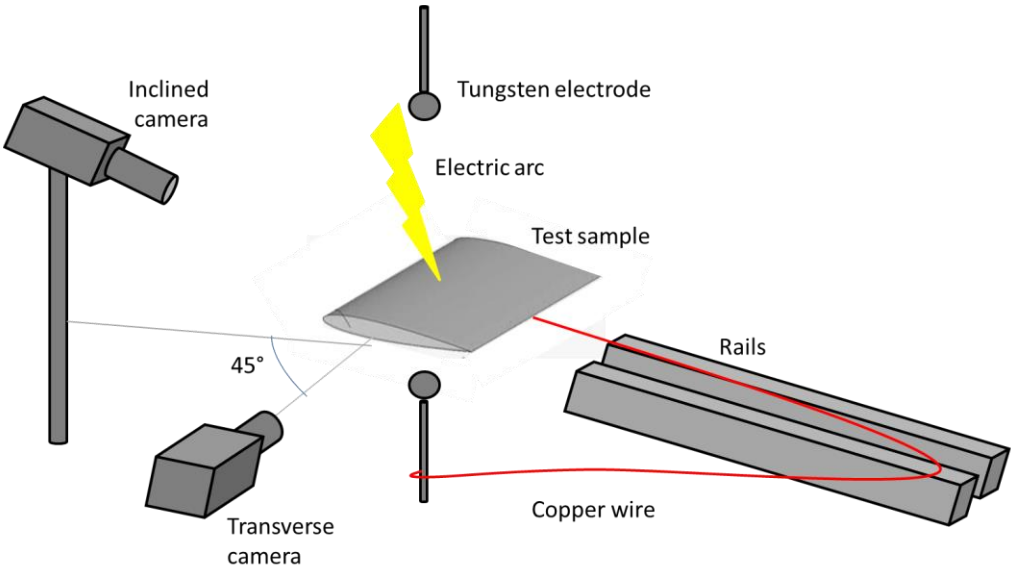

FIG. IV.15 Schematic of the set-up with the two cameras – a transverse camera and an inclined camera.

In the Railgun experiment, the perpendicular camera was positioned to capture images composed of 704 x 160 pixels with a ratio of 1mm/pixel. The interval between two pictures is 17.53 μs. In the wind tunnel experiment, the perpendicular camera was positioned to capture images composed of 512 x 200 pixels with a ratio of 0.833 mm/pixel. The interval between two pictures is 15.87 μs. The second camera presents an inclined visualization of the phenomenon: it is thus not scaled and only provides qualitative information. The interval between two pictures is 30.29 µs and so almost two times slower than the perpendicular camera. The two cameras are synchronized and enable to have an approximate 3D representation of the arc elongation.

It is important to mention that the test samples were cleaned with acetone before every swept-stroke experiment in order to withdraw any oxide layer. Indeed, as it will be discussed more specifically in Chapter V, the presence of a thin oxide layer is able to affect the arc root attachment on the sample.

E. Presentation of the test matrix

The aim of this work is to establish an experimental database for the swept-stroke and to understand the influence of the dataset parameters. The objective is to analyse the effects of arc current, the relative speed between the electric arc and the test sample, the distance between the electrodes, length of the sample, the polarity of the test sample and finally the relative motion system (Railgun or or Wind tunnel facilities). In order to cover all of these parameters, two test matrices were designed – one for the Railgun facility and one for the wind tunnel equipment – and are given in Table IV.1 and Table IV.2.

TABLE IV.1 test matrix for experiments with Railgun facility.

Shot n°	Sample length (mm)	Arc intensity (A)	Polarity	Speed of the projectile (m/s)	Inter-electrode distance (mm)
1	200	400	cathodic	55	200
2	200	400	cathodic	51	200
3	200	400	cathodic	50	200
4	200	400	anodic	57	200
5	200	400	anodic	52	200
6	200	400	cathodic	43	200
7	200	400	cathodic	42	200
8	200	400	anodic	38	200
9	400	400	anodic	45	200
10	400	400	cathodic	37	200
11	400	400	cathodic	36.5	200
12	400	400	anodic	37	200
13	200	400	anodic	35.5	200
14	200	200	cathodic	46	200
15	200	200	cathodic	49	200
16	200	200	anodic	54	200
17	200	200	anodic	52.5	200
18	200	600	cathodic	40	200
19	200	600	cathodic	50	200
20	200	600	anodic	50	200
21	200	600	anodic	54.5	200
22	200	400	cathodic	47	400
23	200	400	anodic	54	400
24	200	400	cathodic	49	200
25	200	400	cathodic	43	200

TABLE IV.2 test matrix for experiments with wind tunnel equipment.

Shot n°	Sample length (mm)	Arc intensity (A)	Polarity	Airflow velocity (m/s)
1	200	400	cathodic	60
2	200	400	cathodic	60
3	200	400	anodic	60
4	200	400	anodic	60
5	200	400	cathodic	40
6	200	400	cathodic	40
7	200	400	anodic	40
8	200	400	anodic	40
9	400	400	cathodic	40
10	400	400	cathodic	60
11	400	400	anodic	40
12	400	400	anodic	60
13	200	200	cathodic	60
14	200	200	cathodic	60
15	200	200	anodic	60
16	200	200	anodic	60
17	200	600	cathodic	60
18	200	600	cathodic	60
19	200	600	anodic	60
20	200	600	anodic	60
21	400	400	cathodic	60
22	400	400	cathodic	40

IV.2 Hydrodynamic and electric description of the arc column

This section aims to give a description of the hydrodynamic and electric behavior of the arc channel depending on the input parameters presented in the test matrix tables IV.1 and IV.2. It is thought that the restrike of an electric arc on a surface is mainly driven by a reduction of its arc voltage for energy minimization (Tholin et al. (2013)). As presented in Chapter II (Sec. II.1), the commonly accepted electrical equivalent model for a 400 A electric arc is a linear resistor so that the study of the spatial behavior and extension of the electric arc column gives direct information about its energy. Another point of discussion is the relative position with the arc channel and the test sample: if the electric arc is bent forward on the test sample due to hydrodynamic effects, the distance between a point of high potential of the column and the test sample is reduced. Thus, it helps the formation of a new electric arc as described in Tholin et al. (2013). The specific interaction of the electric arc and the test sample and the study of the impact area will be discussed in details in Chapter V. For the rest of the work, the abbreviation RGE and WTE will be used respectively for Railgun experiment and Wind tunnel experiment

A. Global description of arc hydrodynamic and electric behaviors for Railgun experiment

A.1 Global description of arc elongation

During the experiment, the electric arc hydrodynamic and electric behaviors are governed by different phases:

- The ignition phase: the arc is formed by the melting of a thin copper of wire producing a plasma column that will sustain the discharge. In this phase, the current is increasing fast and the arc voltage has a peak corresponding to the melting of the wire as described in chapter II. This is visible that the light emitted is becoming brighter corresponding to the hot plasma column formation.

- The static phase: the electric discharge is stable between the two static tungsten electrodes separated by 350 mm. Despite the distance between the two electrodes is constant, the length of the electric arc changes continuously due to the formation of current loops as a consequence of magnetic effects and due to thermal convection. These magnetic loops are increasing with time. However, the formation of new loops is compensated by the extinction of old loops so that the arc voltage remains globally constant.

- The swept-stroke phase: the test sample crosses the electric arc. This last reattaches on the test sample that is connected to the lower electrode by a copper wire thus bypassing the lower arc channel as discussed in Sec. IV.1. The extinction of the lower arc channel whose length is approximatively 100 mm provokes a voltage drop of several 100 V that is observed on the arc voltage measurement. Then, as one arc root is sticking on the upper motionless electrode and the other arc root is involved into complex processes of dwelling and reattachment on the moving test sample, the electric arc is globally elongated. Multiple arc extinctions and arc formations occur due to magnetic loops effects or to the reattachment of electric arc root on the test sample. This might provoke punctual and sudden voltage drops. The global elongation of the arc during this phase generates the global increase of arc voltage despite the occurrence of some measured abrupt and marked voltage drops. Three main reasons can end up this elongation phase:

- The current regulation overpasses the limit duration imposed on the lightning arc generator.
- The arc channel is so long that its voltage overpasses the capacitor voltage of the lightning generator.
- The arc manages to reattach on the initial motionless lower tungsten electrode

In most of the cases, the arc regulation stops after the test sample has passed the field of vision of the cameras – 700 mm in the axis of projectile displacement. Thus, it is important to notice that the successive reattachments of the arc channel on the test sample occur when the current is regulated and so representative of a lightning current as set by the norm.

- Arc reattachment phase: ultimately, an arc reattachment on the initial motionless lower tungsten electrode might occur. This phase only happens in case that the copper wire connecting the sample and the lower electrode is torn due to the extreme mechanical constraint exerted by the sample acceleration, thus creating an electric arc to maintain the electric discharge. This secondary electric arc offers a secondary electric path to the electrode so that the arc sweeping on the test sample bypasses this sample and reattaches on the secondary arc. The electric arc is reformed between the two tungsten electrodes. However the channel of this arc is situated out of the straight line between the two electrodes because it was carried out from there by the projectile. It is then observed that the arc channel is moving backward to the inter-electrode line position by successive reattachments. An example of arc reattachment after the swept stroke phase is represented in Fig. IV.16. In Fig. IV.16(a), the electric arc is sweeping on the test sample. In Fig. IV.16(b), a secondary electric arc is forming at the location where the copper of wire is screwed on the test sample, meaning that this last was pulled out. This arc is extending in Fig. IV.16(c) and reattaches the former arc channel in Fig. IV.16(d) whereas the test sample is pursuing its movement without any arc interaction. It can be observed that resulting electric arc whose shape is not straight. It is important to mention that this kind of ultimate arc reattachment only occurred for few experiments and in this case, only the part with swept-stroke – without the coexistence of the two arc channels – is exploited for the latter measurements.

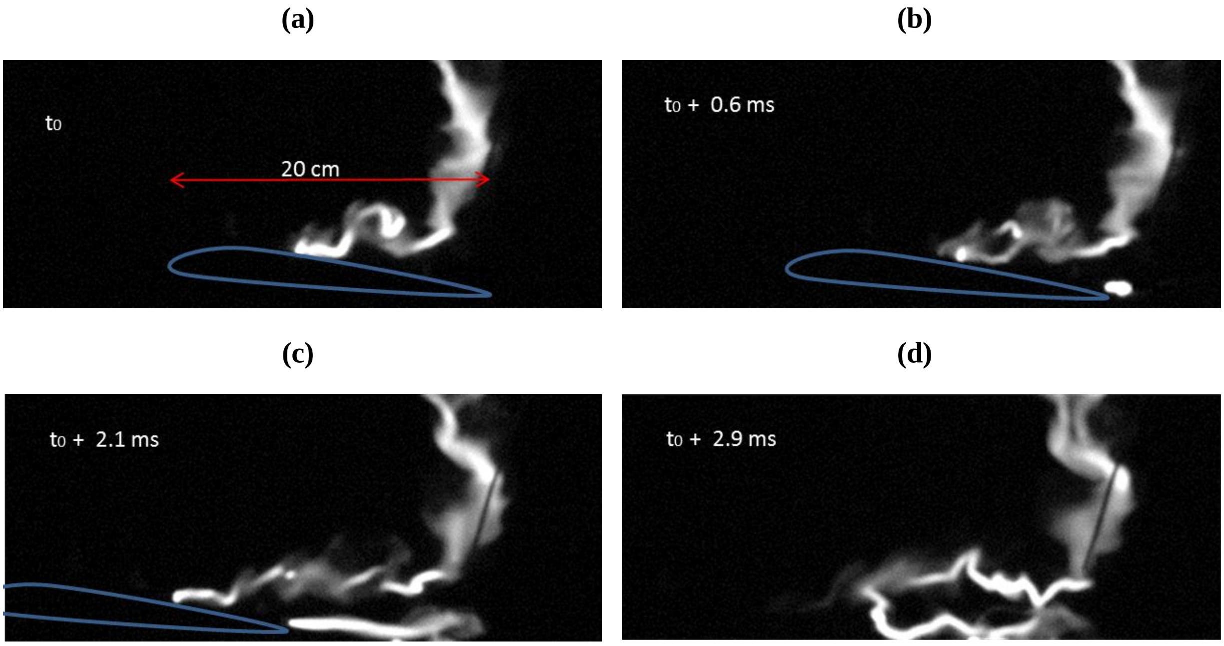

FIG. IV.16 Successive images of an arc reattachment after swept stroke. The arc intensity is 400 A and the sample speed is 50 m/s.

- Arc extinction phase: At the end of the regulation - 50 ms - or when the arc voltage overpasses the lightning generator supply capacitors voltage, the current in the arc channel is slowly dropping and its light emission is fading away. The arc voltage remains to a constant value: the voltage measured between the electrodes does not correspond anymore to the arc channel voltage but to the capacitors remaining voltage.

The different phases mentioned above are illustrated in the measured arc voltage waveform and presented in Fig. IV.17. The ignition phase lasts from 0 to 4.6 ms and is recognizable with its high voltage peak reaching 1950 V occurring at 4.1 ms. The static phase lasts from 4.6 to 17.6 ms and is characterized by a smooth voltage time variation of 100 V around a mean value of 650 V. At 17.6 ms, an abrupt and marked voltage drop of 200 V occurs and corresponds to the first attachment of the electric on the material test sample. Then the swept-stroke phase lasts from 17.6 to 40 ms and is characterized by a mean voltage increase from 380 to 1650 volts with a saw-tooth shape evolution. After 40 ms, the capacitors cannot provide enough power anymore to maintain the 400 A current regulation.

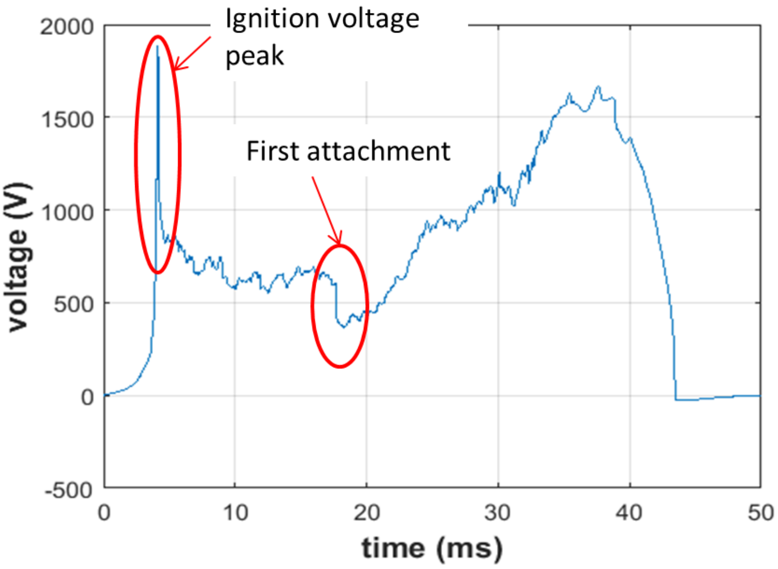

FIG. IV.17 Arc voltage waveform for a case without final arc detachment. After first attachment on the test sample, the electric arc is elongated to ensure the connection with the moving test sample and the fixed tungsten electrode until its voltage exceeds the power supply voltage.

Figure IV.18 also represents an arc voltage waveform but with an ultimate detachment of the arc from the test sample and a reattachment to the initial electrode of tungsten. The ignition phase lasts from 0 to 12.5 ms and is recognizable with its high voltage peak reaching 1600 V occurring at 11.7 ms. The static phase lasts from 11.7 to 14.8 ms and is characterized by a smooth voltage time variation of 100 V around a mean value of 600 V. At 14.8 ms, an abrupt and marked voltage drop of 175 V occurs and corresponds to the first attachment of the electric on the material test sample. Then the swept-stroke phase lasts from 14.8 to 20 ms and is characterized by a mean voltage increase from 440 to 1140 volts with an evolution in saw-tooth shape. Then the electric detaches from the test sample and a reattachment to the initial tungsten electrode occurs. The voltage waveform then varies dramatically with successive phases of saw tooth surge – up to 600 V - and abrupt drops – up to 600 V in less than 400 µs. Then the voltage returns to a mean value of 600 V that it was presenting in the static phase. This is in accordance with the fact that the arc has moved back in the space line between the two tungsten electrodes. Then, at 40 ms, the capacitors cannot provide enough power anymore to maintain the 400 A current regulation.

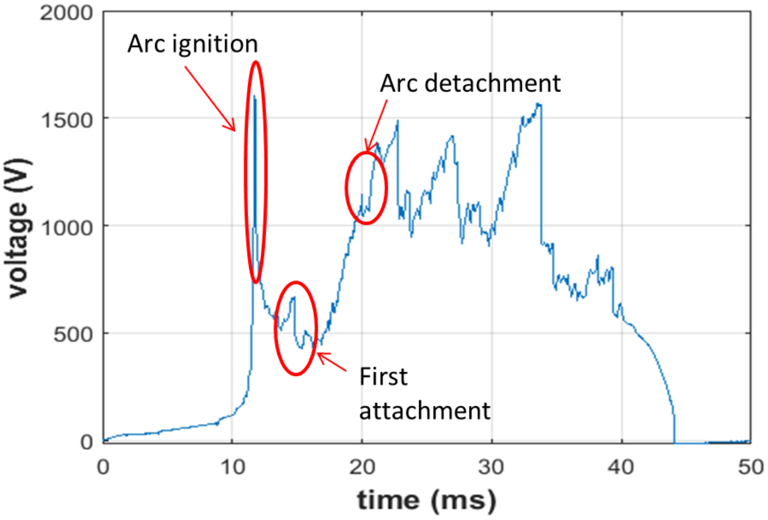

FIG. IV.18 Arc voltage waveform for a case with final arc detachment.

In addition to the global elongation of the electric arc, it is interesting to note few geometric particularities of the arc column that enable to understand the dynamic of the swept-stroke.

Column inclination:

When the arc attaches the test sample, the part of the arc channel near the attachment is extended obliquely as the projectile is displacing on a direction perpendicular to the arc column thus forming an angle between the projectile and the extended channel. The part of the arc channel near the motionless upper tungsten electrode seems to remain undisturbed by the relative motion happening at the other extremity of the channel. Indeed, an important part of the electric arc remains in the initial inter-electrode space line and is just deformed by the magnetic loops. This separation of two hydrodynamic behaviors of the arc column is represented in Fig. IV.19, the inter-electrode distance is 400 mm.

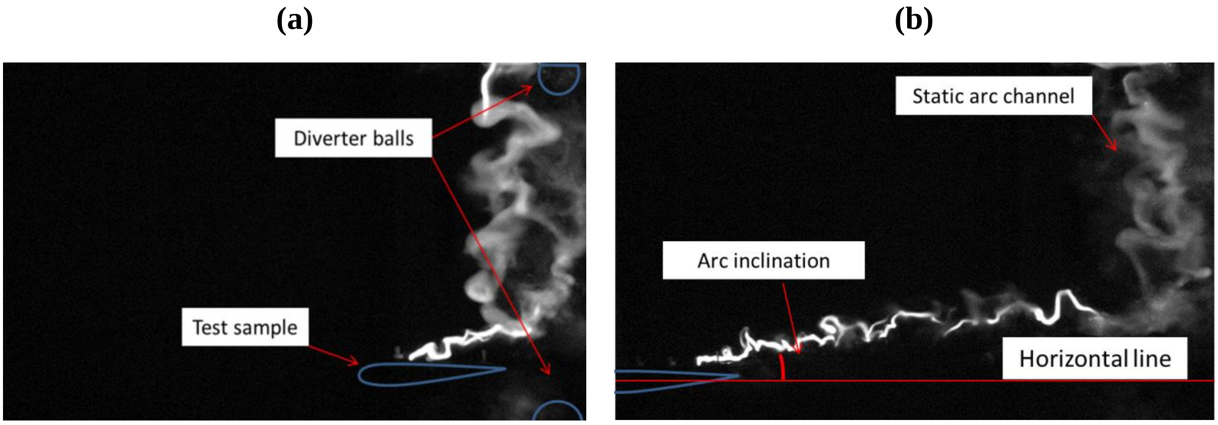

FIG. IV.19 Inclination of arc channel during swept-stroke. The arc channel forms an inclination angle with the test sample trajectory axis.

Depending on the experimental settings, the sizes of the inclined arc channel and the static channel differ. However, as the arc inclination changes during the projectile movement, this quantity was complicated to define. For the following discussion, a relative comparison of arc inclination for several experiments will be developed.

Magnetic loops:

As evoked before, the current flowing through the arc channel provokes a Lorentz force that creates loops that divert the arc channel shape from a straight line. This phenomenon will be mainly discussed in the subsection of this chapter about the effects of current.

Voltage slope measurement:

A good indicator of the arc extension might be the voltage slope (dU/dt) measured during the swept-stroke phase. Indeed, it is supposed to be proportional to the length of the arc channel that is complicated to estimate only with the images from two cameras, even if 3D reconstruction could be considered but would require complex processing. Thus, the evolution of the arc voltage is the image of the evolution of arc length. For this reason the voltage slope is measured from the arc voltage waveform for the swept-stroke phase and is chosen as a criterion to be discussed in this analysis. The voltage slope is defined as the slope between the first attachment and the arc detachment voltage or the end of the swept-stroke phase and is measured directly from the arc voltage waveforms. For all the experiments with Railgun facility, the voltage slope is measured from the first reattachment on the test sample and it is observed that the corresponding starting voltage is around 500 – 600 V independently from the current level. This observation is in good agreement with the experimental results of King (1961), Tanaka et al. (2000) and Sunabe and Inaba (1990) that states that for our range of current, the inner arc column electric field do not vary with the current: so for a same initial inter-electrode distance, it is expected to measure a similar initial voltage level.

Then, the voltage rises and might reach different level for different experimental set-up. As our cameras did not covered the entire trajectory of the projectile for temporal and spatial image resolution issues, only a part of the swept-stroke is recorded whereas the measured voltage waveform corresponds to the arc voltage during all its lifetime from its ignition to its extinction. However, the arc behavior is difficult to predict out of the cameras viewing fields and the arc voltage variation measured then can be the effect of arc detachment or the abrupt stop of the projectile when it hits the sandbox. In these cases, the arc behavior cannot be checked with direct camera visualization for all the arc lifetime, the voltage slope is defined from the instant of first reattachment to the instant when the projectile exits the cameras viewing fields.

However, it also occurs that the arc detaches the test sample before it exits the cameras viewing fields and somehow reconnects as discussed before. In this case, the voltage slope is defined from the instant of first reattachment to the instant when the electric detaches the test sample.

The different voltage slopes for a same configuration of arc root polarity, current level, test sample speed, sample length and inter-electrode distance are averaged. It is important to note that several experiments of the same configuration do not necessarily present the same magnitude of maximum voltage level for the swept-stroke, mainly because of the possibility of reattachment before the projectile exits the cameras viewing fields. Thus, it is chosen to only compare the arc voltage slope with the evoked criteria and not to compare the maximum voltage reached during for swept-stroke phase. An example showing this inhomogeneity of maximum voltage for two experiments with a given configuration is presented in Fig. IV.20. The configuration for these tests are: an anodic arc root, an arc current of 200 A, a mean speed of 53 m/s, a test sample of 200 mm length and an initial inter-electrodes distance of 200 mm.

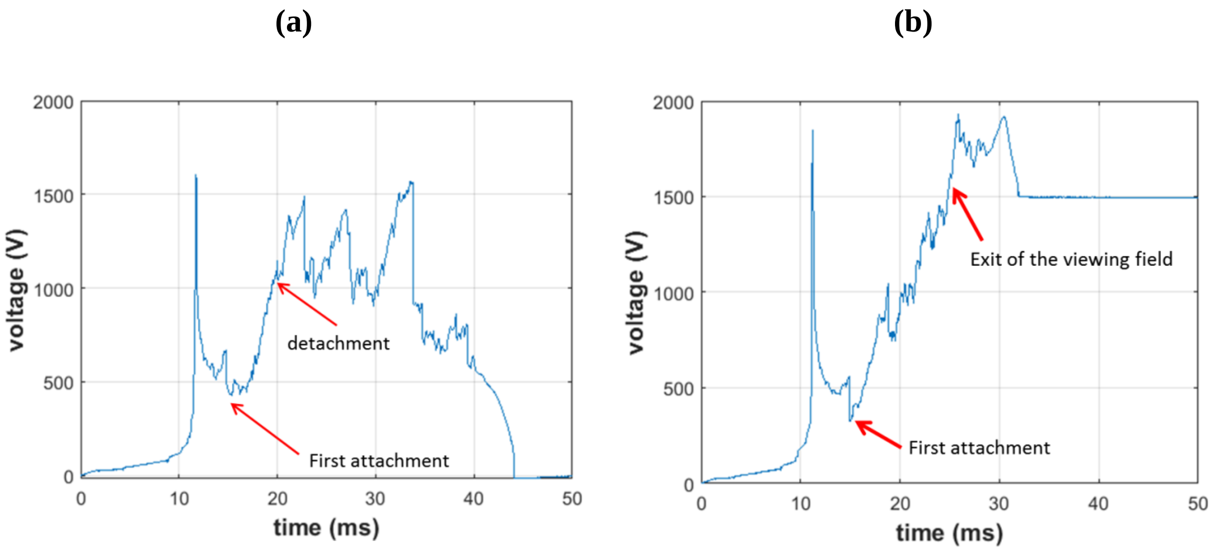

Initial swept-stroke voltage (V)	Final swept-stroke voltage (V)	Arc voltage slope (V/ms)
423	1082	150

Initial swept-stroke voltage (V)	Final swept-stroke voltage (V)	Arc voltage slope (V/ms)
324	1595	124

FIG. IV.20 Voltage characteristics for two swept-stroke experiments with the same configuration and presenting a detachment (a) or no detachment (b).

The chosen layout to represent the results of voltage slope and other quantities in a box of a table takes the following form: 0.9<**2.2**<3.5. The value in blue on the left represents the smallest value reported when gathering all the values measured for a given quantity with given initial conditions. The value in bold and black in the middle represents the mean value of a given quantity after the averaging of the corresponding mean values reported for the experiments with the same given initial conditions. The value in orange on the right represents the highest value reported when gathering all the values measured for a given quantity with given initial conditions. As the number of experiments for a given configuration varies from one to maximum four, it was chosen to only present the minimum value, the average and the maximum value of each quantity and not the dispersion or the standard deviation of the results in order not to encumber the results presentation. Anyway, the comparison of the average with the extreme values provides a good idea of the data dispersion for our small number of repetitions.

A.2 Effect of polarity on the arc column elongation

As will be discussed in Chapter V, the polarity is an important factor to explain the different observations of the interaction between the test sample and the arc column. The polarity is a key factor to understand the arc channel formation and extinction near the electrodes. However, even if these reattachments might provoke dramatic arc voltage drops and are responsible for the saw tooth pattern of the arc voltage waveform, it is possible that they do not affect the global hydrodynamic extension of the electric arc channel.

Table IV.3 summarizes the mean slope of the arc voltage waveform during the swept-stroke phase for experiments with a moving cathodic arc root and with an anodic arc root. The projectile velocities are between 45 and 55 m/s. The results are compared for different arc currents.

Table IV.3 Mean slope for cathodic and anodic polarity for RGE.

Current level (A)	**Arc voltage slope for moving cathodic arc root (V/ms)**	**Arc voltage slope for moving anodic arc root (V/ms)**	**Difference (%)**
200	97<**114**<131	124<**137**<150	17
400	73<**78**<87	77<**85**<94	8
600	31<**45**<59	62<**63**<64	29

Despite that these values are averaged over only two and sometimes three experiments, the measured voltage slopes differs from 8 to 29 % at maximum depending on the settings. This means that the mechanisms governing the arc channel hydrodynamic extension are similar whether the cathodic or the anodic arc root is moving. However the systematic higher values of arc voltage slope for moving anodic arc roots can be interpreted by the difference of inclination angle between the arc column and the direction of test sample motion in this case. Indeed it is observed on the recorded videos that the cathodic arc root presents a strong jet that prevents the arc column from bending down on the test sample surface thus maintaining a relatively high angle between the arc column and the direction of projectile movement. This jet is weaker for the anodic arc root and the column is bending down on the test sample. Moreover, it is visible that the cathodic arc root dwells more time in average than the anodic arc root before extinction and formation of a new arc root, and consequently this inclination is more marked. Figure IV.21 presents this marked difference of arc inclination for an initial inter-electrode distance of 400 mm and an arc current regulation of 400 A.

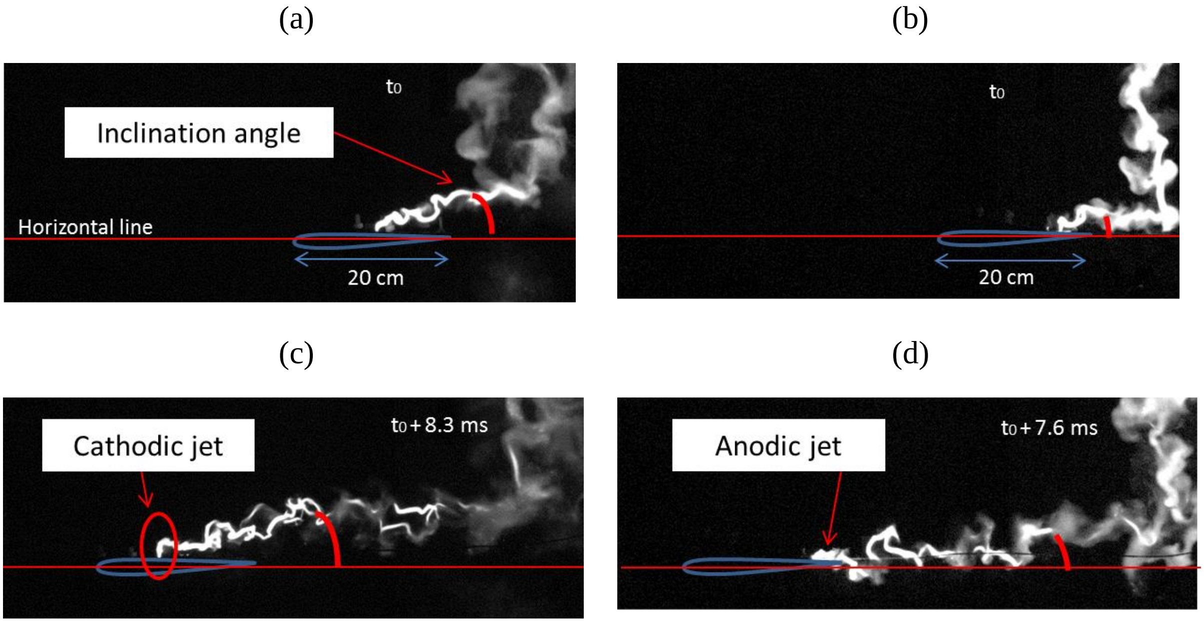

FIG. IV.21 Different inclinations angles for moving cathodic arc root at the debut (a) and the end (c) of the swept stroke phase, and for moving anodic arc root at the debut (b) and the end (d) of the swept-stroke phase. It is visible that the inclination angle between the arc channel and the horizontal line is more marked for the moving cathodic arc root. The stiffness of the cathodic jet is also observable.

In the moving cathodic arc root, it can be observed that, as the arc inclination is relatively high, the arc channel is globally bending to ensure the arc connection to the test sample - as if the mechanical constraint exerted by the arc root on the channel was distributed on the entire channel. On the contrary, in the moving anodic arc root, the arc channel is not bending and rather presents a right angle between a motionless arc column and a column increasing in the same direction that the axis of projectile movement – as if only a restrained part of the column were supporting the arc root constraint. Thus, on the cathodic arc root, it is observed that as the entire arc channel is moving, the formation and extension of the arc column is less necessary to ensure the arc maintenance. On the anodic one, the maintenance of the arc is ensured by the formation and the extension of the arc column in the same direction than the axis of projectile movement so that its voltage slope needs to be higher in average – meaning that arc column is extending faster. A 3D reconstitution of the arc channel would enable to measure the absolute arc elongations to better quantify the differences between the two observed modes of elongation.

A.3 Effect of the sample speed on the arc column elongation

It is intuitive to expect that the speed of the sample has a direct influence on the hydrodynamic mechanisms of the arc expansion: the faster the relative motion between the sample and the arc column, the faster the arc extension. Table IV.4 presents the arc voltage slope for the arc column during the swept stroke phase for different speeds of the test sample. The results are averaged for moving cathodic and anodic arc roots with an arc current regulation of 400 A for both speeds.

Table IV.4 Mean slope for two relative speeds for RGE.

Speed of test sample (m/s)	**Arc voltage slope (V/ms)**
0	0
42±4	31<**40**<57
53±4	73<**81**<94

The first line is inferred from our previous study of static arc channels in Chapter II: it was observed that for a static arc channel – without any exterior perturbation as the arrival of a projectile or a consequent airflow – the voltage reaches a quite stable level after few ms even if some variations of amplitude – roughly ± 100 V still occur. Thus the average voltage slope in this case is zero.

It can be noticed that the arc voltage slope is not proportional to the speed of the test sample. Indeed, as the current is the same for the two speeds and if the assumption of a similar arc linear resistance is made, the arc voltage slope must be directly proportional to the rate of arc column extension – distance of arc channel produced over time in the elongation process, as set by Eq. (IV.4).

$$\frac{\Delta l}{\Delta t} = \frac{\Delta U}{rI\Delta t} = C\frac{\Delta U}{\Delta t} \tag{IV.4}$$

Where l is the length of arc column, t is the time, U is the voltage, r is the arc linear resistance, I is the current and C is a constant for a given current. Thus, as the rate of arc column extension is proportional to the voltage slope and as the voltage slope is not proportional to the test sample speed, it can be inferred that the rate of arc column extension is not proportional to the speed of test sample. Even if three points are not enough to give a tendency, the speed of test sample has a dramatic influence on the arc voltage slope and so on the rate of arc column expansion since an increase of 20% of the speed provokes an increase of 50 % of dU/dt for the given velocities. However, Eq. (IV.4) is limited because it supposes that the arc linear resistance is constant for a given arc current which has to be verified for an arc column set into motion.

Moreover, at low speed – 40 m/s – the difference of arc voltage evolution and arc behavior during the swept-stroke is more marked between the cathodic and the anodic polarities. Indeed, whereas no strong difference can be inferred from the voltage waveforms of cathodic and anodic polarities at 53 m/s – the two polarities presenting a quite regular voltage slope during the entire swept-stroke – at 40 m/s, the cathodic polarity presents a regular voltage slope during the swept-stroke whereas the anodic polarity presents a voltage plateau before starting to increase. Those differences can be observed in Fig. IV.22.

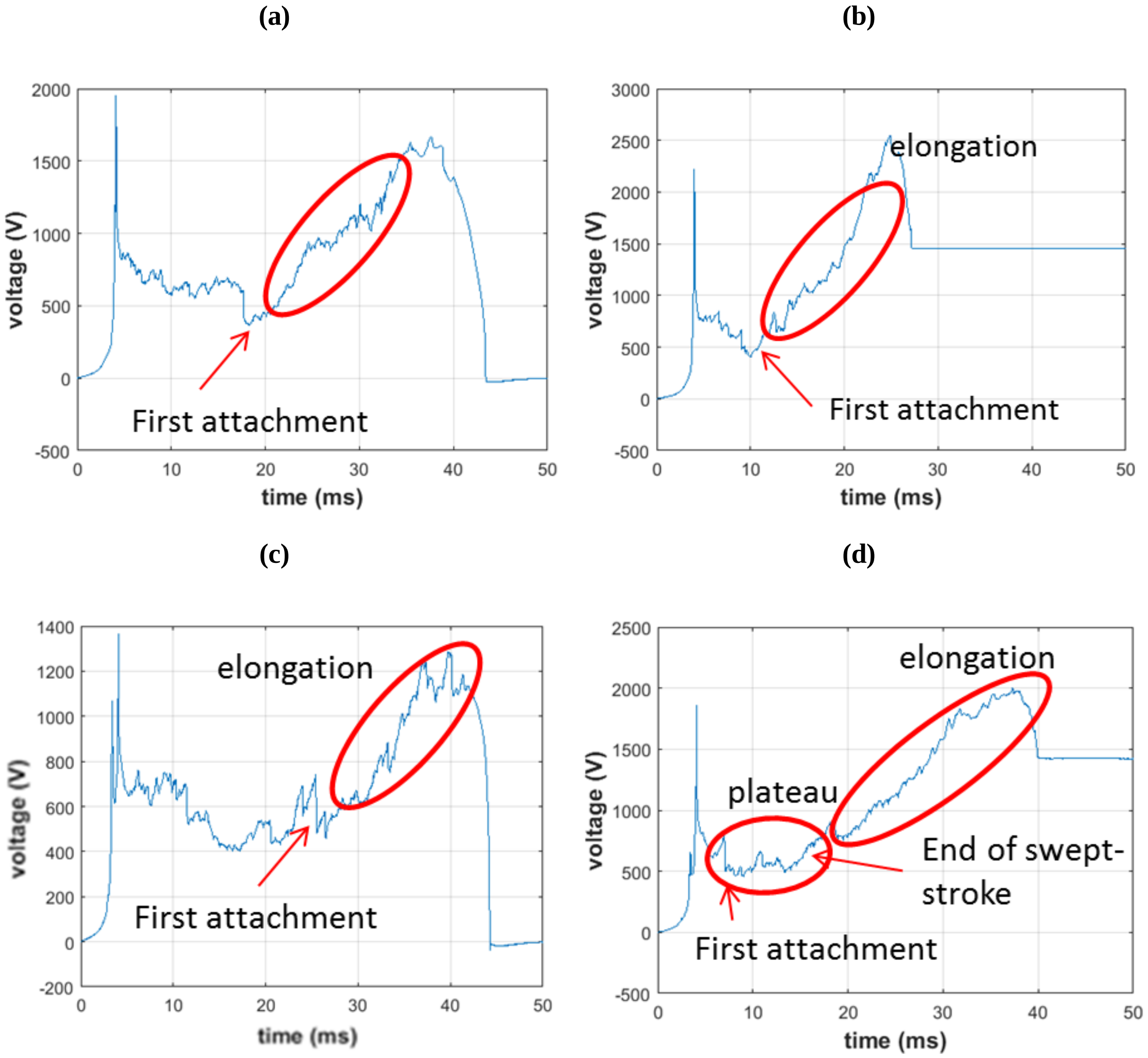

Fig. IV.22 Differences of arc voltage evolution during swept-stroke for different speeds and polarities conditions: 50 m/s and cathodic (a) 52 m/s and anodic (b) 42 m/s and cathodic (c) 38 m/s and anodic (d).

It can be observed with cameras that the plateau observed in Fig. IV.22(d) corresponds to the successive attachments and restrike on the test sample, for the anodic case at 40 m/s. At the end of the plateau - when the voltage starts to increase – the arc attaches the trailing edge of the test sample and the arc is elongated due to the test sample motion. Therefore, no reattachment occurs after the end of the plateau and the swept-stroke phenomenon is over. As the arc voltage is the image of the arc length, it can be inferred that the arc reattachment phenomenon is balancing the arc elongation due to relative motion during the swept-stroke phase. In other words, the arc channel is not globally elongated since the swept-stroke process compensates the arc stretching. This is very interesting since this plateau is not observed for anodic test sample at 53 m/s as shown Fig IV.22(b): the swept-stroke process is not enough to balance the arc stretching and the arc column globally increases in length during the swept-stroke. The cathodic test sample experiments do not present any plateau in their arc voltage waveform: this is mainly due to the arc root different behavior due to more complex physical processes. As it will be discussed in next chapter, the cathodic arc root tends to stick and sweep on the test sample surface so that only few reattachments are observed.

A.4 Effect of current intensity on slope, jet force and magnetic loops

The effects of the intensity on arc voltage slope were observed but not discussed in Table IV.3. Table IV.5 presents the arc voltage slope for the arc column during the swept stroke phase for different arc current regulation. The results are averaged for moving cathodic and anodic arc roots with test sample speed around 53 m/s.

Table IV.5 Mean slope for different currents for RGE.

Current level (A)	**Arc voltage slope (V/ms)**	**Arc Power variation rate (W/s)**
200	97<**125**<150	19<**24**<30
400	73<**81**<94	29<**32**<38
600	31<**56**<73	19<**34**<44

Results show that arc voltage slope for swept-stroke phase is decreasing with the increase of current level. Two main mechanisms can be considered to explain this variation of arc voltage slope:

- The arc resistance varies with the current: according to Sousa-Martins et al. (2016a) and Chemartin (2008) both the electrical conductivity and the diameter of arc channel increase with the current level so that the arc channel resistance decreases with the increase of the arc current.

- According to the measures of King (1961), Tanaka et al. (2000) and Sunabe and Inaba (1990) and the simulation of C-waveform lightning arc of Chemartin (2008), the electric field of the arc channel is independent from the level of arc current. Thus the variation of linear resistance with the current level compensates the variation of current as can be inferred from the following equation:

$$E = r\, I \tag{IV.5}$$

Where E is electric field of the arc channel. Thus, the electric power per unit of arc length, w, is given by:

$$w = E\, I = r\, I^2 \tag{IV.6}$$

The linear electric power is a linear function of current resorting to Eq. (IV.6) and so forming an equivalent length of arc column requires more energy for a 600 A arc channel than for a 200 A arc channel. This is in good agreement with the experimental measurements presented in Table IV.5 : the arc voltage slope and so the extension rate of the arc column decreases with the current – it requires more time for a 600 A arc channel to form a given arc length than from a 200 A channel.
However, the assumption of an electric field that would be independent of the current level is valid for static electric arcs after several ms. Indeed Chemartin (2008) shows that several ms are necessary for the electric arc electric field to stabilize after the arc formation. Thus, it is unsure if this assumption remains verified for an extending and dynamic arc column.

Thus, it is interesting to evaluate the arc power variation rate that represents the variation of arc power during its extension per unit of time and is calculated multiplying the current level to the arc voltage slope. This quantity is thought to be the image of the dynamic of arc power evolution. Table IV.5 shows that the arc power variation rate is almost equivalent for the three current levels even if it is 25% less for arcs of 200 A. This observation tends to demonstrate that the energy processes are one of the main drivers of the arc voltage increase and of the arc spatial extension dynamics since the channel appears to be able to provide a mean given power per unit of time to ensure its spatial extension.

Another visible effect of the arc channel is the formation of magnetic loops: as the current increases, the effect of self-induced Lorentz forces gets more important and provokes the curling of the lightning arc channel. This force is theoretically proportional to the square of the current since the Lorentz force implies the product of the current and the magnetic field – this last being proportional to the current. Figure IV.23 represents this effect for three current levels from the point of view of the inclined camera.

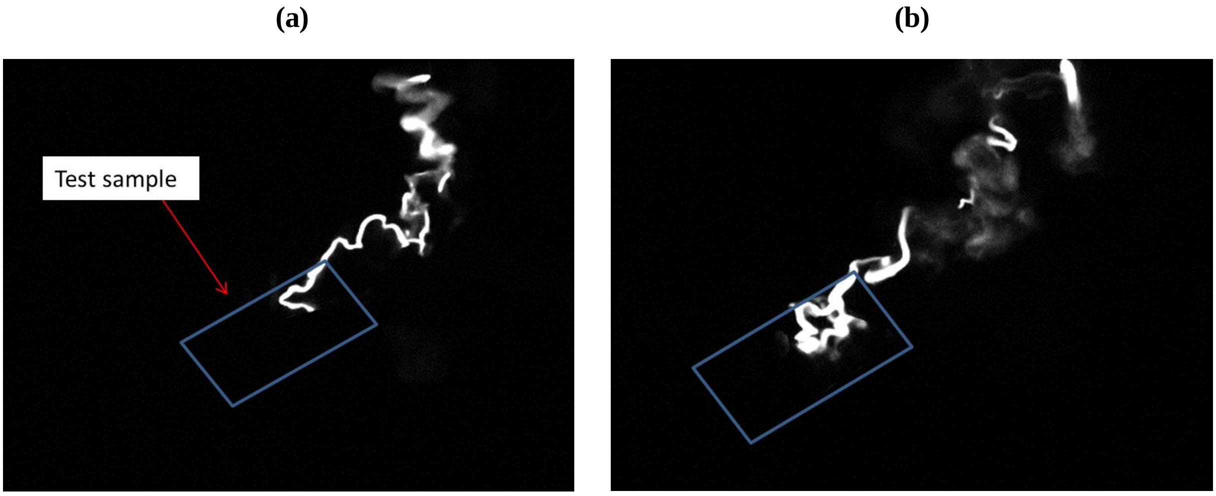

FIG. IV.23 Visualization of arc loops for a 200 A (a) and a 400 A (b) regulation. The inclined camera is positioned to observe the sample movement from a top view.

It can be observed that the arc channel is more straight for a 200 A than for a 400 A arc regulation. This twisting behavior of the arc enhances the probability that a point of the arc channel gets on the surface of the test sample and then to trigger a reattachment. This effect will be discussed in details in Chapter V about the study of reattachment mechanisms.

A.5 Effect of sample length

To ensure the representability of the experiment, the test was conducted for different lengths of test sample. Indeed, for this set of experiments, we suppose that the test sample has sufficient dimensions to be representative of a real aircraft wing. Even if the real aircraft wings are more than 10 times bigger than our test samples, the swept-stroke experiments are conducted expecting that the edge conditions of our test samples do not have a high impact on the physical results. Thus, experiments are led with test samples of lengths 200 and 400 mm to check if the results are similar. Table IV.6 presents the arc voltage slope for the arc column during the swept stroke phase for those different test ample lengths. The results are averaged for moving cathodic and anodic arc roots with test sample speed around 40 m/s and a current arc regulation of 400 A.

Table IV.6 Mean slope for different currents for RGE.

Test sample length (mm)	**Arc voltage slope (V/ms)**
200	31<**40**<57
400	23<**33**<37

It appears that the arc voltage slope and so the arc channel elongation do not differ too much for the two lengths of test sample – 17.5 %. However it is interesting to notice that when the test sample is an anode, a plateau of arc voltage is observed as presented in Fig. IV.24. As discussed in previous section, the swept-stroke occurs during the time of this plateau: at the end of the plateau, the arc attaches the trailing edge of the test sample and cannot reattach another point of the sample anymore. The plateau phase is longer for the test sample of 400 mm since the electric arc has more metallic surface to reattach. As seen in Sec. IV.2.A.3, this plateau appears for anodic polarity of the test sample at 40 m/s but is not marked at 50 m/s. It is thought that at 40 m/s, the electric column resists the arc channel elongation by a reattachment process and that this process is not enough at 50 m/s to prevent the arc channel from being elongated.

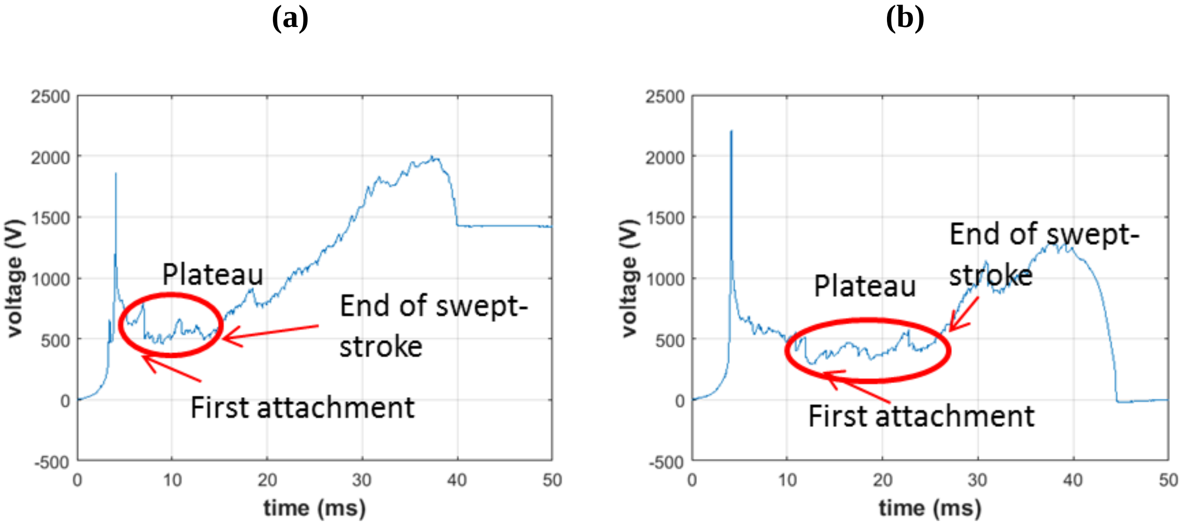

FIG. IV.24 Arc voltage waveform for a test sample of anodic polarity and a length of 200 mm (a) and 400 mm (b) for RGE. The arc current is 400 A.

A.6 Effect of distance inter-electrodes

To ensure the representability of the experiment, the test was conducted for different initial inter-electrode distances. Indeed, for this set of experiments, we suppose that the arc is long enough to ensure that the static arc root on the upper tungsten electrode has no influence on the swept-stroke phenomenon. It is also supposed that a column of 200 mm is representative of a natural lightning arc channel that can be several km long in reality. Thus, if most experiments are conducted for an initial inter-electrode distance of 200 mm, a few experiments are performed with a distance of 400 mm to check if the results are similar. Table IV.7 presents the arc voltage slope for the arc column during the swept stroke phase for different initial inter-electrode distance. The results are averaged for moving cathodic and anodic arc roots with test sample speed around 53 m/s and a current arc regulation of 400 A.

Table IV.7 Mean slope for different initial inter-electrode distance for RGE.

Inter-electrode distance (mm)	**Arc voltage slope (V/ms)**
200	73<**81**<94
400	84<**85**<86

It can be concluded from Table IV.7 that the initial inter-electrode distance does not have an important effect on the arc voltage slope for the same settings. Thus the hydrodynamic extension of the electric arc during swept stroke is not affected by the initial inter-electrode length. However, this assumption might be questioned looking at Fig. IV.25 that presents the arc channel elongation for initial inter-electrode distance of 200 mm and 400 mm for cathodic arc roots.

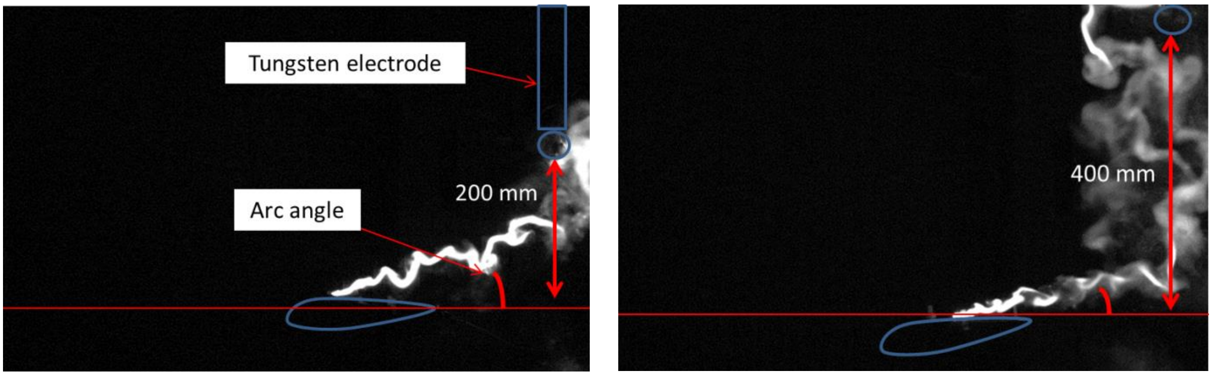
(a)

(b)

FIG. IV.25 Arc channel elongation for initial inter-electrode distance of 200 mm (a) and 400 mm (b). The arc current is 400 A and the test sample speed is around 50 m/s.

It is observed that the arc column angle varies between the two configurations. Thus, the arc inter-electrode distance does have an impact on the arc column extension even if it not visible through the arc slope parameter. As the electric arc is more bending down on the test sample for a higher inter-electrode distance, it facilitates the occurrence of a reattachment.

B. Global description of arc hydrodynamic behavior for Wind tunnel experiment

B.1 Global description of arc elongation

During the experiment, the arc hydrodynamic and electric behaviors are governed by almost the same different phases that for the RGE. However subtle differences appear and are detailed here:

- The ignition phase: the arc is also formed by the melting of a thin copper wire. However, as the wind turbine is activated for the experiment, the wire melting is occurring while being blown by the air flow.

- The static phase: as the arc column is convected from its instant of apparition, it present a flexion and is arcing since its arc roots at its extremities are less affected by the flow than the middle of the column as is represented in Fig. IV.26 Thus the arc channel is not static in this phase. the arc roots are moving in the flow direction so that the arc below crosses the 5 cm that separate the ignition point from the leading edge of the test sample.

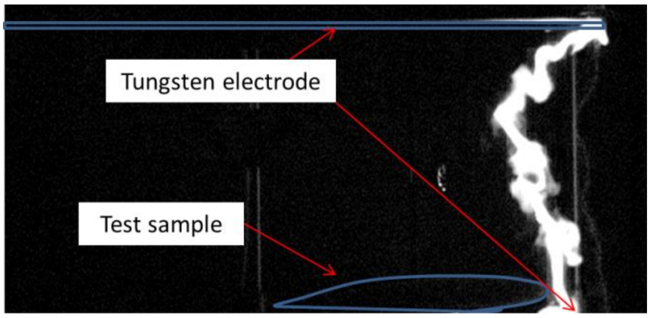

FIG. IV.26 Electric arc after ignition and before first attachment on the test sample.

- The swept-stroke phase: when the arc root first attaches the test sample, the swept-stroke starts. As for the static phase, the arc column seems to be blown by the air flow but the arc roots on the test sample and on the tungsten horizontal electrode are not displacing at the same speed than the column and are lagging behind. Thus the arc column is outpacing the test sample the arc root that moves either by reattachment process or by continuous sweeping. This movement corresponds to the swept-stroke and will be studied in Chapter V.

- Arc elongation phase: when the arc root on the test sample reaches the trailing edge, it cannot go any further and the arc is expending because the arc channel is still blown by the transverse airflow. The arc increases in size and so in voltage. Figure IV.27 represents the elongation phase.

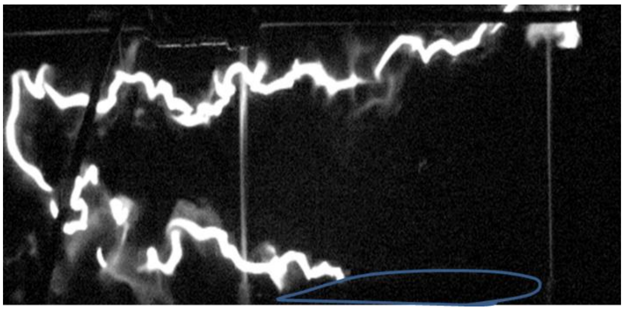

FIG. IV.27 Representation of the arc elongation phase

- Extinction phase: when the arc voltage outreaches the generator voltage, the arc channel extinguishes because the generator cannot provide enough energy to maintain it. The current in the arc channel is dropping and its light emission is fading away.

The different phases mentioned above are illustrated in the measured arc voltage waveform represented in Fig. IV.28. The ignition phase lasts from 0 to 4.4 ms and is recognizable with its high voltage peak reaching 2750 V occurring at 4.15 ms. The static phase lasts from 4.4 to 5.2 ms and is characterized by a smooth voltage time variation of 100 V around a mean value of 870 V. At 5.2 ms, an abrupt and marked voltage drop of 450 V occurs and corresponds to the first attachment of the electric on the material test sample. Then the swept-stroke phase lasts from 5.2 to 16.1 ms and is characterized by a mean voltage increase from 544 to 2973 V with a saw-tooth shape evolution. After 16.1 ms, the capacitors cannot provide enough power anymore to maintain the 400 A current regulation. In this configuration, the extinction phase follows directly the swept-stroke phase without the apparition of the arc elongation phase. Indeed, extinction occurs when the arc root has not reached yet the edge of the sample. After the extinction, the voltage is stable at 1500 V: the arc is extinguished and the voltage measured is the one at the terminals of the capacitor bank.

It can be noticed, in comparison with RGE, that the voltage reaches values two times higher at the end of the swept stroke phase – 3000 V for the WTE and 1500 V to 2000 V for RGE – and this increase is two times faster – 15 ms in average for the WTE and 40 ms in average for the RGE. Indeed, in contrary to the RGE where only the part of the electric arc close to the arc root is elongated, the whole arc column length is elongated with the airflow. Therefore, its length and so its voltage increases faster.

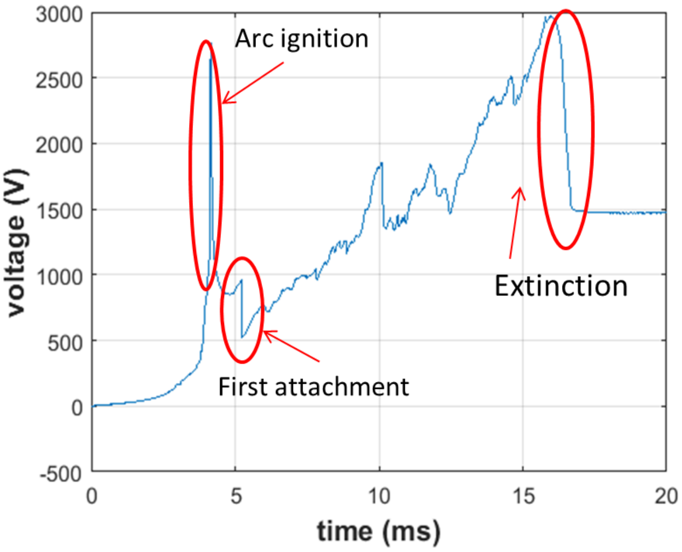

FIG. IV.28 Arc voltage waveform for wind tunnel experiment. The arc is elongated due to the air flow until its voltage exceeds the power supply voltage.

Column inclination

The arc column geometry is more complex for the WTE. It is arcing and extending in the direction of the air flow while the arc roots on the sample and on the tungsten horizontal rod electrode are lagging behind and slowly being pulled in the flow direction by the arc channel. The delay between the front arc column and the arc roots is increasing during the swept stroke phase as represented in Fig. IV.29.

(a)

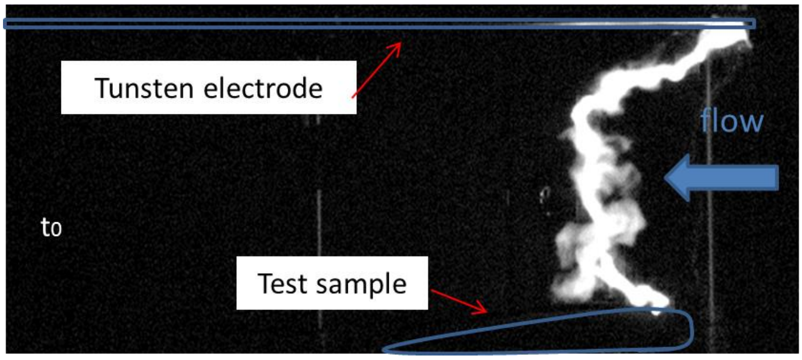

(b)

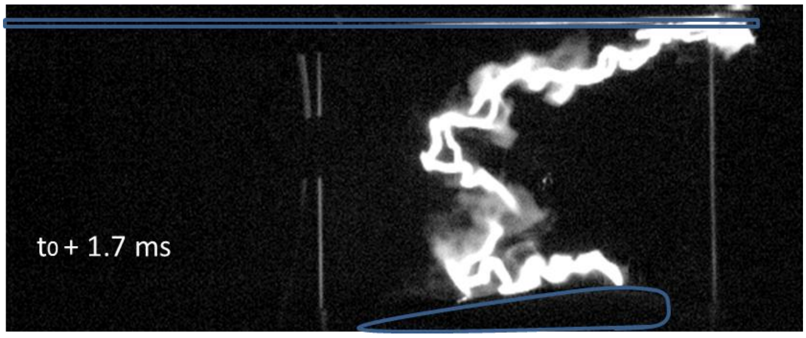

(c)

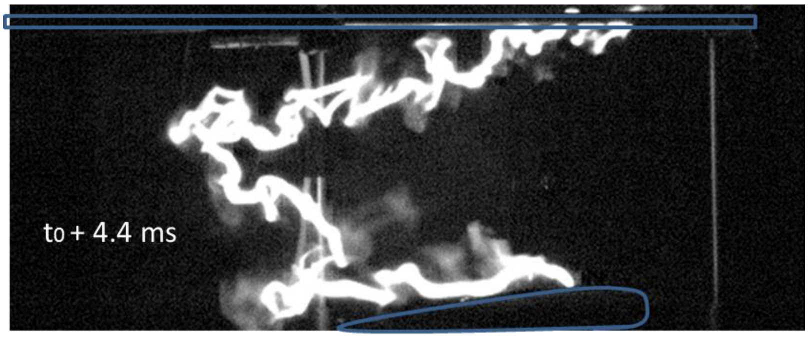

FIG. IV.29 Evolution of the arc column shape during the swept stroke phase at 5.6 ms (a), 7.3 (ms) and 10 ms (c).

Unlike for the RGE configuration, it is complicated to define an arc inclination between a straight arc channel and the arc root position since no part of the arc channel can be considered straight. Indeed, due to the drag forces exerted by the arc roots on the channel and to the non-homogeneous flow of the wind turbine, the arc column is not displacing as a straight channel. Nevertheless, it can be observed on Fig. IV.30(c) that a part of the column at the vicinity of the test sample is bent over it. The same phenomenon occurs at the vicinity of the tungsten rod electrode. Therefore, the relative inclination of the arc channel in the vicinity of the test sample can be visualized.

Arc voltage slope

As for the RGE, the arc voltage slope (dU/dt) is a relevant indirect measure of the arc length and will be discussed in the next section. The initial point of evaluation is the voltage level at first attachment on the test sample but whereas the arc voltage slope is measured until the projectile exits the cameras viewing fields or until arc self-reconnects in the RGE, it is difficult to find a relevant criterion for the WTE. Indeed, since the electric arc channel does not move uniformly, it is irrelevant to set an instant of exit from the camera viewing field. The voltage at the instant of reattachment or arrival at the trailing edge is then considered as a final point.

B.2 Effect of polarity

As for the RGE, the mean slope of arc voltage during the swept-stroke phase can be compared for the anodic and cathodic arc root displacement. However, the experiments involving the wind tunnel are more complex to analyze since the arc root on the tungsten rod electrode is also moving and thus participates on the arc column elongation. Thus a measure of arc slope for a cathodic arc root displacement on the test sample is disturbed by the motion of an anodic arc root on the tungsten rod electrode. Similarly, a measure of arc slope for an anodic arc root displacement on the test sample is disturbed by the motion of a cathodic arc root on the tungsten rod electrode.

Table IV.8 summarizes the mean slope of the arc voltage waveform during the swept-stroke phase for experiments with a moving cathodic arc root and with an anodic arc root. The airflow velocity is 60 m/s. And the results are compared for different arc currents

Table IV.8 Mean slope for cathodic and anodic polarity for WTE**.**

Current level (A)	**Arc voltage slope for moving cathodic arc root (V/ms)**	**Arc voltage slope for moving anodic arc root (V/ms)**	**Difference (%)**
200	242<**277**<313	267<**284**<302	**2**
400	**226**	**205**	**9**
600	130<**141**<152	135<**145**<155	**3**

Despite that these values are averaged over only two and sometimes one experiment, the measured voltage slopes differs from 3 to maximum 9 % depending on the settings. This means that the mechanisms governing the arc channel hydrodynamic extension are similar whether the cathodic or the anodic arc root is moving on the test sample and on the tungsten rod electrode. Thus, for the rest of the section, the results with anodic and cathodic arc roots will be gathered for the different settings.

However, it can be observed that the cathodic and anodic arc root do not present the same shape. It can be seen in Fig. IV.30 that the arc column at the vicinity of the test sample is winding down on the test sample for a cathodic arc root whereas there is a jet in the perpendicular direction of the test sample surface for an anodic arc root. In his example, the current regulation is set to 400 A and the airflow velocity is at 60 m/s.

.

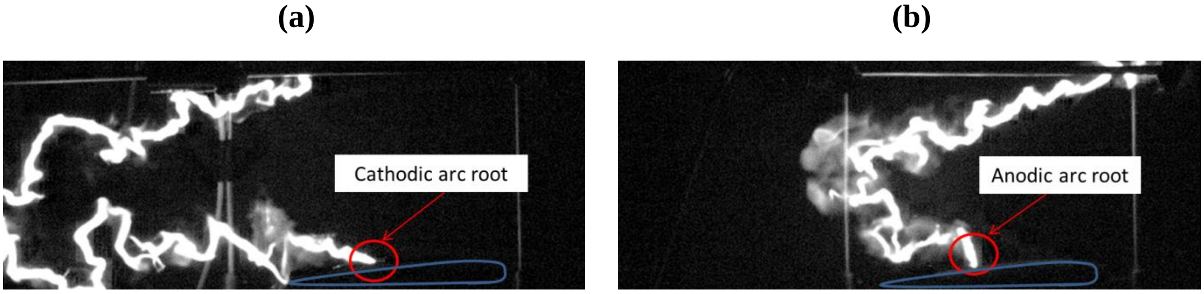

FIG. IV.30 Shapes of cathodic arc root (a) and anodic arc root (b) for wind tunnel experiments.

This difference of behavior appears to be a consequence of the displacement modes of the cathodic and anodic arc roots. As it will developed in Chapter V, the cathodic arc root tends to move forward with a continuous sweeping motion whereas the anodic arc root tends to move with a leaping pattern. Thus, the cathodic arc root is slowly pulled by the moving arc channel. As the arc channel is moving faster, the inclination between the front of the electric arc and the arc root is decreasing with time and the arc channel in vicinity of the arc root is bending down on the electrode surface. The anodic arc root rather jumps and reattaches on the test sample, forming an angle with the arc column as can be observed on Fig IV.30(b). This different mode of displacement will be studied in Chapter V. In general, this behavior does not appear to have an incidence on the voltage slope.

B.3 Effect of the flow velocity on arc shape

The same discussion about the effects of the relative velocity between the electric arc and the test sample can be developed. However, it is difficult to define an arc column velocity since it does not displace as a uniform and straight column but all of its parts are displacing at a different velocity. Thus, the airflow velocity is used as a comparative parameter even if it is probable that none of the parts of the arc column is displacing at the airflow velocity. Table IV.9 presents the arc voltage slope for the arc column during the swept stroke phase for different airflow velocities. The results are averaged for moving cathodic and anodic arc roots with an arc current regulation of 400 A for both speed.

Table IV.9 Mean slope for two airflow velocities for WTE.

Airflow velocity (m/s)	**Arc voltage slope (V/ms)**
0	**0**
40	76**<103<**145
60	205**<215<**226

The results of Table IV.9 show that there is not a linear relation between the airflow velocity and the arc voltage slope as was observed for the RGE. However in this case the arc voltage slope is even more complicated to interpret since the arc column elongation is subject to the swept-stroke phenomenon occurring at the test sample surface and to the arc root displacement on the horizontal rod tungsten electrode.

Contrary to the RGE, no phase of voltage plateau is observed in the arc voltage waveform for an anodic test sample at 40 m/s. It is still unsure if the absence or the presence of this plateau comes from a fundamental difference of physical processes for a relative motion due to blown arc and due to a moving test sample. For the WTE, the absence of this plateau might be due to the presence of another moving arc root on the second electrode. In this case, the arc voltage plateau would disappear in the arc voltage waveform due to the motion of the other extremity of the arc channel.

B.4 Effect of current intensity

Table IV.10 presents the arc voltage slope for the arc column during the swept stroke phase for different arc current regulation. The results are averaged for moving cathodic and anodic arc roots with airflow velocity at 60 m/s.

Table IV.10 Mean slope for cathodic and anodic polarity at 60 m/s for WTE.

Current level (A)	**Arc voltage slope (V/ms)**	**Arc power variation rate (W/s)**
200	242<**281**<313	48<**56**<63
400	205<**215**<226	82<**86**<90
600	130<**143**<155	78<**86**<93

The observations are similar to the ones for RGE: whereas the arc voltage slope is decreasing with the increase of the arc current, the arc power variation rate – the evolution of arc power per unit of time to sustain the arc elongation – is constant. Nevertheless, the arc power for 200 A presents a value 35% inferior in comparison with the other current values. The conclusion is that the arc channel appears to be able to provide a mean value of arc power variation rate to ensure its spatial extension as for the experiments with the railgun facility.

B.5 Effect of sample length

To ensure the representability of the experiment, the test was conducted for different lengths of test sample. Just as for RGE, WTE are led with test samples of lengths 200 and 400 mm to check if the results are similar. Table IV.11 presents the arc voltage slope for the arc column during the swept stroke phase for those different test ample lengths. Whereas in the Railgun configuration, sending a 400 mm long test sample to speed over 50 m/s is not possible with the limited energy available for the propulsion, it is possible in the WTE to blow airflow at a speed of 60 m/s on a test sample of 400 mm long. Thus results for an airflow velocity of 40 m/s and 60 m/s can be compared. Unlikely to RGE, the polarity of the arc root is also an parameter of interest in this experiment since it turns out that the difference of polarity triggers a large different of results at 40 m/s that is not observed at 60 m/s.

Table IV.11 Mean slope for test length for WTE.

Test sample Length (mm)	**Airflow velocity (m/s)**	**Arc voltage slope for moving cathodic arc root (V/ms)**	**Arc voltage slope for moving anodic arc root (V/ms)**	**Difference (%)**
200	40	79**<96<**113	76**<110.5<**145	**13**
200	60	**226**	**205**	**9**
400	40	83**<96<**109	**56**	**42**
400	60	134**<144<**164	**325**	**56**

As presented table IV.11, for a test sample length of 200 mm, the arc voltage slopes are similar between the cathodic and the anodic arc roots at 40 and at 60 m/s. But for a test sample length of 400 mm, those results differ a lot from cathodic to anodic arc root at 40 m/s and 60 m/s. However, just one test was carried out for anodic arc root at 400 mm at 40 m/s and 60 m/s but the difference of results is very significant. The difference of arc slope between test sample lengths of 200 mm and 400 mm is also very marked for a cathodic arc spot at 60 m/s and an anodic arc root at 40 and 60 m/s. In this case, as the results are very different between test sample lengths 200 mm and 400 mm, it can be inferred that the edge conditions are an issue for the representativeness of the results that cannot be neglected for the WTE. The low number of repetitions might also explain the important difference observed. The differences of results are also partly due to the presence of another arc root at the horizontal tungsten rod electrode since its role in the arc elongation is not well understood.

C. Discussion about the main differences of arc behavior between the Railgun and the wind tunnel experiments

As discussed before, the hydrodynamic and electric behaviors are different between the railgun and the wind tunnel experiment. In the RGE, the test sample is moving through a static arc column and the attachment of the arc column provokes its elongation. In the WTE, the arc column is blown by airflow while its extremities reattaches on the test sample and on the tungsten rod electrode. This difference of hydrodynamic behavior has a direct impact on the electrical properties of the arc channel as presented Table IV.12 for a comparable relative velocity and for a current of 400 A

Table IV.12 Mean slope for different mode of relative motion between RGE and WTE.

equipment	**Relative velocity (m/s)**	**Arc voltage slope (V/ms)**	**Arc Power variation rate (W/s)**
Railgun	42±4	31<**40**<57	12<**16**<23
Wind tunnel	40	76<**103**<145	30<**41**<58

Table IV.12 shows that for a comparable configuration of relative motion, the arc voltage slope and the arc power variation rate are around 2.5 times higher for the WTE than for the RGE. One of the principal explanations is the presence of another moving arc root in the case of WTE that is also responsible for the arc column elongation. The geometrical differences of arc channel are also very marked as discussed in this section. Thus the dynamic of the arc spatial expansion and of the evolution of the arc energy are dramatically different even if more experiments have to be done to confirm it for this level of relative velocity and for other relative velocities. It will be discussed in Chapter V if these differences of hydrodynamic and electric behavior do provoke disparate results in the process of successive reattachments during the swept-stroke phase since this process is responsible for the direct damages to aircraft skin and is the main concern of the manufacturers for protection design.

From a more practical concern and without any consideration for the representativeness of the way to produce a relative motion, the wind tunnel facility is likely to elongate faster the electric arc that the Railgun facility during swept-stroke. Thus the energy from the lightning generator is drained out faster. Therefore, the Railgun facility enables to produce a swept-stroke that will consume less energy than the Wind tunnel facility for the same configuration of arc current, relative speed, length of test sample and initial inter-electrode distance.

IV.3 Emission spectroscopy of the arc

The use of optical emission spectroscopy (OES) is a widely known and accepted technique for plasma diagnostics, and specifically for thermodynamic characterization of electric arcs. To mention just a few recent works concerning OES measurement applied to lightning or electric arcs, Cen *et al.* (2011) and Mu *et al.* (2016) have dealt with natural lightning using OES, Valensi *et al.* (2010) and Ma *et al.* (2011) employed this technique to study welding arcs, Sousa Martins *et al.* (2016c) and Sousa Martins *et al.* (2019) used it to the characterization of pulsed lightning arc.

In this work, we will use the OES measurements to detect the main species emitting in the free arc column and in the region close to the aeronautical sample. The identification of the main species allows us to realize an estimation of the arc column temperature based on the most resolved and intense lines.

A. *Experimental setup*

The spectrometer utilized is an AvaSpec ULS3648 from Avantes (Symmetrical Czerny-Turner, 75 mm focal length, wavelength range from 200 to 1100 nm, CDD linear array with 3658 pixels, spectral resolution of 0.34 nm/pixel). The optical fiber is a fused silica, with a core of diameter φ equal to 200 µm and a numerical aperture of 0.22 that is connected to the spectrometer via a SMA connector. An optical setup is used for imaging a portion of the arc column at the entrance of the optical fiber. The optical setup is composed of a lens tube (φ 0.5”) that hold the SMA connector fiber, a fused silica lens with a focal length of 30 mm and a neutral density filter (OD1). This setup is located 2 meters from the phenomenon, allowing the collection of a chord crossing the arc column. Figure IV.31 illustrates the experimental setup. The acquired spectra were calibrated in relative intensity using a DH-2000-CAL Deuterium Tungsten-Halogen Calibration Light Source from Ocean Optics.

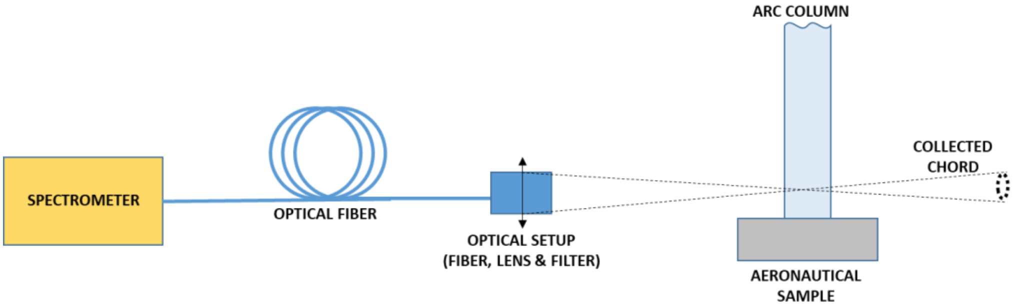

FIG. IV.31 Experimental setup of OES measurements.

The position and size adjustment of the collected chord is performed by analyzing the spot of a laser beam undergoing the reverse optical path. The synchronization of the swept phenomenon with the spectrum acquisition is very difficult, because the electrode/arc column is moving and we cannot know in advance when and where the arc will hang on the aeronautical sample. For that reason, we chose to use a large spot in the collected chord, with a spot diameter of 15 mm, which degrades the spatial resolution, but increase the probability to record the phenomenon. The exposure time was set to 10 µs, which is the spectrometer minimum time, but it is fast enough when compared to the arc motion (less than 1 mm displacement for the considered velocities). The chord spot is set to collect a region starting 10 mm above the aeronautical simple and represents a spatial average of the arc root and arc column.

B. *Measured spectra description*

The figure IV.2 presents an example of the acquired spectra for three cases (static free arc column, arc with Railgun and arc with wind tunnel) at a current level of 400 A.

The small amount of copper originated from the thin ignition wire contaminates significantly the electric arc. The majority of the observed lines are from atomic copper (Cu I). For this specie, we can well identify the two lines around 406 nm, an important group of lines around 458 nm, the five very intense lines around 521 nm, two other close to 578 nm and finally two intense around 800 nm. For a few cases (mostly in the wind tunnel tests), we observed the atomic oxygen (O I) multiplets around 777 nm, and the atomic nitrogen (N I) multiplets between 742 to 747 nm. A few lines of N I and O I are also observed between 818 and 845 nm. Hydrogen Balmer-alpha line (Hα) is also observed in spectra of the electric arc. Atomic hydrogen is probably originated from the molecular dissociation of water vapor present in the laboratory room and was reported in previous works (Sousa Martins *et al.* (2016c)).

(a)

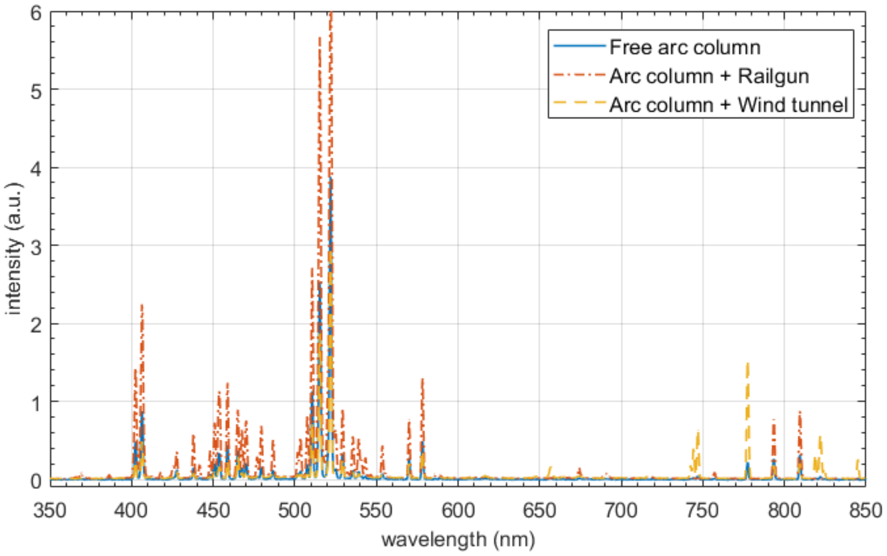

(b)

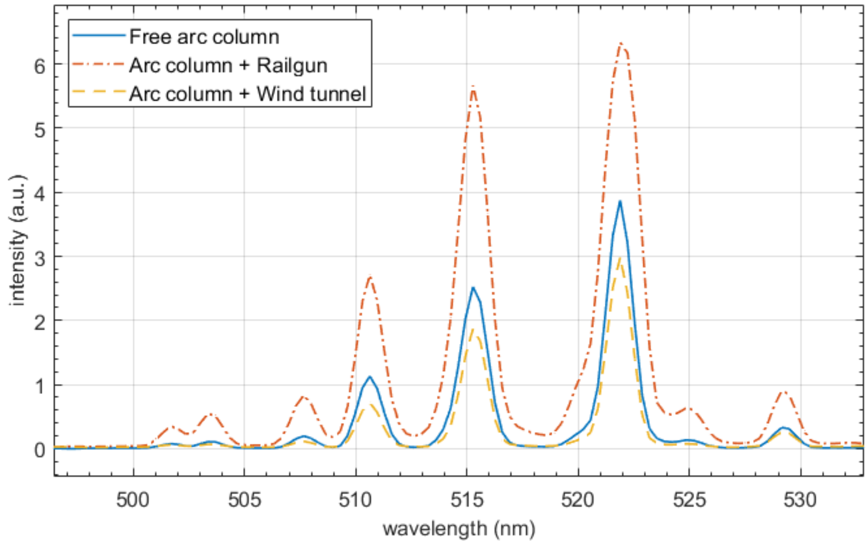

FIG IV.32 (a) Three spectra collected for the cases of a static free arc column, the arc with the electrode accelerated by the Railgun and the arc with a flow generated by the wind tunnel. (b) Detail of copper lines around 515 nm.

Aiming to obtain quantitative information from these spectra, the most suitable lines to deal with are the copper lines, as they are well isolated and very intense. We choose to apply the Boltzmann plot method with these lines to estimate the electron temperature of the arc.

C. Line emission and Boltzmann plot theory

The Boltzmann plot method is a well-known spectroscopic approach for plasma temperature characterization. Two main hypothesis are assumed when applying this method: (i) the considered species are at local thermodynamic equilibrium (LTE) and (ii) the arc column is optically thin to those transitions.

The radiation intensity $I(\lambda)$ along the chord collected by the optical system can be written from the optical energy balance between absorption and emission processes along the chord (Griem (1997)). By considering the LTE assumption and using the Kirchhoff's law, the ratio between the emission coefficient η and the absorption coefficient κ and is equal to the Planck function I_λ^0. Neglecting the scattering phenomenon and any transverse gradient inside the collected chord, the radiative transfer equation for this simple case can be written as:

$$I(\lambda) = I_\lambda^0(1 - \mathrm{e}^{-\kappa_\lambda l}) \qquad \text{(IV.7)}$$

With l being the length crossed within the arc column. If the arc column is considered optically thin, we have the optical thickness $\kappa l \ll 1$ and then Eq. (IV.7) becomes:

$$I(\lambda) = I_\lambda^0 \kappa_\lambda l = \eta_\lambda l \qquad \text{(IV.8)}$$

We observe that the intensity collected by the optical system is directly proportional to the emission coefficient and the length of the plasma crossed by the chord. In its turn, the emission coefficient under LTE assumption and using the Boltzmann distribution can be written as:

$$\eta(\lambda) = \frac{hc}{4\pi} \frac{g_u A_{ul}}{\lambda_{ul}} \frac{N_o(T, N_e)}{Q(T)} e^{-\frac{E_u}{kT}} f(\lambda - \lambda_{ul}, T,\ N_e) \qquad \text{(IV.9)}$$

where h and k are respectively Planck and Boltzmann constants, c is the speed of light, E_u and g_u are respectively the energy and the degeneracy of the upper transition level, A_{ul} is the Einstein emission coefficient for the transition from the upper (u) to the lower (l) level. N_o is the total population of the radiating species which is a function of the temperature T and the electron density N_e and Q is its internal partition function depending on T. λ_{ul} is the central wavelength and f is the normalized spectral line shape of the transition accounting for the broadening mechanisms and which is also a function of T and N_e.

The well-known expression of the Boltzmann plot method for a single transition is obtained by integrating Eq. (IV.9) over the wavelengths and by using Eq. (IV.8):

$$\ln\left(\frac{\int I d\lambda}{\frac{g_u A_{ul}}{\lambda_{ul}}}\right) = -\frac{1}{kT} E_u + \ln\left(\frac{hc}{4\pi}\frac{N_o(T, N_e)}{Q(T)} l\right) \tag{IV.10}$$

We observe that for each transition, the area of the line ($\int I d\lambda$) is directely correlated to the upper energy level E_u. Using different transitions and energy levels we can plot those points and use a linear regression to estimate the temperature from the angular coeficient.

For the observed lines, the spectroscopic constants in equation (IV.10), E_u, g_u, A_{ul} and λ_{ul} were taken from the Atomic spectral line database of NIST (Kramida et al. (2021)) for eigth lines and completed with Kurucz (Kurucz and Bell (1995)) for the three others. Table IV.13 presents the list of the considered lines with the corresponding spectrocopic data.

Table IV.13 Spectroscopic constants data used for the application of the Boltzmann plot.

λ_{ul} (nm)	g_u	A_{ul} (10^8s)	E_u(eV)
402.263	4	0.19	6.867
406.264	6	0.21	6.867
507.617	6	0.077	8.02
510.554	4	0.02	3.82
515.324	4	0.6	6.19
521.820	6	0.75	6.19
529.252	8	0.109	7.737
570.024	4	0.0024	3.817
578.213	2	0.0165	3.786
793.312	2	0.225	5.348
809.263	2	0.459	5.348

D. Temperature results and discussion

Figure IV.33 presents an example of the Boltzmann plot for a static free arc column of 400 A where a temperature of 11700 K is estimated. Generally, the measured data are well adjusted by the linear regression. We made a sensitivity analysis to evaluate the influence of the less intense lines on the linear regression and consequently on the temperature determination. By comparing the results found using the Boltzmann plot with the eleven lines listed in table IV.1 and with the temperature estimated using only the four main lines between 510 to 530 nm, we observed an average discrepancy of 500 K with a maximum of 1400 K. The significant difference of the upper energy level considered for the plot, covering a range of 4.2 eV, helps increase the accuracy of the temperature determination.

Figure IV.34 presents the results of temperature as a function of the current level and Table IV.14 summarizes the results obtained for the studied cases, which cover different parameters between the railgun and the wind tunnel tests.

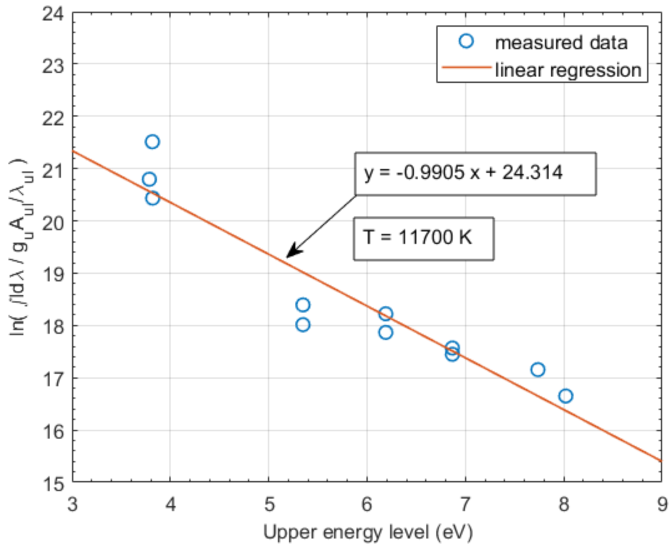

FIG. IV.33 Example of the Boltzmann plot for a static free arc column of 400 A.

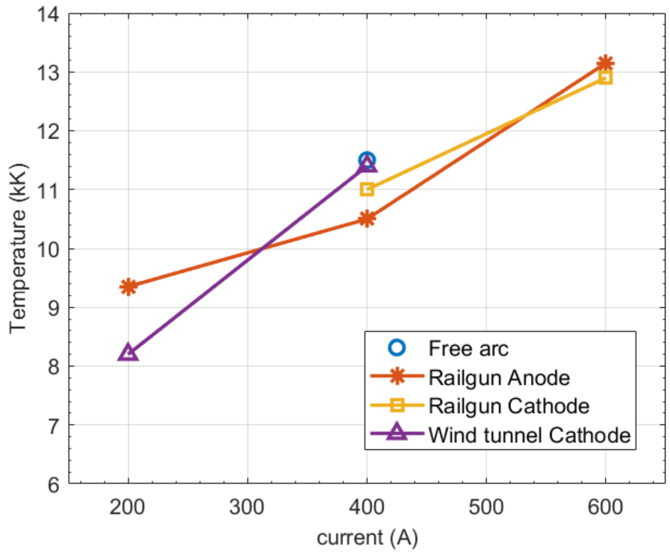

FIG. IV.34 Results of temperature versus current level for different cases.

Generally, the effect of the current level on the temperature is well observed. In the cases of 400 A the temperature is around 11 kK, regardless of the type of relative motion or even for the static free arc column. This increases to approximately 13 kK at 600 A and drops to values between 8.2 and 9.5 kK for 200 A. The effect of others parameters such as velocity, polarity, electrode gap or the type of relative motion cannot be clearly noticed. Between different analyzed cases, the temperature does not change more than 1000 K as a function of these parameters, which remain probably within the uncertainty of our measurements.

In general, this characterization gives us an order of magnitude for the arc temperature by assuming that the copper present in the arc column is at LTE. We observed that the current level has a general impact on the arc but the other parameters probably only have local influences, as in the sheath regions for example. This cannot be assessed with our actual spectroscopic setup. Dedicated measurements with more accurate time and spatial resolution should be performed in further works to characterize these regions and investigate the influence of these additional parameters.

Table IV.14 Summary of the temperature results.

case	L (mm)	I (A)	Polarity	v (m/s)	gap (cm)	T (kK)
Free arc	-	400	-	-	30	11.7
Free arc	-	400	-	-	30	11.3
RG 1	200	400	K	55	20	11.7
RG 7	200	400	K	42	20	10.8
RG 9	200	400	A	45	20	10.5
RG 10	400	400	K	37	20	10.5
RG 16	200	200	A	54	20	9.2
RG 17	200	200	A	52.5	20	9.5
RG 18	200	600	K	40	20	12.9
RG 20	200	600	A	50	20	13.3
RG 21	200	600	A	54.5	20	13.0
WT 1	200	400	K	60	20	11.4
WT 6	200	400	K	40	20	10.5
WT 9	400	400	K	40	20	10.8
WT 10	400	400	K	60	20	12.3
WT 14	200	200	K	60	20	8.2

IV.4 Conclusion

A reference database about the hydrodynamic, electrical and thermal properties of the arc channel during swept-stroke was established through high-speed cameras and electric probes measurements and optical emission spectroscopy technique.

The coupling of the lightning arc generator with the Railgun and the wind tunnel was successfully carried out with test samples presenting a NACA 0012 profile.

The electrical and optical diagnostics were coupled to evaluate the arc channel elongation and the arc power evolution during swept-stroke:

For a moving test sample, launched with the Railgun facility, the polarity of the moving arc root does not seem to influence the global elongation of the arc channel even if at 40 m/s, the anodic arc root reattachment process appears to neutralize the arc column elongation before the arc root reaches the trailing edge of the sample. It was also shown that the arc channel elongation is increasing not linearly with the test sample speed. The arc power variation over time during arc elongation was estimated to be quasi-constant with the arc current level for a mean value of 30 W/s for an average speed of 53 m/s. The test sample length and the initial arc column length did not demonstrate a noticeable influence on the arc elongation.

For a moving electric arc, blown with the wind tunnel, the polarity of the arc root does not seem to influence the global elongation of the arc channel either for different current and airflow velocity levels for a test sample of 200 mm. However, for a test sample of 400 mm, the global elongation manifestly differs between the cathodic and the anodic polarity. The arc channel elongation is also shown to be increasing not linearly with the airflow velocity. The arc power variation over time during arc elongation was estimated to also be quasi-constant with the arc current level for a mean value of 76 W/s for an average speed of 60 m/s. The test sample length presented a marked impact on the arc elongation, mainly for anodic polarity and airflow velocity of 60 m/s.

The mode of relative motion between the electric arc and the test sample dramatically affects the arc elongation. Indeed, for a same value of test sample speed and airflow velocity of around 40 m/s, the electric arc presents an electric power variation and an arc elongation rate around 2.5 times higher for a moving electric arc with the wind tunnel than for a moving test sample with the Railgun. This difference of hydrodynamic behavior is confirmed by the direct visualization and is partially explained by the presence of a second moving arc root on the other electrode and the non-uniform displacement of the arc channel induced by the airflow in the wind tunnel experiment.

Optical emission spectroscopy technique was employed to evaluate the electric arc temperature during swept-stroke. Generally, only the effect of the current level has a significant effect on the arc temperature: in the cases of 400 A the temperature is around 11 kK, regardless of the type of relative motion or even for the static free arc column. This increases to approximately 13 kK at 600 A and drops to values between 8.2 and 9.5 kK for 200 A. The effect of others parameters such as relative velocity, polarity, initial arc column length or the type of relative motion cannot be clearly identified.

For future work, the investigation of the temperature level inside the sheaths regions could provide more results to analyze the physical processes intervening in the arc root during swept-stroke. For this moment, these local temperature measurements cannot be assessed with our actual spectroscopic setup. Techniques of airflow visualization are also considered for future works in order to bring insight into the complex interaction between the electric arc and the airflow during the phenomenon.

The experimental characterization of the arc column during swept-stroke presented in this chapter is dedicated to bring more physical comprehension and to serve as input parameters or comparison for simulation codes. However, as the main concern of the aircraft manufacturers is the assessment of damage to the aircraft cover, it is interesting to focus on the interaction between the arc root and the test sample material and to study the modes of displacement of the arc root.

Chapter V. Study of the arc roots displacements during the swept stroke

In this chapter, the focus will be on the arc roots displacement. The dynamic of the arc root is a key to understanding and predicting the damage produced by the lightning on the aircraft skin.

The chapter first describes the previous experimental works about the observation and the analysis of arc root displacements available in the literature. This description leads to distinguish cathodic and anodic arc roots since they exhibit different physical processes and cause damage in different aspects. Then the physical quantities that will be evaluated to characterize the interaction of the arc root and the material are presented and illustrated for the two arc root polarities. The evaluation of these quantities is therefore achieved with direct visualization through high-speed cameras and electric measurements for different initial conditions. The results are separated by the polarity and discussed to give an insight into the influence of the experimental conditions on the interaction between the electric arc root and the test sample during swept-stroke.

V.1 Previous experiments and observations during the displacement of an arc root

If the experiments dealing with the swept-stroke are reviewed in the Chapter I and other fields of plasma application have already been reviewed, this subsection aims to focus on experimental results of arc root displacement coming from other applications that present a larger literature and where the physical phenomenon occurring are better analyzed and understood. Indeed, there is a large literature for two main applications where the displacement of the arc root is the key preoccupation for the efficiency of the device:

- Circuit breakers: when a high current is interrupted, especially in highly inductive circuits, it creates an electric arc that has to be evacuated by extinction to protect the device. To help this extinction, the arc is displaced in the circuit breaker chamber with means of geometry effects – the arcs length extends by moving along the chamber due to self-induced magnetic forces and reaches an area of arc dividers where the arc is subdivided into smaller arcs by several plates of metal. All of these smaller arcs consume more energy due to the multiple interactions arc-metal formed and the arcs extinguish. This displacement can be enhanced by means of transverse blowing or added magnetic field. The displacement of the arc is directly responsible for the longevity of the device. The faster the displacement of the arc, the fewer the arc roots dwell on the wall of the chamber and the fewer the damages on it (McBride and Jeffery (1999)).

- plasma torches : an electric arc is created between a hollow cathode and anode and a flow - transverse or incident to the electric arc – project out of the device the plasma jet issued from it. The plasma jet is then used for several applications such as arc welding, plasma cutting or plasma spraying. Here as well, the displacement of the arc roots on the electrode is the major parameter for the longevity of the device (Yang and Heberlein (2007)).

In these applications, the characteristic arc lengths differs from one or two order of magnitude from the electric arcs generated by the developed lightning generator, indeed, their length is rarely over few cm. First, this addresses a scale problem: a small distance between the two arc roots greatly impacts the physical mechanisms responsible for their displacement. It is shown in Cui et al. (2017) that the metal vapor and gas ablated from the electrodes are providing strong jets that are likely to bend under the effects or magnetic field coming from the current in the arc. These jets are thus heating the other electrode in a favored direction and affect the physical processes for the establishment of an arc root thus greatly influencing the displacement of the arc roots by enhancing their mutual influence. In our experiment the displacement of the arc root is supposedly not affected by the presence of the other arc root and the arc column is long enough – minimum 20 cm – to be representative of a free arc column. These assumptions will be discussed latter.

The most studied configuration for the displacement of an electric arc is the displacement between parallel electrodes consisting of metallic bars (Cui et al. (2017); Gray et al. (2015); Gray et al. (2018); Choi et al. (2017); Guile and Mehta (1957)) The arc moves forward due to the Laplace force coming for his self-induced magnetic field or enhanced by an external one. The main observation on the displacement mode - for arc intensities up to 1 kA and several mm of distance between the rails - are that the cathodic arc root has a continuous mode of displacement whereas the anodic arc root moves forward along the rails by jumping. Depending on the experimental conditions, the cathode arc may present a jumping pattern of displacement as well and there might be multiple – up to four – distinct anodic arc roots (Cui et al. (2017); Gray et al. (2015); Guile and Mehta (1957); Secker and Guile (1959); Boukhlifa (2021)). In these configurations, the cathodic arc root was either preceding the anodic arc root (Gray et al. (2015); Gray et al. (2018)) or not (Cui et al. (2017); Guile and Mehta (1957)). (Secker and Guile (1959)) also classifies four types of cathodic arc roots tracks that matches different types of displacement: discontinuous (jumping mode), regular (continuous with tracks of a regular size), sticking (continuous with tracks of important size) and high speed (continuous with thin tracks). Then it associated the displacement modes with the following parameters:

- Current intensity: as the current increases, the displacement goes from sticking to regular to high speed to discontinuous even if does not seem to have an influence on the velocity of arc root displacement.

- The materiel: it is shown in (Cui et al. (2017)) that a refractory material with a low work function is likely to present a discontinuous mode. This mechanism will be discussed in the cathodic arc root subsection.
- The inter-electrode distance: it was observed that as this distance increases in the range from 0 to 5 cm, the displacement of the arc roots is faster and the mode of displacement is becoming discontinuous. The speed however presents a saturation threshold.

There are few works of electric arc experiments where the arc roots are displaced due to the relative motion of the electrodes with speeds reaching several tens of m/s. Testé et al. (2015) presents a device consisting of a spinning cylindrical electrode by the use of a drill. The other electrode is a disc concentric with the rotational axis of the spinning electrode and is maintained fixed. A maximum relative speed of 40 m/s was reached for an arc root moving at the extremity of the disc. It was observed for a current of 100 A that the cathodic arc root tracks were either continuous or partially continuous and the anodic arc root tracks were discontinuous – corroborating the previous experimental results. More interesting, it was shown that the anodic arc root was able to move at the limiting speed of the device – 40 m/s whereas the cathodic arc root was only able to move at some cm/s to be maintained and avoid arc extinction. This was attributed to the drastic conditions of heating and electric field thresholds for a cathodic spot to emit electrons so that the arc root cannot be faster than the temperature propagation in the surface of the material. Dobbing and Hanson (1978) paper that was already cited in part I remains the reference that is the closest to our problem with a linear movement of the electrode expelled at a speed up to 72 m/s. This reference proposes experimental data for arc voltage drops for reattachment over painted surfaces, skip distance values between two arc roots in discontinuous modes and dwell time values of the arc root on a specific point for bare metal and carbon fibers. It also evokes a different behavior of the electric arc above and below the moving “wing” electrode and the difference of displacement mode between the cathodic and the anodic arc roots.

Considering studies about the speed of displacement of electric arcs, many references study the effect of the magnetic field, trying to set a formula and neglecting the arc root phenomenon (Bobashev et al. (2010); Daumov and Zhukov (1965); Guile and Naylor (1968); Szente et al. (1988)) or considering it as dragging force depending on the surface state of the electrode (Spink and Guile (1965)). Other references have discussed about the importance of the presence of cathode oxide film that slows down the cathode arc root and so drags the channel column (Lewis and Secker (1961); Guile and Hitchcock (1981); Lichun and Jiazhi (1982)). The nature material of the cathode is also a decisive parameter: refractory cathodes with low work function are observed to be an order of magnitude faster than non-refractory cathodes (Cui et al. (2017)) for arc currents of 100 A and an inter-electrode distance of 25 mm. Thus, there is not a total agreement in the literature about the parameters that influence the most the speed of the arc column. Some formulas are accepted and validated for some specific conditions.

In this breve introduction, it is remarkable that the phenomenon driving the observation about reattachment processes are dramatically different for the cathodic arc root and for the anodic arc root. For this reason, it was decided to separate their studies in two different sections. This division is also facilitated by the fact that the two arc roots are decoupled in our experiences. Indeed, the arc column is supposed to be long enough so that the arc root on the test sample and the arc root on the secondary electrode of tungsten do not interact. Mainly, the vapors and gas ejection of one electrode do not disturb the arc root motion on the other electrode as it occurs for arc-column of a few mm. The cathodic arc root motion will be studied first and then the anodic arc root motion. To understand the observation of this section and to give a base for the analyze of the experiment results, the accepted model of the two arc roots will be first presented in the next subsections before presenting the experimental results.

V.2 Electrode sheaths definitions and presentation of their physical processes

A. Cathode definition and emission processes

The cathodic root is the plasma sheath between the region of metallic conduction and gaseous conduction at the cathode. By extension, the cathode fall region includes the cathode surface and the thin layer of electrode vapor and gas around it. The cathode has a very important role since it regenerates the charged particles of the electric arc and so maintains the discharge. The cathode requires the flow of positive ions and electrons are extracted from it. It is commonly accepted that the cathode emission dominates the displacement of the entire arc column caused by self-induced magnetic field or exterior forces (Mc Bride et al. (1998)) even if some works disagree on this point (Cui et al. (2017)).

The main features of this cathode fall region arc are the presence of a voltage drop between 8 and 20 V occurring over very short distances from the electric surface (Guile (1971)). Thus the electric field in this region has a higher order of magnitude that the one in the arc channel: whereas the field in the arc column is around 10 V/cm, it might exceed 10^7 V/cm in the cathode fall region. The typical current density of this region is also over several order of magnitude than the density in the column (10^4 A/cm^2 to 10^5 A/cm^2 for refractory cathode material, 10^6 A/cm^2 to 10^7 A/cm^2 for non-refractory cathode material (Froome (1948)) and 10^2 to 10^3 in the arc column). There is a large gradient of temperature that makes the temperature of the sheath difficult to measure and to interpret. The root is described to consist in a number of small emitting areas that are close together for atmospheric conditions. Their number is supposed to be proportional to the current so that the current per site is constant, mainly for vacuum arcs (Djakov and Holmes (1971)).

The structure of the cathode sheath is commonly accepted (Cayla et al. (2008)) and represented in Fig. V.1.

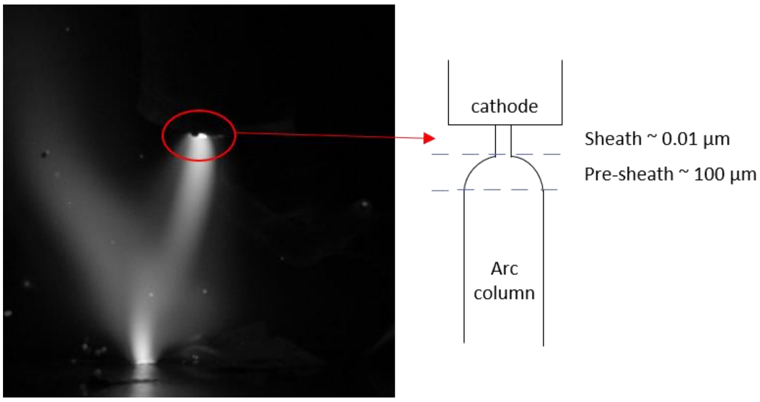

FIG. V.1 Representation of cathodic fall region from a 2 cm electric arc.

Moving from the cathode toward the arc column, it consists respectively in:

- A space-charge zone where charge equilibrium and thermodynamic equilibrium are not respected: its length is in the order of magnitude of the electrons mean free path. In this area, electrons travel faster than ions do in the opposite direction so that the density of positive charges is higher and causes the high electric field.

- An ionized layer or presheath where thermodynamic equilibrium is not respected: as we are leaving the arc channel and getting closer to the cathode, the thermal equilibrium is first lost – the electrons and the protons do not have the same temperature anymore. Then the chemical equilibrium is lost – the electronic density does not respect the Saha ionization equation. Ultimately, the charge equilibrium is lost – the ions density is not equal to the electrons density (Belinov (2008)).

- The cathode fall region is also characterized by its jet: the high current in the arc creates a radial pinch at the cathode sheath and thus an important pressure gradient that provokes a stream of particles from the cathode erosion forming gas and vapor flowing away in a specific direction more or less parallel to the cathode surface (Maecker (1955)). They are described to present a certain and visible ‘stiffness’ as can be seen in Fig. V.2. The velocity of this stream of particles varies from 100 to 1000 m/s (Robertson (1938)). The higher the current, the stronger the jet.

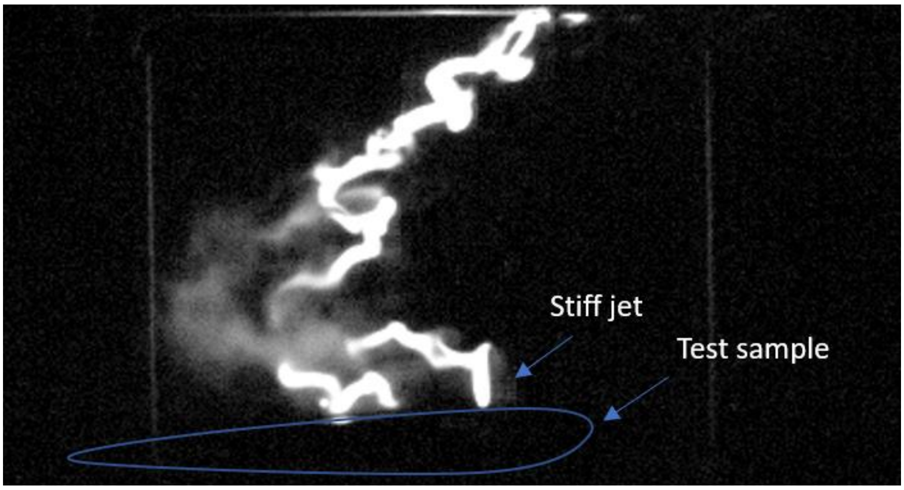

FIG. V.2 Example of cathodic jet ‘stiffness’ for a Wind tunnel experiment.

As a cathodic spot has to be able to emit electrons and receive positive ions to maintain the arc current, a closer description of the emission processes will help us to explain under what conditions a spot of the cathodic surface might become a cathodic spot. This will give us physical insight to explain the leading processes resulting in the macroscopic movement of the arc root. A list of the main mechanisms is given for electron emission and production of positive ions.

Thermionic emission:

When a cathode is heated to a sufficiently high temperature, electrons are emitted under thermionic effect and their current density is given by the Richardson-Dushman equation:

$$j_e = AT^2 \exp(-\frac{e\phi}{kT})$$

Where A is a constant, e is the electron charge, k the Boltzmann’s constant, T the temperature of the material and ϕ the work function of the cathode surface. To be efficient and match the required electron density measured in the cathode, the emission process requires a high cathode surface temperature – minimum 4000 K and so a material whose boiling point is above this value. Thus refractory materials - such as tungsten - are able to sustain the electric arc with thermionic effect and the non-refractory materials emission is not driven by this mechanism. The latter kind of material are also called cold cathodes in this context. As our samples are made of aluminum, this effect cannot explain the arc root behavior.

Field emission:

When a cathode surface is under the influence of a large electric field, electrons are emitted and their current density is given by the Fowler-Nordhein equation (Fowler and Nordheim (1928)):

$$j_e = BE^2\exp(-\frac{C}{E})$$

Where B and C are constants depending on the work function of the material and E is the local electric field. This effect is commonly accepted to have the main influence over the cathodic emission (Murphy and Good (1956)) and is thought to drive the displacement of the arc root (Cui et al. (2017)).

Temperature-plus-Field emission (TF-emission):

Even for cold cathodes, thermionic emission might reach important values even if it is not able to produce the required electron density alone. So that the emission is either produced by the joint effects of thermionic and field emission. This theory, referred to as TF theory, is able to give satisfactory results for some arcs but is not commonly accepted (Lee (1959)).

Other processes of cathode emission have been introduced to sustain the high electron density delivered. These effects are presumably not predominant and are briefly cited: Locally enhanced electric field, electron liberation by Auger capture, electron liberation by photons or by excited and metastable atoms, by lowering of the working function for the presence of a negative space charge inside cathode metal, by excitation of plasma oscillations inside the cathodic metal, by charging of oxide layers and by metallic conduction in high-density vapor (Guile (1971)).

Then the production of ions in the sheath is explained by three main processes:

- The electrons emitted by the previously cited processes are accelerated by the large local electric field of the cathode fall region and produce ions at the end of the region by successive collisions.
- Thermal ionization processes in the high temperature gas at the edge of the sheath respecting the Saha equation and the local thermodynamic equilibrium (LTE).
- Flow of positive ions at the cathode surface producing the liberation of electrons.

This theoretical development gives a basis to explain the different observed modes of arc displacement. As it was observed in Cui et al. (2017), cold cathodes proved to have a continuous and slow arc root displacement whereas thermionic cathodes had either a continuous but faster arc root displacement or a discontinuous one under the same operating conditions. The continuous movement of cold cathodes is explained by the predominance of field effect emission to establish new electrons emitting sites. A region of space charge from ionized metal is therefore required and the movement is limited by the diffusion of metal vapor. It results in a forward continuous motion of the cathodic root as metal vapor is formed at the vicinity of the arc root.

For thermionic cathodes, the arc can move faster in a continuous mode due to the combination of a thermionic emission mode and the presence of a jet that is forwardly bent with magnetic effects. Indeed, the jet consists in the ejection of hot vapor that is able to heat locally the cathode surface and provide a new emitting point with thermionic process. Thus, the formation of a new spot is not limited by the formation of ionized metal and the arc root is able to move faster.

B. *Anode definition*

The anodic root is the plasma sheath between the region of metallic conduction and gaseous conduction at the anode. By extension, the anode region includes the anode surface and the thin layer of electrode vapor and gas around it. Its role is to preserve the current continuity. The anode cannot emit positive ion and the current is carried by electrons entering in it. Thus, as no charge emission conditions are required, the establishment of an anodic arc root is less restrictive that the cathodic one. (Guile (1971)).

The main features of this anode fall region arc are the presence of a voltage drop between 1 and 10 V occurring over very short distances from the electric surface due to a space charge region. This space charge is due to an important concentration of electrons. The current density, unlikely to the cathodic spot, is close to the one in the arc column – 10^2 to 10^4 A/cm^2 (Sommerville (1959)).

The structure of the anode region is commonly accepted and similar to the cathode region: it also consists in a space charge region, a presheath region and has a jet. But this jet is less strong that the cathodic one since it is the result of a magnetic pinch. This magnetic pinch is less marked in the anode since the current density is in the order of magnitude of the one in the arc column (Sommerville (1959)). The structure of the anodic fall region is represented Fig. V.3.

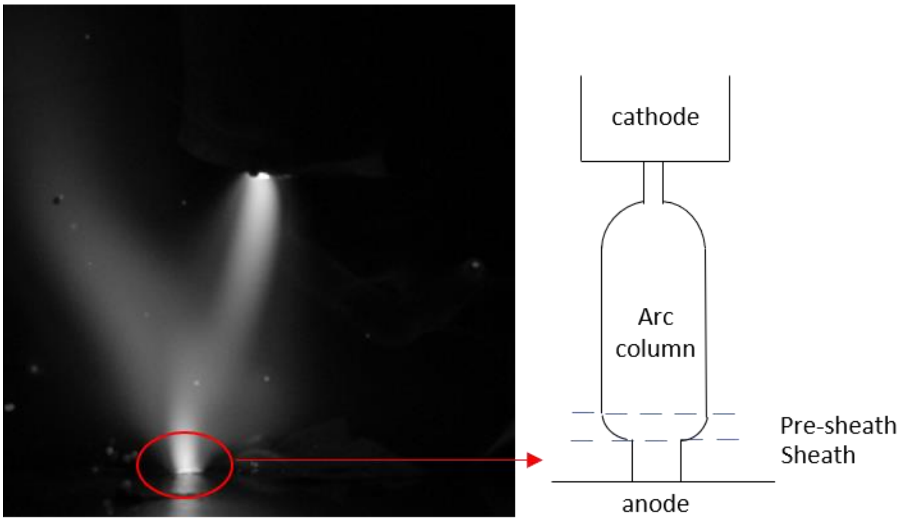

FIG. V.3 Representation of anodic fall region from a 2 cm electric arc.

However, if ions are not emitted from the anodic material, they are emitted in the anodic sheath area to sustain the electric arc. There are two emission processes:

- Thermal ionization processes in the high temperature gas at the edge of the sheath respecting the Saha equation.

- The electrons entering the sheath are accelerated by field effects and are able to ionize the gas in the sheath. However this field effect is less predominant than the thermal ionization for atmospheric arcs (Ecker (1953)).

Thus, the movement of the anodic spot is most governed by thermal processes than field processes so that the establishment of a new anodic arc root is less dependent on the vicinity of an existing anodic spot which could explain a jumping mode of displacement. McBride and Jeffery (1999) also noted that the anodic arc root is more likely to be affected by an additional pressure coming from a venting process than the cathodic spot, supposedly due to the absence of governing emission process.

V.3 Definition of the physical parameters measured in the experiments

As the arc root displacement involves different complex multi-physical mechanisms, its study is carried out by varying the input parameters and measuring, by a set of defined observable quantities, its behavior to give a database that will help to interpret the predominant mechanisms occurring. In this section, the physical parameters relevant for the measurements of the cathodic and anodic arc root displacements will be introduced and discussed.

A. Dwell time

The dwell time is the time between the formation and the extinction of the same arc root. As these instants of formation and extinction are directly measured with the camera, their estimation is limited by the interval between two pictures, 17.53 µs for the Railgun experiment and 15.87 µs for the wind tunnel facility. Five successive images presenting a formation of an arc root are presented in Fig. V.4.

(a) **(b)**

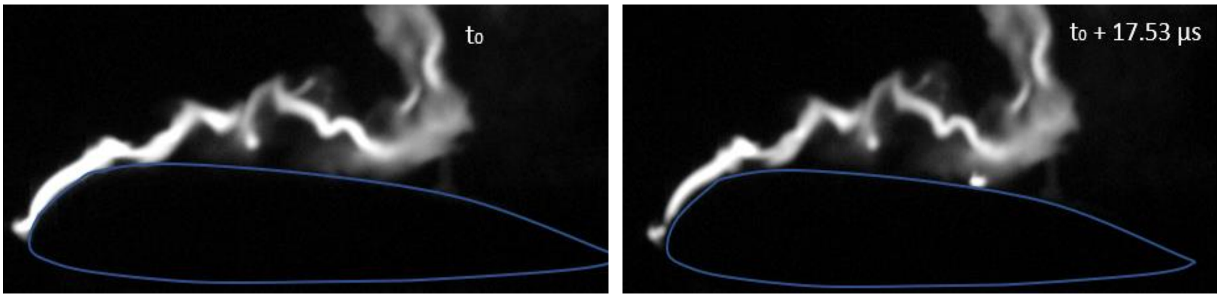

(c) **(d)**

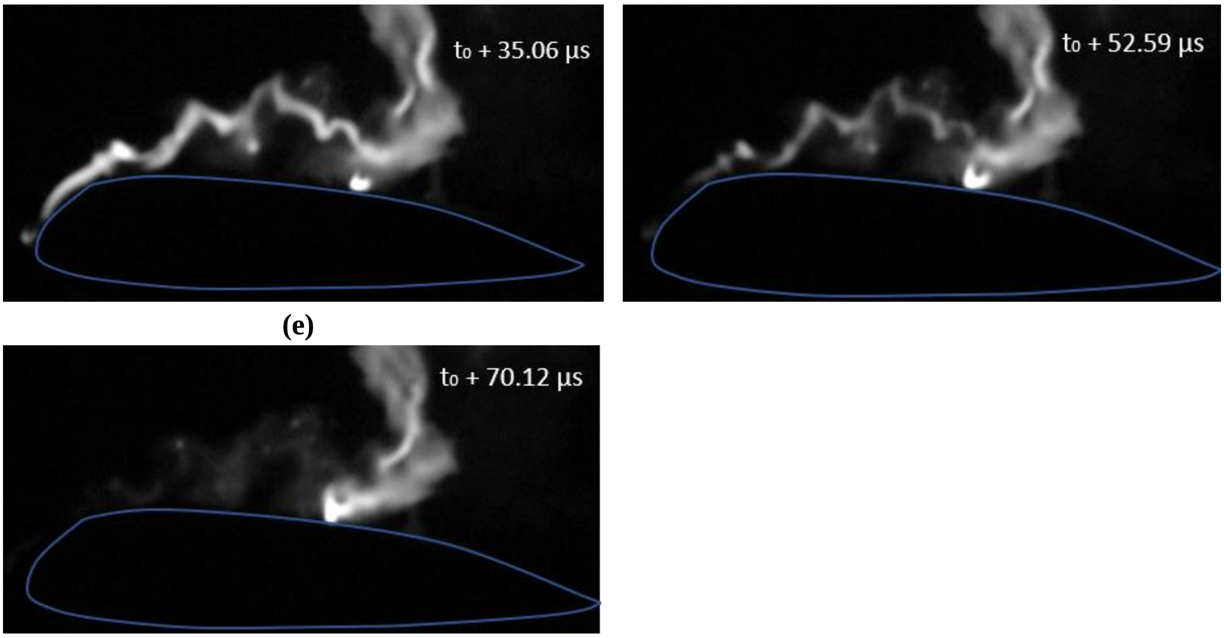

(e)

FIG. V.4 Successive images presenting a formation of an arc root. The exposure time is 17.53 µs.

However, the instants of apparition and extinction of an arc root might be impossible to define by the direct recording with the camera. Indeed, if the new arc root appears in the immediate vicinity of the previous arc root – less than 5 mm – it is not possible to visualize any phenomenon and the arc root appears to move continuously despite the presence of several anodic arc root tracks at this position after the experiment. This problem mainly appears for anodic arc roots and it is not always possible to evaluate a dwell time or a size of extinguished arc. However, the addition of a second HSC camera with an inclined position helps to distinguish two different arc roots that appear united in the perpendicular 2-D visualization from the first camera. Another problem is the coexistence and even sometimes the simultaneous formation of several arc roots. Two arc root formations are said simultaneous when two arc roots appear in the interval of two images recorded by the camera. Several simultaneous arc roots are likely to produce more luminosity and to prevent the arc root borders from being recognized by direct visualization. An example of the presence of simultaneous arc roots is presented in Fig V.5. However, the presence of several arc roots is only observed for anodic arc roots.

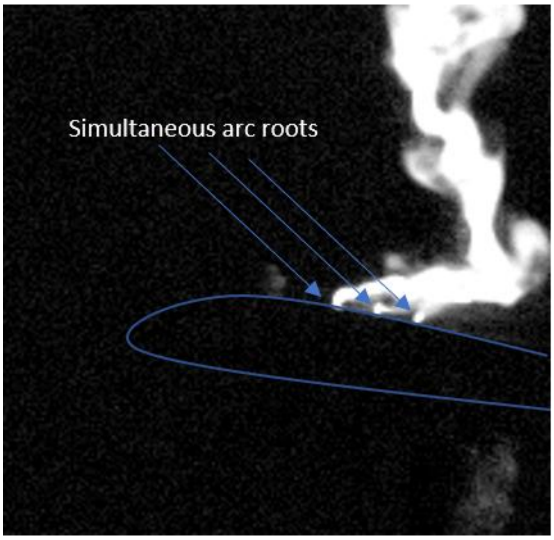

FIG. V.5 Example of the presence of simultaneous anodic arc roots.

For cathodic arc root, a problem of definition appears when considering a continuous arc sweeping. In this case, it is difficult to evaluate the time the arc root dwells on a specific point since it is continuously moving. Thus, the dwell time is defined in this case as the sweeping time of the arc spot before it reattaches another point of the test sample. However, this definition for cathodic arc root addresses a problem: the term dwell time covers two different physical processes considering a sweeping arc root or a static arc root and therefore two different natures of damage. Indeed, damage induced on the material test sample for a given dwell time will be more intense for a static arc root than for a moving one where the damage is distributed between all the points on the passage of the arc root.

B. Skip distance

The skip distance is the distance between two impact areas and is measured directly on the sample after the test. A difficulty occurs when different arc roots coexist since the skip distance to a new forming arc root has as many values as the number of coexisting arc roots. In these cases, the instants of impact successions were recorded with the inclined camera so that it was possible to better visualize the former electrical arc column from which the newly established arc column and arc root are issued and so define a skip distance. It was generally corresponding to the lowest value of skip distances amongst the measured ones. A sample with multiple anodic impacts is presented Fig. V.6. It is interesting to observe that the order of the impacts cannot be determined easily in this case so that the video of two cameras with different orientations is required either to determine their order of apparition and their possible coexistence.

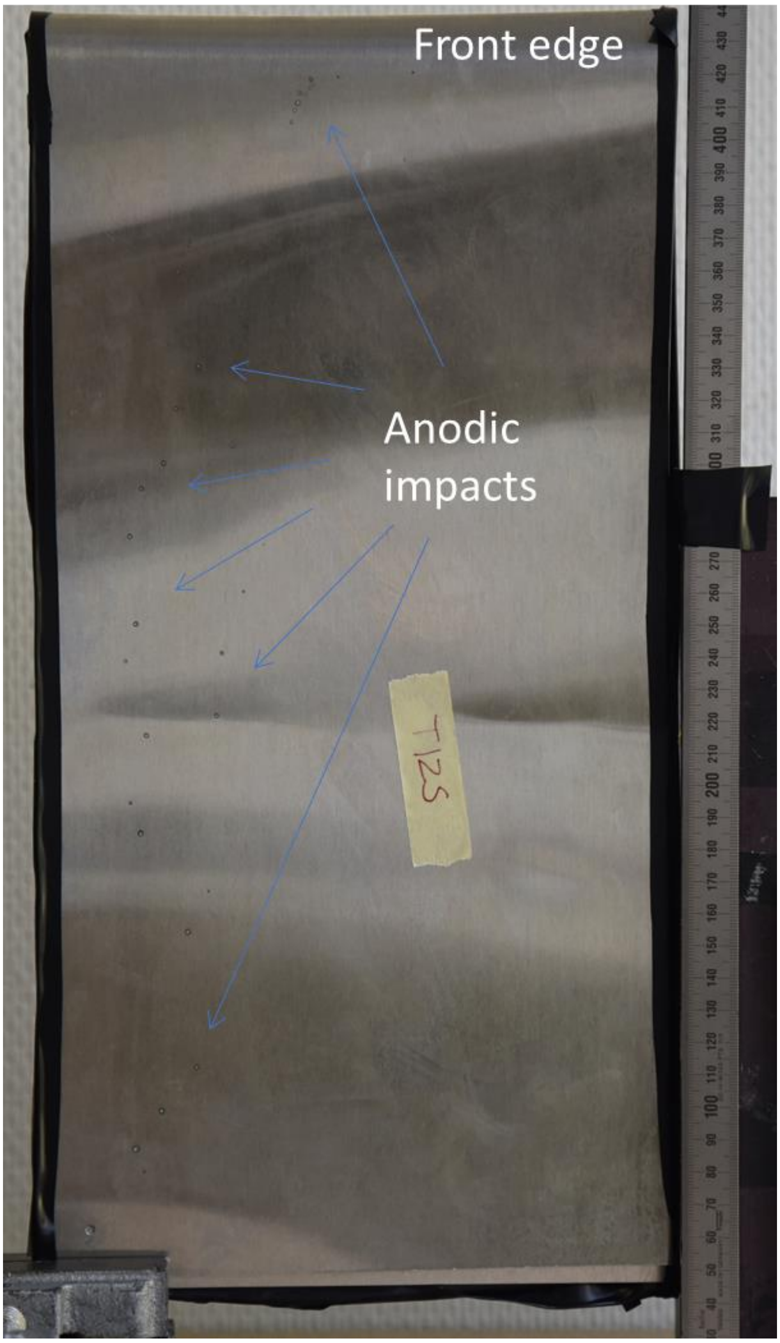

FIG. V.6 Multiple impacts left by an anodic arc root.

Another difficulty was the presence of barely visible tracks of anodic spots on the sample. Looking to the records of the inclined camera it appeared that an arc root was formed but had a dwell time of no more than two images – around 30 µs – and its light emission was barely visible in comparison with another coexistent arc root implying that this arc root conducts a very low portion of the current. This type of arc root was only for the anodic case and the impact spots had a diameter of less than 0.5 mm. For a cathodic arc root, a skip distance is measured only in case of a discontinuous reattachment of the arc root on the test sample.

C. Arc voltage drop

When an arc column and an arc root are extinguished due to a reattachment, there is a voltage drop in the arc voltage. This drop corresponds to the voltage of the free arc column and to the electrode voltage fall. This value is important since it is also the image of the arc power when it is multiplied by the operative current and it gives complementary information on the real arc length in addition to the 2-D visualization. Indeed, neglecting the cathodic and anodic voltage fall, the arc voltage is supposed to be proportional to the total length of the arc channel. However, voltage drops also occur when an arc loop of the free arc column is short-circuited by the formation of a new path of current. Then, if such a phenomenon occurs during a reattachment, the measured arc voltage drop is composed by the voltage drop due to the arc root reattachment and by the one triggered by the extinction of the arc loop. Figure V.7 shows a voltage waveform presenting two important arc voltage drops, one issued from an arc loop reconnection and one from an arc root reattachment. To recognize the nature of the arc voltage drop, the voltage waveform measurements are synchronized with the transverse camera. Therefore, the measured value might present a bias. If a reattachment is observed at a specific time and if for the corresponding time, a voltage drop inferior to 5 V is measured, then the reported value is zero.

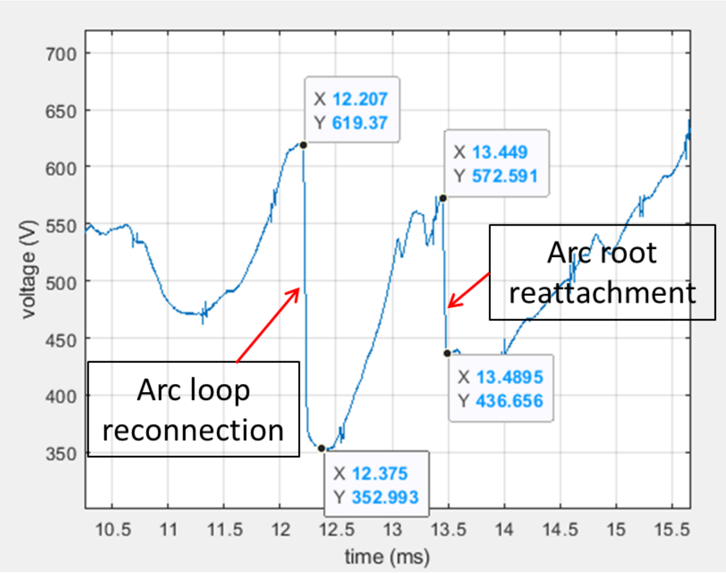

FIG V.7 Presentation of the arc voltage drop measurement method. The voltage level measured after the drop is withdrawn from the voltage level measured before the drop and reported in case of an arc root reattachment after comparison of the instant of the event with the camera.

D. Size of extinguished arc column

The perpendicular camera enables to visualize and to measure the size of an extinguished arc column. This measurement is carried out by image processing: the instant of reattachment is captured with a picture and is treated with measurement software. As the image dimensions are reported with a test-pattern, the reduction of the test column is measured by adjusting the arc column broken line shape with scaled segments as represented in Fig. V.8. The adjusting imprecision for one segment is about 1 to 2 mm. This imprecision cumulates in case of multiple segments. Moreover, this is a 2-D measurement that does not consider the 3D spatial extension of the arc so that this parameter is not representative of the real length of the arc channel. It produces an error of estimation that might be important in certain cases. Moreover, direct visualization does not allow measuring extinguished arc of less than 5 mm with accuracy even if a formation of a new spot can be distinguished.

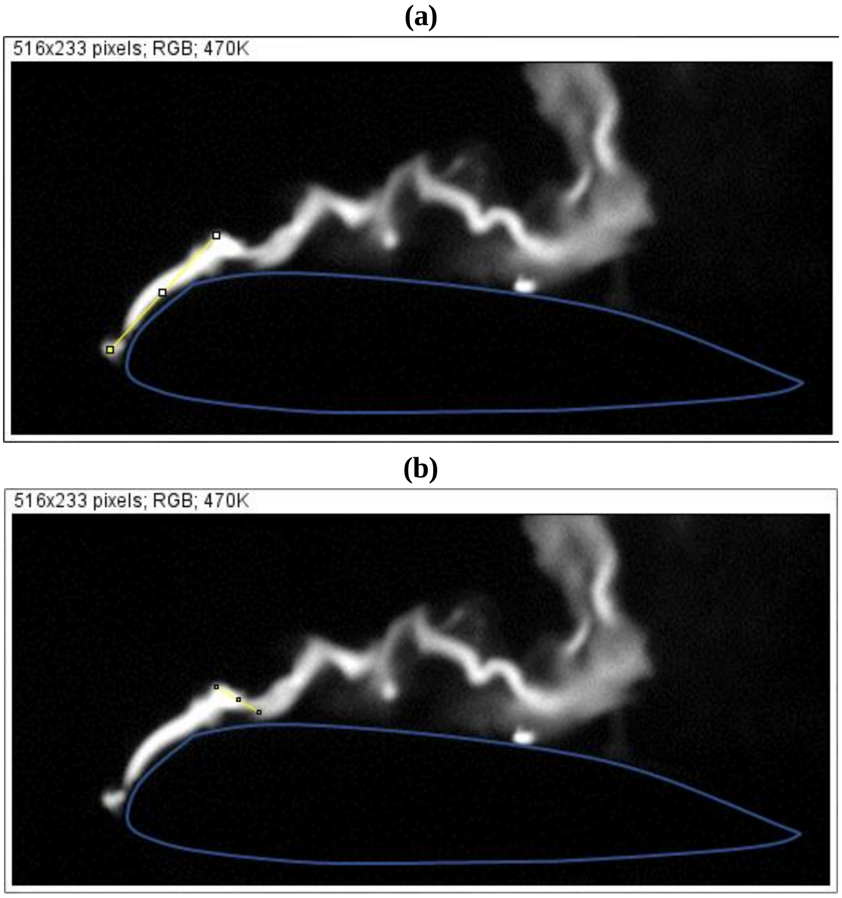
(a)

(b)

FIG. V.8 Two consecutive image adjustments of arc channel length before extinction and reattachment. The yellow lines are adjusted to the different arc column straight portions and their lengths are added to give a measure of the extinguished arc channel portion.

E. Size of the impact

The estimations of size of the impact, size of the tracks and track lengths are made measuring directly the tracks on the test sample after the experiment. It appeared to be difficult to do a precise measure mainly in the Railgun experiments where sample are propelled at high speed and impact the sandbox and thus subject to deformation. A picture of such a deformed test sample is presented in Fig. V.9.

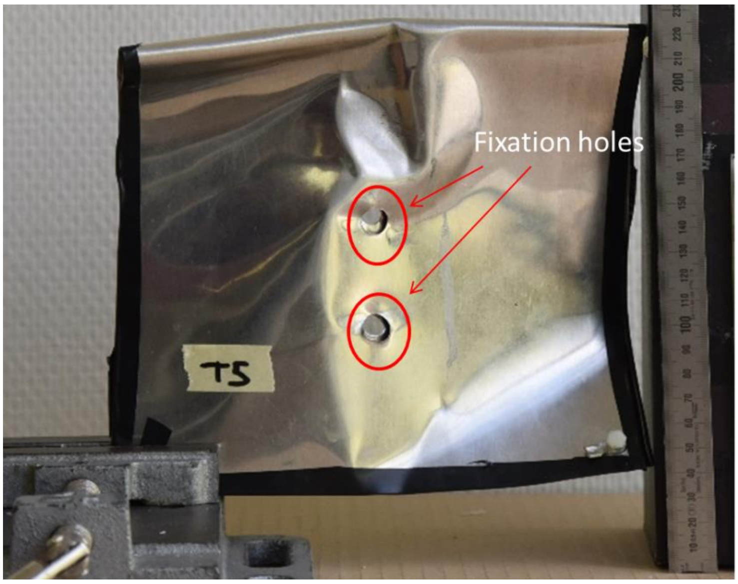

FIG. V.9 Presentation of a test sample deformed after a shot with the Railgun launcher facility.

When the electric arc strikes a point of the surface, this point presents a circular shape whose diameter represents the damages on the structure as a consequence of the different radiative and heat flux mechanisms at the arc root. It is interesting to note that even for a given current level and in the case of a jumping mode for cathodic arc root, the impacts look different as can be observed in Fig. V.10 between cathodic and anodic arc root.

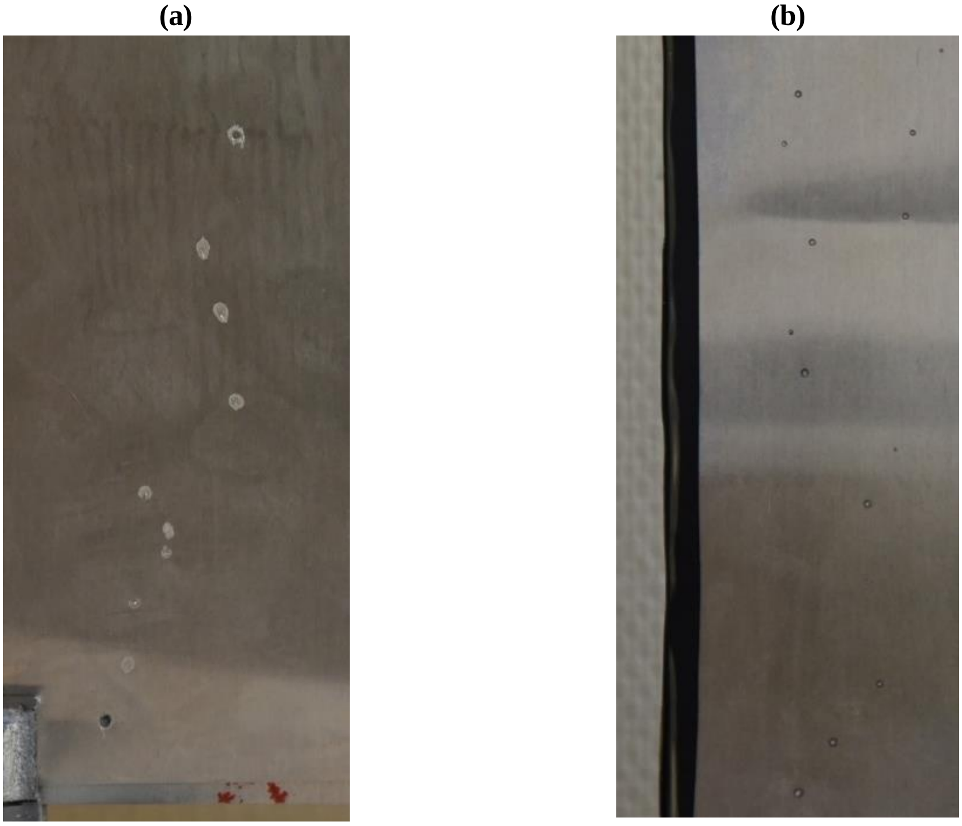

FIG. V.10 Multiple impacts left by a cathodic arc root (a) and an anodic arc root (b).

In general, cathodic arc root spots are more marked with a surrounding circle of barely melted aluminum whereas anodic arc root spots are less marked and do not present this characteristic. It is commonly accepted that these cathodic marks reflect the higher current density of the cathodic spot due to its role of providing electrons to the arc channel to maintain the discharge. For the presented study, the parameter size of the impact is reported measuring the diameter of the arc spot impacts.

F. *Size of the tracks and track length for cathodic arc roots*

When the arc strikes a point of the cathodic surface and forms an arc root before sweeping along the surface, the surface of the initial impact dimensions might appear larger or thinner than the thickness of the track once the arc root starts to move. Thus a distinction between size of the impact and size of the track is presented only for the cathodic arc roots.

The thickness of the tracks might variate along its length, especially at the end of the track where it appears to be sometime thinner. This might be due to a drop in arc root current density happening in arc extinction or a surge in the arc root speed that would produce less damage on the material test sample. A picture of this reduction of tracks thickness at the end is presented in Fig. V.11. In this case, only the maximum thickness of the track is measured. However it is interesting to present the aspect of an impact produced by the cathodic arc root that did not lead to a sweeping movement – the arc jumped to another point.

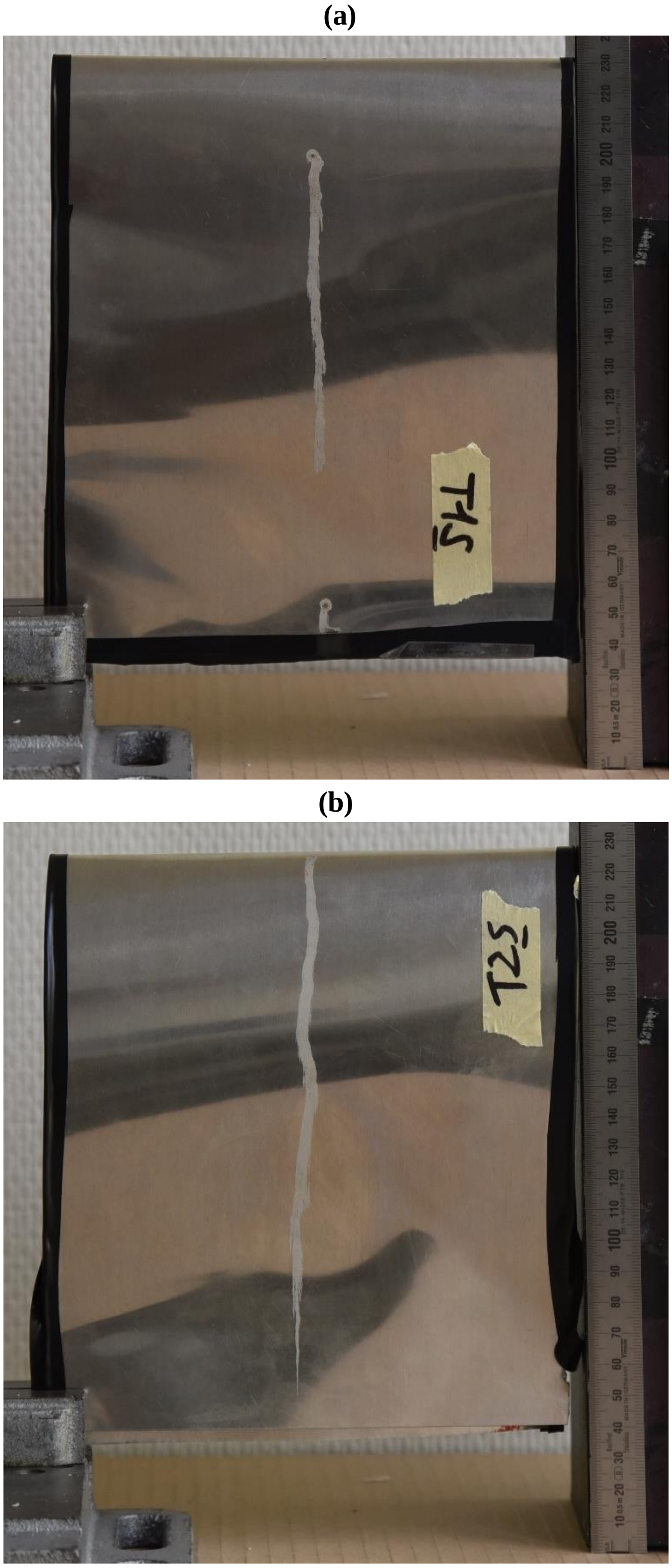
(a)
T15
(b)
T25

(c)

FIG. V.11 Presentation of different kinds of track left by cathodic arc root – normal end and discontinuous tracks (a) thinner end and continuous track (b) jumping tracks (c).

The track length is measured from the initial impact zone to the extremity of the track. It is interesting to notice that the shape of the track is not necessarily a line parallel to the relative motion axis as can be seen in Fig. V.12. Indeed, the track might present a U or a V shape, meaning that the arc root changed of direction in its motion. These non-linear shapes of trail lines are only observed for Railgun experiments.

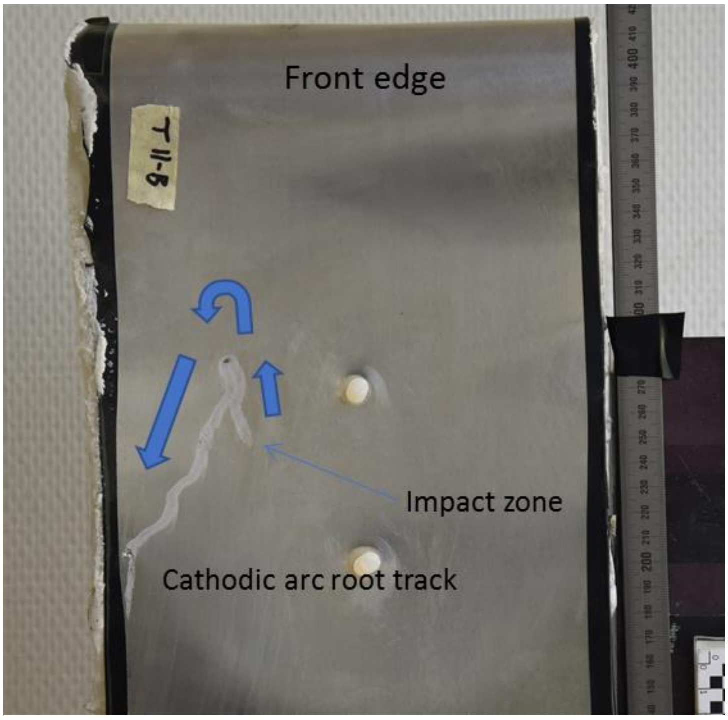

FIG. V.12 V-shape of cathodic arc root trail for Railgun experiment.

G. Relative velocity of the cathodic arc root

As described in Sec. V.2.A, the cathodic arc root presents a continuous displacement for most of the registered experiments. Examples of arc root tracking are presented in Cui et al. (2017) and Mc Bride and Jeffery (1999) using optical fibers or fast recording camera. In our experiment the arc root is tracked using the images recorded by the high-speed camera perpendicular to the direction of projectile motion and airflow and with software of image recognition.

However, in the Railgun experiment, the projectile velocity has to be removed from the measure of the arc root velocity to consider a relative speed. The measure of the projectile speed is made at the exit from the rails and has been recorded previously to drop no more than 5% in the 704 mm distance of launch recorded by the camera. An example of a typical arc root speed evolution during an experiment is given in Fig. V.13 for a Railgun experiment resorting to the software of image recognition.

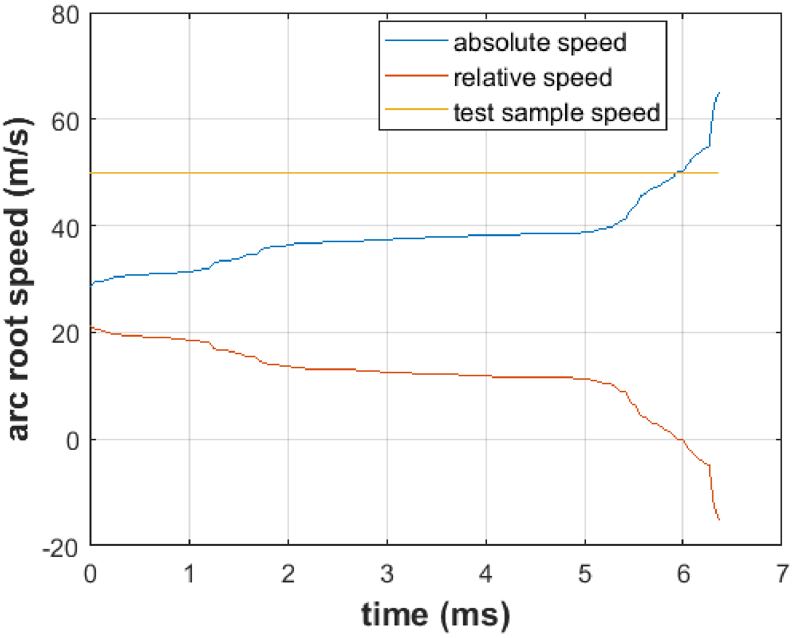

FIG. V.13 Arc root speed during a Railgun experiment. The relative speed of the arc root is the difference between the test sample speed and the absolute speed of the arc root in the laboratory frame. A negative relative speed indicates that the arc root is faster than the test sample.

In Fig. V.13, the test sample has a speed of 50 m/s and the relative speed is defined by the difference between the test sample speed and the absolute arc root speed. The relative speed becomes negative at around 6 ms: it means that the arc root is displacing even faster that the test sample at this moment. In this example, the arc root relative speed drops all along the swept-stroke but this is not always observed.

As discontinuous movements are also partially observed, some experiments of cathodic arc root showed several different continuous movements happening successively and thus several arc root tracking can be recorded in the same experiment. In this case, the resulting relative speed is averaged over all the mean speeds of the tracked arc root. It is also interesting to mention that for some records of tracking for the Railgun experiment, the arc root is able to move even faster that the projectile considering absolute velocity for a part of the sweeping motion. In the Wind tunnel simulation, the cathodic arc root is never observed to be faster than the arc column channel: the arc root is always lagging behind the arc channel in the airflow direction. This difference of behavior is complicated to interpret but definitely shows a difference of arc root behavior between the two configurations.

V.4 Arc root displacement experimental measurements, discussions and interpretations

This section is dedicated to present the results of the experimental campaign carried on in this work: the first noticeable tendencies are observed for different experimental conditions. For every configuration, from two to four experiments have been carried on and for every input parameter, a tendency was observed over two to three operative points averaging the information of experiments with a similar configuration. This already resulted in campaign involving around 50 experiments. However, the number of experiments for every configuration is not sufficient to give statistical results mainly because of the very chaotic behavior of the arc channel behavior during swept-stroke.

The results are reported in the form of tables: indeed, as the influences of four inputs – speed of relative motion, arc intensity, test sample length and initial inter-electrode distance - on six to nine physical quantities, depending on the arc root polarity, are reported with a differentiation between RGE (Railgun experiment) and WTE (wind tunnel experiment), this would have result in 45 graphs of results. It was preferred to gather the results in 14 tables and present a limited quantity of graph to better insist on a few tendencies observed.

Similarly to the Chapter IV, the chosen layout to represent the results in a box of a table takes the following form: 0.9**<2.2<**3.5 with the same meaning of the reported value. As the number of experiments for a given configuration varies from one to maximum four, it was also chosen in this chapter to only present the minimum value, the average and the maximum value of each quantity and not the dispersion or the standard deviation of the results in order not to encumber the results presentation.

A. Experimental measurements for the cathodic arc root

This section aims to present the measurements of the physical parameters described in the previous subsection depending on the speed of the relative motion, the current of the electric arc and the size of the test sample. These parameters are compared for relative motions between electric arc and aeronautical test sample produced by the Railgun facility and the Wind tunnel equipment.

A.1 Influence of speed

Tables V.1 and V.2 present the influence of speed on the physical parameters for the Railgun experiment and for the Wind tunnel experiment, respectively. For all the experiments, the electric arcs current is regulated at 400 A and the length of the test samples is 200 mm.

Table V.1 Influence of speed on physical parameters for RGE.

Speed (m/s)	**Dwell time (ms)**	**Skip distance (mm)**	**Arc voltage drop (V)**	**Size of extinguished arc (mm)**	**Track length (mm)**	**Impact size (mm)**	**Track size (mm)**	**Number of impacts**	**Arc root mean speed (m/s)**
42	0.9<**2.2**<3.5	56<**76**<132	23<**131**<260	77<**89**<100	6<**65**<105	1<**4**<5	2<**4.6**<6	1<**3**<5	**7.3**
53	0.4<**2.9**<12	10<**22**<45	50<**105**<140	24<**46**<108	9<**85**<120	3<**3.8**<5	2<**3.6**<5	2<**2.75**<5	**12.6**

Table V.1 gives the average values of the parameters over few shots – 2 for 42 m/s and 3 for 53 m/s. It can be observed that for a higher speed, the arc roots are likely to dwell more time – even if one shot at 400 A do not present reattachment - to move faster and for a longer length with thinner trails. The number of impacts is comparable but the skip distance, the size of extinguished arc and the arc voltage drop when reattachment occurs are smaller for the experiments with the highest speed. This is a mark for smaller leaps or jumps of the electric arc channel on the test sample and thus, the displacement of the arc root sweeping mode of displacement is more predominant over the jumping mode for a higher speed. However, reattachment does not always occur in the experiments for both speeds and balances this conclusion.

Table V.2 Influence of speed on physical parameters for WTE.

Airflow velocity (m/s)	**Dwell time (ms)**	**Skip distance (mm)**	**Arc voltage drop (V)**	**Size of extinguished arc (mm)**	**Track length (mm)**	**Impact size (mm)**	**Track size (mm)**	**Number of impacts**	**Arc root mean speed (m/s)**
40	0.6<**2.0**<2.9	76<**101**<140	65<**164**<290	37<**120**<213	7<**25**<55	2<**3.8**<5	2<**2.9**<4	3<**4.5**<6	**0.83**
60	0.4<**2.9**<7.7	37<**63**<100	/	**65**	10<**44**<107	2<**3.5**<4	2<**3.2**<4	1<**2.5**<4	**17.4**

Despite the maximum mean speed of the Railgun experiment (RGE) – 53 m/s - is different from the maximum velocity of airflow for the Wind tunnel experiment (WTE), the results are in average comparable and in the same order of magnitude. The trends observed previously for the RGE are globally the same and even more marked for the WTE: for a higher speed, there are fewer impacts and despite the size of the tracks are comparable for 40 m/s and 60 m/s, the arc root speed is faster for 60 m/s and almost zero for 40 m/s. Indeed it can be observed that the arc root for 40 m/s do not move with a sweeping pattern and rather only displaces by jumping.

It is interesting to observe that the dwell times and the number of impacts are similar for the two experiments in terms of value and evolution with speed even if dwell times for RGE were able to reach 13 ms. However, this similar value for dwell times seems to recover two different mechanisms: for the RGE, the skip distances are shorter and the track lengths are longer than for the WTE. Thus the relative motion is more driven by sweeping pattern than jumping pattern for the RGE than for the WTE. It also interesting to consider the evolution of relative arc root mean speed for the two configurations as represented in Fig. V.14.

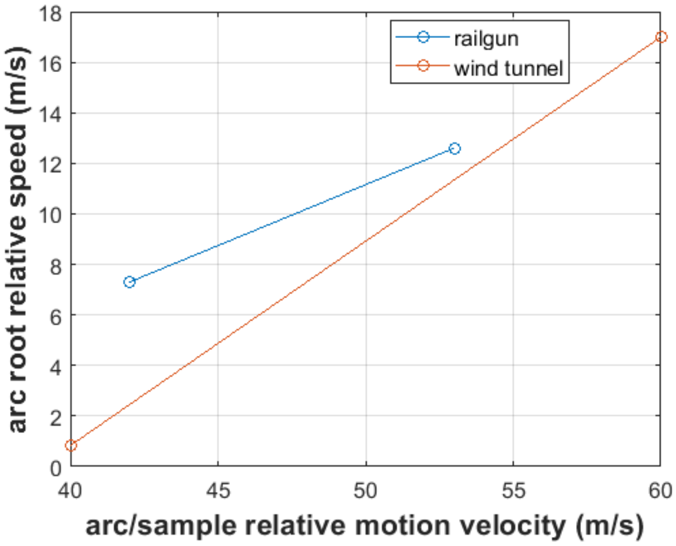

FIG. V.14 Comparison of relative arc root mean speed for RGE and WTE.

It can be observed that a difference of velocity of the airflow has a more dramatic impact on the mode of displacement of the arc root than a difference of test sample speed. Indeed, for the WTE, an increase of 20 m/s of velocity airflow changes the arc root displacement from jumping to sweeping whereas the arc root in RGE keeps a sweeping displacement even if some discontinuities can be observed. However, the velocity of airflow cannot be easily linked to the speed of the relative motion in case of the WTE since the arc channel does not present a homogeneous motion over all its length.

A possible explanation could be the predominance of the field emission for aluminum cathode: if the arc root speed is slower, it has more time to heat locally the electrode material and create a strong amount of metal vapor that increases the local electric field (Cui et al. (2017)). A strong electric field is likely to stabilize and stall the cathodic arc root despite of the arc channel motion. Thus, it produces reattachments with the extinction of longer arc channels because in the energy balance, the extinction of a longer size of resistive arc channel is required to overcome the high electric field. For a faster cathodic arc root motion, thermal effects do not have enough time to produce the same amount of local metal vapor and the local electric field is weaker and so easier to overcome with the extinction of a smaller and less resistive arc channel. Nevertheless, this explanation is not experimentally verified in the present work. Electric field measurements near the cathodic arc root, as well as the evaluation of the quantity of metal vapor formed, would need to be implemented to validate this hypothesis.

A.2 Influence of current intensity

Tables V.3 and V.4 present the influence of current on the physical parameters for the RGE and for the WTE. For the RGE, the speed of the test sample is around 50 m/s and the test sample length is 200 mm. For the WTE, the airflow velocity is 60 m/s and the test sample length is 200 mm.

Table V.3 Influence of current on physical parameters for RGE.

Current (A)	**Dwell time (ms)**	**Skip distance (mm)**	**Arc voltage drop (V)**	**Size of extinguished arc (mm)**	**Track length (mm)**	**Impact size (mm)**	**Track size (mm)**	**Number of impacts**	**Arc root mean speed (m/s)**
200	0<3.1<6.2	0<3.1<6.2	/	/	95	1<1.5<2	3	1<1.5<2	12.6
400	0.4<2.7<12	10<24<53	50<75<140	10<45<230	9<73<120	2<3.5<5	2<3.7<5	2<3.8<5	12.6
600	0.1<2.6<9.8	5<55<148	0<107<250	0<69<168	10<62<125	2.5<4.5<9	2<4.4<6	2<4.7<7	5.6

Table III gives the average values of the parameters over few shots – 2 for 200 A, 4 for 400 and 3 for 600 A. The two experiments at 200 A do not present any reattachment of the arc column on the test sample: only one arc root sweeping on the test sample all along the experiment is observed. Thus, no skip distance, arc voltage drop nor size of extinguished column can be measured.

The dwell times are similar for the three current levels but the increase of the current can be related to a higher number of impacts, a longer skip distance, a more important arc voltage drop, a longer size of extinguished arc column and longer track lengths. Thus an increase of current seems to foster the jumping mode displacement with formation and extinction of longer arc channels over the continuous sweeping displacement. It is also interesting to notice that the higher the current, the more important the sizes of the impact and of the trails. This observation may be explained by the fact that the mechanisms driving the thermal heat flux on the cathode, as the energy balance of ions and electrons that are reaching and leaving the electrode or the radiative flux, are mainly depending on the current level (Sousa-Martins et al. (2020)).

Table V.4 Influence of current on physical parameters for WTE.

Current (A)	**Dwell time (ms)**	**Skip distance (mm)**	**Arc voltage drop (V)**	**Size of extinguished arc (mm)**	**Track length (mm)**	**Size impact (mm)**	**Size track (mm)**	**Number of impacts**	**Arc root mean speed (m/s)**

200	**0.3<0.7<1.5**	**9<26<72**	**67<105<120**	**0<20<65**	**24<92<155**	**1<2<4**	**1<1.1<1.5**	**2<4.5<7**	**22.7**
400	**0.4<2.9<7.7**	**43<63<100**	/	**65**	**10<112<180**	**2<3.5<4**	**2<3.2<4**	**1<2.5<4**	**17.4**
600	**0.2<1.2<3.9**	**5<43<110**	**83<170<340**	**82<104<156**	**20<41<63**	**3<4<5**	**3<3.8<5**	**5**	**8.3**

Table V.4 presents the results for the wind tunnel. An important difference can be observed for the results at 200 A. Indeed, the average results for two experiments are considered. However these two experiments present a very different arc root displacement: one arc root is only presenting a jumping mode whereas the other presents only a continuous mode without any reattachment. Thus, only the measurements for the first experiments are reported for parameters dwell time, skip distance, arc voltage drop and size of extinguished arc. In addition, the arc voltage drops for the two 400 A experiments are not reported since one experiment do not present reattachment and voltage measurement was not obtained for the other experiment.

For the WTE, the influence of the current is less visible for the parameters of dwell time and skip distance. The arc voltage drop and size of extinguished arc appear to be increasing with current as for the RGE even if the values are globally higher in WTE. The sizes of the impacts and of the tracks are also increasing with current and the order of magnitude is the same as can be observed on the pictures of Fig. V.15. The trails for the RGE are bigger than the trails for the WTE as represented in Fig. V.16. The influence of current on the arc root mean speed is more marked in WTE than in RGE: the arc root mean speed seems to decrease with the increase of current.

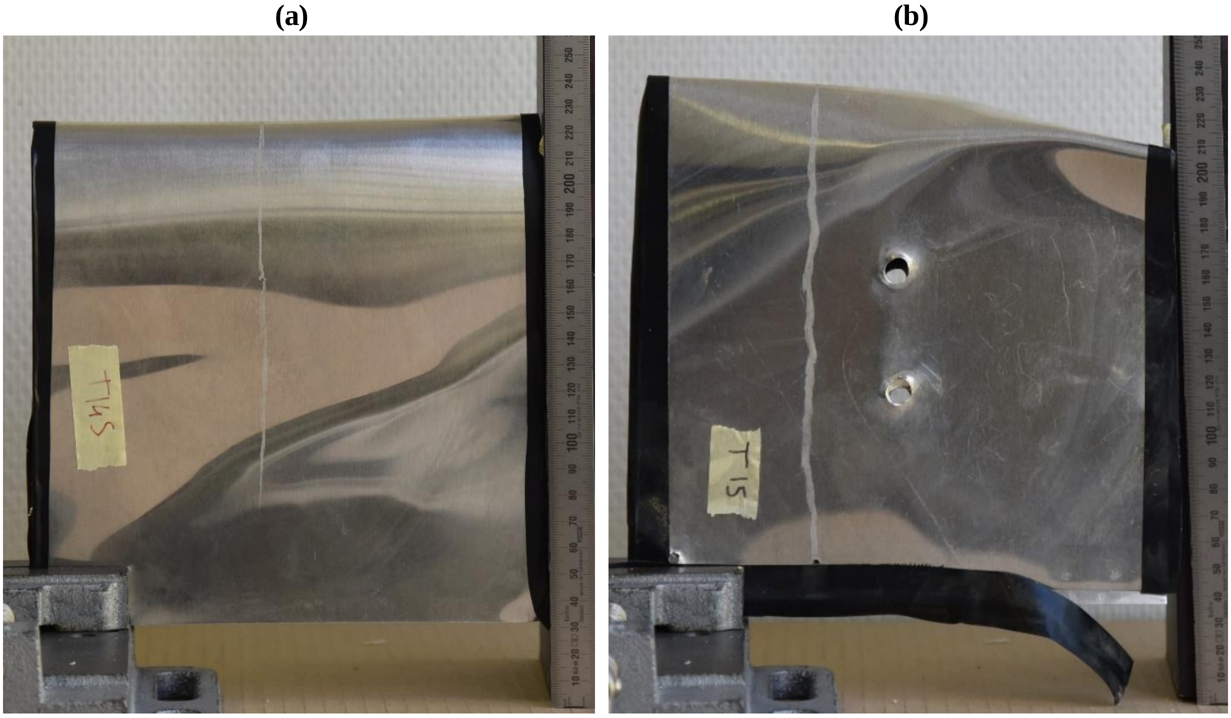

(c)

(d)

(e)

(f)

FIG. V.15 Comparison of impacts and trails for different currents for the WTE – 200 A (a), 400 (c), 600 (e) - and RGE – 200 A (b), 400 (d), 600 (f).

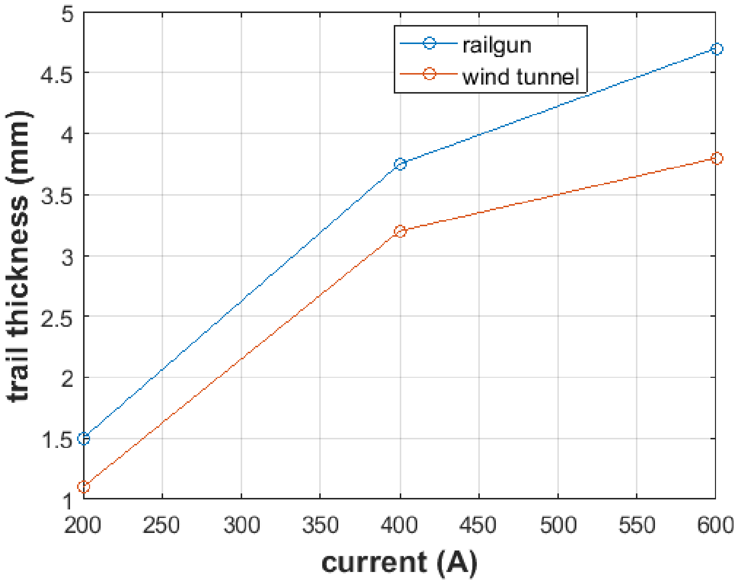

FIG. V.16 Comparison of trails thickness for RGE and WTE for three values of current – 200, 400 and 600 A.

Therefore, even if it is less evident for the WTE, mainly due to very different results for 200 A, it seems that the increase of current fosters a jumping arc root displacement mode with formation and extinction of longer arc channels and a slower relative motion of the arc root. This observation might be explained by two factors. First, a higher current produces a higher magnetic field that creates more important tortuosities. These tortuosities facilitate the rapprochement between the arc channel and test sample surface, increasing the opportunities for a reattachment to occur. Secondly, as seen in Sec. V.2, aluminum is a cold cathode and the arc root displacement is driven by electric field emission. The higher the current, the higher the required electric field on a spot to sustain the electric discharge. Thus, as the cathode arc root is limited by the diffusion of metal vapor to form charges (Cui et al. (2017)) and locally increase the electric field, a higher electric field requirement needs the formation of more metal vapor and thus slow down the arc sweeping displacement. However, as the electric arc of 600 A is higher in temperature, it is more able to form a new cathodic spot through temperature plus field emission (Lee (1959)) thus explaining the observed jumping pattern. However, these possible interpretations would need to be verified by measurements of the arc root physical properties – electric field and temperature, quantities of metal vapor.

A.3 Influence of sample length

Tables V.5 and V.6 present the influence of sample length on the physical parameters for the RGE and for the WTE. It enables to verify the influence of the test sample geometry on the swept-stroke experiment. For the RGE, the speed of the test sample is around 40 m/s and the current level is 400 A. For the WTE, the airflow velocity is 40 m/s and the current level is 400 A.

Table V.5 Influence of sample length on physical parameters for RGE.

Sample length (mm)	**Dwell time (ms)**	**Skip distance (mm)**	**Arc voltage drop (V)**	**Size of extinguished arc (mm)**	**Track length (mm)**	**Size impact (mm)**	**Size track (mm)**	**Number of impacts**	**Arc root mean speed (m/s)**
200	0.9<**2.2**<3.5	40<**76**<132	23<**131**<260	77<**89**<100	6<**65**<105	3<**4**<5	2<**4.6**<6	1<**3**<5	**7.3**
400	2.4<**5.7**<12	85<**143**<195	100<**269**<335	153<**214**<254	18<**95**<153	2<**2.9**<4	2.5<**4.9**<6	2<**3**<4	**5.8**

Table V.5 gives the average values of the parameters over few shots for RGE – 2 for 200 mm and 2 for 400 mm. The results given for 200 mm have also to be interpreted with caution since for two experiments, one presents no reattachment and the other present multiple events. However, when reattachment occurs, the values of measured dwell time, skip distance, arc voltage drop and size of extinguished are about two times more important for a 400 mm test sample than for a 200 mm test sample. The dynamic of the arc root seems to be equivalent since the size of the tracks, the arc root mean speed and the number of impact are similar but the arc root are dwelling more time in the case of a longer sample length – only considering the experiments with reattachment occurring – and the formed and extinguished electric arc are longer. This difference might be explained by the edges boundary conditions: as only few reattachments are observed, the influence of the edges and of the limited dimensions cannot be neglected. Indeed, the skip distance is in the order of magnitude of the test sample length so that the phenomenon is highly dependent on this value. This problem highlights the representability issue. An additional discussion can be done about the number of Reynolds: indeed, a sample of length two times superior implies a Reynolds number two times superior as well and affect somehow the phenomenology of the turbulences and so the arc column behavior.

Table V.6 Influence of sample length on physical parameters for WTE.

Sample length (mm)	**Dwell time (ms)**	**Skip distance (mm)**	**Arc voltage drop (V)**	**Size of extinguished arc (mm)**	**Track length (mm)**	**Size impact (mm)**	**Size track (mm)**	**Number of impacts**	**Arc root mean speed (m/s)**
200	0.6<**2.0**<2.9	25<**101**<140	65<**164**<290	37<**120**<213	7<**25**<55	2<**3.8**<5	2<**2.9**<4	3<**4.5**<6	**0.83**
400	1.7<**3.0**<6.4	9<**95**<105	65<**232**<280	44<**193**<320	8<**61**<217	1<**4.2**<5	3<**4.1**<5	1<**2.5**<5	**4.5**

The results for WTE also present the same trend between the two sizes of sample length; however the differences are less marked. The arc root mean speeds and the track length are reduced and it is visible on the recorded videos that the arc roots present a more marked jumping mode than for RGE, mainly for the 200 mm experiment. The same commentaries about the edge conditions than for the RGE can be developed. However, it was discussed in the influence of speed that the displacement mode of the electric arc is very sensitive to the airflow velocity for WTE: for airflow of 40 m/s, the predominant mode of displacement is the jumping mode for a 200 mm sample length. This observation remains partially true for the same airflow velocity and a 400 mm sample length: the number of impacts is less important and the track length is globally longer.

To give a comparison point, it is interesting to consider the work of Dobbing and Hanson (1978). They reproduced a swept-stroke experiment with a sample speed moving at 52 m/s. Their current waveform is not stable and decreases almost linearly from 700 A to zero A in 120 ms. As its mean value is 350 A over 120 ms, the results of their experiments for electrodes of aluminum can be compared with caution to our experiments with a regulated current of 400 A and test sample speed of 50 m/s for the RGE. In their experiment the test sample is 2.4 m long plate of aluminum: this dimension is more representative of a real aircraft wing that the dimensions used for our experiments and their Reynolds number is between 6 and 12 times higher than our cases.

For the cathodic arc root, they measured the skip distance and the dwell time. The average skip distance on bar aluminum cathode was 260 mm and the average dwell time was 6.5 ms. These values are around 2.5 times higher than for the sample of 400 mm for barely similar set-up condition – equivalent average current and initial inter-electrode distance of 20 cm. This important difference might be partly attributed to the difference of current waveform but the most evident difference between the two experiments is the test sample size. Thus, the representativeness of our experiments is questionable and the effect of length variation has to be explored to conclude on this point. However, the alloy of aluminum might be different for the two experiments and as discussed in Secs. V.1 and V.2, the presence and the dimension of a thin oxide layer at the surface of the metal is able to dramatically modify the arc behavior. In our case this fine layer was withdrawn by cleaning the test sample with acetone before every experiment.

A.4 Influence of initial inter-electrodes distance

Tables V.7 presents the influence of initial inter-electrodes distance – distance between the upper tungsten electrode and the test sample at first attachment - on the physical parameters for the RGE. It enables to verify the representability of an electric arc with an initial length of 200 mm before the arrival of the test sample. Indeed, the experiments have been led with an initial inter-electrodes distance that was thought to be long enough for the arc to be considered as a free arc column not influenced by the second electrode. The speed of the test sample is around 50 m/s and the current level is 400 A and the sample length is 200 mm.

Table V.7 Influence of initial inter-electrodes distance on physical parameters for RGE.

Inter-electrodes distance (mm)	**Dwell time (ms)**	**Skip distance (mm)**	**Arc voltage drop (V)**	**Size of extinguished arc (mm)**	**Track length (mm)**	**Size impact (mm)**	**Size track (mm)**	**Number of impacts**	**Arc root mean speed (m/s)**
200	0.4<**3.8**<12	10<**29**<52	52<**92**<140	24<**53**<108	9<**63**<120	1<**3.7**<5	2<**3.7**<5	2<**3**<5	**11.9**
400	**8.0**	**53**	**90**	**62**	9<**46**<83	2<**3**<4	4<**5.5**<7	**2**	**8.2**

Table V.7 gives the average values of the parameters over few shots for RGE – 4 for 200 mm and 1 for 400 mm. It is particularly complicated to interpret the difference of dwell time and skip distance since the only experiment led with an inter-electrode distance of 400 mm presents only two impacts and so an only reattachment. However, the values for arc voltage drop, size of extinguished arc, track length and arc root mean speed are comparable. Therefore, the small number of experiments at 400 mm prevents from asserting a definitive conclusion. Nevertheless the hypothesis that from a certain distance between the electrodes, the length of the arc channel does not influence the swept-stroke is plausible in regards of these first results.

B. Experimental measurements for the anodic arc root

This section aims to present the measurements of the physical parameters described in the previous subsection depending on the speed of the relative motion, the current of the electric arc and the size of the test sample for the anodic arc root. These parameters are compared for relative motions between electric arc and aeronautical test sample produced by the Railgun facility and the Wind tunnel equipment. In general, only a jumping mode displacement is observed for an anodic arc root even if for some experiments, it appears to have a continuous mode of displacement looking at the HSC. In those cases, the arc high luminous intensity prevents from delimitating clearly the shape of the arc root and of the arc channel in its vicinity and consequently to consider a leap between two arc roots. The number of impacts might be under-evaluated for this reason but the resulting tracks on the test sample demonstrate that there is no sweeping of the anodic arc root.

B.1 Influence of speed

Tables V.8 and V.9 present the influence of speed on the physical parameters for the Railgun experiment (RGE) and for the Wind tunnel experiment (WTE). For all the experiments, the electric arc currents are regulated at 400 A and the length of the test samples is 200 mm.

Table V.8 Influence of speed on physical parameters for RGE.

Speed (m/s)	**Dwell time (ms)**	**Skip distance (mm)**	**Arc voltage drop (V)**	**Size of extinguished arc (mm)**	**Size impact (mm)**	**Number of impacts**
41.5	0<**0.6**<3.6	6<**17**<60	0<**24**<75	0<**27**<80	0.5<**1.5**<2.5	12<**12.5**<13
54	0.3<**1.0**<2.6	5<**22**<60	0<**49**<180	5<**32**<83	0.5<**1.6**<3	10<**10.5**<11

Table V.8 gives the average values of the parameters over few shots – 2 for 41.5 m/s and 2 for 54 m/s. It can be observed that the dwell time, the skip distance, arc voltage drop and the size of extinguished arc are more important for a higher speed with a comparable number of impacts. Thus, for a higher speed, the anodic arc roots present a jumping mode displacement with an alternation of longer dwell times and reattachments of longer arc channels and therefore more marked leaps.

Table V.9 Influence of speed on physical parameters for WTE.

Airflow velocity (m/s)	**Dwell time (ms)**	**Skip distance (mm)**	**Arc voltage drop (V)**	**Size of extinguished arc (mm)**	**Size impact (mm)**	**Number of impacts**
40	0.2<**0.7**<2.4	3<**21**<42	0<**46**<200	15<**43**<77	0.5<**1.6**<3	9<**9.5**<10
60	0<**1.2**<5.0	2<**21**<55	0<**21**<80	0<**26**<79	0.5<**1.3**<3.5	9<**9.5**<10

The results for WTE presented in Table V.9 show a different trend. Whereas the dwell time also increases with a higher speed, the arc voltage drop and the size of extinguished arc column are smaller for a higher speed. Thus, contrary to RGE, the anodic arc root present a jumping mode displacement with an alteration of longer dwell time but reattachments of shorter arc channels and less marked leaps.

B.2 Influence of current

Tables V.10 and V.11 present the influence of current on the physical parameters for the RGE and for the WTE. For the RGE, the speed of the test sample is around 50 m/s and the test sample length is 200 m. For the WTE, the airflow velocity is 60 m/s and the test sample length is 200 m.

Table V.10 Influence of current on physical parameters for RGE.

Current (A)	Dwell time (ms)	Skip distance (mm)	Arc voltage drop (V)	Size of extinguished arc (mm)	Size impact (mm)	Number of impacts
200	0.1**<0.6<**1.5	3**<12<**35	0**<11<**45	0**<10<**30	0.5**<0.8<**1	7**<11<**15
400	0.3**<1.0<**2.6	5**<23<**60	0**<49<**180	**5<32<**83	0.5**<1.6<**3	8**<9.5<**11
600	0**<0.8<**3.1	6**<39<**145	**0<37<**90	**5<51<**83	0.5**<2.3<**6	4**<5<**6

Table V.10 gives the average values of the parameters over few shots – 2 for 200 A, 2 for 400 A and 2 for 600 A. It can be observed that for 200 A, the dwell time, the skip distance, the size of extinguished arc and the number of impacts are smaller than for the other currents: the HSC videos show that the anodic arc root is subject to multiple reattachments with small jumps. It is more difficult to compare the results for 400 A and 600 A: the 400 A experiments present fewer reattachments than the 600 A experiment but the evolution of skip distance and size of extinguished arc are not in agreement with the evolution of arc voltage drop, and consequently, no clear trend can be observed. However, the increase of impact diameter with the level of current is visible as for the cathodic arc root.

Table V.11 Influence of current on physical parameters for WTE.

Speed (m/s)	Dwell time (ms)	Skip distance (mm)	Arc voltage drop (V)	Size of extinguished arc (mm)	Size impact (mm)	Number of impacts
200	0.1**<0.5<**1.5	0**<7.5<**37	0**<30<**180	0**<23<**72	0**<0.3<**0.5	10**<12.5<**15
400	0**<1.2<**5	2**<21<**55	0**<21<**80	0**<26<**79	0.5**<1.3<**3.5	9**<9.5<**10
600	0.2**<0.6<**1.4	3**<26<**58	0**<22<**50	0**<26<**95	0.5**<1.6<**2	8**<8.5<**9

The results for WTE are even harder to interpret since no trend can be easily drawn. The parameters do not present a clear evolution with the increase of current even if the number of impacts remains higher or smaller currents and the size of impacts remains higher for higher current. Figure V.17 presents pictures of the evolution of the shape of impacts with current for RGE and WTE

(a) **(b)**

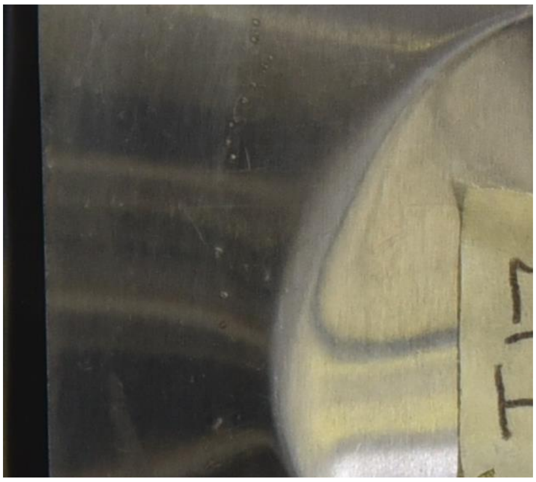

(c) **(d)**

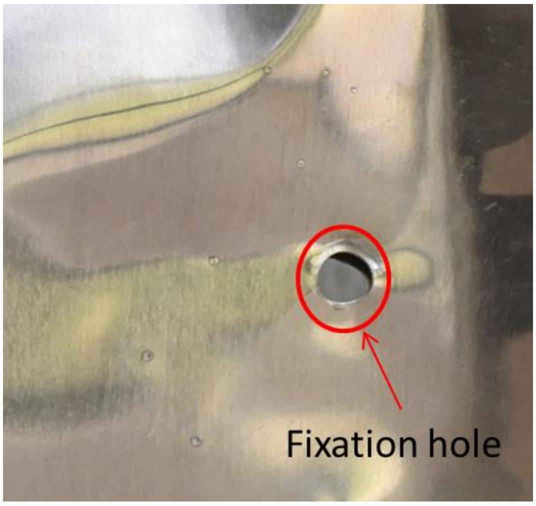

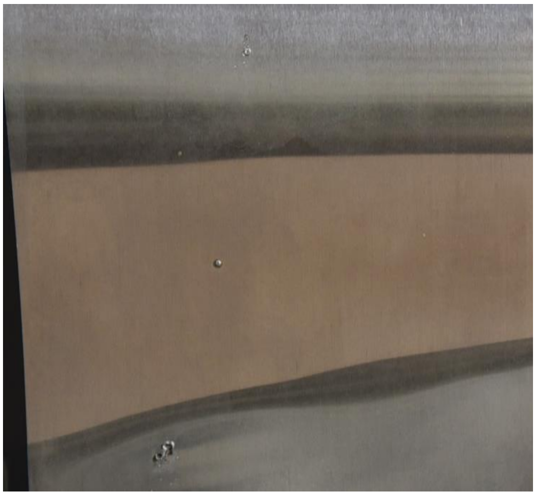

(e) **(f)**

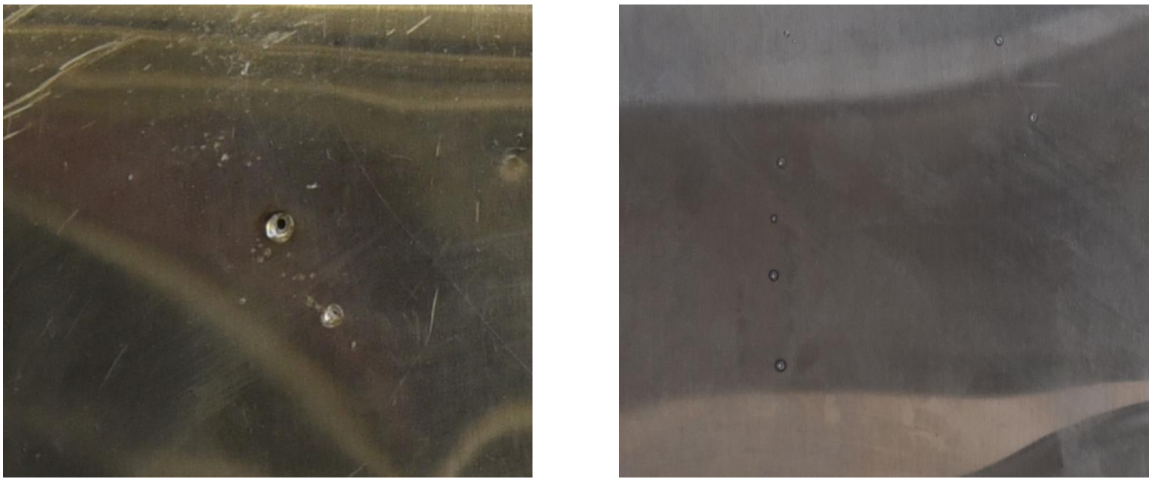

FIG. V.17 Evolution of the shape of impacts for RGE at 200 A (a), 400 A (c) and 600 (e) and WTE at 200 (b), 400 A (d) and 600 A (f).

B.3 Influence of sample length

Tables V.12 and V.13 present the influence of sample length on the physical parameters for the RGE and for the WTE. It enables to verify the influence of the test sample geometry on the swept-stroke experiment. For the RGE, the speed of the test sample is around 40 m/s and the current level is 400 A. For the WTE, the airflow velocity is 40 m/s and the current level is 400 A.

Table V.12 Influence of sample length on physical parameters for Railgun experiment

Sample Length (mm)	**Dwell time (ms)**	**Skip distance (mm)**	**Arc voltage drop (V)**	**Size of extinguished arc (mm)**	**Size impact (mm)**	**Number of impacts**
200	0<**0.6**<3.6	6<**17**<60	0<**24**<75	0<**27**<80	0.5<**1.5**<2.5	12<**12.5**<13
400	0.2<**1.9**<5.3	18<**51**<85	25<**55**<96	33<**76**<163	1<**3.0**<6	**7**

Table V.12 gives the average values of the parameters over few shots – 2 for 200 mm, 2 for 400 mm. It is visible that dwell time, skip distance, arc voltage drop, size of extinguished arc and the size of impacts are more important for a longer sample length whereas the number of impacts is higher for a shorter sample length. This is inconsistent with the larger surface of test sample available for reattachment and complicated to interpret. For a longer test sample, the anodic arc root present more marked jumps with longer dwell times for the arc roots. Even if the skip distance values remain in the order of magnitude of the test sample dimensions, the higher number of impacts in comparison of the cathodic case could imply that the edge boundaries have a more limited impact on the swept-stroke phenomenon. But as the difference of physical parameters between the two lengths of test samples is very marked, the edge boundaries do represent a limit for the representativeness of the experiment. It can also be stated that the difference of dimension of the test sample triggers a difference of Reynolds number and thus a different regime for the turbulences.

Table V.13 Influence of sample length on physical parameters for Wind tunnel experiment

Sample Length (mm)	Dwell time (ms)	Skip distance (mm)	Arc voltage drop (V)	Size of extinguished arc (mm)	Size impact (mm)	Number of impacts
200	0.2<**0.7**<2.4	3<**21**<42	0<**46**<200	14<**43**<77	0.5<**1.6**<3	9<**9.5**<10
400	0.2<**2.1**<14	15<**35**<60	8<**37**<97	15<**45**<109	0.5<**1.9**<4	**14**

The differences of results are less marked for the two different sample lengths in the WTE even if the difference of dwell time remains pronounced. The number of impacts is also logically increasing with the length of the test sample. As discussed for the RGE, even if the values of the physical parameters measured for 200 and 400 mm have the same order of magnitude, some differences – mainly the dwell time and the number of impacts - are highly different and question the representativeness of the use of a subscale test sample.

For the effects of the length of the test sample on the swept-stroke, a comparison point is also given by Dobbing and Hanson (1979) for the anodic arc root. The average skip distance on bar aluminum anode was 130 mm and the average dwell time was 2.8 ms for a 2.4 m long test sample. The skip distance is 2.4 times higher and the dwell time is 1.5 times higher than the test case for a 400 mm sample. This important difference might be partly attributed to the difference of current waveform but the most evident difference between the two experiments is the test sample size. Thus, as for the cathodic arc root, the representativeness of our experiments is questionable and the effect of length variation has to be explored to conclude on this point. However, the aluminum alloy might be different for the two experiments and the presence and the thickness of an oxide layer at the surface of the metal is able to modify dramatically the arc root behavior as discussed for the cathodic arc root.

B.4 Influence of initial inter-electrodes distance

Tables V.14 presents the influence of initial inter-electrodes distance on the physical parameters of anodic arc root for the RGE. It enables to verify the representability of an electric arc with an initial length of 200 mm at first attachment on the test sample. The speed of the test sample is around 50 m/s, the current level is 400 A and the sample length is 200 mm.

Table V.14 Influence of inter-electrodes distance on physical parameters for RGE.

Inter-electrodes distance (mm)	**Dwell time (ms)**	**Skip distance (mm)**	**Arc voltage drop (V)**	**Size of extinguished arc (mm)**	**Size impact (mm)**	**Number of impacts**
200	0.3<**1.0**<2.6	5<**23**<60	0<**49**<180	5<**32**<83	0.5<**1.6**<1.3	8<**9.5**<11
400	0.1<**0.7**<3.2	3<**19**<53	0<**27**<80	0<**20**<73	0<**1.1**<3	**13**

Table V.14 gives the average values of the parameters over few shots for RGE – 3 for 200 mm and 1 for 400 mm. Whereas the dwell times and the skip distances are similar, the arc voltage drop and the size of extinguished arc differ by almost a factor 2. Thus, the number of experiments at 400 mm is not sufficient to assert a definitive conclusion and more inter-electrodes distances would need to be tested. Nevertheless, the hypothesis that, from a certain distance between the electrodes, the initial length of the arc column does not have any impact on the swept-stroke phenomenon seems to be verified.

V.5 Summary of Railgun and Wind Tunnel results

Tables V.15 and V.16 present the main trends observed for cathodic and anodic spots during the swept-stroke with a comparison between RGE and WTE. As the orders and magnitude and the values have already been reported in the previous tables of the chapter, these new tables are thought to summarize the main difference observed for the behavior of cathodic and anodic spots between the RGE and the WTE. A simple ascending or descending arrow (↗ or ↘) represents an augmentation or a reduction of the measured parameter value between 20 % and 100 % when the input parameter varies from its lowest value to its highest value. A double ascending or descending arrow (↗↗ or ↘↘) presents an evolution that exceed 100 % of variation. A stable arrow (→) represents an evolution of value within ± 20 % and a simple line (-) represents a lack of information or the impossibility to establish a trend. In this last case, this only concerns the results for current parameter since it is the only quantity that is tested for more than two operative points.

It is also important to notice that the input parameters are not tested for a similar range of variation: for example, the relative velocity varies of 21 % for the RGE between its lowest and its highest value whereas the current varies of 200 %. Thus, the use of a uniform sign system to represent the variation of all the input parameters is limited.

Table V.15 Summary of the parameters variations of swept-stroke for cathodic arc spot**.**

RAILGUN / WIND TUNNEL	**Dwell time**	**Skip distance**	**Arc voltage drop**	**Size of extinguished arc**	**Track length**	**Impact size**	**Track size**	**Number of impacts**	**Arc root mean speed**

Relative velocity ↗	↗/↗	↘↘/↘	→/ -	↘/↘	↗/↗	→/→	↘/→	→/↘	↗/↗↗
Current ↗	→/-	↗/-	↗/↗	↗/↗↗	↘/-	↗↗/↗↗	↗/↗↗	↗↗/-	↘↘/↘↘
Sample Length ↗	↗↗/↗	↗/→	↗↗/↗	↗↗/↗	↗/↗↗	↘/→	→/↗	↗/↘	↗/↗↗
Inter-electrodes distance ↗	↗↗	↗	→	→	↘	↘	→	→	↘

Table V.16 Summary of the parameters variations of swept-stroke for anodic arc spot.

RAILGUN / **WIND TUNNEL**	**Dwell time**	**Skip distance**	**Arc voltage drop**	**Size of extinguished arc**	**Size impact**	**Number of impacts**
Relative velocity ↗	↗/↗	↗/→	↗/ ↘	→/↘↘	→/→	→/→
Current ↗	-/-	↗↗/↗↗	-/-	↗↗/→	↗↗/↗↗	↘↘/↘
Sample Length ↗	↗↗/↗↗	↗↗/↗	↗↗/↘	↗↗/→	↗↗/→	↘/↗
Inter-electrodes distance ↗	↘	→	↘	↘	↘	↗

V.6 Conclusion

This chapter aimed to quantify the behavior of cathodic and anodic arc roots for different experimental set points and to compare the results for RTE and WTE. The different input parameters are the relative velocity, the electric arc current, the sample length and the inter-electrodes distance. The physical parameters of interest chosen to attempt to characterize and describe the arc root behavior were the mean dwell time, skip distance, arc voltage drop, size of extinguished arc, size and the number of impacts for cathodic and anodic arc roots and the mean track length, size tracks and arc root velocity for cathodic arc roots only. It is important to notice that these parameters are not sufficient to give a faithful idea of the complexity of the physical processes occurring during the swept-stroke but are aimed to set a database that could be used as an entry point for validating simulation codes or predict damages for aircraft protections.

The results show that the limits between the displacement modes of the cathodic arc root - that can be continuous, partly discontinuous or jumping - are not possible to define clearly with the given criteria since over the few experiments carried for every setup, dramatic changes of behavior were observed even for a given setup. In this sense, every setup would require to be tested an important number of times for future work to reveal statistic trends. However, some trends have been observed for the considered range of input parameters:

- A higher relative speed between the electric arc and the test sample fosters a continuous sweeping mode over a jumping mode and this effect is more marked for the WTE than for the RGE.

- A higher current of the arc channel seems to favor a jumping mode and this effect is more marked for the RGE than for the WTE.

- A factor 2 on the sample dimensions dramatically affects the dimensions of the swept-stroke physical parameters. Indeed, whereas the mode of displacement does not seem to be affected, the dwell time, skip distance and length of extinguished arc channel are multiplied by two. This variation is supposed to be a consequence of the dimension of the test sample that has the same order of magnitude than the physical lengths that characterize the swept stroke phenomenon as the skip distance and the length of extinguished arc. This dramatic variation directly addresses an issue about the representability of the study. This difference is more marked for the RGE than for the WTE.

- For a factor 2 on the initial distance between the upper electrode and the test sample, the variations of the physical parameters are not marked enough to conclude that the total length of the arc channel has an impact on the local swept-stroke phenomenon when this channel measure more than few tens of cm.

For the anodic arc root, only a jumping mode is observed. However, its behavior remains complex and the experiments implemented do not present marked trends and the same conclusion than the one for cathodic arc roots can be applied: more tests need to be carried out to give confidence to the results. The following conclusions can be exposed:

- A higher relative speed between the electric arc and the test sample, the anodic arc roots present a jumping mode displacement with an alternation of longer dwell times and reattachments of longer arc channels and so more marked leaps for RGE whereas the leaps and arc channel extinctions are less important for WTE.

- The current variation provokes effects difficult to understand and compare for RTE and WTE and no real trend is observed, except the increase of size of impact with the current increase.

- A factor 2 on the sample dimensions dramatically affects the dimensions of the swept-stroke physical parameters. Indeed, the dwell time, skip distance, arc voltage drop and length of extinguished arc channel are multiplied by more than two for RGE. This variation is less marked for the WTE.

- For a factor 2 on the initial distance between the upper electrode and the test sample, the variations of the physical parameters are not marked enough to conclude that the total length of the arc channel has an impact on the local swept-stroke phenomenon when this channel measures more than a few tens of cm.

It is important to recall that the given results and partial conclusion have been conducted on a basis of a restricted number of experiments and thus do not stand as statistical study results. These results represent a first contribution to the problem that is aimed at being used as a comparative work for future experiments and computational simulations.

General Conclusion

As the modern aircraft industry is currently facing the imperatives to reduce greenhouse gas emissions and fuel consumption with the massive utilization of carbon fiber composite for future aircraft programs, the aircraft protection to lightning hazard redefines the certification process. Indeed, as the relatively low thermal and electrical conductivity of the composite materials induce more damage on the structure with the formation of an arc impact, the risk of exposition of any part of the aircraft due to the swept-stroke process forces the resort to heavy and extended metallic protections. Thus, a fine understanding of the physical processes driving the swept-stroke would enable an accurate and optimized protection for the aircraft, reducing the costs and the delays of additional experimental test certifications while respecting the imperatives of energy savings. To bring these optimizations, the models and computational codes would require an experimental reference database to validate their results or to provide physical inputs. Such a reference database is currently not available in the literature, mainly because of the experimental difficulties to implement the coupling between instruments that would reproduce the swept-stroke in lab and fine, sophisticated and accurate electrical and optical diagnostics.

Aiming at producing and study the swept-stroke in laboratory to give an insight into the physical processes driving the phenomenon, the first objective of this research work was to design, develop and experimentally implement two instruments providing the required performances: a lightning arc generator and an aeronautical test sample launcher.

- Considering the lightning arc generator:

A theoretical and experimental study comparing the performances of Buck and Buck-boost topologies as high current generators for lightning arc up to 1.5 m long and respecting the C* waveform was carried out.

As previous electric simulations of arcs showed that such C*-waveform arcs can be modeled as linear resistors from 2.4 to 8 Ω/m, a comparison of DC/DC converters Buck and Buck-boost topologies and RLC circuit, using a capacitive load as energy source, was conducted considering the lowest level of energy criterion to furnish a C*-waveform through an 8 Ω resistor. Buck topology turned out to require an initial voltage level of 3.5 kV in the capacitor whereas the Buck-boost topology only needed 1.5 kV from a capacitor bank of 100 mF.

The experimental implementations of Buck and Buck-boost topologies have been conducted focusing on the optimization of the feedback loop for the current regulation. The need to find a compromise between the accuracy of the regulation and the respect of the operative electrical parameters of every device of loop has been addressed. Amongst other problems, the transient overvoltage peak occurring at the switching-off of IGBT switch devices – that is likely to break components – is solved by designing a Snubber filter and by reducing the commutation frequency, as well as the reduction of peripheral parasitic inductance coming from the geometry.

With these last optimizations, the Buck and Buck-boost configurations have been experimentally tested and compared with the given performance criteria for a 4 Ω load resistor and for electric arcs from 0.1 to 1.5 m. Whereas the Buck configuration performed a C*-waveform through both the load resistor and electric arcs starting from 100 mm and up to a value of 1.5 m, the Buck-boost configuration turned out to be inefficient to reproduce this waveform for electric arcs. In the other hand, Buck-boost had a best performance for a static resistor of 4 Ω, requiring 1.6 kV against 2 kV for the Buck configuration. This diversion of the Buck-boost experimental performances from the simulations is likely to be caused by the limitation current in the intermediate coil that was implemented to avoid damaging the switching devices. Eventually, the 1.5 m C*-waveform electric arc has been achieved with an initial voltage of 2.3 kV and an equivalent linear resistance of 2.5 Ω/m was experimentally found for 400 A arcs. It proved also to provide an accurate regulation even in case of a restrike phenomenon.

- Considering the launcher:

An experimental implementation of an unconventional Railgun capable of launching projectiles of a few hundreds of grams at speeds up to 100 m/s with an initial voltage of around 20 V was carried out to study the interaction between an electric arc representative of the lightning C* waveform and an aeronautical aluminum test sample.

As a first overview of the means of linear propulsion showed that electromagnetic launchers are a relevant solution in terms of acceleration performances and of safety issues, a design of a railgun electric circuit was realized: this circuit differs from the conventional Railgun electric circuits since it involves high capacitive and low voltage capacitors, also referred to as Ultra capacitors in the literature. It has the direct advantage to perform a launch with an operating voltage of only 20 V which makes it safe to use since it is meant to be coupled with a high-power lightning facility.

With this electrical configuration, the experimental implementation of a Railgun has been conducted. The low operating voltage and the requirement of a good sliding contact time duration of several tens of ms raise experimental issues that have not been discussed before in the literature. The different problematic aspects are the maintenance of a good electric contact through the study of the mechanical frictions and of the electric resistance of the circuit. The addition of permanent magnets providing a supplementary magnetic field of 300 mT and the problems of overvoltage are also discussed.

Once these technical problems have been addressed, Railgun shots were operated for different initial conditions such as the payload of the projectile, the initial friction force and the peak current in order to perform ballistic studies. A model of friction forces during the shot is then developed analyzing the motion of the projectile and establishing a force balance. The model shows that a constant friction force can be assessed to fit the data after the projectile has started to move and is interesting to predict the performances of shots varying the initial conditions. Then, projectiles from 100 to 200 g have been propelled to speeds between 66 and 100 m/s. As this range of speed is in the order of magnitude of the speed of an aircraft when the risk of lightning strike is more probable – at the takeoff or the landing phases, the developed Railgun proved relevant to the study of the swept stroke phenomenon.

Once these two instruments have been developed and coupled, an experimental campaign of in-lab swept-stroke reproduction was carried-on. This was a first campaign which made it possible to define an experimental protocol and to set up the first diagnostics of optical and electrical characterizations in the allotted time. The results obtained in this work enabled us to provide first answers to the questions raised in the introduction:

- *How the arc channel is affected by the swept-stroke?*

  In a macroscopic point of view, how its shape and length varies during the phenomenon for different initial conditions? For electrical concerns, how its voltage, current and electric power varies during the motion? What is the temperature of the arc channel when it is elongated? What are the influences of the test sample speed, the arc current, the test sample length, the arc spot polarity and the initial length of the arc column on these values?

A reference database about the hydrodynamic, electrical and thermal properties of the arc channel during swept-stroke was established through high-speed cameras and electric probes measurements and optical emission spectroscopy technique.

The coupling of the lightning arc generator with the Railgun and the wind tunnel was successfully carried out with test samples presenting a NACA 0012 profile.

Electrical and optical diagnostics were coupled to evaluate the arc channel elongation and the arc power evolution during swept-stroke:

For a moving test sample, launched with the Railgun facility, the polarity of the moving arc root does not seem to influence the global elongation of the arc channel even if at 40 m/s, the anodic arc root reattachment process appears to neutralize the arc column elongation before the arc root reaches the trailing edge of the sample. It was also shown that the arc channel elongation is increasing not linearly with the test sample speed. The arc power variation over time during arc elongation was estimated to be quasi-constant with the arc current level for a mean value of 30 W/s for an average speed of 53 m/s. The test sample length and the initial arc column length did not demonstrate a noticeable influence on the arc elongation.

For a moving electric arc, blown with the wind tunnel, the polarity of the arc root does not seem to influence the global elongation of the arc channel either for different current and airflow velocity levels for a test sample of 200 mm. However, for a test sample of 400 mm, the global elongation manifestly differs between the cathodic and the anodic polarity. The arc channel elongation is also shown to be increasing not linearly with the airflow velocity. The arc power variation over time during arc elongation was estimated to also be quasi-constant with the arc current level for a mean value of 76 W/s for an average speed of 60 m/s. The test sample length presented a marked impact on the arc elongation, mainly for anodic polarity and airflow velocity of 60 m/s.

Optical emission spectroscopy technique was employed to evaluate the electric arc temperature during swept-stroke. Generally, only the effect of the current level has a significant effect on the arc temperature: in the cases of 400 A the temperature is around 11 kK, regardless of the type of relative motion or even for the static free arc column. This increases to approximately 13 kK at 600 A and drops to values between 8.2 and 9.5 kK for 200 A. The effect of others parameters such as relative velocity, polarity, initial arc column length or the type of relative motion cannot be clearly identified.

- *How the arc root motion on the test sample is affected by the swept-stroke?*

  How the mode of arc spot displacement – continuous, partially discontinuous or jumping modes – varies with the initial conditions. What is the average dwell time of an arc spot on a specific point? During a reattachment between two points of the test sample, what are the spatial and electrical characteristics of the portion of arc channel that extinguishes for the formation of a new conductive portion of arc channel? What is the skip distance between those two points? What are the size and the length of the impacts on the test samples? What are the influences of the test sample speed, the arc current, the test sample length, the arc spot polarity and the initial length of the arc column on these values?

The results show that the limits between the displacement modes of the cathodic arc root - that can be continuous, partly discontinuous or jumping - are not possible to define clearly with the given criteria since over the few experiments carried for every setup, dramatic changes of behavior were observed even for a given setup. In this sense, every setup would require to be tested an important number of times for future work to reveal statistic trends. However, some trends have been observed for the considered range of input parameters:

A higher relative speed between the electric arc and the test sample fosters a continuous sweeping mode over a jumping mode and this effect is more marked for the WTE than for the RGE.

A higher current of the arc channel seems to favor a jumping mode and this effect is more marked for the RGE than for the WTE.

A factor 2 on the sample dimensions dramatically affects the dimensions of the swept-stroke physical parameters. Indeed, whereas the mode of displacement does not seem to be affected, the dwell time, skip distance and length of extinguished arc channel are multiplied by two. This variation is supposed to be a consequence of the dimension of the test sample that has the same order of magnitude than the physical lengths that characterize the swept stroke phenomenon as the skip distance and the length of extinguished arc. This dramatic variation directly addresses an issue about the representability of the study. This difference is more marked for the RGE than for the WTE.

For a factor 2 on the initial distance between the upper electrode and the test sample, the variations of the physical parameters are not marked enough to conclude that the total length of the arc channel has an impact on the local swept-stroke phenomenon when this channel measure more than few tens of cm.

For the anodic arc root, only a jumping mode is observed. However, its behavior remains complex and the experiments implemented do not present marked trends and the same conclusion than the one for cathodic arc roots can be applied: more tests need to be carried out to give confidence to the results. The following conclusions can be exposed:

A higher relative speed between the electric arc and the test sample, the anodic arc roots present a jumping mode displacement with an alternation of longer dwell times and reattachments of longer arc channels and so more marked leaps for RGE whereas the leaps and arc channel extinctions are less important for WTE.

The current variation provokes effects difficult to understand and compare for RTE and WTE and no real trend is visible but the increase of size of impact with the current increase.

A factor 2 on the sample dimensions dramatically affects the dimensions of the swept-stroke physical parameters. Indeed, the dwell time, skip distance, arc voltage drop and length of extinguished arc channel are multiplied by more than two for RGE. This variation is less marked for the WTE.

For a factor 2 on the initial distance between the upper electrode and the test sample, the variations of the physical parameters are not marked enough to conclude that the total length of the arc channel has an impact on the local swept-stroke phenomenon when this channel measures more than a few tens of cm.

- *What are the differences of physical processes considering a swept-stroke produced by a moving test sample and a static electric arc and a swept-stroke produced by a static test sample and a moving electric arc?*

The two modes of relative motion can be produced through a test sample launcher that is developed during this work as an original instrument and through wind tunnel equipment that is able to blow the arc channel. Then, do the effects of the swept-stroke on the arc channel and on the arc motion depend on the mode of relative motion between the test sample and the electric arc?

The mode of relative motion between the electric arc and the test sample dramatically affects the arc elongation. Indeed, for a same value of test sample speed and airflow velocity of around 40 m/s, the electric arc presents an electric power variation and an arc elongation rate around 2.5 times higher for a moving electric arc with the wind tunnel than for a moving test sample with the Railgun. This difference of hydrodynamic behavior is confirmed by the direct visualization and is partially explained by the presence of a second moving arc root on the other electrode and the non-uniform displacement of the arc channel induced by the airflow in the wind tunnel experiment. The arc temperatures do not seem to be remarkably affected by the mode of relative motion.

Considering the effects of the relative motion mode on the arc root displacements, similar results presenting the same orders of magnitudes are reported. However, different evolution trends with the experimental conditions are also observed with certain experimental conditions having a more or less marked impact on the displacement mode of the arc root, as mentioned in the previous paragraph. A few important differences are also noticeable as the possibility for the arc root to be faster than the test sample in the RGE whereas the arc root is never faster than the airflow in the WTE, inferring a possible fundamental difference of physical process between the two modes of relative motion.

However, with practical considerations, the growing rate of the electric arc in the WTE drains out the energy of the arc generator faster than the one in the RGE so that the swept-stroke phenomenon carried out with RGE, besides being more representative of the in-flight conditions phenomenon, consumes less energy from the electric generator.

For future works, a few improvements could be brought to enhance the instruments performances:

- For the electric arc channel, in order to study longer electric arcs – electric arcs that are able to be elongated more before draining out the energy of the lightning generator – an increase of voltage operative level could be implemented with the addition of other capacitors. Doubling the number of capacitors would enable to multiply by two the voltage level to work with 5 kV and possibly create electric arc of 3 m long. However, the additional transient overvoltage during switching will have to be taken into account since the current IGBT model used present a limit voltage of 4.5 kV. They have to be replaced with 6.5 kV limited IGBT model. They can also be connected in series to divide the voltage level. Snubber filters would need to be redesigned to evacuate the surcharge for this new operative level. A solution that will not require the augmentation of the capacitor voltage would be to implement a Buck-boost configuration since it optimizes the use of magnetic energy: to solve the problem with the double regulation, a solution with switching technology with higher frequency could be implemented. Indeed, the frequency of the feedback loop could be enhanced with an FPGA and a faster switch. However, the power requirements prevent the use of the fastest technologies available and new improvements of SiC IGBT should be expected. Nevertheless forming a longer arc channel is not the limiting parameter for the swept-stroke study since it largely exceeds the test sample length.

- For the Railgun, in order to launch longer test sample with an increased velocity, a higher current level have to be injected into the rail. As the augmentation of the number of ultra-capacitors in parallel to increase the maximum current level has to come along an augmentation of the number of ultra-capacitors in series to increase the operating voltage, the number of ultra-capacitor has to be multiplied by a factor 4 to allow the doubling of the current level. Doubling the current level would approximatively double the speed of a test sample for a given mass or would multiply by 4 the mass for a given speed keeping the same rails length. However, the injection of a 2 times higher current would provoke different thermal and electrical constraints for the sliding contact and it is probable that a new operating point for the mechanical design and the insertion of the projectile in the rails will have to be found.

- For the wind tunnel, equipment with more power would enable to observe the phenomenon for airflow with a higher velocity, expecting to reach a speed of 100 m/s. A wider aperture would enable to study the effect of the arc channel initial length on the phenomenon. A wind tunnel presenting better flow quality (less vorticity, pressure and temperature fluctuation of the flow) could also be used.

Concerning the study of the phenomenon, the campaign carried on in this work aimed at providing the first noticeable tendencies observed with different experimental conditions. For every configuration, from two to four experiments have been carried on and for every input parameter, a tendency was observed over two to three operative points averaging the information of experiments with a similar configuration. This already resulted in campaign involving around 50 shots. However, it is evident that the number of experiment for every configuration is not sufficient to give statistical results mainly because of the very chaotic behavior of the arc channel behavior during swept-stroke. More operative points should also be used to better assess the influence of the experimental inputs. It would be also interesting to conduct experimental campaigns for different materials, for example carbon composites, and for different aeronautical test sample geometries. It is interesting to evaluate how the presence of a surface irregularity, such as a fastener or a tip, diverts the arc spot trajectory for protection design.

Beside the multiplication of experimental campaigns with the diagnostics developed in this work, the implementation of other fine diagnostics was also considered in this work and rejected for a lack of time going along with difficulties of experimental implementation or drastic data processing development. The main ideas are summarized as follow:

- Flow visualization techniques have been considered to better characterize the interaction with the electric arc and the flow. This characterization could be easily implemented with smoke technics, as we roughly mentioned it in this work, accompanied with laser-sheet illumination. This would already enable to observe differences between the fluids streamline interactions for the RGE and the WTE. To obtain more information about the absolute velocity of the streamlines, more drastic diagnostics can be developed such as the PIV (Particle Image Velocity). These technics would bring new insight into the interactions of the arc roots and the arc channel with the flow. To be more precise, the main questions of interest are about the influence of the flow behavior: does a laminar flow, a laminar separation bubble or a turbulent flow affect the arc reattachment process or the arc root displacement?

- Optical measurement spectroscopy techniques could be reinforced in order to collect data of the entire arc column and therefore evaluate the temperature of different parts of the arc channel. This could be implemented with the multiplication of the optic fibers as carried out in (McBride (1999)). The aim is to check if an increase of temperature can be measured at the vicinity of the arc spot and if the arc channel temperature is homogeneous and if we observe differences between RGE and WTE. An improvement in the spectral resolution should be considered to allow accurate measurements of line broadening and the evaluation of the electron density of the arc. Aiming to improve the time and spatial resolution, an important attention must be addressed to the synchronization of the spectra acquisition and the swept stroke phenomenon.

- A laser Thomson scattering system was also considered since it is able to measure the temperature and the electron density of the sheath region. Indeed, this technique was successfully implemented to carry on measurements on the anodic sheath for constricted arcs of 12 mm and a current of 100 A interacting with argon (Yang and Heberlein (2007)). The spatial resolution was 25 µm and the technique appears to be adapted to measure our levels of temperature and electronic density. However it requires a specific laser and light collection instruments and drastic experimental conditions to be able to measure the Thomson scattering. The synchronization of the measurements and the arc attachment on the test sample is a supplementary difficulty. Such measurements of temperature and electronic density in the sheath region of the cathodic arc root would represent an important step in the modeling of the arc root motion. Indeed, as the dimension of the airflow perturbations exceeds the length of the plasma sheaths, their impact on the complex physical processes occurring remains under discussions.

- Tomography techniques are also considered to evaluate the 3D length and shape of the electric arc. Indeed, the 2D direct visualization with the high-speed camera and the voltage measurements of the arc do not enable to measure the exact length and shape of the arc channel. This technique was already implemented in the team for 3D reconstruction of static electric arcs of 10 cm. However it requires synchronizing several high-speed cameras with the swept-stroke phenomenon and the reconstruction algorithm is computationally expensive. The precise 3D measurement of the arc channel length during reattachment, along with the electric measurements, would enable to evaluate the electric resistance, the energy and the electric field of the extinguished arc portion. The objective is to evaluate the energy loss of the electric arc during the reattachment.

- Schlieren techniques could be synchronized with reattachment to observe the formation and the displacement of the shock wave and then characterize its interaction with the flow and its influence on the arc root motion.

All these techniques aim at exploring the complex physical processes intervening in the phenomenon to enlarge the information provided by the experimental database established in this work.

Annex

This annex is aimed at presenting some models and calculations whose results are presented in Chapter III (Sec. III.1) to evaluate the possibility for a given mean of propulsion to achieve the launching of a test sample at speeds in the order magnitude of the swept-stroke phenomenon. These calculations and models are reported in the annex because they are not essential for the whole understanding of Chapter III and might encumber its fluidity. The examples are reported in this annex in their order of apparition in Chapter III. The developments aim to provide a row order of magnitude required for the physical quantities intervening in the different models with an approach corresponding to a study of feasibility. Thus the models are basic and severe simplifications are done. Considering mechanical energy release, models and calculations are developed for stretch elastic release and for compressed spring release. Considering propulsion by expulsion of a body to gain momentum, liquid and gas propulsion models are presented. Considering Electromagnetic propulsion, the performances of spinning motors are evaluated.

A. Stretched elastic release

An elastomer is a polymer with viscoelasticity and has very weak intermolecular forces, generally low Young's modulus and high failure strain compared with other materials. A sudden release of an elastomer is thus a source of potential energy that could be used to furnish kinetic energy when the elastic recovers its normal length.

To calculate the order of magnitude of the force that can apply the releasing elastic, a rod model is considered. The rod accumulates potential energy form four different kind of deformations as depicted in Fig. A.1:

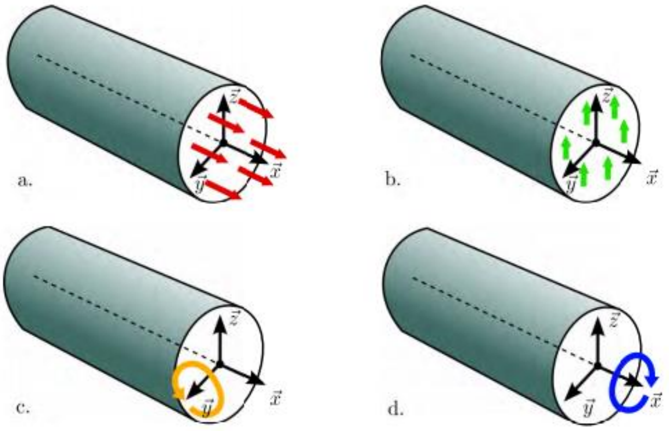

FIG A.1 Four types of rod deformation: tensile stress (a), shear stress (b), flexion (c) and torsion (d). (Roussel (2015)).

Considering that before the release, the elastic is straight elongated, flexion and torsion are not taken into account. The elastic is subject to tensile stress and to shear stress. The tensile strength of a material is the ability to undergo elongation under the application of a tensile force and tensile diagrams represent the evolution of the stress (the ratio of the tensile force on the surface of the materiel section under test) considering the relative elongation of the materiel. Referring to Fig. A.2, three domains are distinguished when the elongation increases:

- The elastic domain of reversible deformation – if the tensile force is withdrawn, the material find back its normal length – is roughly linear even if for the elastomers, the slope drops when the strain increases to more than 50% the normal length (Ramier (2004)). This linear domain introduces the Hooke's law and elasticity modulus or Young modulus E:

$$E = \frac{\sigma}{\varepsilon} \tag{A.1}$$

$$\sigma = \frac{F}{S} \tag{A.2}$$

$$\varepsilon = \frac{l - l_0}{l_0} \tag{A.3}$$

With l, l_0 , F and S being respectively the elongated length, the normal length, the tensile force and the surface of the material sample under test. For an elastomer, the Young Modulus depends on temperature and time of stressing.

- From the yield point to the ultimate strength, the deformation becomes permanent – that is to say if the stress force is withdrawn, the material under test does not find back its initial natural length and keeps a permanent elongation.
- From the ultimate tensile strength, necking appears – the surface of the material starts tightening irreversibly until fracture or breaking stress occur.

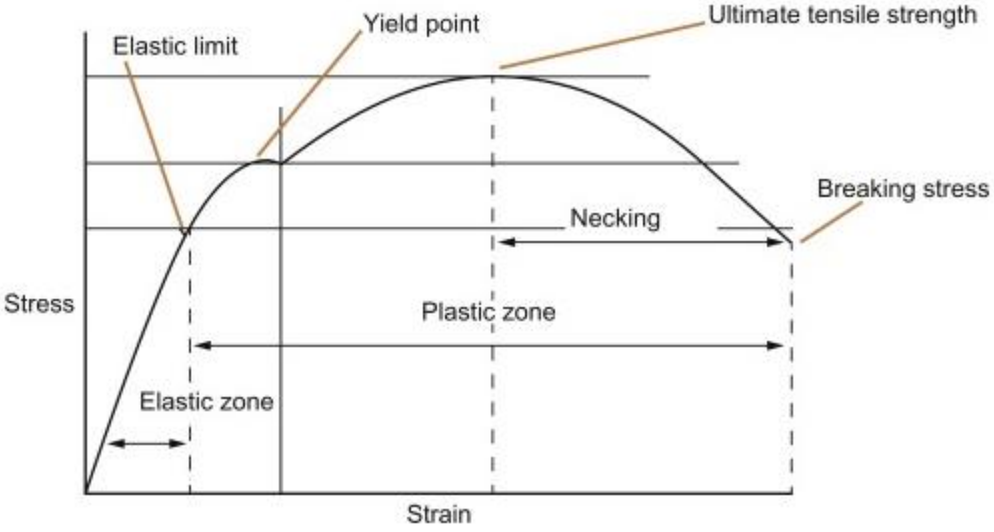

FIG. A.2 Regular stress-strain curve (Singh and Verma (2017)).

Along with the strain stress curve and the Young's modulus, a shear stress curve also represents the ability for a material to undergo elongation when subject to shear stress. The linear part of this curve defines the Shear's modulus as the ratio of the shear stress to the elongation. Landau et al. (2020) establish a link between Young's modulus and shear's modulus given G by:

$$G = \frac{E}{2(1+\nu)} \tag{A.4}$$

ν the Poisson's ratio of the material. Poisson's ratio is a measure of the Poisson effect, the phenomenon in which a material tends to expand in directions perpendicular to the direction of compression. Most materials have Poisson's ratio values ranging between 0.0 and 0.5. Incompressible materials such as elastomers have a ratio near 0.5. In our application, while elongated to its maximal possible length before entering the strain hardening area, the different parts of the elastic band are subject to both tensile stress and shear stress that can be represented using a Cauchy stress tensor referring to continuum mechanics. As the Poisson's ratio of elastomers is 0.5, the Young's modulus is three times higher than the shears modulus so that the best case scenario in terms of force requirement is when the tensile stress contribution is the only one that has to be considered. Figure A.3 represents the repartition of the different kinds of stress all along an elastic band in a configuration adapted to propel a test sample.

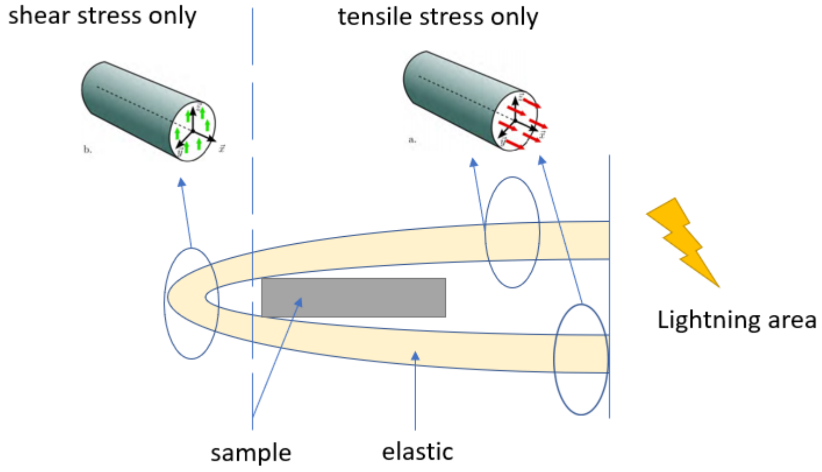

FIG. A.3 Repartition of the stress types along an elastic stretch band.

In this configuration, the maximum force F_m that can be delivered to the sample is given by:

$$F_m = (\sigma_t + \sigma_s)S = \frac{E(l - l_1 - l_0)S}{l_0} + \frac{G l_1 S}{l_0} \tag{A.5}$$

With σ_t, σ_s, S, l, l_1, l_0 being respectively the the tensile stress surface constraint, the shear stress surface constraint, the surface of the section of the elastic band, the length of elastic subject to tensile stress, the length of elastic subject to shear stress and the length of elastic without any stress. To get an upper bound approximation of this formula, the part of the elastic subject to shear stress can be neglected so that the second term is neglected and the length subject to tensile stress can be written as the total elongated length of the circuit Δl. Then the formula becomes:

$$F_m = \frac{E \Delta l S}{l_0} \tag{A.6}$$

As described in Vermorel et al. (2007), an order of magnitude of this force can be given considering that in the range of stretching between 0 and 100 percent, the elastic behavior of the rubber remains linear with a Young modulus E = 1.5 MPa and no significant hysteretic behavior or stress softening of the rubber is observed. For higher stretching, significant deviation from the ideal Hooke behavior is observed and in most experiments the stretching is been limited to the range 0 to 100 percent. So, at maximum, the factor $\Delta l/l_0$ is equal to 1 and F_m/S is theoretically equal to 1.5 MN/m^2 which would mean that a 10 cm-ray elastic rod could be able to deliver an initial acceleration of few times 1000g. However, the speed of sound in the material limits the maximum speed of stretching release.

B. Release of a spring

In order to design the dimension a spring for a propulsion application, two points have to be respected: first, the spring has to resist to the maximal loads that are applied on it – an admissible constraint resistance is usually set up. Second, the spring's stiffness has to satisfy the need for compression force.

In order to take into account the admissible constraint resistance, a section of the spring has to be considered to have a closer look on the repartition of the constraints which is described in Fig. A.4.

The application of an axial force F develops a normal force N, a tangential force T, a torsion torque M_t and a flexion torque M_f so that the total torque M is tangential and:

$$N + T = -F \tag{A.7}$$

$$M = M_t + M_f = \frac{FD}{2} \tag{A.8}$$

Where D is the spring winding diameter or mean diameter of a loop. The normal force and the flexion torque are supposed to be negligible so that T = F and Mt = FD/2.

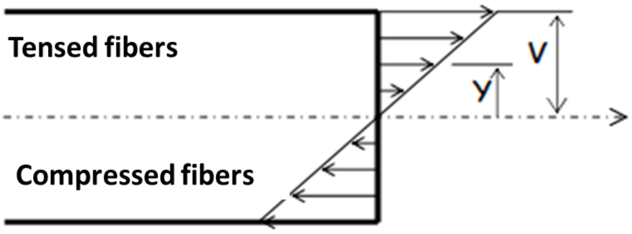

FIG. A.4 Repartition of the constraints in a spring rod subject to compression.

The formula of the constraint σ applied on the material at a distance y from the tangential axis of the section due to a torque is given in:

$$\sigma = \frac{M}{I_0} y \tag{A.9}$$

Where M is the torque and I_0 is the second area moment or area moment of inertia with respect to the center of the circle that depends only on the dimensions of the section. Considering a circle, I_0 is equal to $\pi d^4/32$ – where d is the diameter of the section - and so the maximal constraint is applied at the extremity of the circle for a distance d/2 and is equal to:

$$\sigma = \frac{16M}{\pi d^3} = \frac{8FD}{\pi d^3} \tag{A.10}$$

There is also an additional influence of a shear force which is an internal force on the section of a rod that enables the relative gliding of a section in respect to another. It's a uniformly distributed constraint that adds to the exterior compression constraint. Thus, the distribution of the constraint is not equally distributed over the spring section and is higher on the point close to the internal axis of the spring winding. This point is subject to fatigue breakdown in case of overload as can be observed in Fig. A.5.

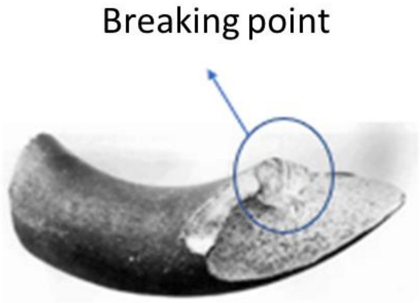

FIG. A.5 Breakdown of a spring after overload (Milan (2004)).

In order to take this additional shear force into account, the constraint is defined considering a correction factor K that only depends on the ratio η of the spring winding diameter D on the spring section diameter d and that can be either taken from empirical formulas that can be found in Wahl 1963), Duchemin (1986) or in an abacus. Therefore, the total constraint resistance is given by:

$$\sigma_m = K\sigma = \frac{8KFD}{\pi d^3} \tag{A.11}$$

The ratio η is fixed between 4 and 20 according to the norm DIN 2098; lower than 4 the spring wire cannot be wrapped anymore at cold temperature of fabrication and above 20, the relaxation of the wire no longer allows the value of the winding diameter D to return to its initial value. Thus, K is between 1.1 and 1.3 using empirical formulas from Wahl (1963) and Duchemin (1986) for those ratios.

To access to the constraint value, there is a need to evaluate the force that it is necessary to apply on the spring so that it is able to provide the test sample the acceleration and the speed that are required. Considering the model of a mass that is subject to a spring force in the assumption of a harmonic oscillator, the maximum speed of the mass is given in:

$$v = \Delta l \sqrt{\frac{k}{m}} = \sqrt{\frac{\Delta l\, F}{m}} \tag{A.12}$$

With k being the stiffness of the resulting spring so that $F = k\ \Delta l$ and Δl being the relative deformation (compression or elongation) of the spring. Thus, considering a mass of hundreds of g and a desired speed of 100 m/s, the product $\Delta l\ \times\ F$ has to be around 5 kN.m and as the laboratory length is less than 5 meters, so that Δl can be maximum around few meters maximum (not considering the complication of finding such a long spring in a first time) and F has to be around 1 to 5 kN. Thus, considering Eq. (A.11), a value of 4 for η and that the maximum admissible constraint resistance for steel - which is one of the most shear-resistant materials and the most used for spring manufacturing - that is around 400 MPa, the minimum diameter of the spring wire has to be above:

$$d > \sqrt{\frac{8KF\eta}{\pi\sigma_m}} = 6\,mm \tag{A.13}$$

This diameter is under the maximum value of 17 mm mentioned in the norm DIN 2098 that sets the dimensions that the spring has to respect to apply the usual formulas of compression springs. With this dimension for the diameter of the spring wire, a model of deformation of a massive spring has to be set to access to the maximum velocity of the waves in the spring. If it is lower than the desired speed of 100 m/s, then this method is irrelevant for the application. Considering a spring with a linear mass μ, N spires, a stiffness k and a length L on the x-axis, it is possible to prove - taking into account the horizontal displacement $s(x,t)$ of a spire through the displacement of a perturbation propagating in the axis of the spring x and applying the fundamental principle of dynamics on this spire - that $s(x,t)$ is subject to a wave Alembert equation of motion:

$$\frac{\partial^2 s}{\partial t^2} = c^2 \frac{\partial^2 s}{\partial x^2} \tag{A.14}$$

With c being the speed of propagation of the compression and elongation waves in the spring and defined by:

$$c = \sqrt{\frac{kL}{\mu}} \tag{A.15}$$

Where μ is the linear mass of the spring. For our application, $F = kL = 1 - 5$ kN and for a spring, the linear mass can be found considering that the volume of the spring wire is the product of the section to the helicoidal length which can be approximated by N times the length of a loop - πD. The length of the spring in respect to the x-axis of the spring is N times the step of the spring. The step of the spring is usually manufactured to be around $0.3D$ (Parades (2000)).

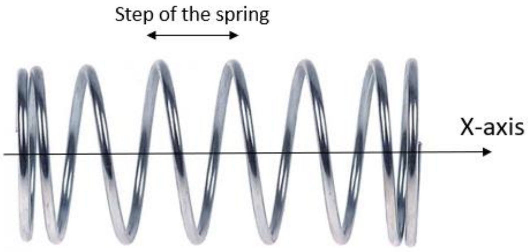

FIG. A.6 Illustration of the notion of step of a spring.

Thus, the linear mass of the spring is:

$$\mu = \frac{m_{spring}}{L} = \frac{\rho_{steel}\pi\left(\frac{d}{2}\right)^2 N\pi D}{0.3\ N\ D} = \frac{\pi^2}{0.12}\rho_{steel}d^2 \tag{A.16}$$

With ρ_{steel} being the steel density equals to 7500 kg/m^2. Considering the minimal acceptable spring wire diameter so that no breakdown occurs, the linear mass of the spring is at minimum 22 kg/m. The value is reported in Eq. (A.15) and the final limit speed of waves in the spring becomes 15 m/s which is insufficient for our application.

C. Liquid propulsion

The basic calculations are developed to have an order of magnitude of the reachable speed for our application for liquid propulsion. The set-up configuration is represented in Fig. A.7: it consists in a bottle of a volume *V* - composed by a volume *V1* of pressurized air and a volume *V2* of water - and a maximal pressure *P*, it is shaped as cylinder of section *Se* except for the nozzle section *s*. The mass of the empty bottle is m_0, the mass of the fluid is m_f and the mass flow rate is D_m the speed of propelled water is *u*.

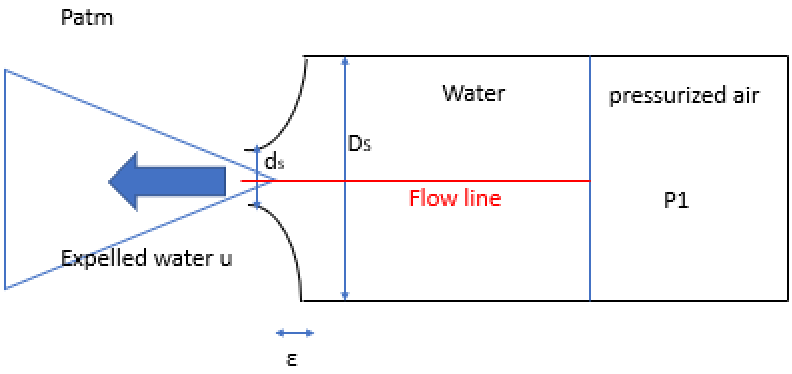

FIG. A.7 Schematic of a water rocket.

Considering the sample test has a mass m = 1kg and a speed v, the fundamental principle of dynamic applied to the system composed of the sample test and the bottle gives the equation:

$$(m + m_0 + m_f - D_m t)\frac{dv}{dt} = D_m u \tag{A.17}$$

Integrating this equation over time *t*, the speed of the rocket becomes:

$$v(t) = u\ln\left(\frac{m + m_0 + m_f}{m + m_0 + m_f - D_m t}\right) \tag{A.18}$$

The conservation of the flow rate implies:

$$v_{bottle} = u\left(\frac{d_s}{D_s}\right)^2 \tag{A.19}$$

The equation of Navier-Stokes for in a fluid without external forces is written for a flow line and constant linear acceleration a in respect to the x-axis:

$$-\frac{\partial}{\partial x}\left(\rho\frac{v^2}{2}+P\right)=\rho a \tag{A.20}$$

Then a flow line is considered between the nozzle of the bottle – where the pressure of the air is 1 atm, the speed and the acceleration are respectively u and a in the frame of the bottle – and the interface between water and pressurized air at the other extremity of the bottle – where the pressure is P_1 and the water has a speed v_{bottle}:

$$\frac{u^2}{2}\left(1-\left(\frac{d_s}{D_s}\right)^4\right)+a\varepsilon=\frac{\Delta P}{\mu} \tag{A.21}$$

Where ε is the distance of acceleration of the flow that is to say the length of variation of the bottle area from section S to s. for a bottle, it is considered that ε is 10 cm maximum and D_s is minimum 3 times d_s. As the acceleration is under 100g as it will be checked later, the factor aε is negligible in respect to $u^2/2$ thus, it can be written:

$$u=\sqrt{\frac{2\Delta P}{\mu}} \tag{A.22}$$

$$D_m=\frac{\pi}{4}d_s^2\sqrt{2\Delta P\mu} \tag{A.23}$$

Supposing that the air in the bottle is an ideal gas subject to an adiabatic relaxation, the pressure of the air in the bottle at the end of the motion, when all the water has been expelled, is:

$$P_1=P_{initial}\frac{V_1^\gamma}{V_0^\gamma} \tag{A.24}$$

$$\Delta P=P_{initial}\frac{V_1^\gamma}{V_0^\gamma}-\ P_{atm} \tag{A.25}$$

Where γ is the adiabatic index (ratio of the heat capacity at constant pressure by heat capacity at constant volume) and is equal to 1.4 for a diatomic gas. As the speed of the bottle is proportional to u and so to the square root of P but also to $\ln(m+m_0+m_f)$, there is a compromise to find between the initial volume of air and the initial volume of water to optimize the propulsion. To obtain a lower bound estimation of the values, it is considered that the pressure remains at $P_{initial}$ during the relaxation.

To estimate the need for pressure and for the quantity of water, a desired speed of 100 m/s is considered for the maximum speed of the rocket and a distance of around 5 meters for the acceleration is assumed. Thus all the water has to be expelled within a duration τ = *d/v* = 5 ms. Thus, the two following equations have to be verified:

$$v_{max}=\sqrt{\frac{2\Delta P}{\mu}}\ln\left(\frac{m+m_0+m_f}{m+m_0}\right)=100\ m/s \tag{A.26}$$

$$\tau = \frac{m_f}{D_m} = \frac{m_f}{\frac{\pi}{4} d_s^2 \sqrt{2\Delta P \mu}} = 5\, ms \tag{A.27}$$

Assuming the parameter of interest are the mass of the fluid in the bottle m_f, the initial pressure difference between the air in the bottle ΔP and the nozzle diameter d_s, Eq. (A.26) induces a non-linear relation between ΔP and m_f and Eq. (A.27) induces a non-linear equation between ΔP, $d_s$and m_f. Plots of ΔP and m_f depending on the nozzle diameter are presented in Fig. A.8 with the mass of the PET plastic bottle m_0 neglected in respect to the mass m of the sample test.

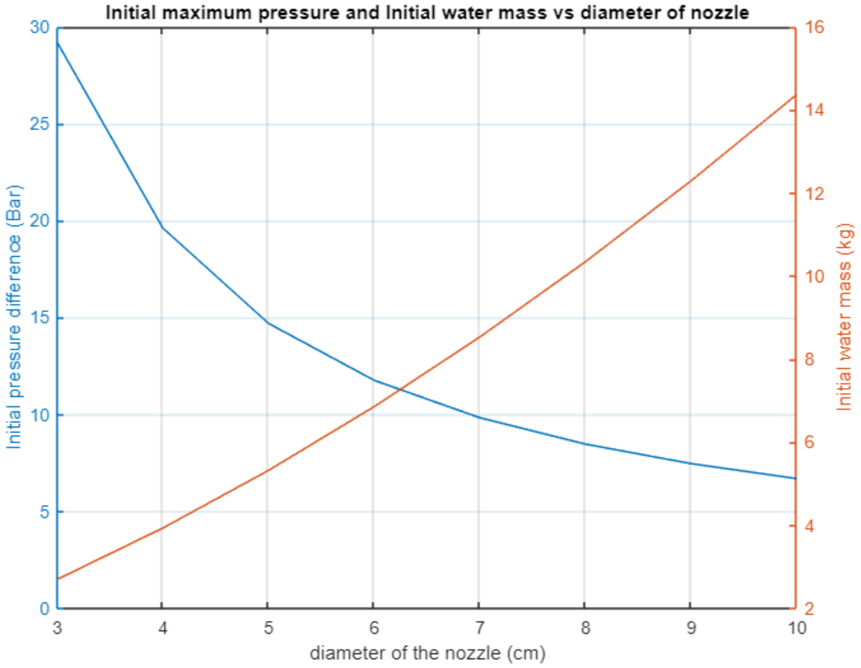

FIG. A.8 Dependence of Initial pressure and water mass in the PET bottle on the nozzle diameter to achieve the required performances of a final velocity of 100 m/s and duration of expulsion of 5 ms. Eqs (A.26) and (A.27) are used.

As the maximum acceptable pressure in a PET plastic bottle is around 10 bar, the solution that uses the minimum water is for a mass of 10 kg and a nozzle diameter of 8 cm. Thus, the rocket bottle must contain at least 10 L of water in addition to the pressurized air. So this experiment seems to be achievable but would require specific infrastructures to expel the water.

D. Gas propulsion – light gas gun

The performances of the light air gun only depend on the pressure in the gas chamber. For the modelling, it is assumed that the gas tank is an infinitely long tube with the same constant section than the one of the barrel so that reflection and refraction wave phenomenon - due to a high gradient of section size along the flow (that is likely to exist between the gas tank and the barrel) – are neglected.

The relaxation of the gas – due to the increase of volume available in the gas chamber when the test sample moves along the barrel – has to be taken into account. Indeed, even if a sabot is used to carry the projectile in the barrel so that its section fits the barrels (the pressure is thus focused on the sabot for an optimized thrust) (Plassard et al. (2011)), the section of the barrel has barely the same than the test sample's one –10cm × 1.6mm = 1.6 cm^2. So, considering the barrel is maximum 5-meter-long, the gas in the chamber gets an additional volume of 800 cm^3 which is not negligible considering the usual volumes of gas tank are in the range of 1000 to 5000 m^3 (Rahner et al. (2014)). Thus, the evolution of pressure during the relaxation is given by:

$$P = P_0\left(\frac{V_0}{V_0 + Sx}\right) = \frac{P_0}{1 + \frac{Sx}{V_0}} \tag{A.28}$$

Where P is the pressure inside the gas chamber, P_0 is the initial pressure in the gas chamber, V_0 the volume of the gas chamber - the initial volume available for the pressurized gas. S is the section of the barrel and x the displacement of the sample test in the barrel.

A relation between the pressure in the barrel and the velocity is obtained with the conservation laws of an isentropic flow relaxation of an ideal gas (it is considered that the relaxation is reversible and adiabatic). p, ρ, u and γ being respectively the pressure, the density, the speed and the heat capacities ratios of the gas along the relaxation, the mass conservation, the momentum conservation and the isentropic transform sets:

$$\frac{d\rho}{\rho} = \frac{du}{u} \tag{A.29}$$

$$\rho u du = -dp \tag{A.30}$$

$$\frac{dp}{p} = \gamma\frac{d\rho}{\rho} \tag{A.31}$$

Mixing those laws, [Siegel 1965] gives the link of the pressure in the gas and the speed of the sample test during the relaxation:

$$P = P_0\left(1 - \frac{(\gamma - 1)v}{2a_0}\right)^{\frac{2\gamma}{\gamma-1}} \tag{A.32}$$

Where v is the speed of the projectile and a_0 is the speed of sound in the pressurized gas whose expression is given by the relation:

$$a_0 = \sqrt{\frac{\gamma p}{\rho}} \tag{A.33}$$

The pressure of the gas in front of the projectile also differs from the atmospheric pressure due to the velocity of the projectile. This pressure is given in [Siegel 1965]:

$$P_r = P_{atm}\left(1 + \left(\frac{v}{a_1}\right)^2\frac{\gamma_1(\gamma_1 + 1)}{4} + \frac{\gamma_1 v}{a_1}\sqrt{1 + \frac{\gamma_1(\gamma_1 + 1)}{4}\left(\frac{v}{a_1}\right)^2}\right) \tag{A.34}$$

P_{atm} being the atmospheric pressure and a_1, γ_1 being the speed of sound and the heat capacities ration of atmosphere. Then, the performances of the light gas gun are obtained by integrating the fundamental equation of mechanics and looking for the lowest required pressure to achieve a muzzle speed of 100 m/s for a barrel of maximum 5 meters:

$$\frac{dv}{dt} = \frac{(P - P_r)S}{m} \tag{A.35}$$

P being given by Eq. (A.33) and P_r by Eq. (A.34). So considering a_0 and a_1 are respectively 1000 m/s and 340 m/s, $\gamma_1 = \gamma = 1.4$ and a volume of 5 L for the gas tank, the minimum required pressure for the desired performance is 100 Bar (140 Bar for 1L of gas tank volume). Figure A.9 shows the evolution of the projectile velocity and displacement in respect to time in the barrel.

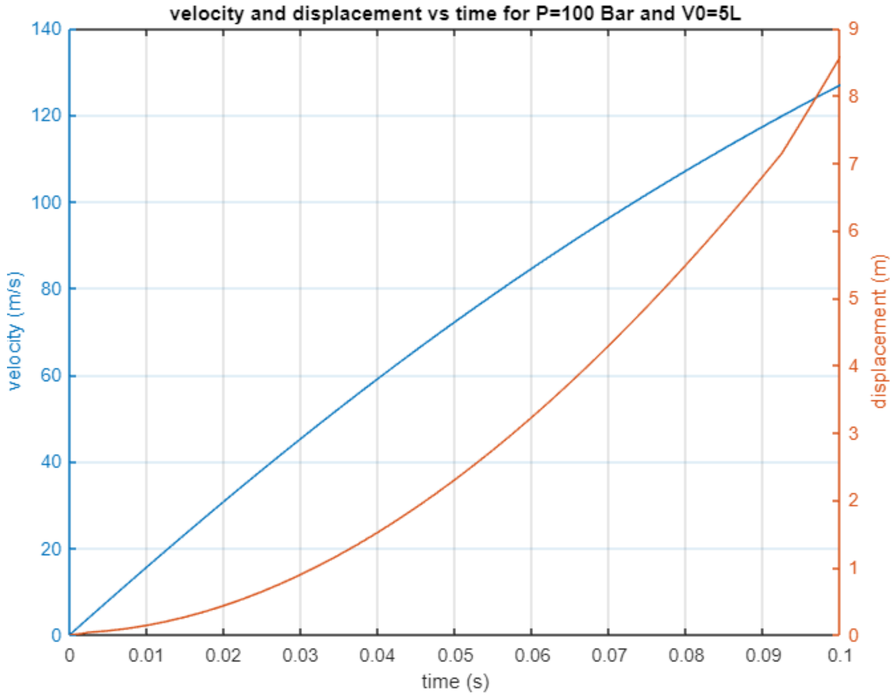

FIG. A.9 Projectile velocity and displacement over time for an initial pressure of 100 bar and a tank volume of 5 L. Eqs. (A.35) and (A.36) are used.

The price for such an equipment for a two-stages light gas gun that does not require the complex ergol injection system of a chemical gas gun, is estimated about 150000 euros by the builder Thiot.

E. Spinning motor

A first configuration would consist in the objective to reach a velocity of 100 m/s as a linear motion from the dragged sample test considering a mean constant acceleration during the movement to simplify the calculation. The motor is supposed to start from zero rad/s and the transformation factor – that is the ratio of the motor's speed of rotation on the linear speed of the sample test – due to the screw tread of the reducer, is constant. The resistive torque coming from the frictional dragging of the sample test is neglected. The movement equation of the motor with a total inertia moment brought back to the motor axis is thus:

$$\left(J_m + m\left(\frac{v}{\Omega_\mathrm{m}}\right)^2\right)\frac{d\Omega_m}{dt} = T_m \tag{A.36}$$

J_m being the inertia moment of the motor, m the mass of the sample test, $\Omega_m$the rotational speed of the motor, v the linear speed of the sample test and T_m the motor torque. The constant transformation factor leads to:

$$\frac{d\Omega_m}{dt} = \frac{d\left(v\frac{\Omega_m}{v}\right)}{dt} = v\frac{d\left(\frac{\Omega_m}{v}\right)}{dt} + \frac{dv}{dt}\frac{\Omega_m}{v} = \gamma\frac{\Omega_m}{v} \tag{A.37}$$

Where γ is the linear acceleration of the sample test. Thus, combining Eqs. (A.36) and (A.37) gives:

$$T_m = \gamma(J_m\frac{\Omega_m}{v} + \frac{m}{\frac{\Omega_m}{v}}) \tag{A.38}$$

The minimal torque that has to be provided by the motor is given in deriving the previous equation in respect to the transformation factor. The following parameters are obtained:

$$T_m = 2\gamma\sqrt{m\,J_m} \tag{A.39}$$

$$\frac{\Omega_m}{v} = \sqrt{\frac{m}{J_m}} \tag{A.40}$$

So, considering that the maximum desired velocity is 100 m/s, the motor has a required power P_m of:

$$P_m = T_m\Omega_m = 2\gamma\sqrt{m\,J_m}\,v\sqrt{\frac{m}{J_m}} \tag{A.41}$$

As γ is a constant factor, assuming l is the displacement of the test sample, the additional following equations are taken into account:

$$v = \gamma t \tag{A.42}$$

$$l = \gamma\frac{t^2}{2} \tag{A.43}$$

$$\gamma = \frac{v^2}{2l} \tag{A.44}$$

Thus,

$$P_m = \frac{mv^3}{l} \tag{A.45}$$

As it is required that a speed of 100 m/s is reached within a distance of five meters, a motor with a peak power of 200 kW minimum is required. This order of magnitude for electric motors is common and its price is around 15 000 euros.

A second configuration would consist in the objective to reach a velocity of 100 m/s as a linear motion from the dragged sample test considering the motor is active and spinning at its nominal velocity without any resistive charge. The wire linked to the sample test is attached suddenly to the reducer axis and the dragging of the sample test creates an additional inertia to the motor. The movement equation of the motor with a total inertia moment brought back to the motor axis is thus:

$$\Omega_m \frac{d\left(J_m + m\left(\frac{v}{\Omega_m}\right)^2\right)}{dt} = T_m \tag{A.46}$$

With the previous hypothesis, it results in:

$$\frac{m}{\Omega_m}\frac{dv^2}{dt} = T_m \tag{A.47}$$

Thus, integrating this equation in respect to time, it is shown that:

$$v = \sqrt{\frac{T_m \Omega_m}{m} t} \tag{A.48}$$

The displacement of the sample test is thus given integration the previous equation in respect to time:

$$l = \frac{2}{3}\sqrt{\frac{T_m \Omega_m}{m}} t^{\frac{3}{2}} \tag{A.49}$$

Using the previous equations with the desired performances of a linear speed of 100 m/s reached within 5 meters, the required power becomes:

$$P_m = \frac{2}{3}\frac{mv^3}{l} \tag{A.50}$$

This results in a minimum required power of 133 kW whose price in also around 15000 euros. This technology is thus affordable. But the main difficulty of this application is to assure that the dragging of the test sample doesn’t represent a safety issue: an inextensible wire of minimum 5 meters is getting wrapped around an axis at a speed of several thousand rounds per minute. Supposing the wire is detached or cut during the motion, its movement will become unpredictable and dangerous.

Résumé en français

Introduction

La foudre est l'un des risques météorologiques courants les plus méconnus et les moins compris et représente par conséquent un défi majeur pour la sécurité en vol. Les dommages causés aux aéronefs par la foudre se présentent sous la forme de points d'impacts - appelés pieds d'arc - ancrés sur le revêtement métallique ou de trous centimétriques dans le fuselage. Ce risque est pris en compte dès la conception de l'avion puisque le phénomène se produit statistiquement toutes les 1000 à 10000 heures de vol, soit environ une ou deux fois par an. Comme le foudroiement implique à la fois un canal de foudre statique dans le référentiel terrestre et un aéronef en mouvement, il y a un déplacement du pied d'arc sur le revêtement de l'aéronef. Ce phénomène est appelé « le balayage ». Le déplacement peut être soit continu avec le glissement du pied d'arc le long de l'aéronef, soit discontinu avec le saut des pieds d'arcs. Par conséquent, toutes les pièces de l'aéronef sont exposées au risque de dommages électriques et thermomécaniques directs lors du passage du pied d'arc. Par exemple, en 1976, un Boeing 747 d'Iran Air s'est écrasé à cause de l'explosion d'un réservoir de carburant provoquée par un arc issu d'un effet direct de la foudre. Ainsi, même si pour un revêtement métallique, les propriétés électriques et thermiques permettent une bonne répartition des dommages directs sur la structure de l'avion, le balayage a été étudié expérimentalement avec des essais en laboratoire. Néanmoins, les difficultés expérimentales pour reproduire des tests représentatifs en laboratoire - principalement dues aux exigences de vitesse des échantillons d'essai, environ 100 m/s pendant les phases de décollage ou d'atterrissage, et les premières conclusions sur la majoration des dommages produits par le phénomène spécifique de balayage - ont provoqué la suspension des essais au milieu des années 80. Cette suspension a ralenti la compréhension des processus physiques intervenant lors du phénomène car cela n'était pas indispensable pour assurer la sécurité de l'avion.

La nécessité de comprendre ce phénomène est cependant repassée au premier plan ces dernières années : en effet, les constructeurs aéronautiques cherchent à remplacer le revêtement métallique par des matériaux composites en fibre de carbone. Cette décision vise à la fois à réduire le poids du véhicule et à faciliter la fabrication à grande échelle. Par exemple, les masses du Boeing 787 Dreamliner et de l'Airbus A350XWB sont composées d'environ 50 % de fibre de carbone et Airbus envisage ce matériau pour optimiser les performances des ailes de l'A321 neo. Cependant, les composites en fibres de carbone sont plus vulnérables aux impacts de la foudre car leurs conductivités thermique et électrique relativement faibles ne permettent pas une répartition équilibrée des dommages sur la totalité de la structure de l'avion. Ces composites sont utilisés dans des pièces exposées à la formation de pieds d'arc en raison du phénomène de balayage. Pour contrer cela, des treillis métalliques supplémentaires ont été conçus et testés expérimentalement pour la certification foudre, ce qui a augmenté les coûts et les délais de fabrication. À l'avenir, cette phase de conception et de test de la protection foudre pourrait être accélérée grâce à une compréhension plus approfondie des processus physiques intervenant lors du balayage. Au cours des dernières décennies, de nombreux modèles de simulation de balayage ont été développés pour prédire le comportement de l'arc de foudre et ainsi concevoir des protections plus précises. Cependant, aucune mesure expérimentale significative du phénomène n'a produit de caractérisation physique fine du comportement de l'arc et du déplacement du pied d'arc afin de fournir des données d’entrée ou de comparaison aux résultats des codes de simulation pour leur validation. Il n'y a pas non plus de base de données de référence décrivant l'évolution des quantités physiques en jeu lors du phénomène pour des conditions expérimentales pertinentes. Au-delà de l'établissement d'une telle base de données, le but de ce travail est de donner un aperçu sur les processus physiques régissant le phénomène. Ainsi, nous estimons que les interrogations suivantes doivent être résolues :

- Comment le canal d'arc est-il affecté par le balayage ?

D'un point de vue macroscopique, comment sa forme et sa longueur varient au cours du phénomène pour différentes conditions initiales ? Pour les grandeurs électriques, comment sa tension, son courant et sa puissance varient pendant le mouvement ? Quelle est la température du canal d'arc lorsqu'il est allongé ? Quelles sont les influences de la vitesse de l'échantillon, du courant d'arc, de la longueur de l'échantillon, de la polarité du pied d'arc et de la longueur initiale de la colonne d'arc sur ces valeurs ?

- Comment le mouvement du pied d'arc sur la surface de l’échantillon d’essai est-il affecté par la course balayée ?

Comment le mode de déplacement – continu, partiellement discontinu ou par saut – du pied d'arc varie-t-il avec les conditions initiales ? Quel est le temps de maintien moyen du pied d'arc sur un point spécifique de l’échantillon ? Lors d'un rattachement entre deux points, quelles sont les caractéristiques spatiales et électriques de la portion de canal d'arc qui s'éteint pour la formation d'une nouvelle portion conductrice de canal d'arc ? Quelle est la distance de saut entre ces deux points ? Quelles sont la taille et la longueur des impacts sur les échantillons de test ? Quelles sont les influences de la vitesse de l'échantillon, du courant d'arc, de la longueur de l'échantillon,, de la polarité du pied d’arc et de la longueur initiale de la colonne d'arc sur ces valeurs ?

- Quelles sont les différences entre les processus physiques en jeu pour le balayage produit par un échantillon d'essai en mouvement et un arc électrique statique d’un part et pour le balayage produit par un échantillon d'essai statique et un arc électrique en mouvement d’autre part ?

Les deux modes de mouvement relatif peuvent être produits grâce à un lanceur d'échantillons d'essai original qui est développé au cours de ce travail et grâce à un équipement de soufflerie capable de mettre en mouvement le canal d'arc. Ainsi, les effets du balayage sur le canal d'arc et sur le mouvement du pied d'arc dépendent-ils du mode de mouvement relatif entre l'échantillon d'essai et l'arc électrique ?

Afin de répondre à ces questions, les défis techniques suivants doivent être surmontés :

- Mettre en place un dispositif expérimental permettant de reproduire en laboratoire le phénomène de balayage : des instruments expérimentaux doivent être développés et couplés pour assurer une réalisation représentative du phénomène respectant les ordres de grandeurs des quantités physiques en jeu. Il s'agit de générer des arcs électriques représentatifs d'un canal de foudre et de développer une installation compacte pour un lanceur capable de propulser des matériaux d'essais aéronautiques à la vitesse d'un avion dans les dimensions du laboratoire. Afin de mener un nombre important d'expériences pour produire des résultats quantitatifs, les performances des instruments doivent assurer une bonne répétabilité et présenter une robustesse suffisante. Comme les instruments développés ne sont pas disponibles dans l'industrie et ne sont pas la reproduction d'instruments déjà existants dans la littérature, une attention particulière sera portée sur leur caractérisation expérimentale et sur l’optimisation de leurs performances.

- Développer des méthodes et des diagnostics expérimentaux pour mesurer les propriétés physiques du canal d'arc de foudre et du déplacement du pied d'arc lors du balayage une fois le banc d'essai validé. Les principales grandeurs considérées pour la caractérisation et l'analyse de l'arc électrique lors du balayage sont les propriétés hydrodynamiques, électriques et thermiques du canal. Les propriétés macroscopiques et électriques du déplacement du pied d’arc sont également étudiées.

L'ensemble de ces instruments et toutes les informations acquises permettront de constituer une base de données expérimentale qui servira à la comparaison et à la validation des codes de calcul. D’autre part, en dehors de l’étude du balayage, ce travail présente également un apport pour la recherche dans les domaines de l'électronique de puissance et de l'électrotechnique puisque sur les trois années de thèse, plus de deux ans ont été consacrés au développement des deux instruments qui sont couplés pour effectuer le balayage. De tels instruments présentent des performances non atteintes dans l'industrie ou dans la littérature pour la technologie correspondante. Ces instruments consistent en :

- Un générateur de foudre régulé en courant adapté d'une topologie Buck capable de reproduire des arcs de foudre de 1,5 m respectant la forme d'onde du courant de foudre continu de la norme aéronautique ARP5412A.

- Un lanceur électromagnétique de type Railgun augmenté à basse tension capable de propulser des échantillons aéronautiques de 100 à 250 g à des vitesses comprises entre 60 et 100 m/s sous 2 m d’accélération.

Le développement de ces instruments et les problèmes expérimentaux spécifiques rencontrés lors de leur mise en œuvre sont discutés et analysés dans le présent travail. Cette thèse abordera les problématiques évoquées au cours des cinq chapitres suivants :

Le Chapitre I consiste en un aperçu du phénomène de la foudre en général et spécifiquement dans le contexte des impacts sur les aéronefs avec une description des procédés de protection des aéronefs. Une présentation plus précise du phénomène de balayage est proposée et les études expérimentales et théoriques antérieures sont passées en revue et discutées. L'accent est également mis sur les autres domaines de la physique des plasmas qui ont pour objet d’étude un arc électrique mobile. Les principaux objectifs de ce travail sont ensuite présentés pour conclure le chapitre.

Le Chapitre II décrit le développement, la mise en œuvre et l'analyse du générateur de foudre. L'arc électrique de foudre balayé est d'abord modélisé comme un composant électrique pour établir les performances électriques requises en termes de conception de générateur. Différentes topologies de circuits de commutation sont ensuite comparées théoriquement et mises en œuvre expérimentalement pour créer un générateur régulé en courant. Des protections contre les surtensions sont développées et ajoutées aux circuits. Ainsi, des arcs électriques avec une taille atteignant jusqu'à 1,5 m et respectant la norme foudre aéronautique sont réalisés en laboratoire.

Le Chapitre III se consacre au développement, à la mise en œuvre et à l'analyse d'un moyen de propulsion permettant de lancer des échantillons aéronautiques à la vitesse d'un avion dans laboratoire compact. Après une comparaison de différentes technologies, un principe de lanceur électromagnétique de type Railgun augmenté est adapté pour une application basse tension. Le générateur électrique et l'équipement mécanique sont présentés et des problèmes expérimentaux comme le contact glissant sont approfondis. Un modèle pour évaluer les performances du lanceur à partir de mesures balistiques et de courant est développé.

Le Chapitre IV étudie la caractérisation du canal de l'arc électrique pendant le balayage : le générateur d'arcs électriques est couplé au Railgun ou à une soufflerie. Des caméras à grande vitesse et des mesures électriques sont utilisées pour évaluer les propriétés hydrodynamiques et électriques du canal d'arc en extension. Des techniques de spectroscopie d'émission optique sont mises en œuvre pour évaluer la température de l'arc. Les influences de la vitesse, de l'intensité de l'arc, de la polarité du pied d'arc, de la longueur de l'échantillon et de la longueur initiale de la colonne d'arc sur ces propriétés sont mesurées et discutées. Les résultats sont comparés pour un échantillon de test mobile avec Railgun et un arc déplacé avec une soufflerie.

Le Chapitre V traite plus spécifiquement du déplacement du pied d'arc sur l'échantillon d'essai aéronautique pendant le balayage. Un aperçu rapide des expériences d'arcs électriques en mouvement dans la littérature et des processus physiques se produisant à la cathode et à l'anode est présenté. Grâce à des caméras à grande vitesse et à des mesures électriques, l'interaction entre l'arc et le matériau, ainsi que le comportement électrique et spatial du pied d'arc, sont caractérisés. Les influences de la vitesse, de l'intensité de l'arc, de la longueur de l'échantillon et de la longueur initiale de la colonne d'arc sur ces valeurs sont discutées. Les résultats sont comparés pour un échantillon de test mobile avec Railgun et un arc déplacé avec une soufflerie.

Conclusion générale

Alors que l'industrie aéronautique moderne est actuellement confrontée aux impératifs de réduction des émissions de gaz à effet de serre et de la consommation de carburant qu’elle compte partiellement résoudre par l'utilisation massive de composites en fibre de carbone pour les futurs programmes aéronautiques, la protection des aéronefs contre le risque foudre redéfinit le processus de certification. En effet, comme les conductivités thermique et électrique relativement faibles des matériaux composites provoquent davantage de dommages sur la structure lors de la formation d'un impact d'arc, le risque d'exposition de toute partie de l'avion dû au processus de balayage oblige l’ajout de protections métalliques pesantes. Ainsi, une compréhension fine des processus physiques à l'origine du balayage permettrait une protection précise et optimisée de l'aéronef, et ainsi une réduction des coûts et des délais des certifications d'essais expérimentaux supplémentaires tout en respectant les impératifs d'économies d'énergie. Pour apporter ces optimisations, les modèles et codes de calcul nécessiteraient une base de données expérimentale de référence pour valider leurs résultats ou fournir des paramètres physiques d’entrée. Une telle base de données de référence n'est actuellement pas disponible dans la littérature, principalement en raison des difficultés expérimentales à mettre en œuvre le couplage entre des instruments qui reproduiraient le balayage en laboratoire et la synchronisation du phénomène avec des diagnostics électriques et optiques sophistiqués et précis.

Visant à produire et à étudier le balayage en laboratoire pour présenter un aperçu des processus physiques à l'origine du phénomène, le premier objectif de ce travail de recherche était de concevoir, développer et mettre en œuvre expérimentalement deux instruments présentant les performances requises : un générateur d'arc de foudre et un lanceur d'échantillons d'essais aéronautiques.

- Considérant le générateur d'arc de foudre :

Une étude théorique et expérimentale comparant les performances des topologies Buck et Buck-boost en tant que générateurs d’arcs de foudre jusqu'à 1,5 m de long et respectant la forme d'onde C* a été réalisée.

Comme les simulations électriques précédentes d'arcs ont montré que de tels arcs avec la forme d'onde C * peuvent être modélisés comme des résistances linéaires de 2,4 à 8 Ω/m, une comparaison des topologies de convertisseurs DC/DC Buck et Buck-boost et du circuit RLC utilisant une charge capacitive comme source d'énergie, a été menée en considérant le critère de plus bas niveau d’énergie initial pour fournir une forme d'onde C* en courant à travers une résistance de 8 Ω. La topologie Buck s’avère nécessiter un niveau de tension initial de 3,5 kV dans le condensateur alors que la topologie Buck-boost ne nécessite que 1,5 kV à partir d'une batterie de condensateurs de 100 mF.

Les implémentations expérimentales des topologies Buck et Buck-boost ont été menées en se concentrant sur l'optimisation de la boucle de rétroaction pour la régulation du courant. La nécessité de trouver un compromis entre la précision de la régulation et le respect des limites de fonctionnement électriques chaque appareil a été abordée. Parmi les problèmes, celui du pic de surtension transitoire se produisant à l'ouverture des dispositifs de commutation IGBT - qui est susceptible de casser des composants - est résolu en concevant un filtre Snubber et en réduisant la fréquence de commutation, ainsi qu'en réduisant l'inductance parasite périphérique venant de la géométrie du circuit et de la disposition relative des composants.

Avec ces dernières optimisations, les configurations Buck et Buck-boost ont été testées expérimentalement et comparées aux critères de performance donnés pour une résistance de charge de 4 Ω et pour des arcs électriques de 0,1 à 1,5 m. Alors que la configuration Buck a permis de produire une forme d'onde C* à travers une résistance équivalente statique et des arcs électriques à partir d'une longueur de 100 mm et atteignant jusqu'à 1,5 m, la configuration Buck-boost s'est avérée inefficace pour reproduire cette forme d'onde pour des arcs électriques. En revanche, la topologie Buck-boost présentait de meilleures performances pour une résistance équivalente statique de 4 Ω, nécessitant seulement 1,6 kV contre 2 kV pour la configuration Buck. Cettte inadaptation des performances expérimentales du cirucit Buck-boost pour un arc électrique comparée aux résultats des simulations est susceptible d'être causé par l'addition d'une boucle de limitation de courant dans la bobine intermédiaire qui a été mis en place pour éviter d'endommager les dispositifs de commutation. Finalement, un arc électrique de forme d'onde C* de 1,5 m a été produit avec une tension initiale de 2,3 kV et une résistance linéaire équivalente de 2,5 Ω/m pour l'arc a été déterminée expérimentalement pour un courant d'arc de 400 A. La topologie Buck s'est également avérée fournir une régulation en courant précise même en cas de phénomène d'extinction de l'arc.

- Considérant le lanceur:

Une mise en œuvre expérimentale d'un Railgun non conventionnel capable de lancer des projectiles de quelques centaines de grammes à des vitesses allant jusqu'à 100 m/s avec une tension initiale d'environ 20 V a été réalisée pour étudier l'interaction entre un arc électrique représentatif de la foudre C* forme d'onde et un échantillon de test d'aluminium aéronautique.

Un premier tour d'horizon des moyens de propulsion linéaire ayant montré que les lanceurs électromagnétiques sont une solution pertinente en termes de performances d'accélération et de problématiques de sécurité, une conception d'un circuit électrique railgun a été mise en place. Ce circuit diffère des circuits électriques Railgun conventionnels puisqu'il intègre des condensateurs de type haute capacité et basse tension appelés ultra condensateurs dans la littérature. Il a l'avantage direct d'effectuer un lancer avec une tension de fonctionnement de seulement 20 V ce qui rend son utilisation plus sûre en cas de couplage avec une installation de forte puissance telle que le générateur de foudre développé auparavent.

Avec cette configuration électrique, la mise en œuvre expérimentale d'un Railgun a été menée. La faible tension de fonctionnement et l'exigence d'un temps de contact glissant important de plusieurs dizaines de ms posent des problèmes expérimentaux qui n'ont pas été abordés auparavant dans la littérature. Les différents aspects problématiques sont le maintien d'un bon contact électrique avec la prise en compte des frottements mécaniques et de la résistance électrique du circuit. L'ajout d'aimants permanents fournissant un champ magnétique supplémentaire de 300 mT et les problèmes de surtension lors de la formation d’arcs secondaires sont également abordés.

Une fois ces problèmes techniques résolus, des tirs de Railgun ont été opérés pour différentes conditions initiales telles que la charge du projectile, la force de frottement initiale et le niveau maximal de courant afin de réaliser des études balistiques. Un modèle des forces de frottement lors du tir est ensuite développé en analysant le mouvement du projectile et en établissant un bilan des forces. Le modèle montre qu'une force de frottement constante peut être utilisée pour s'adapter aux données expérimentales une fois que le projectile a commencé à se déplacer et est intéressante pour prédire les performances des tirs avec une variation des conditions initiales. Ensuite, des projectiles de 100 à 250 g ont été propulsés à des vitesses comprises entre 66 et 100 m/s. Comme cette plage de vitesse est de l'ordre de grandeur de la vitesse d'un aéronef lorsque le risque de foudroiement est plus probable – au décollage ou à l'atterrissage – le Railgun développé peut être utlisé pour l’étude du balayage.

Une fois ces deux instruments développés et couplés, une campagne expérimentale de reproduction du balayage en laboratoire a été menée. Il s'agissait d'une première campagne qui a permis de définir un protocole expérimental et de mettre en place les premiers diagnostics de caractérisations optiques et électriques dans les délais impartis. Les résultats obtenus dans ce travail nous ont permis d'apporter des premières réponses aux questions posées en introduction :

- *Comment le canal d'arc est-il affecté par le balayage ?*

D'un point de vue macroscopique, comment sa forme et sa longueur varient au cours du phénomène pour différentes conditions initiales ? Pour les grandeurs électriques, comment sa tension, son courant et sa puissance varient pendant le mouvement ? Quelle est la température du canal d'arc lorsqu'il est allongé ? Quelles sont les influences de la vitesse de l'échantillon, du courant d'arc, de la longueur de l'échantillon, de la polarité du pied d'arc et de la longueur initiale de la colonne d'arc sur ces valeurs ?

Une base de données de référence sur les propriétés hydrodynamiques, électriques et thermiques du canal d'arc lors du balayage a été établie grâce à des mesures de caméras à grande vitesse et de sondes électriques et à l’utilisation de méthodes de spectroscopie d'émission optique.

Le couplage du générateur d'arc de foudre avec le Railgun et la soufflerie a été réalisé avec succès avec des échantillons aéronautiques présentant un profil NACA 0012.

Des diagnostics électriques et optiques ont été couplés pour évaluer l'allongement du canal d'arc et l'évolution de la puissance de l'arc lors de la course balayée :

Pour un échantillon d'essai mobile, projeté avec le lanceur Railgun, la polarité du pied d'arc mobile ne semble pas influencer l'allongement global du canal d'arc même si à 40 m/s, le processus de rattachement du pied d'arc anodique semble neutraliser l'allongement de la colonne avant que le pied n'atteigne le bord de fuite de l'échantillon. Il a également été montré que l'allongement du canal d'arc n'augmente pas de manière linéaire avec la vitesse de l'échantillon d'essai. La variation temporelle de la puissance de l'arc lors de l'allongement de l'arc a été estimée quasi-constante avec le niveau de courant de l'arc avec une valeur moyenne de 30 W/s pour une vitesse de 53 m/s. La longueur de l'échantillon d'essai et la longueur initiale de la colonne d'arc n'ont pas démontré d'influence notable sur l'allongement de l'arc.

Pour un arc électrique en mouvement, déplacé par soufflerie, la polarité du pied d’arc ne semble pas influencer l'allongement global du canal d'arc non plus pour différents niveaux de courant et de vitesse d'écoulement d'air avec un échantillon d'essai de 200 mm de long. Cependant, pour un échantillon de 400 mm, l'allongement global diffère notablement entre la polarité cathodique et anodique. L'allongement du canal d'arc s'avère également non linéaire avec le paramètre vitesse du flux d'air. La variation temporelle de la puissance de l'arc pendant son allongement a été estimée comme étant également quasi-constante avec le niveau de courant de l'arc avec une valeur moyenne de 76 W/s pour une vitesse de 60 m/s. La longueur de l'échantillon d'essai a présenté une influence marquée sur l'allongement de l'arc, principalement pour la polarité anodique et une vitesse d’écoulement d’air de 60 m/s.

La technique de spectroscopie d'émission optique a été utilisée pour évaluer la température de l'arc électrique pendant le balayage. En général, seul l'effet du niveau de courant a un effet significatif sur la température de l'arc : pour un niveau de 400 A, la température est d'environ 11 kK quelque soit le dispositif de mise en mouvement relatif ou même pour la colonne d'arc libre statique. Cette température augmente à environ 13 kK à 600 A et chute à des valeurs comprises entre 8,2 et 9,5 kK pour 200 A. L'effet d'autres paramètres tels que la vitesse relative, la polarité, la longueur initiale de la colonne d'arc ou le dispositif de mise en mouvement relatif ne peut pas être clairement identifié.

- *Comment le mouvement du pied d'arc sur la surface de l’échantillon d’essai est-il affecté par la course balayée ?*

Comment le mode de déplacement – continu, partiellement discontinu ou par saut – du pied d'arc varie-t-il avec les conditions initiales ? Quel est le temps de maintien moyen du pied d'arc sur un point spécifique de l’échantillon ? Lors d'un rattachement entre deux points, quelles sont les caractéristiques spatiales et électriques de la portion de canal d'arc qui s'éteint pour la formation d'une nouvelle portion conductrice de canal d'arc ? Quelle est la distance de saut entre ces deux points ? Quelles sont la taille et la longueur des impacts sur les échantillons de test ? Quelles sont les influences de la vitesse de l'échantillon, du courant d'arc, de la longueur de l'échantillon, de la polarité du pied d’arc et de la longueur initiale de la colonne d'arc sur ces valeurs ?

Les résultats montrent que les limites entre les modes de déplacement du pied d’arc cathodique - modes continu, partiellement discontinu ou par saut - ne peuvent pas être clairement définies avec les critères donnés car sur les quelques expériences réalisées pour chaque configuration, des changements spectaculaires de comportement ont pu être observés pour une configuration donnée. Pour engendrer des conclusions tranchées, chaque configuration nécessiterait d'être testée un nombre important de fois afin d’aboutir à des tendances statistiques. Cependant, certaines tendances ont été observées pour la gamme de paramètres d'entrée considérée :

Une vitesse relative plus élevée entre l'arc électrique et l'échantillon favorise un mode de balayage continu par rapport à un mode par saut et cet effet est plus marqué pour le WTE que pour le RGE.

Un courant plus élevé du canal d'arc semble favoriser un mode de saut et cet effet est plus marqué pour le RGE que pour le WTE.

Un facteur 2 sur les dimensions de l'échantillon affecte considérablement les dimensions des paramètres physiques de balayage. En effet, alors que le mode de déplacement ne semble pas affecté, le temps de maintien, la distance de saut et la longueur du canal d'arc éteint sont multipliés par deux. Cette variation est supposée être une conséquence de la dimension de l'échantillon qui est du même ordre de grandeur que les longueurs physiques mesurées qui caractérisent le phénomène de balayage comme la distance de saut et la longueur d'arc éteint. Cette variation spectaculaire remet directement en question la représentativité de l'étude pour l’échelle réelle. Cette différence est plus marquée pour le RGE que pour le WTE.

Pour un facteur 2 sur la distance initiale entre l'électrode et l'échantillon, les variations des paramètres physiques ne sont pas assez marquées pour conclure que la longueur totale du canal d'arc a un impact sur le phénomène de balayage local lorsque ce canal mesure plus de quelques dizaines de cm.

Pour le pied d'arc anodique, seul un mode de déplacement par saut est observé. Cependant, son comportement reste complexe et les expériences mises en œuvre ne présentent pas de tendances marquées et la même conclusion que celle pour les pieds d'arc cathodiques peut être dessinée : davantage de tests doivent être effectués pour consolider les résultats. Les conclusions suivantes peuvent cependant être exposées au vu des premiers résultats :

Pour une vitesse relative plus élevée entre l'arc électrique et l'échantillon, les pieds d'arc anodiques présentent un déplacement en mode par saut avec une juxtaposition de temps de maintien plus longs et de rattachements de canaux d'arc plus longs et donc de sauts plus marqués pour le RGE alors que les sauts et extinctions de canaux d'arc sont moins importants pour le WTE.

La variation de courant provoque des effets difficilement appréhendables et comparables pour le RTE et le WTE et aucune véritable tendance n'est visible à part l'augmentation de la taille de l'impact avec l'augmentation du niveau de courant.

Un facteur 2 sur les dimensions de l'échantillon affecte considérablement les dimensions des paramètres physiques de balayage. En effet, le temps de maintien, la distance de saut, la chute de tension d'arc et la longueur du canal d'arc éteint sont multipliés par plus de deux pour le RGE. Cette variation est moins marquée pour le WTE.

Pour un facteur 2 sur la distance initiale entre l'électrode et l'échantillon, les variations des paramètres physiques ne sont pas assez marquées pour conclure que la longueur totale du canal d'arc ait un impact sur le phénomène de balayage local lorsque ce canal mesure plus de quelques dizaines de cm.

- *Quelles sont les différences entre les processus physiques en jeu pour le balayage produit par un échantillon d'essai en mouvement et un arc électrique statique d’un part et pour le balayage produit par un échantillon d'essai statique et un arc électrique en mouvement d’autre part ?*

> *Les deux modes de mouvement relatif peuvent être produits grâce à un lanceur d'échantillons d'essai original qui est développé au cours de ce travail et grâce à un équipement de soufflerie capable de mettre en mouvement le canal d'arc. Ainsi, les effets du balayage sur le canal d'arc et sur le mouvement du pied d'arc dépendent-ils du mode de mouvement relatif entre l'échantillon d'essai et l'arc électrique ?*

Le mode de mouvement relatif entre l'arc électrique et l'échantillon d'essai affecte considérablement l'allongement de l'arc. En effet, pour une même valeur de vitesse de l'échantillon et de vitesse d'écoulement du flux d'air d'environ 40 m/s, l'arc électrique présente une variation de puissance électrique et un taux d'allongement d'arc environ 2,5 fois plus élevés pour un arc électrique en mouvement avec la soufflerie que pour un échantillon de test en mouvement avec le Railgun. Cette différence de comportement hydrodynamique est confirmée par la visualisation directe et s'explique en partie par la présence d'un deuxième pied d'arc mobile sur l'autre électrode et le déplacement non uniforme du canal d'arc provoqué en partie par la non-uniformité de l'écoulement du flux d'air dans l'expérience en soufflerie. Les températures de l'arc ne semblent pas être remarquablement affectées par le mode de mouvement relatif.

Considérant les effets du mode de mouvement relatif sur les déplacements de pied d'arc, des résultats similaires présentant les mêmes ordres de grandeurs sont rapportés. Cependant, des tendances d'évolution différentes avec les conditions expérimentales sont également observées avec certaines conditions expérimentales ayant un impact plus ou moins marqué sur le mode de déplacement du pied d'arc, comme mentionné au paragraphe précédent. Quelques différences importantes sont également perceptibles comme la possibilité que le pied d'arc soit plus rapide que l'échantillon d'essai dans le RGE alors qu'il n'est jamais plus rapide que l'écoulement d'air dans le WTE, ce qui souligne une possible différence fondamentale de processus physique entre les deux modes de mouvement relatif.

Cependant, avec des considérations pratiques, le taux de croissance temporel de l'arc électrique dans le WTE draine l'énergie du générateur d'arc plus rapidement que celui du RGE, de sorte que le phénomène de balayage réalisé avec le RGE, en plus d'être plus représentatif du phénomène dans les conditions de vol, consomme moins d'énergie du générateur électrique. Cela permet d'obtenir expérimentalement un balayage plus long pour une même énergie initiale.

Pour les travaux futurs, quelques améliorations pourraient être apportées pour rehausser les performances des instruments :

- Pour le générateur d'arcs électriques, afin d'étudier des arcs plus longs – des arcs électriques pouvant s'allonger davantage avant d'épuiser l'énergie du générateur de foudre - une augmentation du niveau de tension en fonctionnement pourrait être mise en œuvre avec l'ajout d'autres condensateurs au générateur de foudre. Doubler le nombre de condensateurs permettrait ainsi de multiplier par deux le niveau de tension pour travailler avec 5 kV et éventuellement créer un arc électrique de 3 m de long. Cependant, la surtension transitoire supplémentaire lors de la commutation devra être prise en compte puisque le modèle IGBT actuel utilisé présente une tension limite de 4,5 kV. Ils doivent être remplacés par un modèle IGBT existant, limité à 6,5 kV. Ils peuvent également être connectés en série pour diviser le niveau de tension. Les filtres d'amortissement devraient être repensés pour évacuer la surcharge pour ce nouveau niveau opérationnel. Une solution qui ne nécessitera pas l'augmentation de la tension du banc de condensateurs serait de mettre en œuvre une configuration Buck-boost puisqu'elle optimise l'utilisation de l'énergie magnétique : pour résoudre le problème de la double régulation, une solution avec une technologie de commutation à fréquence plus élevée pourrait être mise en œuvre. En effet, la fréquence de la boucle de rétroaction pourrait être améliorée avec un FPGA et un commutateur plus rapide. Cependant, les besoins en puissance empêchent l'utilisation des technologies les plus rapides disponibles et il faudra encore attendre de nouvelles améliorations de l'IGBT SiC. Néanmoins, la formation d'un canal d'arc plus long n'est pas le paramètre limitant pour l'étude de balayage car il dépasse largement la longueur de l'échantillon d'essai.

- Pour le Railgun, afin de lancer un échantillon de test plus long avec une vitesse accrue, un niveau de courant plus élevé doit être injecté dans le rail. Comme l'augmentation du nombre des ultra-condensateurs en série pour augmenter le niveau de courant maximal doit s'accompagner d'une augmentation du nombre des ultra-condensateurs en parallèle pour augmenter la tension de fonctionnement, le nombre d'ultra-condensateurs doit être multiplié par un facteur 4 pour permettre le dédoublement du niveau de courant actuel. Multiplier par 2 le niveau de courant doublerait approximativement la vitesse d'un échantillon d'essai pour une masse donnée ou multiplierait par 4 la masse pour une vitesse donnée en gardant la même longueur de rails. Cependant, l’injection d’un courant deux fois plus élevé provoquerait des contraintes thermiques et électriques différentes au regard du problème du contact glissant et il est très probable qu’un nouveau point de fonctionnement pour la conception mécanique du circuit et pour l’insertion du projectile dans les rails avec une attention portée sur la force mécanique de contact soit à définir.

- Pour la soufflerie, des équipements plus puissants permettraient d'observer le phénomène pour un écoulement d'air avec une vitesse plus élevée, avec un objectif d’une vitesse d’écoulement de 100 m/s. Une ouverture plus large permettrait d'étudier l'effet de la longueur initiale du canal d'arc sur le phénomène. Une soufflerie présentant une meilleure qualité d'écoulement (une vorticité plus faible, moins de fluctuation de pression et de température de l'écoulement) pourrait également être utilisée.

Concernant l'étude du phénomène, la campagne menée dans ce travail visait à fournir les premières tendances perceptibles observées avec différentes conditions expérimentales. Pour chaque configuration, de deux à quatre expériences ont été menées et pour chaque paramètre d'entrée, une tendance a été observée sur deux à trois points de fonctionnement en faisant la moyenne des résultats des expériences avec une configuration similaire. Cela a déjà abouti à une campagne expérimentale comportant environ 50 essais réalisés. Cependant, il est évident que le nombre d'expériences pour chaque configuration n'est pas suffisant pour donner des résultats statistiques principalement en raison du comportement très chaotique du comportement du canal d'arc lors du balayage. Plus de points de fonctionnement devraient également être utilisés pour mieux évaluer l'influence des paramètres expérimentaux d’entrée. Il serait également intéressant de mener des campagnes expérimentales pour différents matériaux, par exemple des composites de carbone, et pour différentes géométries d'échantillons d'essais aéronautiques. Il est intéressant d'évaluer comment la présence d'une irrégularité de surface, telle qu'une vis d’attache ou une pointe, détourne la trajectoire du pied d'arc pour des questions de protection de l’appareil.

Outre la multiplication des campagnes expérimentales avec les diagnostics développés dans ce travail, la mise en place d'autres diagnostics fins a également été envisagée dans ce travail et rejetée par manque de temps car elle s'accompagnerait de difficultés de mise en œuvre expérimentale ou de développement informatique drastique. Les idées principales sont résumées comme suit :

- Des techniques de visualisation des écoulements ont été envisagées pour mieux caractériser l'interaction entre l'arc électrique et l'écoulement. Cette caractérisation pourrait être facilement mise en œuvre avec des techniques de fumée, comme nous l'avons déjà grossièrement mis en œuvre dans ce travail, accompagnées d'un éclairage par nappe laser. Cela permettrait déjà d'observer des différences entre les interactions des couches de fluide pour le RGE et le WTE. Pour obtenir plus d'informations sur la vitesse absolue des lignes de courant, des diagnostics plus drastiques peuvent être développés comme le PIV (Particle Image Velocity). Ces techniques apporteraient de nouvelles connaissances sur les interactions des pieds d'arc et du canal d'arc avec l'écoulement. Pour être plus précis, les principales questions d'intérêt portent sur l'influence du comportement de l'écoulement : est-ce qu'un écoulement laminaire, une bulle de séparation laminaire ou un écoulement turbulent agit sur le processus de rattachement de la colonne d’arc ou sur le mouvement du pied d’arc.

- Les techniques de spectroscopie de mesure optique pourraient être renforcées afin de collecter des données sur l'ensemble de la colonne d'arc et donc d'évaluer la température des différentes parties du canal d'arc. Cela pourrait être mis en œuvre avec la multiplication des fibres optiques comme effectué dans (McBride (1999)). Le but est de vérifier si une augmentation de température peut être mesurée au voisinage du pied d'arc, si la température du canal d'arc est homogène et si l'on observe des différences entre le RGE et le WTE. Une amélioration de la résolution spectrale doit être envisagée pour permettre des mesures précises de l'élargissement des raies et l'évaluation de la densité électronique de l'arc. Dans le but d'améliorer la résolution temporelle et spatiale, une attention importante doit être portée à la synchronisation de l'acquisition des spectres et du phénomène de balayage.

- Un système de diffusion Thomson induite par laser a également été envisagé car il est potentiellement capable de mesurer la température et la densité électronique de la région de la gaine. En effet, cette technique a été mise en œuvre avec succès pour effectuer des mesures sur la gaine anodique pour des arcs constrictés de 12 mm et un courant de 100 A en interaction avec l'argon (Yang et Heberlein (2007)). La résolution spatiale était de 25 µm et la technique semble adaptée pour mesurer nos niveaux de température et de densité électronique. Cependant elle nécessite un laser et des instruments de collecte de lumière spécifiques ainsi que des conditions expérimentales drastiques pour pouvoir mesurer la diffusion Thomson. La synchronisation des mesures et la fixation de l'arc sur l'échantillon représente une difficulté supplémentaire. De telles mesures de température et de densité électronique dans la région de la gaine de la racine de l'arc cathodique représenteraient cependant une étape importante dans la modélisation du mouvement de la racine de l'arc. En effet, comme la dimension des perturbations du flux d'air dépasse la longueur des gaines de plasma, leur impact sur les processus physiques complexes qui se produisent reste à étudier précisément.

- Des techniques de tomographie sont également envisagées pour évaluer la longueur et la forme 3D de l'arc électrique. En effet, la visualisation directe 2D avec les caméras rapides et les mesures de tension de l'arc ne permettent pas de mesurer la longueur et la forme exacte du canal d'arc. Cette technique était déjà mise en œuvre dans l'équipe pour la reconstruction 3D d'arcs électriques statiques de 10 cm. Cependant, cela nécessite de synchroniser plusieurs caméras à grande vitesse avec le phénomène de balayage et d'autre part l'algorithme de reconstruction est coûteux en calculs. La mesure 3D précise de la longueur du canal d'arc lors du rattachement, ainsi que les mesures électriques, permettraient d'évaluer la résistance électrique, l'énergie et le champ électrique de la portion d'arc éteinte. L'objectif est d'évaluer la perte d'énergie de l'arc électrique lors du raccrochage dans le but d'éventuellement proposer un seuil de raccrochage de l'arc.

- Les techniques de Schlieren pourraient être synchronisées avec le rattachement pour observer la formation et le déplacement de l'onde de choc puis caractériser son interaction avec l'écoulement et son influence sur le mouvement du pied d'arc.

Toutes ces techniques visent à explorer les processus physiques complexes intervenant dans le phénomène pour enrichir les informations fournies par la base de données expérimentales constituée dans ce travail.

References

Abbott, I. H., & Doenhoff, A. E. (1959). Families of Wing Sections. *Theory of Wing Sections, Dover Publications, INC., New York*, 111-123.

Abdelal, G., & Murphy, A. (2014). Nonlinear numerical modelling of lightning strike effect on composite panels with temperature dependent material properties. *Composite Structures*, *109*, 268-278.

AGATE NASA (2002). Lightning direct effect handbook. AGATE-WP 3.1-031027-043.

Ahmed, H. B., Multon, B., & Ruellan, M. (2005). Actionneurs linéaires directs et indirects. *La Revue 3 E. I*, pp-38.

Ahmed, H. B., Multon, B., Bernard, N., & Kerzreho, C. (2007). Le stockage inertiel électromécanique. *La Revue 3 E. I*, pp-18.

Ahmed, T., Amin, M. T., Islam, S. R., & Ahmed, S. (2014). Computational study of flow around a NACA 0012 wing flapped at different flap angles with varying Mach numbers. *Global Journal of Research In Engineering*.

Algaddafi, A., & Elnaddab, K. (2016, November). Modelling and designing the RC snubber circuit for a buck converter and testing its effectiveness. In *2016 International Renewable and Sustainable Energy Conference (IRSEC)* (pp. 554-559). IEEE.

Allen, N. L., and P. N. Micropoulos (1999), Dynamics of streamer propagation in air, J. Phys. D Appl. Phys., 32, 913 – 919.

Al Mutairi, J., ElJack, E., & AlQadi, I. (2017). Dynamics of laminar separation bubble over NACA-0012 airfoil near stall conditions. *Aerospace Science and Technology*, *68*, 193-203.

Amiryar, M. E., & Pullen, K. R. (2017). A review of flywheel energy storage system technologies and their applications. *Applied Sciences*, *7*(3), 286.

Bailey, J. C., & Anderson, R. V. (1987). *Experimental Calibration of a Vector Electric Field Meter Measurement System on an Aircraft*. NAVAL RESEARCH LAB WASHINGTON DC.

Barber, J. P., Bauer, D. P., Jamison, K., Parker, J. V., Stefani, F., & Zielinski, A. (2003). A survey of armature transition mechanisms. *IEEE Transactions on Magnetics*, *39*(1), 47-51.

Bazelyan, E.M., & Raizer, Y.P. (1998). Spark Discharge (1st ed.). Routledge.

Benilov, M. S. (2008). Understanding and modelling plasma–electrode interaction in high-pressure arc discharges: a review. *Journal of Physics D: Applied Physics*, *41*(14), 144001.

Blau, P. J., ASM Handbook, vol 18, Friction, Lubrification and Wear (1992).

Bobashev, S. V., Zhukov, B. G., Kurakin, R. A., Ponyaev, S. A., Reznikov, B. I., & Rozov, S. I. (2010). Generation of high-velocity plasma flows in railgun channels filled with gases of various density. *Technical Physics Letters*, *36*(1), 72-75.

Boeing. (1963). Aircraft Accident Report, Boeing 707-12, N709PA Pan American World Airways, Inc, Near Elkton, Maryland, Dec. 8, 1963. Civil Aeronautic Board File n° 1-0015.

Boukhlifa, M. (2021). Contribution à l’étude des arcs électriques sur réseau HVDC (540 VDC) en conditions aéronautiques. Ph. D. thesis, Université Paris-Saclay.

Boulay. J. (1994). Interactions de la foudre sur un aeronef ´ ONERA Internal Report No 5/6777 PN

Buchroithner, A., Haan, A., Preßmair, R., Bader, M., Schweighofer, B., Wegleiter, H., & Edtmayer, H. (2016, October). Decentralized low-cost flywheel energy storage for photovoltaic systems. In *2016 International Conference on Sustainable Energy Engineering and Application (ICSEEA)* (pp. 41-49). IEEE.

Bublievskii, A.F. (1978) . An approximative model of an electric arc in transverse mutually perpendicular aerodynamicand magnetic fields, J. Engrg. Phys. 35, 1424–1429.

Caldwell, M., & Martinez, L. E. (2005, August). The Sandia lightning simulator: recommissioning and upgrades. In *2005 International Symposium on Electromagnetic Compatibility, 2005. EMC 2005.* (Vol. 2, pp. 368-371). IEEE.

Cassat, A., Corsi, N., Moser, R., & Wavre, N. (2003, September). Direct linear drives: Market and performance status. In *Proceedings of the 4th International Symposium on Linear Drives for Industry Applications* (pp. 1-11). UK: Birmingham.

Castellani, A., Bondiou-Clergerie, A., Lalande, P., Bonamy, A., & Gallimberti, I. (1998). Laboratory study of the bi-leader process from an electrically floating conductor. I. General results. *IEE Proceedings-Science, Measurement and Technology*, *145*(5), 185-192.

Castellani, A., Bondiou-Clergerie, A., Lalande, P., Bonamy, A., & Gallimberti, I. (1998). Laboratory study of the bi-leader process from an electrically floating conductor. Part 2: Bi-leader properties. *IEE Proceedings-Science, Measurement and Technology*, *145*(5), 193-199.

Cayla, F., Freton, P., & Gonzalez, J. J. (2008). Arc/cathode interaction model. *IEEE transactions on plasma science*, *36*(4), 1944-1954.

Cen, J., Yuan, P., Qu, H. and Zhang, T. (2011). Analysis on the spectra and synchronous radiated electric field observation of cloud-to-ground lightning discharge plasma. *J. Plasma Phys.*, 18, 113506.

Chawla, K. K. (2012). Composite Materials. 3rd edition (New York: Spinger Science+Business Media).

Chemartin, L., Lalande, P., Delalondre, C., Cheron, B., & Lago, F. (2011). Modelling and simulation of unsteady dc electric arcs and their interactions with electrodes. *Journal of Physics D: Applied Physics*, *44*(19), 194003.

Chemartin, L., Lalande, P., Peyrou, B., Chazottes, A., Elias, P. Q., Delalondre, C., ... & Lago, F. (2012). Direct effects of lightning on aircraft structure: analysis of the thermal, electrical and mechanical constraints. *AerospaceLab*, (5), p-1.

Chemartin, L. (2008). Modélisation des arcs électriques dans le contexte du Foudroiement des aéronefs. Ph. D. thesis, Université de Rouen.

Chen, J., & Lv, Q. (2018, July). Research Progress on Interface Lubricating of Sliding Electrical Contact with low velocity in Electromagnetic Railgun. In *IOP Conference Series: Earth and Environmental Science* (Vol. 170, No. 4, p. 042089). IOP Publishing.

Chilingarian, A., Chilingaryan, S., Karapetyan, T., Kozliner, L., Khanikyants, Y., Hovsepyan, G., ... & Soghomonyan, S. (2017). On the initiation of lightning in thunderclouds. *Scientific reports*, *7*(1), 1-10.

Christiansen, E.L. & Miller J.E., (2016) NASA Johnson Space Center, IADC Vulnerability Report, IT32-21.

Choi, Y. J., Gray, M., Sirohi, J., & Raja, L. L. (2017). Effects of anchoring and arc structure on the control authority of a rail plasma actuator. *Journal of Physics D: Applied Physics*, *50*(35), 355203.

Clifford, D. W., Crouch, K. E., & Schulte, E. H. (1982). Lightning simulation and testing. *IEEE Transactions on Electromagnetic Compatibility*, (2), 209-224.

Clifford, D. W. (1974). Simulated lightning test shuttle. 03 scale model.[(space shuttle orbiter)].

Crabb, J. A., and J. Latham (1974), Corona from colliding drops as a possible mechanism for the triggering of lightning, Q. J. R. Meteorol. Soc., 100, 191 – 202.

Cui, Y., Niu, C., Wu, Y., Zhu, M., Yang, F., & Sun, H. (2017, October). An investigation of arc root motion by dynamic tracing method. In *2017 4th International Conference on Electric Power Equipment-Switching Technology (ICEPE-ST)* (pp. 647-650). IEEE.

Dai, L., Zhang, Q., Zhong, H., Lin, F., Li, H., Wang, Y., ... & Chen, X. (2015). A 16 MJ compact pulsed power system for electromagnetic launch. *Review of scientific instruments*, *86*(7), 074703.

Daumov, G. Y., & Zhukov, M. F. (1965). Some generalizations relating to the study of electric arcs. *Journal of Applied Mechanics and Technical Physics*, *6*(2), 89-97.

Djakov, B. E., & Holmes, R. (1971). Cathode spot division in vacuum arcs with solid metal cathodes. *Journal of Physics D: Applied Physics*, *4*(4), 504.

Dobbing, J. A. and Hanson. A. W. (1978), A swept stroke experiment with a rocked sled. IEEE International Symposium on Electromagnetic compatibility, pages 390-395.

Duchemin, M., (1986) "Ressorts – Force coaxiale", Techniques de l'Ingénieur, Traité Génie Mécanique, B 5 435, 1986.

Dwyer, J. R. (2003). A fundamental limit on electric fields in air. *Geophysical Research Letters*, *30*(20).

Dwyer, J. R., & Uman, M. A. (2014). The physics of lightning. *Physics Reports*, *534*(4), 147-241.

Eack, K. B., Beasley, W. H., Rust, W. D., Marshall, T. C., & Stolzenburg, M. (1996). Initial results from simultaneous observation of X-rays and electric fields in a thunderstorm. *Journal of Geophysical Research: Atmospheres*, *101*(D23), 29637-29640.

Ecker, G. (1953). Die Stabilisierung des Lichtbogens vor Anode und Kathode. *Zeitschrift für Physik*, *136*(1), 1-16.

Eleni, D. C., Athanasios, T. I., & Dionissios, M. P. (2012). Evaluation of the turbulence models for the simulation of the flow over a National Advisory Committee for Aeronautics (NACA) 0012 airfoil. *Journal of Mechanical Engineering Research*, *4*(3), 100-111.

EUROCAE ED-105 "Aircraft Lightning Test Methods" April 2005

EUROfusion, (2016). Spot on JET Technology: Power Supply

Fair, H. D. (1997). Electromagnetic launch: A review of the US national program. *IEEE Transactions on Magnetics*, *33*(1), 11-16.

Fair H. D. (1999) Electric launch: an inevitable technology". 18th International Symposium on Ballistics, p. 318-333.

Fisher, B., Taeuber, R., & Crouch, K. (1988, January). Implications of a recent lightning strike to a NASA jet trainer. In *26th Aerospace Sciences Meeting* (p. 394).

Fisher, B., Brown, P., Plumer, A., Wunschel A. (1988). Final results of the NASA storm hazards program, Int. Aerospace and Ground Conf. on Lightning and Static Electricity, Oklahoma, USA, NOAA Special Report.

Fowler, R. H., & Nordheim, L. (1928). Electron emission in intense electric fields. *Proceedings of the Royal Society of London. Series A, Containing Papers of a Mathematical and Physical Character*, *119*(781), 173-181.

Froome, K. D. (1948). The rate of growth of current and the behaviour of the cathode spot in transient arc discharges. *Proceedings of the Physical Society (1926-1948)*, *60*(5), 424.

Fuad, Y., De Koning, W. L., & Van Der Woude, J. W. (2001). Pulse-width modulated dc-dc converters. *International journal of electrical engineering education*, *38*(1), 54-79.

Gallant, J., & Lehmann, P. (2005). Experiments with brush projectiles in a parallel augmented railgun. *IEEE Transactions on Magnetics*, *41*(1), 188-193.

Gault. D. E. (1949). Boundary-layer and stalling characteristics of the NACA433 63-009 airfoil section, Technical Note NACA-TN-1894, National Advisory 434 Committee for Aeronautics. 435.

Gaster. M. (1969). The structure and behaviour of laminar separation bubbles, 436 Tech. Rep. R.&M. No. 3595, British ARC, 437.

Giacoletto,. L.J (1977). Electronic Designer's Handbook, McGraw-Hill Book Company

Go, B. S., Le, D. V., Song, M. G., Park, M., & Yu, I. K. (2018). Design and electromagnetic analysis of an induction-type coilgun system with a pulse power module. *IEEE Transactions on plasma science*, *47*(1), 971-976.

Gray, M. D., Choi, Y. J., Sirohi, J., & Raja, L. L. (2015). Structure of propagating arc in a magneto-hydrodynamic rail plasma actuator. *Journal of Physics D: Applied Physics*, *49*(1), 015202.

Gray, M., Choi, Y. J., Sirohi, J., & Raja, L. L. (2018). Study of the dynamic behavior of the rail plasma actuator arc. *Journal of Physics D: Applied Physics*, *51*(31), 315203.

Griem, H. R. (1997). *Principles of Plasma Spectroscopy*. (Cambridge: Cambridge University Press).

Griffiths, R. F., and J. Latham (1972), The emission of corona from falling drops, J. R. Meteorol. Soc. Jpn., 50, 416 – 422.

Griffiths, R. F., and C. T. Phelps (1976), A model for lightning initiation arising from positive corona streamer development, J. Geophys. Res., 81(21), 3671 – 3676.

Guerra-Garcia, C., Nguyen, N. C., Peraire, J., & Martinez-Sanchez, M. (2016). Arc reattachment driven by a turbulent boundary layer: implications for the sweeping of lightning arcs along aircraft. *Journal of Physics D: Applied Physics*, *49*(37), 375204.

Guile, A. E., & Mehta, S. F. (1957). Arc movement due to the magnetic field of current flowing in the electrodes. *Proceedings of the IEE-Part A: Power Engineering*, *104*(18), 533-540.

Guile, A. E., & Naylor, K. A. (1968, September). Further correlation of experimental data for electric arcs in transverse magnetic fields. In *Proceedings of the Institution of Electrical Engineers* (Vol. 115, No. 9, pp. 1349-1354). IET.

Guile, A. E. (1971, September). Arc-electrode phenomena. In *Proceedings of the Institution of Electrical Engineers* (Vol. 118, No. 9, pp. 1131-1154). IET.

Guile, A. E., & Hitchcock, A. H. (1981). Effect of transverse magnetic field on erosion rate of cathodes of rotating arcs. *IEE Proceedings A-Physical Science, Measurement and Instrumentation, Management and Education-Reviews*, *128*(2), 117-122.

Gurevich, A. V., G. M. Milikh, and R. Roussel-Dupre (1992), Runaway electron mechanism of air breakdown and preconditioning during a thunderstorm, Phys. Lett. A, 165, 463 – 468.

Gurevich, A. V., L. M. Duncan, Y. V. Medvedev, and K. P. Zybin (2002), Radio emission due to simultaneous effect of runaway breakdown and extensive atmospheric showers, Phys. Lett. A, 301, 320 – 326.

[H2W] https://www.h2wtech.com/category/linear-induction#productInfo1

Heberlein, J., Mentel, J., & Pfender, E. (2010). The anode region of electric arcs: a survey. *Journal of Physics D: Applied Physics*, *43*(2), 023001.

Hirano, Y., Katsumata, S., Iwahori, Y., & Todoroki, A. (2010). Artificial lightning testing on graphite/epoxy composite laminate. *Composites Part A: Applied Science and Manufacturing*, *41*(10), 1461-1470.

Holm, R., (1967). Electric Contacts: Theory and Application,

Hsu, K. C., Etemadi, K., & Pfender, E. (1983). Study of the free-burning high-intensity argon arc. *Journal of applied physics*, *54*(3), 1293-1301.

Hundertmark, S., Vincent, G., Simicic, D., & Schneider, M. (2017). Increasing launch efficiency with the PEGASUS launcher. *IEEE Transactions on Plasma Science*, *45*(7), 1607-1613.

Jamet F. & Wegner V., (1989) Les canons électriques. Revue scientifique et technique de la Défense, Vol. 2, p. 69-99.

Jones. B. M. (1933). An experimental study of the stalling of wings, Tech. Rep. 431 ARC R&M No. 1588, Aeronautical Research Committee. 432.

Jones, C. C. R., Rowse, D., & Odam, G. A. M. (2001). *Probabilities of catastrophe in lightning hazard assessments* (No. 2001-01-2877). SAE Technical Paper.

Kadivar, A., Niayesh, K., Støa-Aanensen, N. S., & Abid, F. (2020). Metal vapor content of an electric arc initiated by exploding wire in a model N2 circuit breaker: Simulation and experiment. *Journal of Physics D: Applied Physics, 54*(5), 055203.

Katsuki, S., Akiyama, H., Eguchi, N., Sueda, T., Soejima, M., Maeda, S., & Sato, K. N. (1995). Augmented railgun using a permanent magnet. *Review of scientific instruments, 66*(8), 4227-4232.

Keen, B.E.; Kupschus, P. (1987). JET Joint Undertaking Progress Report, JET-Operation and Developement: Pulsed Power Supplies for JET Coils; JET Joint Undertaking: Abingdon, UK.

Kelkar, M., & Heberlein, J. (2000). Physics of an arc in cross flow. *Journal of Physics D: Applied Physics*, *33*(17), 2172.

King, L. A., (1961).The voltage gradient of the free burning arc in air or nitrogen, Proceedings of the 5th International Conference on Ionization Phenomena in Gases, Munich

Koka, T. R., & Mathew, A. T. (2016). Simulation driven quantification of projectile uncertainties of a single stage compressed gas gun during design. In *NAFEMS India Conference 2016 Engineering Modeling, Analysis, Simulation and 3D Printing*.

Kolsky, H. (1949). An investigation of the mechanical properties of materials at very high rates of loading. *Proceedings of the physical society. Section B, 62*(11), 676.

Kovalchuk, B. M., Kharlov, A. V., Zherlytsyn, A. A., Kumpyak, E. V., & Tsoy, N. V. (2016). Pulse generator with intermediate inductive storage as a lightning simulator. *Review of Scientific Instruments*, *87*(6), 063505.

Kramida, A., Ralchenko, Yu., Reader, J., and NIST ASD Team (2021). NIST Atomic Spectra Database (ver. 5.9), [Online]. Available: https://physics.nist.gov/asd. National Institute of Standards and Technology, Gaithersburg, MD. DOI: https://doi.org/10.18434/T4W30F

Kurucz, R.L. and Bell, B. (1995). *Atomic Line Data Kurucz CD-ROM No. 23.* (Cambridge: Smithsonian Astrophysical Observatory).

Lago, F., Gonzalez, J. J., Freton, P., & Gleizes, A. (2005). A numerical modelling of an electric arc and its interaction with the anode: Part I. The two-dimensional model. *Journal of Physics D: Applied Physics*, *37*(6), 883.

Lalande, Ph., Bondiou-Clergerie, A. and Laroche, P. (1999) Analysis of available in-flight measurements of lightning strikes to aircraft. Int. Conf. on Lightning and Static Electricity, Toulouse, France.

Landau, L. D., Lifshitz, E. M., Atkin, R. J., & Fox, N. (2020). The theory of elasticity. In *Physics of Continuous Media* (pp. 167-178). CRC Press.

Larsson, A., Lalande, P., Bondiou-Clergerie, A., & Delannoy, A. (2000). The lightning swept stroke along an aircraft in flight. Part I: thermodynamic and electric properties of lightning arc channels. *Journal of Physics D: Applied Physics*, *33*(15), 1866.

Larsson, A. (2002). The interaction between a lightning flash and an aircraft in flight. *Comptes Rendus Physique*, *3*(10), 1423-1444.

Lee, T. H. (1959). T-F theory of electron emission in high-current arcs. *Journal of Applied Physics*, *30*(2), 166-171.

Lehmann, P., Peter, H., & Wey, J. (2001). First experimental results with the ISL 10 MJ DES railgun PEGASUS. *IEEE Transactions on Magnetics*, *37*(1), 435-439.

Leichauer, P., (2019) Design and development of lightning waveform generators . Ph.D thesis. Cardiff University – Morgan-Botti Lightning Laboratory (MBLL).

Le Vine, D. M. (1980). Sources of the strongest RF radiation from lightning. *Journal of Geophysical Research: Oceans*, *85*(C7), 4091-4095.

Lewis, T. J., & Secker, P. E. (1961). Influence of the cathode surface on arc velocity. *Journal of Applied Physics*, *32*(1), 54-64.

Li, X., Luo, Y., Duan, Y., Liu, B., Huang, Y., & Sun, F. (2018, November). Stray inductance extraction of high-power IGBT dynamic test platform and verification of physical model. In *2018 IEEE International Power Electronics and Application Conference and Exposition (PEAC)* (pp. 1-6). IEEE.

Lichun, C., & Jiazhi, X. (1982). Motion of magnetically driven arcs on oxidized electrodes. *IEEE Transactions on Components, Hybrids, and Manufacturing Technology*, *5*(1), 86-89.

Ma, S., Gao, H., Zheng, S. and Wu, L. (2011). Spectroscopic measurement of temperatures in pulsed TIG welding arcs. *J. Phys. D: Appl. Phys.*, 44, 405202.

Maecker, H. (1955). plasmastromungen in lichtbogen infolge eigenmagnetitischer compression. *Journal of Physics* , *141* (1-2), 198-216.

Maecker, H. H. (1971). Principles of arc motion and displacement. *Proceedings of the IEEE*, *59*(4), 439-449.

Mao, R. H., Meguid, S. A., & Ng, T. Y. (2008). Transient three dimensional finite element analysis of a bird striking a fan blade. *International Journal of Mechanics and Materials in Design*, *4*(1), 79-96.

Marshall, T. C., McCarthy, M. P., and Rust, W. D. (1995), Electric field magnitudes and lightning initiation in thunderstorms, *J. Geophys. Res.*, 100(D4), 7097– 7103

Mazur, V., Fisher, B. D., & Gerlach, J. C. (1984). Lightning strikes to an airplane in a thunderstorm. *Journal of Aircraft*, *21*(8), 607-611.

McBride, J. W., Weaver, P. M., & Jeffery, P. A. (1998). Arc root mobility during contact opening at high current. *IEEE Transactions on Components, Packaging, and Manufacturing Technology: Part A*, *21*(1).

McBride, J. W. and Jeffery, P. A. (1999). Anode and cathode arc root movement during contact opening at high current, in *IEEE Transactions on Components and Packaging Technologies*, vol. 22, no. 1, pp. 38-46.

McCullough, G. B., & Gault, D. E. (1951). *Examples of three representative types of airfoil-section stall at low speed* (No. NACA-TN-2502).

McNab, I. R. (2003). Launch to space with an electromagnetic railgun. *IEEE Transactions on magnetics*, *39*(1), 295-304.

Meyer, T. N. (1977). Rail arcs: Interaction of magnetic and fluid dynamic forces. *IEEE Transactions on Power Apparatus and Systems*, *96*(4), 1324-1328.

Moreau, J. P., Alliot, J. C., & Mazur, V. (1992). Aircraft lightning initiation and interception from in situ electric measurements and fast video observations. *Journal of Geophysical Research: Atmospheres*, *97*(D14), 15903-15912.

Mu, Y., Yuan, P., Wang, X. and Dong, C. (2016). Temperature distribution and evolution characteristic in lightning return stroke channel. *J. Atmos. Sol. Terr. Phys.* 145 98-105.

Murphy, E. L., & Good Jr, R. H. (1956). Thermionic emission, field emission, and the transition region. *Physical review*, *102*(6), 1464.

Mustapha, B. M., & Bababe, A. B. Propulsion of Magnetic Levitation Train. *International Journal of Enhanced Research in Science, Technology & Engineering ISSN*, 2319-7463.

Novak, J. P., & Fuchs, V. (1974, January). Dynamic equation and characteristics of a short arc moving in a transverse magnetic field. In *Proceedings of the Institution of Electrical Engineers* (Vol. 121, No. 1, pp. 81-84). IET.

Ogasawara, T., Hirano, Y., & Yoshimura, A. (2010). Coupled thermal–electrical analysis for carbon fiber/epoxy composites exposed to simulated lightning current. *Composites Part A: Applied Science and Manufacturing*, *41*(8), 973-981.

Oh, L. L., and Schneider, S. D. (1975). Lightning strike performance of thin metal skins. Proceedings of the 1975 Conference on Lightning and Static Electricity (ICOLSE).

Parker, J. V. (1982). Electromagnetic projectile acceleration utilizing distributed energy sources. *Journal of Applied Physics*, *53*(10), 6710-6723.

Paredes, M., (2000) Développement d'outils d'assistance à la conception optimale des liaisons élastiques par ressorts. INSA de Toulouse, France.

Parker, J. V. (1989). Why plasma armature railguns don't work (and what can be done about it). *IEEE Transactions on Magnetics*, *25*(1), 418-424.

Pellerin, S., Richard, F., Chapelle, J., Cormier, J. M., & Musiol, K. (2000). Heat string model of bi-dimensional dc Glidarc. *Journal of Physics D: Applied Physics*, *33*(19), 2407.

Petersen, D., Bailey, M., Beasley, W. H., and Hallett, J. (2008), A brief review of the problem of lightning initiation and a hypothesis of initial lightning leader formation, *J. Geophys. Res.*, 113, D17205.

Peyrou, B. (2012). Modélisation MHD d'un arc de Foudroiement d'aéronef. Ph. D. thesis, Université de Rouen.

Pilz, N., Adirim, H., Lo, R., & Schildknecht, A. (2004, October). Hot Water Propulsion for Horizontal Rocket Assisted Take-Off Systems for Future Reusable Launch Vehicles. In *ESA Special Publication* (Vol. 557).

Pitts, F. L., & Thomas, M. E. (1981). IN-FLIGHT DIRECT STRIKE LIGHTNING RESEARCH. The 1980 Aircraft Safety and Operating Problems, Part 1, 359.

Plassard, F., Mespoulet, J., & Hereil, P. (2011, May). Analysis of a single stage compressed gas launcher behaviour: from breech opening to sabot separation. In *8th European LS-DYNA Users Conference* (pp. 1-11).

Plumer, J. A. (1973). Lightning effects on general aviation aircraft. GENERAL ELECTRIC CO PITTSFIELD MASS HIGH VOLTAGE LAB.

Plumer, J. A. (2012, September). Laboratory test results and natural lightning strike effects: How well do they compare. In *2012 International Conference on Lightning Protection (ICLP)* (pp. 1-17). IEEE.

Polhamus, E. C. (1996). A survey of Reynolds number and wing geometry effects on lift characteristics in the low speed stall region. NASA CR 4745, June 1996

Rahner, C., Al-Qureshi, H. A., Stainer, D., Hotza, D., & Fredel, M. C. (2014). Numerical evaluation of a light-gas gun facility for impact test. *Modelling and Simulation in Engineering, 2014*.

Ramier, J. (2004). *Comportement mécanique d'élastomères chargés: influence de l'adhésion charge-polymère: influence de la morphologie* (Doctoral dissertation, Lyon, INSA).

Rashleigh, S. C., & Marshall, R. A. (1978). Electromagnetic acceleration of macroparticles to high velocities. *Journal of Applied Physics*, *49*(4), 2540-2542.

Reazer, J. S., Serrano, A. V., Walko, L. C., & Burket, C. H. (1987). Analysis of correlated electromagnetic fields and current pulses during airborne lightning attachments. *Electromagnetics*, *7*(3-4), 509-539.

Reess, T., P. Ortega, A. Gibert, P. Domens, and P. Pignolet (1995), An experimental study of negative discharge in a 1.3 m point-plane air gap: The function of the space stem in the propagation mechanism, J. Phys. D Appl. Phys, 28, 2306 – 2313

Richards, C. N., and G. A. Dawson (1971), The hydrodynamic instability of water drops falling at terminal velocity in vertical electric fields, J. Geophys. Res., 76(15), 3445 – 3455.

Robertson, R. M. (1938). The force on the cathode of a copper arc. *Physical Review*, *53*(7), 578.

Rodriguez, E. (2006). *Etude du comportement des ressorts coniques et ressorts de torsion en vue du développement d'outils de synthèse associés* (Doctoral dissertation, Institut National des Sciences Appliquées de Toulouse).WAHL, A. M. "Mechanical Springs", Mac Graw Hill, 1963.

Roussel, M., Tristant, F., Fustin, F., Even, A., Chazottes, A., & Lalande, P. (2015). In-service Falcon lightning strike events.

Roussel, O. (2015). *Planification de mouvement pour tiges élastiques* (Doctoral dissertation, Université Paul Sabatier-Toulouse III).

Rustan, P. L. and Moreau, J. P. (1985). Aircraft Lightning Attachment on low altitudes – 10th international aerspace and ground conference on lightning and static electricity.

SAE ARP 5416 "Aircraft Lightning Test Methods" SAE International March 2005.

Schmitt, A. G. (1998). *Evaluation des forces exercées sur des projectiles accélérés par un lanceur électromagnétique à rails* (Doctoral dissertation, Mulhouse).

Schneider, M., Eckenfels, D., & Hatterer, F. (2003a). Transition in brush armatures. *IEEE transactions on magnetics*, *39*(1), 76-81.

Schneider, M., Eckenfels, D., & Nezirevic, S. (2003b). Doppler-radar: A possibility to monitor projectile dynamics in railguns. *IEEE transactions on magnetics*, *39*(1), 183-187.

Secker, P. E., & Guile, A. E. (1959). Arc movement in a transverse magnetic field at atmospheric pressure. *Proceedings of the IEE-Part A: Power Engineering*, *106*(28), 311-320.

Severns, R., & Reduce, E. M. I. (2009). Design of snubbers for power circuits. *International Rectifier Corporation*.

Sharma, P., & Bhatti, T. S. (2010). A review on electrochemical double-layer capacitors. *Energy conversion and management*, *51*(12), 2901-2912.

Sheldahl, R. E., & Klimas, P. C. (1981). *Aerodynamic characteristics of seven symmetrical airfoil sections through 180-degree angle of attack for use in aerodynamic analysis of vertical axis wind turbines* (No. SAND-80-2114). Sandia National Labs., Albuquerque, NM (USA).

Singer, I. L., Veracka, M. J., Boyer, C. N., & Neri, J. M. (2010). Wear behavior of lubricant-conditioned copper rails and armatures in a railgun. *IEEE Transactions on Plasma Science*, *39*(1), 138-143.

Singh, J. P., & Verma, S. (2017). *Woven Terry Fabrics: Manufacturing and Quality Management*. Woodhead Publishing.

Sommerville, J. M. The Electric Arc (Methuen and Company, Ltd, London, 1959).

Sousa Martins,. S. (2016a) Experimental and theoretical studies of lightning arcs and their interaction with aeronautical materials. PhD thesis, Université Paris Saclay.

Sousa Martins, R.., Chemartin, L., Zaepffel, C., Lalande, P., & Soufiani, A. (2016b). Electrical and hydrodynamic characterization of a high current pulsed arc. *Journal of Physics D: Applied Physics*, *49*(18), 185204.

Sousa Martins, R., Zaepffel, C., Chemartin, L., Lalande, Ph. and Soufiani, A. (2016c). Characterization of a high-pulsed arc using optical emission spectroscopy. *J. Phys. D: Appl. Phys.*, 49, 415205.

Sousa Martins, R., Zaepffel, C., Chemartin, L., Lalande, Ph. and Lago, F. (2019). Characterization of high-pulsed arcs ranging from 100-250 kA peak. *J. Phys. D: Appl. Phys.*, 52, 185203.

Sousa Martins, R., Rivière, P., Zaepffel, C., Passilly, F., & Soufiani, A. (2020). Analysis of energy exchanges during the interaction between pulsed lightning arcs and metallic plates. *Journal of Applied Physics*, *128*(22), 223301.

Starr, S. O., Youngquist, R. C., & Cox, R. B. (2013). A low voltage “railgun”. *American Journal of Physics*, *81*(1), 38-43.

Spink, H. C., & Guile, A. E. (1965). The movement of high-current arcs in transverse external and self-magnetic fields in air at atmospheric pressure.

Stock, M. G., Krehbiel, P. R., Lapierre, J., Wu, T., Stanley, M. A., and Edens, H. E. (2017), Fast positive breakdown in lightning, *J. Geophys. Res. Atmos.*, 122, 8135– 8152,

Sunabe, K., & Inaba, T. (1990). Electric and moving characteristics of DC kilo-ampere high current arcs in atmospheric air. *The transactions of the Institute of Electrical Engineers of Japan. A*, *109*(3), 95-102.

Swanson, R. C., & Langer, S. (2016). *Comparison of NACA 0012 laminar flow solutions: structured and unstructured grid methods*. National Aeronautics and Space Administration, Langley Research

Sweers, G., Birch, B. and Gokcen, J. (2012). Lightning strikes: protection, inspection and repair. Aero Quarterly, 4, QTR 04-12.

Szente, R. N., Munz, R. J., & Drouet, M. G. (1988). Arc velocity and cathode erosion rate in a magnetically driven arc burning in nitrogen. *Journal of Physics D: Applied Physics*, *21*(6), 909.

Tamura, H., Sawaoka, A. B., Oda, Y., Onozuka, M., Kuribayashi, S., & Shimizu, K. (1992). Laser-prearc railgun: Development for the application to a fuel pellet injector of a nuclear fusion reactor. *Review of scientific instruments*, *63*(5), 3102-3107.

Tanaka, S., Sunabe, K., Goda, Y.,(2000). Three dimensional behaviour analysis of DC free arc column by image processingtechnique, Paper No A41, XIII Int. Conf. on Gas Discharges and their Applications Glasgow, UK.

Tholin, F., Chemartin, L. and Lalande, Ph. (2013). Numerical investigation of the interaction of a lightning and an aeronautic skin during the pulsed arc phase. Int. Conf. on Lightning and Static Electricity, Toulouse, France

Uhlig F, Jones C, Vile M. and Tagliana B. (1999). Setup and statistical analysis of an database on in-flight lightning strike incidents Int. Conf. on Lightning and Static Electricity, Toulouse, France.

Uranga A. (2011). Investigation of transition to turbulence at low Reynolds numbers using Implicit Large Eddy Simulations with a Discontinuous Galerkin method . Ph. D. thesis, MIT.

Valensi, F., Pellerin, S., Boutaghane, A., Dzierzega, K., Zielinska, S., Pellerin, N. and Briand, F. (2010). Plasma diagnostics in gas metal arc. J. Phys. D: Appl. Phys., 43, 434002.

Vermorel, R., Vandenberghe, N., & Villermaux, E. (2007). Rubber band recoil. *Proceedings of the Royal Society A: Mathematical, Physical and Engineering Sciences*, *463*(2079), 641-658.

Vérité, J. C., Boucher, T., Comte, A., Delalondre, C., Robin-Jouan, P., Serres, E., ... & Fievet, C. (1995). Arc modelling in SF6 circuit breakers. *IEE Proceedings-Science, Measurement and Technology*, *142*(3), 189-196.

Vlastós, A. E. (1969). Restrike channel resistance of thin exploding wires. *Journal of Applied Physics*, *40*(12), 4752-4760.

Vlastós, A. E. (1972). The resistance of sparks. *Journal of Applied physics*, *43*(4), 1987-1989.

Wang, Y. (2017). Multiphysics analysis of lightning strike damage in laminated carbon/glass fiber reinforced polymer matrix composite materials: A review of problem formulation and computational modeling. *Composites Part A: Applied Science and Manufacturing*, *101*, 543-553.

Weizel, W., & Rompe, R. (1947). Theorie des elektrischen Funkens. *Annalen der Physik*, *436*(6), 285-300.

Wilson, C. T. R. (1924), The electric field of a thundercloud and some of its effects, Proc. Phys. Soc. London, 37, 32D – 37D, doi:10.1088/1478-7814/ 37/1/314.

Wilson, C. T. R. (1925), The acceleration of b-particles in strong electric fields such as those of thunderclouds, Proc. Cambridge Philos. Soc., 22, 534 – 538.

Winslow, J., Otsuka, H., Govindarajan, B., & Chopra, I. (2018). Basic understanding of airfoil characteristics at low Reynolds numbers (10 4–10 5). *Journal of Aircraft*, *55*(3), 1050-1061.Schlichting, Hermann (1979), *Boundary-Layer Theory*, 7th ed., McGraw Hill, New York, U.S.A.

Wong, C. W., & Rinoie, K. (2009). Bubble Burst Control for Stall Suppression on a NACA 631-012 Airfoil. *Journal of aircraft*, *46*(4), 1465-1468.

Wutzke, S. A., Pfender, E., & Eckert, E. R. G. (1967). Study of electric arc behavior with superimposed flow. *AIAA journal*, *5*(4), 707-713.

Wutzke, S. A., Pfender, E., & Ecker, E. R. G. (1968). Symptomatic behavior of an electric arc with a superimposed flow. *Aiaa Journal*, *6*(8), 1474-1482.

Xiangteng, M. A., Fusheng, W. A. N. G., Han, C. H. E. N., Donghong, W. A. N. G., & Bin, X. U. (2020). Thermal damage analysis of aircraft composite laminate suffered from lightning swept stroke and arc propagation. *Chinese Journal of Aeronautics*, *33*(4), 1242-1251.

Yamashita, Y., Furuta, J., Inamori, S., & Kobayashi, K. (2017, July). Design of RCD snubber considering wiring inductance for MHz-switching of SiC-MOSFET. In *2017 IEEE 18th Workshop on Control and Modeling for Power Electronics (COMPEL)* (pp. 1-6). IEEE.

Yang, G., Cronin, P., Heberlein, J. V., & Pfender, E. (2006). Experimental investigations of the anode boundary layer in high intensity arcs with cross flow. *Journal of Physics D: Applied Physics*, *39*(13), 2764.

Yang, G., & Heberlein, J. V. (2007). The anode region of high intensity arcs with cold cross flow. *Journal of Physics D: Applied Physics*, *40*(18), 5649.

Zhu, C. Y., & Li, B. M. (2020). Analysis of sliding electric contact characteristics in augmented railgun based on the combination of contact resistance and sliding friction coefficient. *Defence Technology*, *16*(4), 747-752

université PARIS-SACLAY

DOCTORAL SCHOOL
Electrical, Optical, Bio:
Physics and Engineering
(EOBE)

Titre : Etude expérimentale du phénomène de balayage de l’arc électrique lors du foudroiement d’un aéronef

Mots clés : arcs électriques, foudre, générateur haute puissance, railgun, diagnostics électriques et optiques

Résumé : Lors du foudroiement d’un aéronef, il y a un mouvement relatif entre l’arc électrique de foudre et l’aéronef, qui peut voler jusqu’à 100 m/s en phases de décollage ou d’atterrissage, alors qu’il ne peut éviter l’impact. Ainsi le point d’attachement de la foudre n’est pas statique mais peut se mouvoir sur toute la surface de l’avion – on parle de balayage de l’arc électrique de foudre. Face à ce danger, les avionneurs doivent prévoir de protéger toutes les parties de l’aéronef d’autant plus que les nouveaux modèles d’avions en carbone supportent moins les dommages thermiques et électriques causés que leurs prédécesseurs recouverts d’aluminium. Actuellement, le manque de retour d’expérience ne permet pas de justifier le caractère prédictif des outils de simulation existants de balayage d’arc électrique. L’objectif de cette thèse est dans un premier temps de reproduire une expérience en laboratoire répétable et représentative d’un foudroiement d’aéronef afin de réaliser dans un second temps une base de données expérimentale sur les grandeurs physiques mesurables du phénomène de balayage dans des situations standardisées. Cette base expérimentale pourra servir de référence pour des protections aéronautiques ou pour valider des outils de simulation.

Pour reproduire une expérience représentative du foudroiement d’un aéronef, un générateur électrique haute puissance de type Buck capable de reproduire un arc électrique respectant la norme de foudre aéronautique est conçu, réalisé et testé. Des arcs de quelques kV représentatifs de l’onde continue de foudre – une consigne de 400 A pendant 50 ms – sont formés et étirés jusqu’à 1.50 m afin de recréer une colonne d’arc libre. La propulsion de plaques test de matériau aéronautiques à des vitesses de plusieurs dizaines de m/s est rendue possible par la conception, le développement et la réalisation d’un lanceur électromagnétique de type Railgun: avec un banc de supercondensateurs, l’injection d’un courant de 25 kA pendant environ 50 ms dans un système de rails de Laplace permet de projeter des plaques de quelques centaines de g aux vitesses voulues en 2 m d’accélération. Le couplage du générateur électrique et du lanceur électromagnétique permet alors la reproduction et l’étude du phénomène de balayage: des mesures électriques et des diagnostics optiques par caméras rapides et spectroscopie permettent de remonter aux grandeurs électriques, hydrodynamiques et thermodynamiques de la colonne d’arc en mouvement ainsi que de caractériser le déplacement du point d’impact sur le matériau aéronautique. Ces mesures et analyses sont aussi effectuées avec soufflerie qui provoque le mouvement de l’arc sur la plaque test fixe en remplacement du Railgun. Ceci permet d’établir une comparaison entre les deux modes de reproduction d’un mouvement relatif arc électrique/plaque aéronautique.